Fabián Antonio Torres Méndez

Numerical Simulation of Gas Flooding, Water-Alternating-Gas Injection, and Foam-Assisted Chemical Flooding

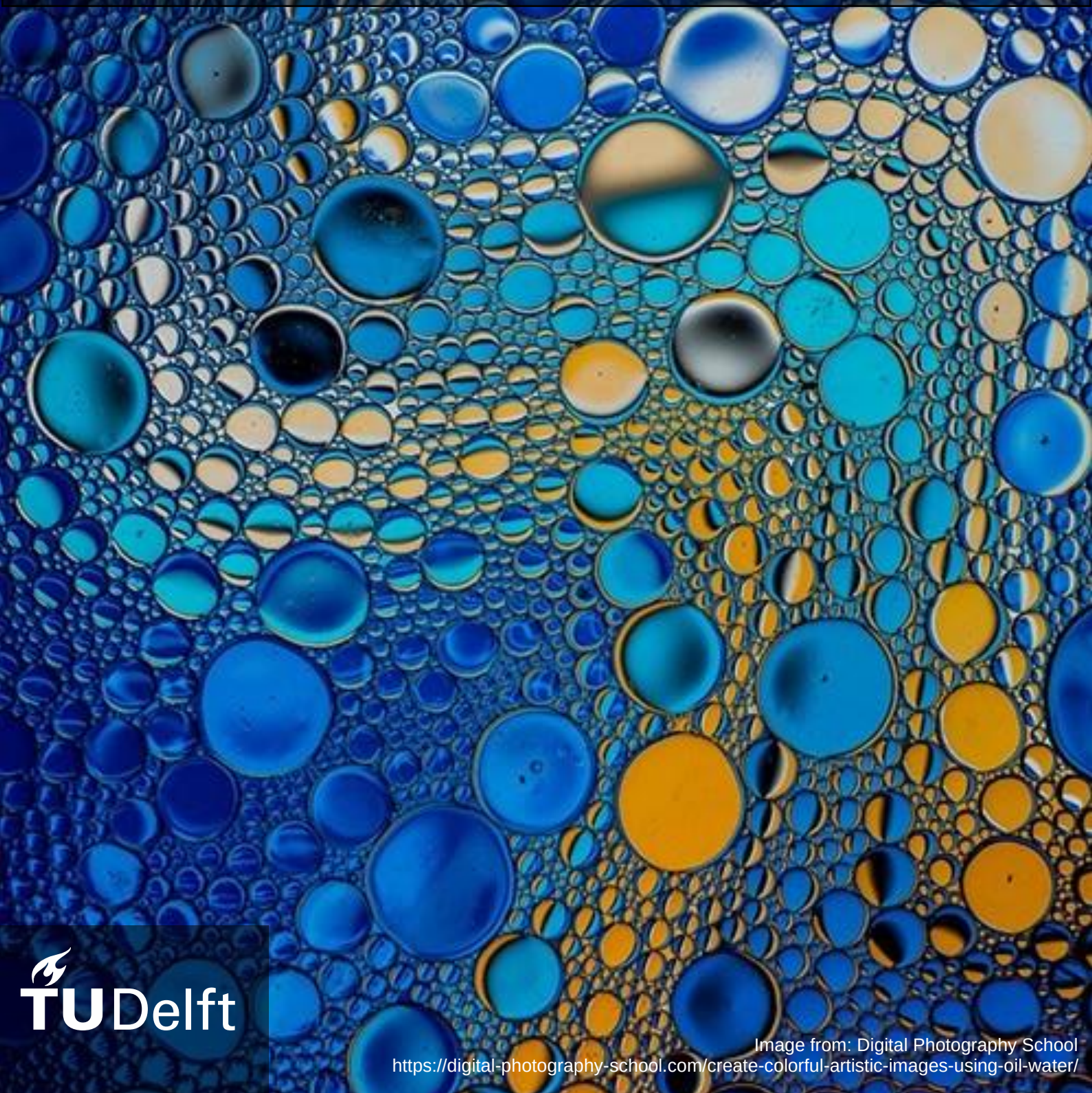

TU Delft

Image from: Digital Photography School
https://digital-photography-school.com/create-colorful-artistic-images-using-oil-water/

Numerical Simulation of Gas Flooding, Water-Alternating-Gas Injection, and Foam-Assisted Chemical Flooding

By

Fabián Antonio Torres Méndez

in partial fulfilment of the requirements for the degree of

Master of Science
in Applied Earth Sciences – Petroleum Engineering

at the Delft University of Technology,
to be defended publicly on Thursday, September 26, 2019 at 3:00 PM.

Student number:	4748859	
Supervisors:	Prof. Dr. P. L. J. Zitha,	Delft University of Technology
	M. T. G. Janssen, MSc, (PhD candidate)	Delft University of Technology
Thesis committee:	Prof. Dr. P. L. J. Zitha,	Delft University of Technology
	Prof. Dr. W. R. Rossen,	Delft University of Technology
	Prof. Dr. F. J. Vermolen,	Delft University of Technology
	Prof. Dr. G. Chapiro,	Universidade Federal de Juiz de Fora
	M. T. G. Janssen, MSc, (PhD candidate)	Delft University of Technology

ABSTRACT

Chemical Enhanced Oil Recovery (CEOR) methods can increase the oil recovery of a reservoir to more than 60% of the volumes originally in-situ. Typical oil recoveries range from 20% to 40% of OIIP under traditional primary and secondary recovery stages, the understanding of the mechanisms that control such complex processes is essential considering the continuously growing worldwide energetic demand. History matching of core flooding experiments data through numerical modelling is a powerful tool to understand the physical parameters and mechanisms that control the flow of fluids in novel recovery strategies as Foam-Assisted Chemical Flooding (FACF) in which the effects of oil/water interfacial tension generated by surfactant are combined with mobility control provided by foam.

This report presents the mechanistic modelling study of seven experiments on different core flooding techniques including continuous gas injection, Water-Alternating-Gas injection (WAG), surfactant injection and Foam-Assisted Chemical Flooding (FACF) on Bentheimer sandstone cores. During the experiments, CT scan images were acquired to monitor the evolution of saturation distributions, starting from the primary drainage stage. A 1D model was built for each experiment to history match the saturations revealed by the CT scan imaging along the cores at different pore volumes injected (PVI), as well as observed pressure drops, production fractions and oil recovery. Good agreement between simulation results and experiments was obtained, where minor mismatches in breakthrough times (0.04 ± 0.02 PVI) for some experiments.

For the history match of primary drainage and forced imbibition, the parameters of Brooks-Corey equation for calculating relative permeabilities were obtained from a regression analysis on the available observed data. This led to the conclusion that actual residual saturations are lower than the average saturations reported at the end of each flooding stage.

History-matching of the continuous gas injection at waterflooding residual oil saturation and WAG at connate water saturation experiments, demonstrated that the initial water saturation in secondary and tertiary gas injection strategies is a parameter that greatly controls gas mobility. Gas trapping and its effect on the flooding was confirmed for the WAG experiment.

The mechanistic modelling of surfactant injection at under-optimum salinity conditions allowed to conclude that the geochemical modelling to determine initial ionic concentrations in the aqueous phase can be neglected in absence of naphthenic acids in the oleic phase, even when alkali is present in the solution. This stage of the study allowed to conclude that the shape and size of the oil bank formed after mobilization of residual oil is greatly controlled by a proper numerical representation of the phase behavior in the oil/microemulsion system, whilst other features as oil bank velocity are controlled by surfactant adsorption. Relative permeability curves at low trapping numbers (forced imbibition) and high trapping numbers (under-optimum salinity conditions) were obtained.

Finally, history match of the drive foam in FACF led to the conclusion that the local equilibrium model for foam model implemented in UTCHEM may not be able to cover the entire range of possible mechanisms controlling the foam formation. The mechanism by which foam is generated due to increase in interstitial velocity and local pressure drop in zones of reduced effective porosity near a previously formed oil bank.

Keywords: Core flood history match, mechanistic modelling, immiscible gas injection, WAG, FACF, foam, mobility control, EOR, CEOR, Bentheimer sandstone, CT scan.

Acknowledgments

The author would like to thank Professor Dr. Pacelli Zitha and PhD candidate Martijn T. G. Janssen from Technische Universiteit Delft – TU Delft, whose guidance and encouragement were key aspects in overcoming the faced challenges during the completion of this research. I will remember this team of professionals not only for providing me with vital experimental data, lessons learnt and for helping me to shape the strategy to obtain important conclusions for the project but for exponentially boosting my learning curve and further nurture my passion for Reservoir Engineering.

Table of Contents

List of Figures

List of Tables

1 INTRODUCTION

1.1 Background

The productive life of an oil field can be divided into three main stages: primary, secondary and tertiary recovery. Primary recovery corresponds to the initial part of the production and is entirely driven by natural energy present in the reservoir (gas cap expansion, solution-gas expansion, aquifer influx, rock compaction and gravity drainage). This stage continues until the original energy source is no longer able to generate profitable rates (Muskat, 1949).

Once the relatively low reservoir pressure does not allow oil production, secondary recovery methods, such as water injection in the productive zone or gas injection in the gas cap, are implemented in order to increase reservoir pressure and displace remaining oil towards production wells to extend the life of the field. This stage finishes when water or gas are produced in considerable amounts making the process unprofitable (Muskat, 1949).

After the secondary recovery flooding stage, capillary forces prevail over viscous forces in the porous media and significant amounts of oil might be left behind. In tertiary recovery, initial in-situ fluid and rock-fluid properties are altered using three major techniques: miscible displacement (injection of carbon dioxide (CO_2) or hydrocarbon gas when reservoir pressure conditions are favorable), thermal recovery (steam injection and in-situ combustion) and chemical flooding (alkaline, surfactant, polymer or any combination); these techniques are also known as Enhanced Oil Recovery (EOR) methods and can also be applied during primary and secondary recovery stages (Lake, 1989).

Chemical EOR techniques are designed to increase oil recovery after traditional waterflooding based on two main mechanisms. The first mechanism consists on reducing interfacial tension (IFT) between oil and displacing water (increasing displacement efficiency). The second consists on making mobility ratio more favorable (increasing volumetric sweep efficiency) (Guo, et al., 2011).

The most common chemical method for increasing microscopic displacement efficiency is the injection of surface-active molecules like surfactants (Hosseini-N & Zitha, 2015; Janssen, et al., 2019a; Janssen, et al., 2019b; Janssen, et al., 2019c). The surfactant can generate the so-called middle phase micro-emulsions that exhibit ultra-low IFT with excess brine and oil phases between which they coexist (Huh, 1979). This IFT reduction to ultra-low values translates to a significant capillary number increase reducing the residual oil saturation.

Surfactant injection can be combined with injection of a high pH agent. The injection of a high pH agent is known as alkaline flooding (Sheng, 2015). Alkali main purposes are generation of in-situ surfactant when reacting with oleic acids present in crude oil (saponification) and, in the case of anionic surfactant injection, reduction of chemical adsorption in the formation by reversing the charge of the positively charged clays, which are the main surfactant adsorption sites (Guo, et al., 2011; Janssen, et al., 2019a; Janssen, et al., 2019b; Janssen, et al., 2019c). However, most common alkali agents react with divalent cations such as Calcium (Ca^{2+}) or Magnesium (Mg^{2+}) in formation water to form insoluble salts that precipitate (Srivastava, et al., 2009). Additionally, alkali can also generate corrosion problems in production strings and transportation networks (Berger & Lee, 2006; Janssen, et al., 2019a).

One of the most common recovery methods is gas injection. Simple gas injection efficiency is frequently low due to an unfavorable mobility ratio between the displacing gas and the displaced fluids. Unfavorable mobility ratio and density contrast cause viscous fingering and gravity segregation. In formations with large permeability contrasts between layers, gas channeling through high permeability zones can occur leaving significant amounts of oil behind (Janssen, et al., 2019b).

A method for improving mobility contrast is alternate water and gas (WAG) injection. Although it performs better than continuous gas injection WAG may not completely eliminate viscous instabilities and gravity segregation (Bhoendie, et al., 2014; Janssen, et al., 2018).

Foaming of gas might be a suitable alternative for controlling gas mobility. Foam is a dispersion of gas in a liquid continuum, is characterized by a much higher apparent viscosity than gas or water, which translates in a better mobility control and improved volumetric sweep efficiency. Foam can be generated in two ways: (1) by co-injection or (2) by alternate injection of gas and surfactant solution (Jong, et al., 2016).

One of the most widely used methods to generate mobility control is polymer flooding (Srivastava, et al., 2009). Polymer increases viscosity of the drive fluid, which improves the mobility ratio between displacing and displaced phases. However, in low permeability reservoirs, typical high molecular weight polymers are not suitable due to their tendency to block pore throats. Moreover, low molecular weight polymers are often uneconomic. Additionally, polymers are often unstable under high temperatures (>120 °C) and can easily degrade due to shear stress in chokes or perforations at high rates, not to mention polymers can unfavorably react with surfactants (Srivastava, et al., 2009).

In contrast, foams are less susceptible to thermal, shear and even biological degradation, and are more affordable than polymer. Additionally, foam can be implemented in low permeability formations, high salinity formation water environments and can be used in sandstones and carbonates (Cottin, et al., 2012; Szlendak, et al., 2013), Moreover, Nguyen et al., (2005) used X-ray CT imaging on sandstone and glass bead cores to study gas and water flow in presence of foam and observed foam successfully generated fluid diversion from high to low permeability zones. In fact, foams can provide a better conformance control in formations with high permeability contrasts than polymer solutions (Guo, et al., 2011; Hosseini-N & Zitha, 2015; Srivastava, et al., 2009).

A synergic strategy known as Foam-Assisted Chemical Flooding (FACF), is a process where residual oil to waterflood is first partly mobilized by a surfactant slug and subsequently mobility control is achieved by generation of drive foam. Several authors have proved the benefits of FACF (also known as low tension gas (LTG), alkaline-surfactant-gas (AGS) and alkaline-surfactant-foam (FACF) flooding): Kamal & Marsden (1973), conducted a series of experiments that showed that foam can displace micellar slugs in a similar way as polymer. Lawson & Reisberg (1980), obtained a successful overall recovery by alternating gas and surfactant solution. Hirasaki & Lawson (1985) concluded in his experiments that foam could be used as drive in alkaline-surfactant-polymer (ASP) processes. Wang, et al., (2001), documented the first field test combining chemical and foam co-injection for EOR. After 20 months of injection, 16.7% of oil initially in place (OIIP) was recovered and gas/oil ratio (GOR) was significantly reduced compared to the WAG flooding base case. Wang L. (2006), concluded that the co-injection of ASP slug and gas drive is more effective at low oil saturations due to better foam stability. Li, et al., (2008), achieved almost piston-like displacement of oil by alternate injection of surfactant and gas in

both slug and gas injection phases. Srivastava (2010), showed efficient mobilization and displacement of oil after waterflooding by means of alkaline-surfactant-gas (ASG) injection with recoveries up to 97% of remaining oil saturation and proved that foam mobility control is maximized at non-extreme foam qualities. Janssen et al., (2019b) implemented CT scan analysis for proving the benefit of the FACF processes and found that a lower drive foam quality favors oil bank displacement and that the amount of clean oil produced by the oil bank is not affected by the drive foam quality.

This study focusses on the mechanistic modelling of water flooding, gas flooding, WAG, surfactant flooding and FACF processes. Core-flood experiments performed by Janssen et al., (2019) are history matched using the four-phase chemical flooding simulator UTCHEM. This study analyzes the methodology for modeling the phase behavior of the four-phase system (oil, water, micro-emulsion and gas).

1.2 Research Questions

The main questions to answer in this study are:

- Is it possible to determine the physical parameters controlling the incremental oil recovery during WAG over continuous gas flooding based on numerical simulation results?
- How should the main mechanisms controlling incremental oil recovery in FACF processes (oil mobilization by lowering oil-water IFT and oil displacement by using foam as drive agent) and the related parameters be history matched?
- How does the uncertainty in relevant parameters affect the simulation results?
- What is the most efficient systematic workflow for matching core flooding experimental data?

1.3 Methodology

Oil mobilization and oil bank formation during surfactant flooding is caused by the decrease of oil-water (o/w) IFT. In order to model IFT reduction between oil and water, UTCHEM

recalculates the parameters for estimating relative permeabilities (residual saturations, endpoint relative permeabilities and exponents) as a function of the trapping number, which can effectively model viscous, capillary and gravity forces. (Delshad, et al., 1996). In UTCHEM, the relative permeability parameters are a function of a low trapping number (at high o/w IFT, i.e. water flooding) and a high trapping number (at low o/w IFT, i.e. near-miscible conditions). Additionally, surfactant-oil phase behavior needs to be matched to obtain o/w IFT reduction as a function of salinity.

In a FACF process micro-emulsion and oil bank are pushed towards the producer by a foam drive. To decrease the mobility behind the surfactant flooding front, two options are available for foam generation: alternate injection or co-injection of gas and surfactant solution to generate in-situ foam. One approach for decreasing mobility by foam generation is by reducing gas relative permeability. Foam also reduces liquid relative permeability by increasing trapped or residual gas saturation, but this effect is not commonly incorporated in most foam models since it is negligible when compared with gas relative permeability reduction.

Foam quality is defined as gas fractional flow in foam. Foam exists in at least two steady-state flow regimes as a function of foam quality (high and low) with transition occurring at a certain threshold quality. Such threshold separating the two foam regimes depends on surfactant formulation and concentration, among other fluid and porous media properties. A foam model should consider both foam-flow regimes. Cheng et al., (2000), provided a simple procedure to set up the simulation-input parameters for a set of steady-state core-flood data. The foam model in UTCHEM is based on the model of Cheng et al., (2000). Although foam impacts gas relative permeability and viscosity, this foam model assigns the reduction of gas mobility, due to foam generation, to the reduction in gas relative permeability. In the model of Cheng *et al*., foam forms if (1) surfactant is present and its concentration is above a threshold value, and (2) water saturation exceeds a certain threshold value. The model in UTCHEM calculates gas relative permeability in presence of foam as a function of threshold values of surfactant concentration, water saturation and oil saturation, as well as the foam resistance factor. In addition, the model can use Newtonian foam behavior or shear thinning behavior as a function of the foam resistance factor, the maximum gas mobility reduction in presence of foam. Moreover, a procedure to account for the effect of permeability and heterogeneity that uses

the concept of critical capillary pressure and varying foam strength is included in UTCHEM (2018).

At the high-quality regime, water saturation is lower than the threshold value. In contrast, at the low-quality regime, water saturation is higher than the threshold and foam reduces gas mobility by a large constant factor.

History match of previously generated experimental data (Janssen, et al., 2019b) will be performed based on the previously mentioned concepts. The available information on rock properties, fluid properties, CT scan images (rock properties distribution and fluid saturation distribution), pressure gradients and effluent data will be used in this regard. In previous simulation studies, two surfactant agents are used, one for residual oil mobilization by IFT reduction and another for foam generation and stabilization, this with the purpose of tracing the foam agent in UTCHEM (Delshad, et al., 1996). Although in their experiments, Janssen et al., (2019b) only used one surfactant formulation for both purposes, differentiating the foam-associated surfactant from the mobilization-asociated surfactant for simulation purposes can be usefull to trace the advance of the foam front. In this study, only one surfactant will be considered for both purposes.

Experimental results on phase behavior as a function of salinity will be used to determine fitting parameters (i.e. solubilization ratios) to be used in the simulator. Experimental relative permeability parameters at high IFT between oil and water will be used as parameters at low trapping numbers (end-point relative permeabilities for oil and water during primary drainage and forced imbibition, respectively, as well as residual saturations based on CT scan information). High trapping number parameters for relative permeabilities (at low o/w IFT) will be implicitly obtained with the history match process of the phase behavior study. For foam modeling, several parameters such as foam resistance factor, critical oil saturation for collapsing foam, critical surfactant concentration for foam formation, among others, will be sensitized to represent several drive foam strengths.

1.4 Software and Data

1.4.1 UTCHEM

Compositional and black oil commercial reservoir simulators can only model equilibrium for compressible three-phase systems (oil/water/gas). Only a small group of simulators such as UTCHEM, Reveal or GEM (see Appendix A) can model microemulsion equilibrium required in ASP, SP, steam-surfactant-foam and other tertiary recovery strategies. To successfully honor the physics behind a complex EOR process such as FACF, a tool that can handle four-phase equilibrium is required.

UTCHEM is a three-dimensional, four-phase, non-isothermal, finite difference compositional simulator developed by the Center for Petroleum and Geosystems Engineering at The University of Texas at Austin. This simulator can model alkaline, surfactant, polymer and foam/gas flooding at miscible and immiscible conditions. UTCHEM can simulate the related physical phenomena that must be considered in these complex processes such as adsorption, o/w IFT reduction, four-phase relative permeability, capillary desaturation and mobility reduction due to foam generation (Anderson, 2006; Mohammadi, 2008; Lashgari, et al., 2015).

For Chemical Enhanced Oil Recovery (CEOR) simulation with gas, UTCHEM combines a black-oil model for oil-water-gas systems, with Hand's rule (Hand, 1939) for micro-emulsion phase behavior (oil-water-micro-emulsion systems). Hand's rule has been used to estimate the oil-water-surfactant phase behavior as function of salinity and concentrations (Figure 1.1).

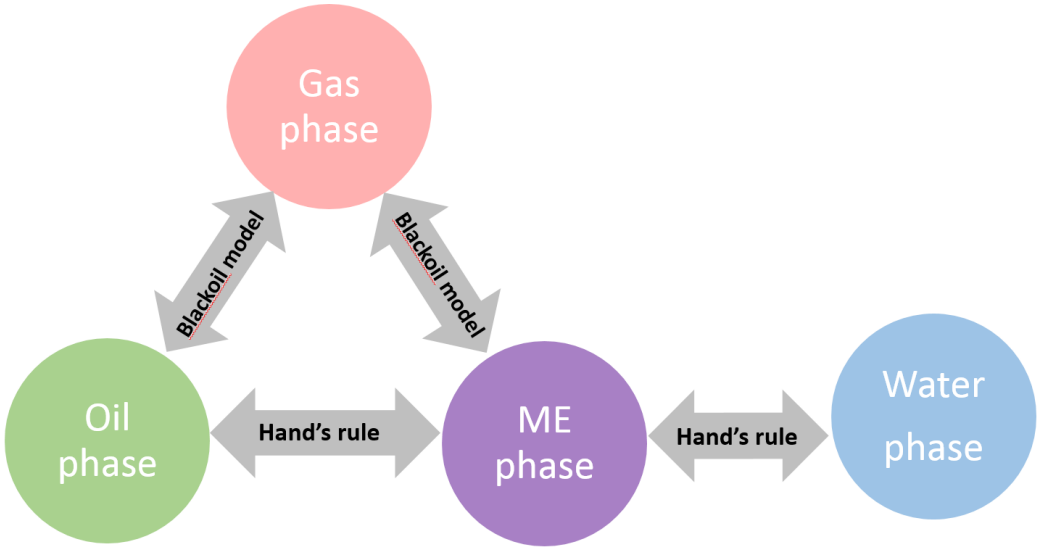

Figure 1.1. Four-phase connection scheme in UTCHEM for an oil-water-gas-ME system.

In UTCHEM, pressure and temperature are solved implicitly, and concentrations are solved explicitly (IMPEC). It can simulate several *species* such as aqueous (water), chemical (cations, anions, surfactant, polymer, co-solvents and tracers) and oleic (crude oil) (Lashgari, et al., 2015; Mohammadi, 2008). This simulator can couple black oil model with micro-emulsion phase behavior model (using Hand's rule) which is used to calculate the phase behavior of microemulsion, oil and water species as a function of salinity and concentrations, so mass transfer and equilibrium between coexisting phases can be calculated. (Lashgari, et al., 2015).

Appendix A shows a brief comparison between UTCHEM and the most commonly used simulators. This comparison is the starting point for selecting UTCHEM as simulation tool since it can honor complex physics behind the processes in analysis: reason why it is used in this study.

1.4.2 Experimental Data Set

For this study, two experimental data sets are considered. Janssen et al., (2018) obtained the first set. It studied immiscible nitrogen flooding for EOR purposes. In this study, continuous gas injection and alternate water/gas injection were performed.

The first study demonstrated that WAG leads to a higher oil recovery than continuous gas injection. The additional benefit is most likely related to the increasing trapped gas saturation compared to the continuous scheme.

The second experimental data set was obtained by Janssen et al., (2019b) and it analyzed FACF flooding. In this study, core-flood experiments studied the formation of the oil bank and its displacement by drive foams of varying quality by means of a) bulk phase behavior analysis and foam testing studies using a single internal olefin sulfonate surfactant and b) CT scanning of core-floods in Bentheimer sandstone samples. The experiments were performed at under-optimum salinity conditions.

The study suggests that a lower drive foam quality favors oil bank displacement and that the amount of clean oil produced by the oil bank is not affected by the drive foam quality. Such phenomena will be matter of study in the numerical simulation approach.

1.5 Report Structure

In Chapter 2, a literature review of basic EOR concepts is presented. The principles behind sweep efficiency and microscopic displacement efficiency enhancement using foam and surfactant, respectively, are described.

In Chapter 3, available experimental data is reviewed and main parameters to consider in the history matching process are listed.

In Chapter 4, the methodology to be implemented in this study is summarized. Here, the most important aspects to consider during the history match process will be highlighted.

In Chapter 5, the results on a numerical simulation modeling study for history matching of experimental data is presented and discussed.

Finally, in Chapter 6, the conclusions and recommendations and future improvement opportunities are shared.

2 LITERATURE REVIEW

2.1 Basic EOR Concepts

The ultimate oil recovery corresponds to a portion of the OIIP due to pore-scale trapping, channeling, viscous fingering, gravity override, among others (Knol, 2015). The oil recovery is given by the following expressions:

$$N_p = \frac{RF\ S_{oi}\ V_p}{B_{oi}} \tag{2.1}$$

$$RF = E_D\ E_V \tag{2.2}$$

where, N_p represents the cumulative oil recovery, RF the recovery factor, E_D the microscopic displacement efficiency, E_V the volumetric sweep efficiency, S_{oi} the initial oil saturation, V_p the pore volume and B_{oi} the oil volumetric factor. In this equation it can be observed that an increase in E_D or E_V is proportional to an increase in N_p. Figure 2.1 shows how RF, E_D and E_V are related.

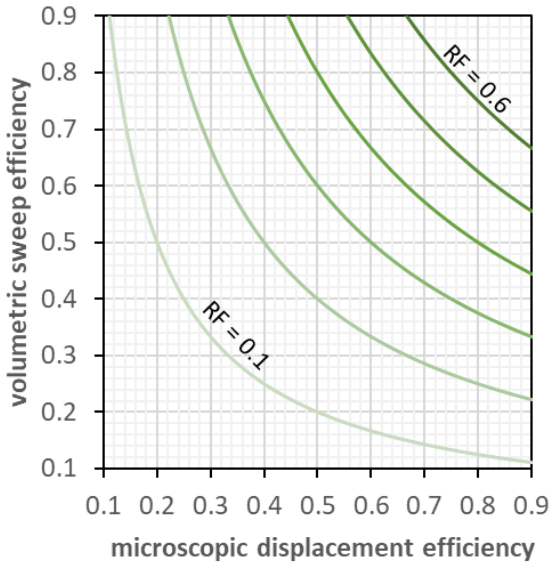

Figure 2.1. Microscopic displacement efficiency vs. volumetric sweep efficiency for several recovery factors. Based on van Lingen (1998).

The definitions of E_D and E_V showed in this section are based on Lake et al. (2014). The following expression defines the microscopic displacement efficiency if oil density is constant:

$$E_D = \frac{Amount\ of\ oil\ displaced}{Amount\ of\ oil\ contacted\ by\ displacing\ agent} \tag{2.3}$$

Microscopic displacement inefficiencies are caused by capillary forces, small scale heterogeneities and viscosity contrasts and are strongly influenced by initial conditions, the type of displacing agent and the amount of displacing agent and rock-fluid interactions.

In contrast, E_V is defined as:

$$E_V = \frac{Amount\ of\ oil\ contacted\ by\ displacing\ agent}{Amount\ of\ oil\ originally\ in\ place} \tag{2.4}$$

There are two components in E_V, as showed by the following equation:

$$E_V = E_A\, E_I \tag{2.5}$$

where E_A corresponds to the areal sweep efficiency and E_I to the vertical sweep efficiency. E_A is defined as the ratio between the area contacted by the displacing agent and the total area, whilst E_I is defined as the ration between cross-sectional area contacted by the displacing agent and the total cross-sectional area. The principal volumetric sweep inefficiencies are caused by viscous fingering, gravity over-run and under-run, reservoir-scale heterogeneities, and coning or cusping, among others.

The goal of EOR is to increase the capillary number and lower the mobility ratio, improving E_D and E_V, respectively. The FACF technique is designed to reduce o/w IFT (capillary number increase) by means of surfactant injection and provide mobility control (mobility ratio decrease) through generation of foam as drive agent.

2.1.1 Capillary Number

As stated before, residual oil saturation is mainly caused by the interaction between viscous and local capillary forces. The relation between such forces is defined as the local capillary number, N_C, and is described in its simplest form by the following equation:

$$N_C = \frac{u\,\mu}{\sigma} \tag{2.6}$$

where u and μ represent the Darcy velocity and the viscosity of the displacing agent, and σ the interfacial tension between the oil and the displacing agent.

The capillary desaturation curve (CDC) shows the relation between the residual wetting and non-wetting saturations and N_C. Figure 2.2 shows an example of a typical CDC. Typically values of N_C for a traditional waterflooding process ranges between 10^{-7} and 10^{-6} (Melrose & Brandner, 1974). As observed, when increasing N_C, the oil residual saturation decreases and E_D is significantly improved. In addition, pore size distribution has a significant impact on the CDC, as showed by Figure 2.3.

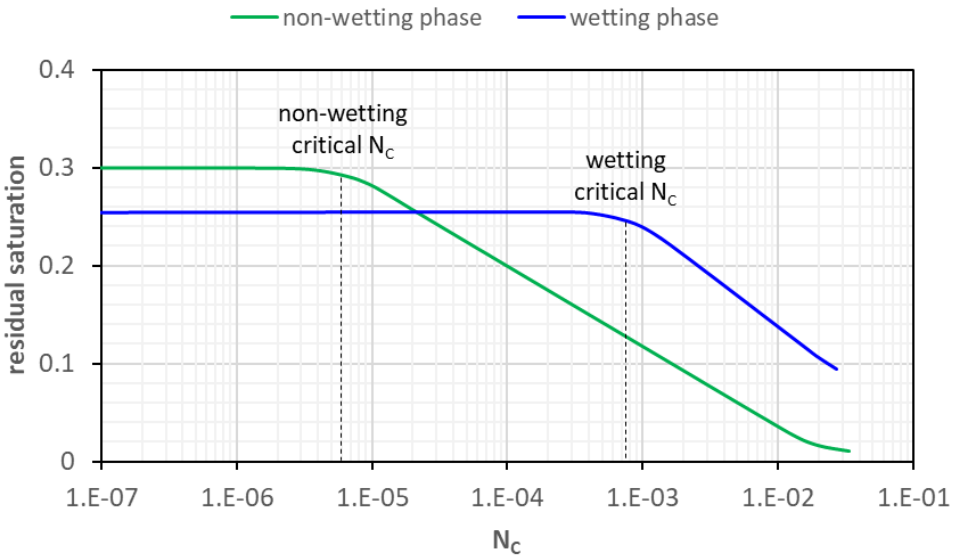

Figure 2.2. Schematic CDC for both wetting and non-wetting phases. Based on Lake et al., (2014).

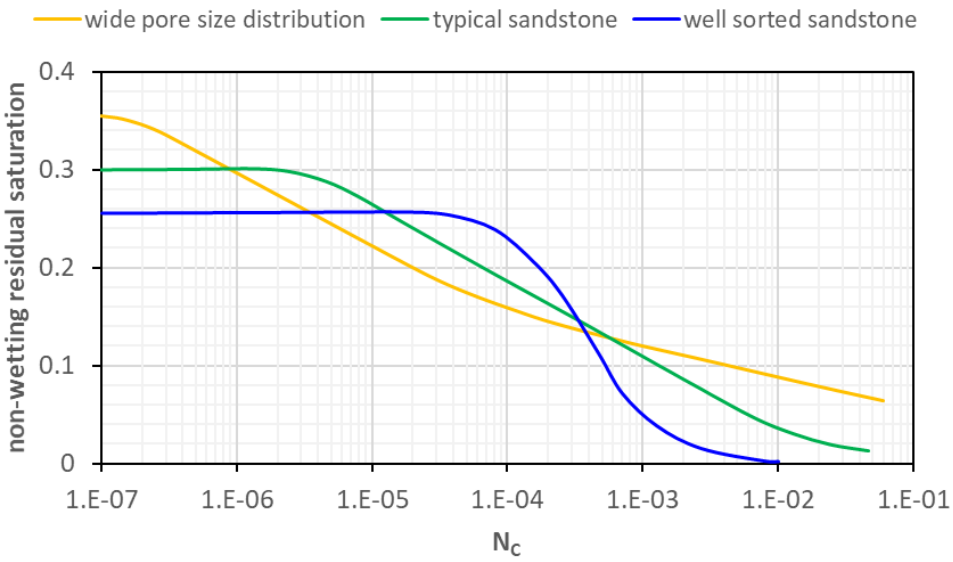

Figure 2.3. Schematic CDC for different pore size distributions. Based on Lake et al., (2014).

2.1.2 Mobility Ratio

With the mass-conservation equation for isothermal, incompressible and immiscible flow of oil and water as starting point, the Buckley-Leverett theory (Buckley & Leverett, 1942) describes the time and space evolution of saturations in a displacement process. A key concept in the theory is the fractional flow of water, f_w, described by the following equation:

$$f_w = \frac{\lambda_{rw}}{\lambda_{rw} + \lambda_{ro}}\left(1 - \frac{k\,\lambda_{ro}\,\Delta\rho\,g\sin\alpha}{u}\right) \tag{2.7}$$

where λ_{ri} $(i = w, o)$ is the relative mobility of oil and water, k is the absolute permeability, $\Delta\rho$ the difference in density between oil and water, g the gravity constant and α the dip angle. Here, the relative mobility is given by

$$\lambda_{ri} = \frac{k_{ri}}{\mu_i};\ (i = w, o) \tag{2.8}$$

where k_{ri} represents the relative permeability of each phase and is given by the Brooks-Corey equation (Brooks & Corey, 1964), as follows:

$$k_{ri} = k_{ri}^0 \, {S_{ei}}^{n_i};\ (i = w, o) \tag{2.9}$$

$$S_{ei} = \frac{S_i - S_{ir}}{1 - S_{wr} - S_{or}} \tag{2.10}$$

In these expressions, k_{ri}^0 is the end-point relative permeability (relative permeability at residual saturation of the other phase) S_{ei} the effective or reduced saturation, S_i the total saturation, S_{ir} the residual saturation and n_i the curve shape coefficient for each phase.

When rewriting and rearranging the fractional flow expression using the Brooks-Corey equation for relative permeability, its dependence on the end-point mobility ratio, M^0, can be obtained:

$$f_w = \frac{1 - N_g^0 \, (1 - S_{ew})^{n_o} \sin\alpha}{1 + \dfrac{(1 - S_{ew})^{n_o}}{M^0 \, {S_{ew}}^{n_w}}} \tag{2.11}$$

where N_g^0, the gravity number, is given by

$$N_g^0 = \frac{k \, k_{ro}^0 \, \Delta\rho \, g}{\mu_o \, u} \tag{2.12}$$

and the end-point mobility ratio by

$$M^0 = \frac{k_{rw}^0 \, \mu_o}{\mu_w \, k_{rw}^0} \tag{2.13}$$

Figure 2.4 shows the effect of M^0 in f_w. As it can be observed, a smaller mobility ratio improves the efficiency in the process and results in a more stable oil displacement. Figure 2.5 shows how M^0 affects the displacement efficiency and the saturation distribution in a Buckley-Leveret type displacement. As it can be observed, a lower M^0 results in a delayed breakthrough time, a larger final displacement efficiency and a more stable sweep.

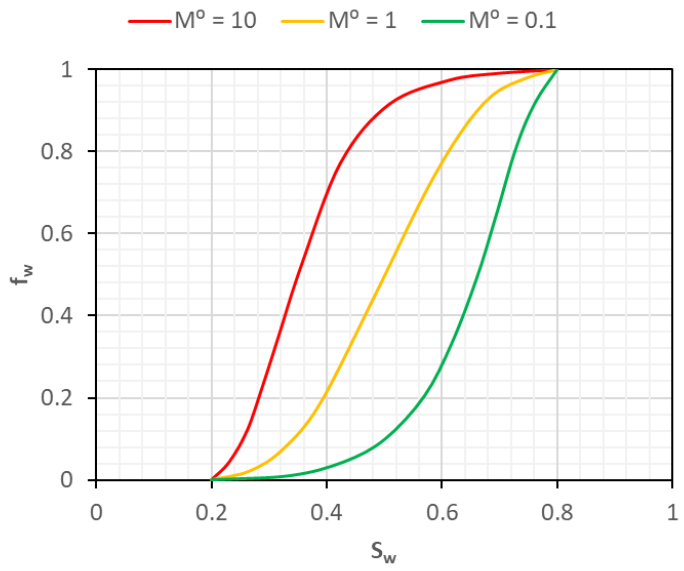

Figure 2.4. Schematic fractional flow curves for different end-point mobility ratios. Based on Lake et al., (2014).

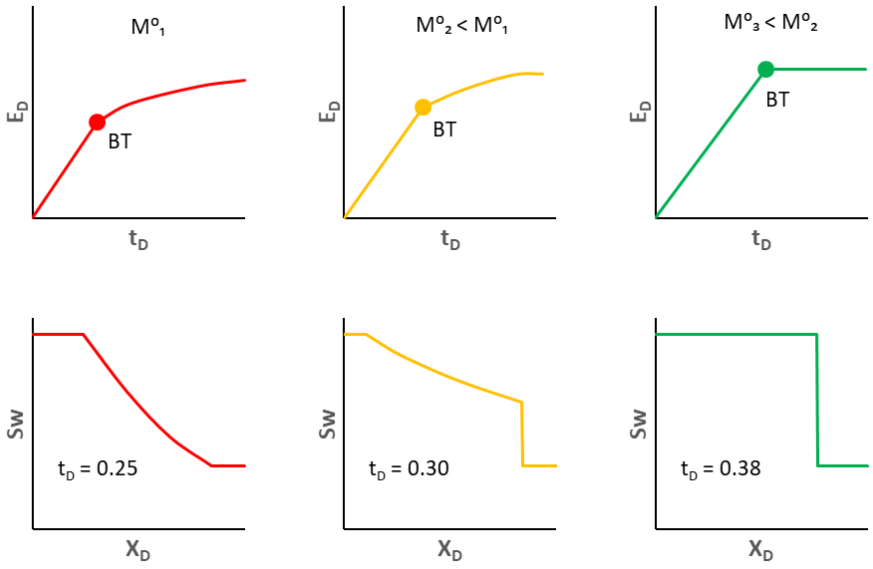

Figure 2.5. Effect of end-point mobility ratio on displacement efficiency and water saturation distribution at a given time. Modified from Lake et al., (2014).

In addition, the M^0 also have an important effect in E_A. Several correlations have been developed to obtained E_A as a function of the reciprocal of mobility and the dimensionless time (t_D), as the one showed in Figure 2.6 for a five-spot injection pattern. Some other authors have proposed similar correlations for different confined and unconfined injection patterns (Claridge, 1972; Craig, 1971).

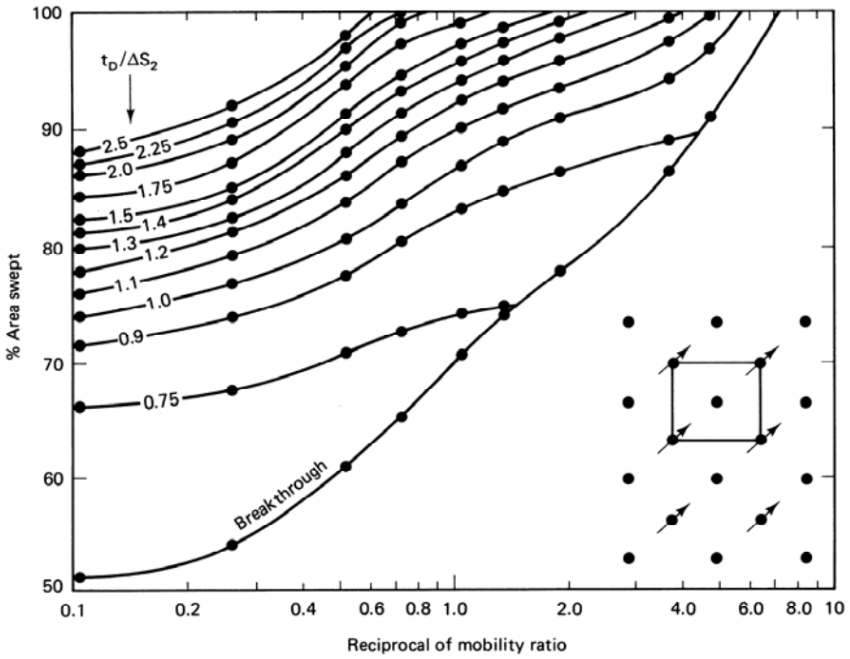

Figure 2.6. Correlation for areal sweep efficiency as a function of reciprocal of mobility ratio and dimensionless time for a confined five-spot injection pattern. Based on the work by Dyes et al., (1954). (Lake et al., 2014).

2.2 Surfactant Flooding

One of the most commonly used CEOR techniques is the injection of a surface-active agent (surfactant), also known as micellar, detergent, low-tension, soluble oil or microemulsion flooding. A combination of surfactant and polymer (SP) or alkaline, surfactant and polymer (ASP) are also commonly implemented.

A surfactant agent reduces the interfacial tension between immiscible phases, oil and water, since the molecule consists of a hydrophilic (like water) and a lipophilic (likes oil) part. Surfactant molecules are classified into four types, as follows (Lake, et al., 2014):

- Anionic: Negatively charged and balanced with a positive charge (metal cation). It presents relatively low adsorption in sandstones and represents the most commonly used type of surfactant.

- Cationic: Positively charged and balanced with an inorganic cation. Usually implemented to alter the wettability condition in the rock (Stadnes & Austad, 2002).

- Nonionic: Not charged. Commonly used as cosurfactants. Used to improve the performance of the main surfactant by forming a mixed micelle with better water solubility.

- Amphoteric: Positively and negatively charged at the same time and can switch between one charge and the other, depending on pH conditions.

In this study, IOS 2024 was used as surfactant agent (Figure 2.7). It corresponds to an anionic molecule. When an anionic surfactant is dissolved in an aqueous solution, it is dissociated into a cation and a monomer. When the concentration of surfactant is increased, the lipophilic part associates to form the so-called micelles that contain several monomers (Lake et al., 2014). Above the critical micelle concentration (CMC) (Figure 2.8), an increase in surfactant cause only increase in the concentration of micelles. This is the predominant condition in most surfactant solutions.

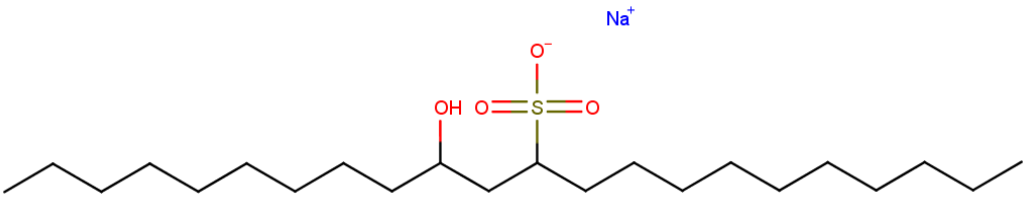

Figure 2.7. IOS 2024 structure. Based on (Lake, et al., 2014)

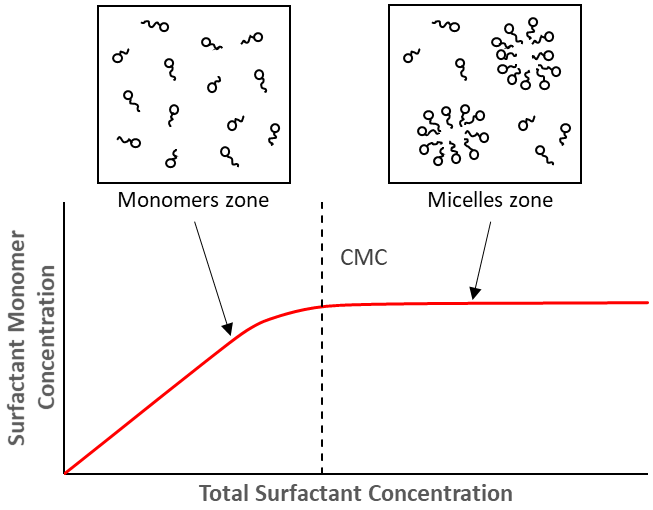

Figure 2.8. Definition of the critical micelle concentration (CMC). Based on (Lake, et al., 2014).

Once the surfactant solution contacts oil, the surfactant molecules reallocate in the water/oil interface, with the lipophilic and the hydrophilic parts dissolved in the oleic and aqueous phases, respectively. This behavior causes the reduction in o/w IFT.

2.2.1 Salinity and Phase Behavior

Once the micelles solubilize oil, a thermodynamically stable phase known as microemulsion is formed. Surfactant concentration is not a major parameter in the phenomena. However, the phase behavior of the water/oil/microemulsion system is greatly affected by salinity. The phase behavior of the system, at constant surfactant concentration, can be represented with ternary diagrams as follows:

- Type II(-): At low salinity, an anionic surfactant is much more soluble in water than in oil. This condition generates a two-phase system: excess oil and water-external microemulsion known as Type II(-). The ternary diagram for this condition shows a two phase zone with a plait point, P_R, close to the oil apex and tie lines with negative slope (Figure 2.9). This microemulsion type contains small amounts of solubilized oil confined in the core of the swollen micelles.

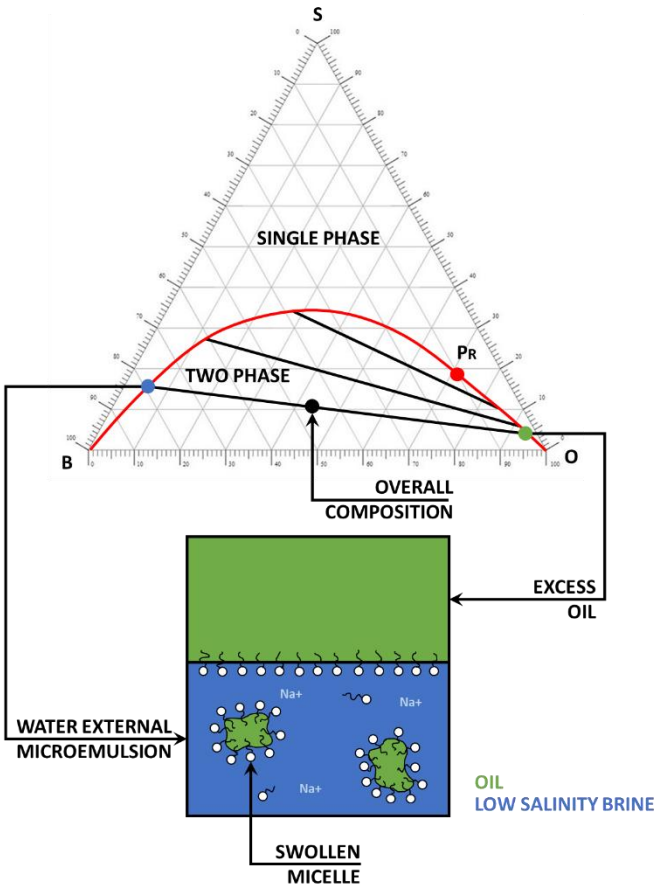

Figure 2.9. Schematic of a Type II(-) microemulsion. Based on Lake et al., (2014).

- Type II(+): On the other hand, at high salinities, solubility preference switches (surfactant is now more soluble in oil than in water). Again, a two-phase system is formed but this time they correspond to excess brine and oil-external microemulsion known as Type II(+). The ternary diagram corresponds to a mirrored Type II(-) microemulsion (Figure 2.10), with plait point, P_L, close to the brine apex and tie lines with positive slope. This microemulsion contains small amounts of solubilized brine confined in the core of inversed micelles.

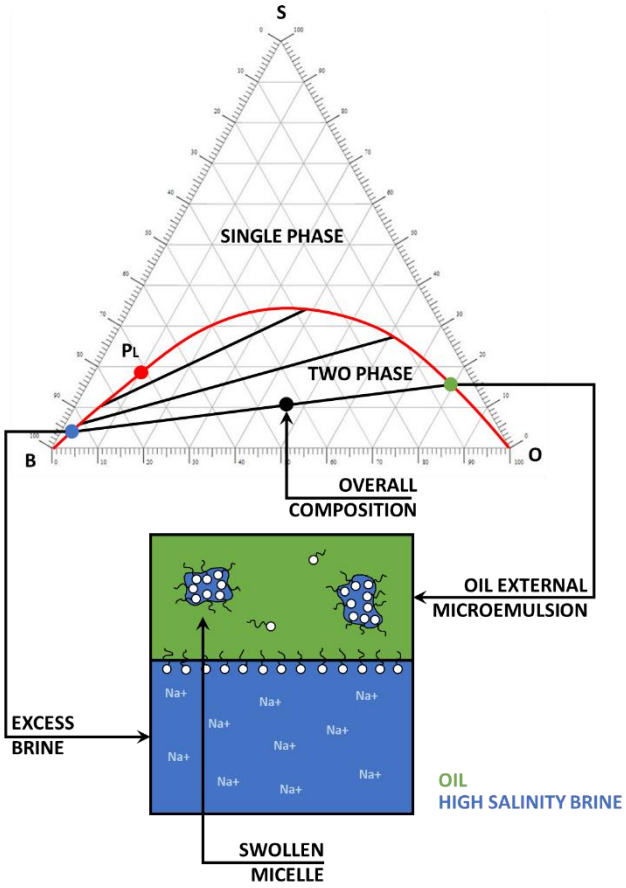

Figure 2.10. Schematic of a Type II(+) microemulsion. Based on Lake et al., (2014).

- Type III: Finally, at intermediate salinities, surfactant solubility balances between oil and water and a three-phase system is formed: excess brine, excess oil and a bicontinuous surfactant-rich microemulsion known as Type III. In the ternary diagram of this system, two two-phase regions are present (the previously described biphasic regions, each with its plait point, P_R and P_L), and a three-phase region takes place below the previous regions (Figure 2.11). The point at which the three regions converge is known as invariant point. Normal and inverse micelles coexist in the microemulsion.

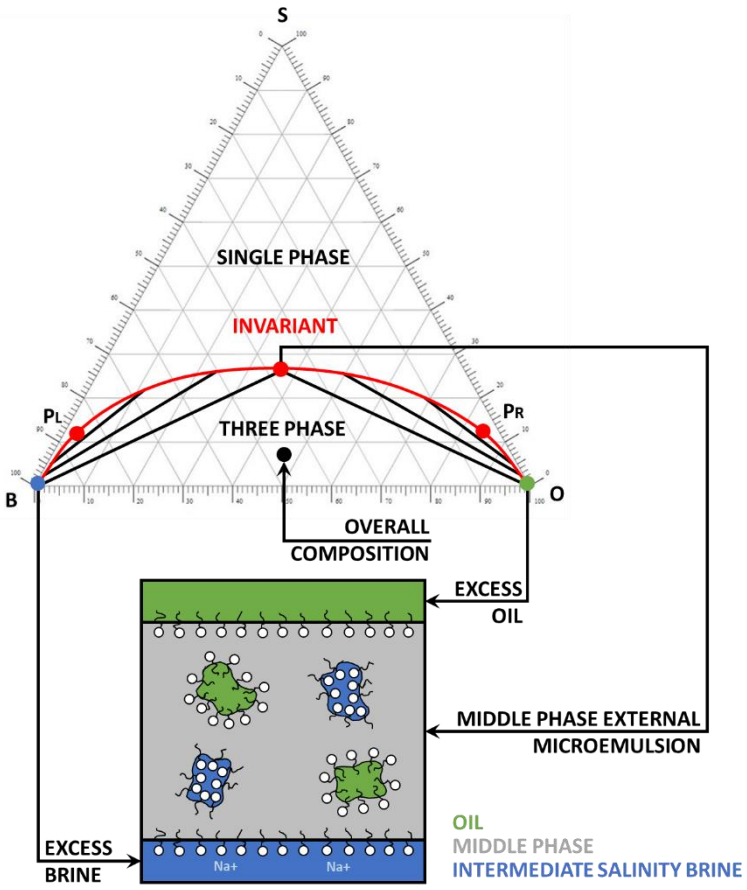

Figure 2.11. Schematic of a Type III microemulsion. Based on Lake et al., (2014).

Several authors have investigated how measured IFTs strongly correlate with the microemulsion phase behavior. Huh (1979), derived an expression for determining IFT as a function of phase behavior measurements, i.e., as a function of solubilization parameters, defined as:

$$R_{23} = \frac{C_{23}}{C_{33}} \tag{2.14}$$

$$R_{13} = \frac{C_{13}}{C_{33}} \tag{2.15}$$

where, C_{13}, C_{23} and C_{33} represent the volumetric fractions of water, oil and surfactant in the microemulsion phase, respectively, and $R_{13}$and R_{23} the solubilization parameters of water and oil, respectively. In this way, the IFT, in mN/m, can be approximated with the following simplified version of equation proposed by Huh (1979), as follows:

$$\sigma_{i3} = \frac{0.3}{R_{i3}^2}, \qquad i = o, w \tag{2.16}$$

where σ_{i3} represents the IFT between phase i and microemulsion phase (3). Figure 2.12 shows an example of how IFT and solubilization parameters are related with salinity in a salinity scan that covers Type II(-), Type III and Type II(+) microemulsions. Note that in the Type III microemulsion, there is a salinity condition at which $\sigma_{23} = \sigma_{13}$ and $R_{23} = R_{13}$. This is known as the optimal salinity and corresponds to the ultra-low IFT in the system.

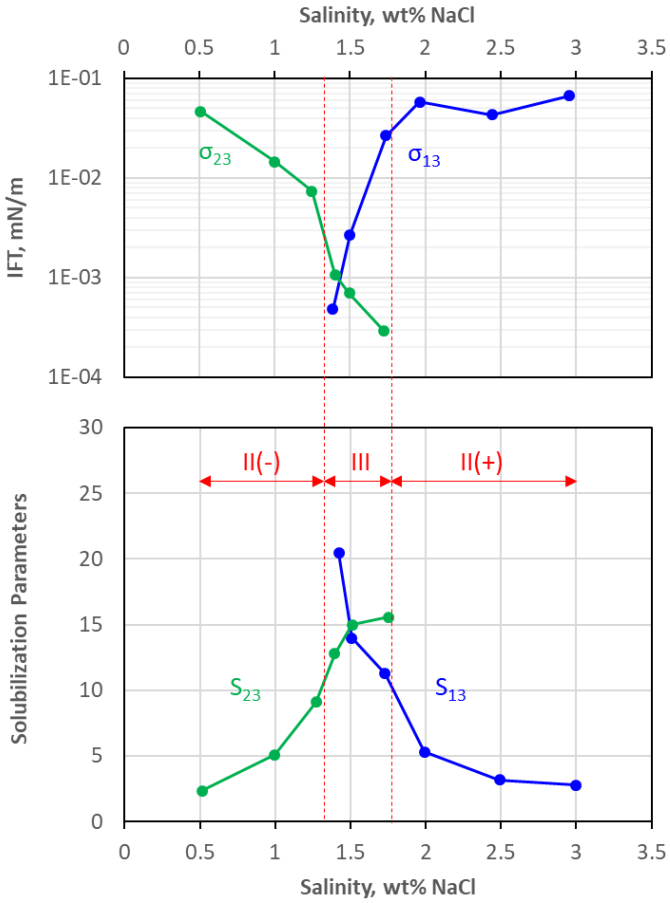

Figure 2.12. IFT and solubilization parameters vs salinity. Based on Reed and Healy (1977).

One important parameter that needs quantification in surfactant flooding applications is surfactant retention. Ideally, the surfactant should have poor selectivity for fluid/rock interfaces. However, in reality at higher surfactant concentrations, a correspondingly greater adsorption will occur (Belhaj, et al., 2019). The surfactant adsorption can be modelled with a Langmuir-type

isotherm (see Chapter 4). This behavior resembles the relation showed in Figure 2.8 since after CMC, the monomer supply becomes constant as well as the adsorption.

2.3 Foam Flooding

Gas injection is one of the most suitable methods to increase oil recovery. However, it is also well known that at field level, volumetric sweep efficiency is often poor with the injection of gases (steam, CO_2 or hydrocarbon gases) because of permeability variations in the formation, high mobility and low density of the gas (Lake et al., 2014).

When gas reaches a production well and the path is saturated with gas, most of the subsequently injected gas follows such path. In these cases, foam represents an ideal solution since it directly reduces gas mobility. By increasing the magnitude of horizontal viscous or pressure forces relative to the effects of gravity, it can also reduce gravity segregation (Lake et al., 2014).

Foam is defined as a dispersed gas phase in a continuous liquid phase stabilized by surfactants (Hirasaki, 1989). It is useful controlling mobility of gases in porous media (Kovscek & Radke, 1993; Lake, et al., 2014). The principal purpose of foam is to deliver gas to a larger volume of the reservoir where it can recover oil.

Within porous media, foam bubbles can be smaller, as large or larger than the individual pores, where a “lamella”, a thin liquid film, separates two bubbles of gas (Bikerman, 1973) as it is shown in Figure 2.13.

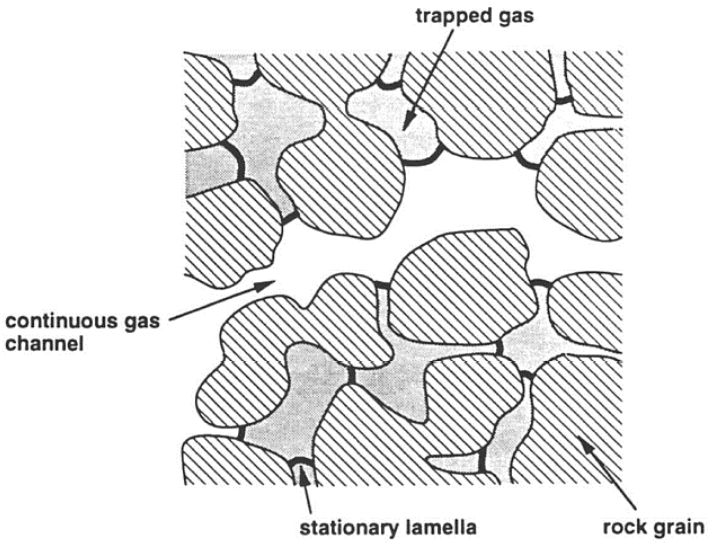

Figure 2.13. Foam in porous media. Taken from (Kovscek & Radke, 1993).
Foam bubbles exceed the pore size and a stationary lamella is dividing two bubbles of gas.

The required force to sustain the lamella is known as "disjoining pressure". It is the combination of three forces: van der Waals force, adsorption and protrusion and/or hydration forces (Hematpour et al., 2016). Surfactant molecules adsorbed on the opposite gas-liquid interface bounding the lamellae repel each other, enabling the lamella to resist the greater pressure in the gas phase than in the liquid within the lamella (Figure 2.14).

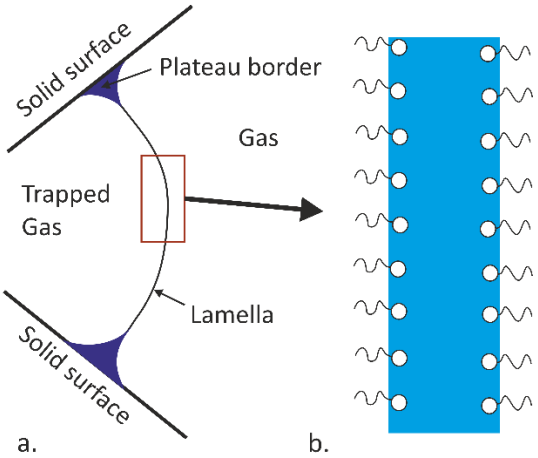

Figure 2.14. Schematic of a lamella in porous media. Modified from (Lake et al., 2014).
a) Pore scale view (100 µm) of a lamella between two solids with Plateau borders (a liquid-filled border bounded by two liquid/gas interfaces and a liquid/solid interface) at the solid surfaces. b) Interior of the lamella (100nm approx.) showing surfactant molecules: hydrophilic head group (circles), hydrophobe (lines).

The number of lamellae per unit is called “foam texture”. Although this parameter is one of the most important for the foam characterization, there is no direct method to measure foam texture inside porous media (Hematpour et al., 2016).

A distinctive feature of foam development in porous media is drastic reduction in gas-phase mobility. Gravity override and viscous fingering through high-permeability streaks can be mitigated as a result (Kovscek & Radke, 1993). Gas mobility reduction increases as bubble size decreases (Falls et al., 1989).

Gas mobility, λ_g, is defined as follows:

$$\lambda_g = \frac{k\, k_{rg}}{\mu_g} \tag{2.17}$$

where k_{rg} is the gas relative permeability and μ_g the gas viscosity.

Foam reduces the gas mobility in porous media, thus increasing the apparent gas viscosity and reducing the gas relative permeability. Since trapped gas saturation is high, only a fraction of gas flows, which results in a decrease of the gas relative permeability (Knol, 2015). In a discontinuous flow, the resistance of foam to flow through the pore system produces a rise only in the apparent gas viscosity due to the presence of liquid lamellae, not in the viscosity of the gas itself; while in the continuous flow, foam only affects the gas relative permeability because the gas flows easily without liquid lamellae blocking the way. Water does not present direct mobility effects in presence of foam (Lake, et al., 2014).

A foam providing a large reduction in gas mobility is called “strong” foam in which lamellae are more stable. Therefore, more lamellae present increases resistant to flow (Lake, et al., 2014). A “weak” foam presents low foam texture (Hematpour, et al., 2016); it can be formed at lower pressure gradient as gas flows across a sharp transition from lower to higher permeability (Tanzil, et al., 2002). When gas/water capillary pressure exceeds the limiting capillary pressure, P_c^*, foam is destroyed (Khatib, et al., 1988). Since capillary pressure depends on water saturation, the condition for stability could be described as $S_w^* = S_w(P_c^*)$. At $S_w = S_w^*$,

an abrupt change in gas mobility occurs, from very low gas mobility for $S_w > S_w^*$ to a much higher mobility for $S_w < S_w^*$ (Lake, et al., 2014).

In the absence of oil, strong foams exist in two regimes, high-quality and low-quality regimes which transition is a strong change delineated by the critical foam quality (f_g) (Alvarez, et al., 2001). In the high-quality regime, foam flow behaviour is controlled by gas bubble union, whereas in the low-quality one, is a function of gas bubble trapping. Foam apparent viscosity is mainly governed by the aqueous phase superficial velocity (inversely proportional to f_g) and conducted by the gas flow rate (foam strength directly proportional to f_g), in the high-quality and low-quality regime, respectively (Alvarez, et al., 2001).

The high-quality regime is a result of foam collapse at P_c^* and S_w^*, where foam is strongest in higher-permeability layers and spontaneously diverts flow to lower-permeability layers, its behavior can be Newtonian, shear-thinning, or shear-thickening, while in the low-quality regime, $S_w > S_w^*$, foam would not deflect flow to lower-permeability layers (Lake, et al., 2014).

Foam stability in presence of oil is one of the major concerns when applying foam as EOR method. Many experiments have showed the decrease of foam stability in presence of oil (the same effect of a de-foaming agent). Not only foam mobility in the presence of oil is much higher, but it also experiences higher coarsening. Since the liquid phase becomes continuous in the porous media, the lamellae can only be stable if the surface of the rock is water-wet; in oil-wet rocks, due to de-wetting of water films from the rock surface, lamellae will collapse (Farajzadeh, et al., 2012). Several authors have proposed different mechanisms for explaining the effect of oil in foam flooding. However, none of them can entirely cover the available experimental results in the literature. In the same way, available numerical modelling tools try to quantify this effect, but they are still far from representing the role of gas and surfactant solution in foam generation at different conditions. One of the methodologies for modelling the effect of oil saturation in foam is altering the limiting water saturation for foam formation when oil is present, i.e., making this parameter a function of oil saturation (Farajzadeh, et al., 2012).

2.4 Computed Tomography (CT) Scanning

One of the most useful tools in quantification of saturations during a core flooding experiment is computed tomography (CT) scanning. CT scanning response is measured in

Hounsfield units and then used to calculate porosities and saturations at different injection stages and pore volumes injected (PVI) with the following expressions:

$$\phi = \frac{CT_{wet} - CT_{dry}}{CT_{brine} - CT_{air}} \tag{2.18}$$

$$S_{o-2p} = \frac{1}{\phi}\left(\frac{CT - CT_{wet}}{CT_{oil} - CT_{brine}}\right) \tag{2.19}$$

$$S_{o-3p} = \frac{A - B}{\phi^1 C - \phi^2 D} \tag{2.20}$$

$$S_{g-3p} = \frac{\phi^2 E - \phi^1 F}{\phi^2 D - \phi^1 C} \tag{2.21}$$

$$A = (CT^1 - CT^1_{wet})(CT^2_{dry} - CT^2_{wet}) \tag{2.22}$$

$$B = (CT^2 - CT^2_{wet})(CT^1_{dry} - CT^1_{wet}) \tag{2.23}$$

$$C = (CT^1_{oil} - CT^1_{brine})(CT^2_{dry} - CT^2_{wet}) \tag{2.24}$$

$$D = (CT^2_{oil} - CT^2_{brine})(CT^1_{dry} - CT^1_{wet}) \tag{2.25}$$

$$E = (CT^1 - CT^1_{wet})(CT^2_{oil} - CT^2_{brine}) \tag{2.26}$$

$$F = (CT^2 - CT^2_{wet})(CT^1_{oil} - CT^1_{brine}) \tag{2.27}$$

where, ϕ is the porosity, S_{o-2p} and S_{o-3p} the two-phase and three-phase oil saturation, respectively, S_{g-3p} the three-phase gas saturation, and CT_{dry}, CT_{wet}, CT_{brine}, CT_{oil} and CT_{air} the CT response to dry core, brine-saturated core, water phase, oil phase and air phase in Hounsfield units. Single and dual energy modes are used in the process. For two-phase saturations, single 140 KeV images are used, whilst for three-phase saturations, dual 80 KeV and 140 KeV are used. Superscripts 1 and 2 indicate dual 140 KeV and 80 KeV measurements, respectively (Janssen, et al., 2019b).

3 EXPERIMENTAL DATA REVIEW

Two main experimental data sources will be considered. The first corresponds to a study on several immiscible nitrogen flooding schemes and the second to a study on oil recovery by FACF flooding. One more FACF experiment at different salinity will also be considered. The available data set to be history matched will be described in the following sections.

3.1 Immiscible Nitrogen Flooding

In this study, Janssen et al., (2018) performed several immiscible nitrogen injection experiments in Bentheimer sandstone cores. Continuous gas injection (CGI) and WAG injection schemes were used as described in Table 3.1. Initially, core samples were flushed with CO_2 and then saturated with brine (3 wt% NaCl). After this, oil was injected to mimic primary drainage. Most experiments started at connate water saturation conditions; only one started at residual oil after a complete waterflooding (WF).

Table 3.1. Configuration of immiscible nitrogen injection experiments.

Experiment	**Procedure**	**Gas Rate** (cm^3/min)	**Liquid Rate** (cm^3/min)	**WAG Ratio** (water to gas)	**Backpressure** (bar)	**CT Scan**
A1	CGI	5 – 0.083	-	-	0 - 60	no
A2	CGI	1	-	-	5	no
A3	CGI	0.5	-	-	10	no
A4	WF + CGI	0.5	2	-	5	yes
A5	WAG	0.5	2	1:6	5	yes

Authors concluded that (1) pressure increment during CGI at connate water injection slightly benefits oil recovery, (2) for immiscible nitrogen injection, a three-phase flow scheme leads to a lower residual oil saturation compared with a two-phase flow scheme, and (3) the lower residual oil saturation in the WAG experiment is most likely related to an improved mobility control due to partial gas trapping.

From this data set, only experiments A4 and A5 will be considered for history matching purposes. The objective in these exercises is to become familiar with the complexities related to gas flooding simulation in UTCHEM, as well as set a starting point for determining the complexities associated with foam simulation.

3.1.1 Fluid Properties

- The oil used in the experiments was n-hexadecane ($CH_3(CH_2)_{14}CH_3$) with 0.006 wt% of $C_6H_{24}N_4O$, a red colorant for improving visualization. The brine was a 3 wt% solution of NaCl in demineralized water. As mentioned in the previous paragraphs, the used gas was N_2.

To enhance contrast in CT scans, oleic and aqueous phases were doped with 1-iododecane ($CH_3(CH_2)_9I$) and potassium-iodide (KI), respectively. Table 3.2 and Table 3.3 show dopant concentration, density and viscosity (at 20 °C and atmospheric pressure) for oleic, aqueous and gas phases used in experiments A4 and A5, respectively.

Table 3.2. Phase properties for experiment A4.

Phase	**Dopant Concentration** (wt%)	**Density*** (g/cm^3)	**Viscosity*** (cP)
Oleic	7.5	0.798 ± 0.001	3.19 ± 0.06
Aqueous	7.5	1.078 ± 0.001	0.97 ± 0.08
Gas	-	1.165E-3	1.76E-2

* at 20 °C and atmospheric pressure

Table 3.3. Phase properties for experiment A5.

Phase	**Dopant Concentration** (wt%)	**Density*** (g/cm^3)	**Viscosity*** (cP)
Oleic	5	0.790 ± 0.001	3.22 ± 0.07
Aqueous	15	1.142 ± 0.001	1.01 ± 0.06
Gas	-	1.165E-3	1.76E-2

* at 20 °C and atmospheric pressure

3.1.2 Core Properties

Bentheimer sandstone core samples were used in the aforementioned experiments. For experiments A4 and A5, samples were 17 cm long and had a diameter of 3.9 cm. Table 3.4 shows the porosity and permeability estimations as well as the calculated pore volume for each sample.

Table 3.4. Core properties for experiments A4 and A5 on immiscible nitrogen injection.

Experiment	**Porosity** (%)	**Permeability** (D)	**Pore Volume** (cm^3)
A4	23.1 ± 0.1	1.94 ± 0.14	46.9 ± 0.2
A5	23.6 ± 0.1	2.30 ± 0.18	47.9 ± 0.2

3.1.3 Core Flooding Procedure

Table 3.5 and Table 3.6 show the pore volumes injected (PVI) and the initial local injection rates in experiments A4 and A5, respectively, starting from the primary drainage stage. Figure 3.1 and Figure 3.2 show the local injection rate schemes for each experiment. For experiment A5, it can be observed that 12 WAG cycles were performed. Note that the variation in rates at the end of primary drainage and forced imbibition in each experiment was designed to calculate the relative permeabilities of oil and water, respectively.

Table 3.5. Injection scheme in experiment A4.

Stage	PVI	Initial Oil Rate (cm^3/min)	Initial Water Rate (cm^3/min)	Initial Gas Rate (cm^3/min)
Primary Drainage	6.64	5	-	-
Water Injection	5.36	-	2	-
Gas Injection	11.59	-	-	0.5

Table 3.6. Injection scheme in experiment A5.

Stage	PVI	Initial Oil Rate (cm^3/min)	Initial Water Rate (cm^3/min)	Initial Gas Rate (cm^3/min)
Primary Drainage	5.92	2	-	-
WAG	17.02*	-	2	0.5

* Each WAG cycle starts with a N_2 slug (≈ 1.19 PV) followed by a brine slug (≈ 0.23 PV)

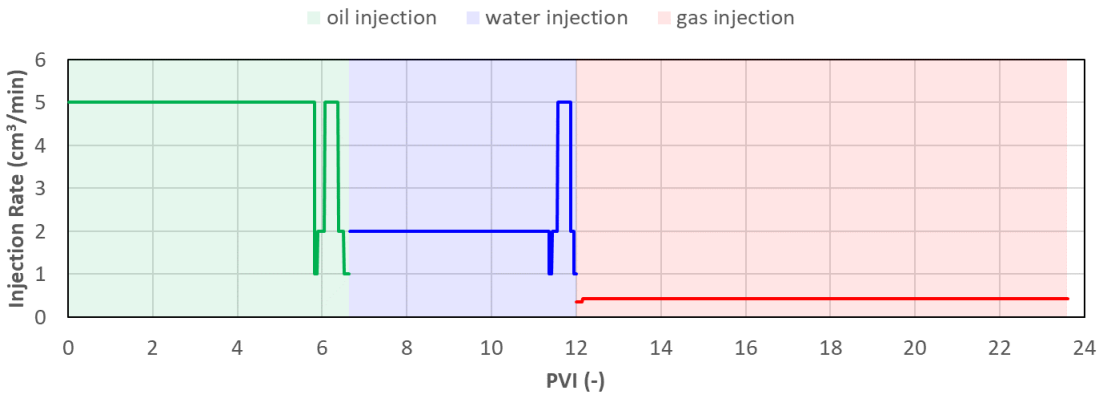

Figure 3.1. Injection rates in experiment A4.

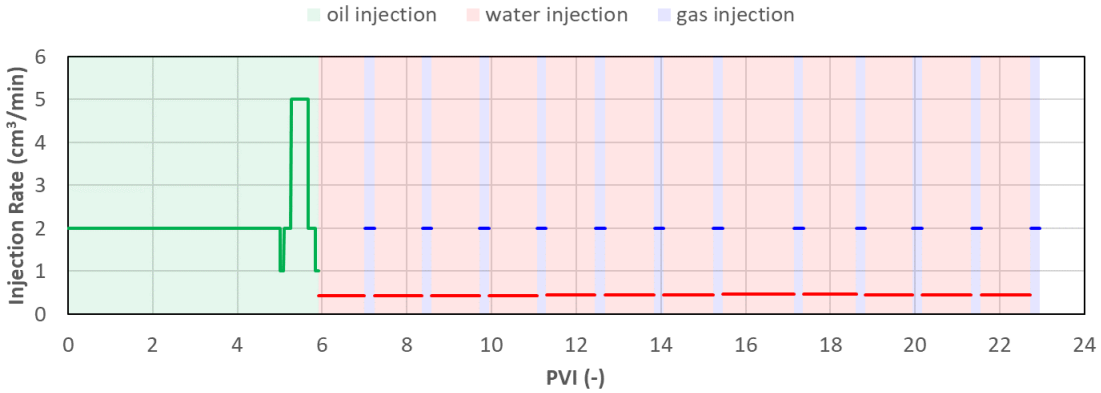

Figure 3.2. Injection rates in experiment A5.

3.1.4 Pressure Gradients

Figure 3.3 and Figure 3.4 show the measured pressure difference between core inlet and outlet (i.e. pressure drop) as a function of PVI for experiments A4 and A5, respectively.

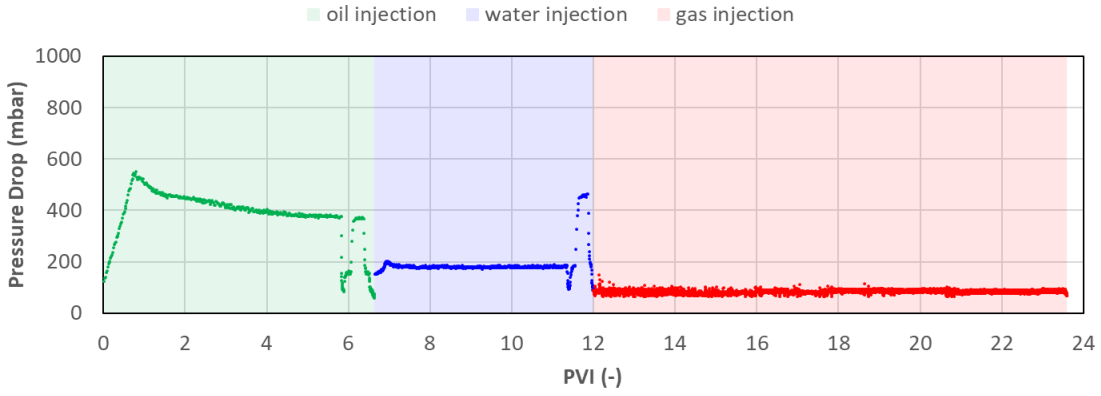

Figure 3.3. Pressure drop during experiment A4.

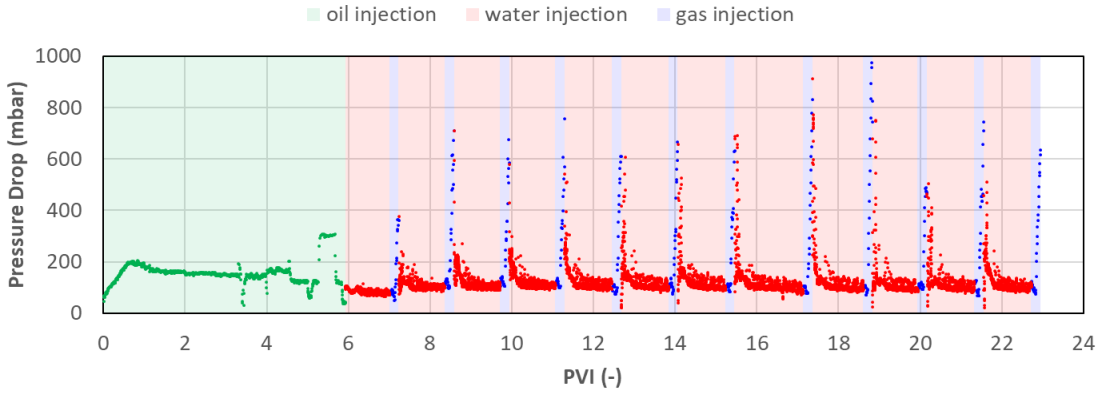

Figure 3.4. Pressure drop during experiment A5.

3.1.5 Production Data

The experimental procedure included measurements of liquid rates (oil and water) during the water flooding, gas flooding and WAG injection stages. Figure 3.5 and Figure 3.6 show the resulting oil recovery factor (fraction of OIIP), and the oil, water and gas cuts as a function of PVI for experiments A4 and A5, respectively.

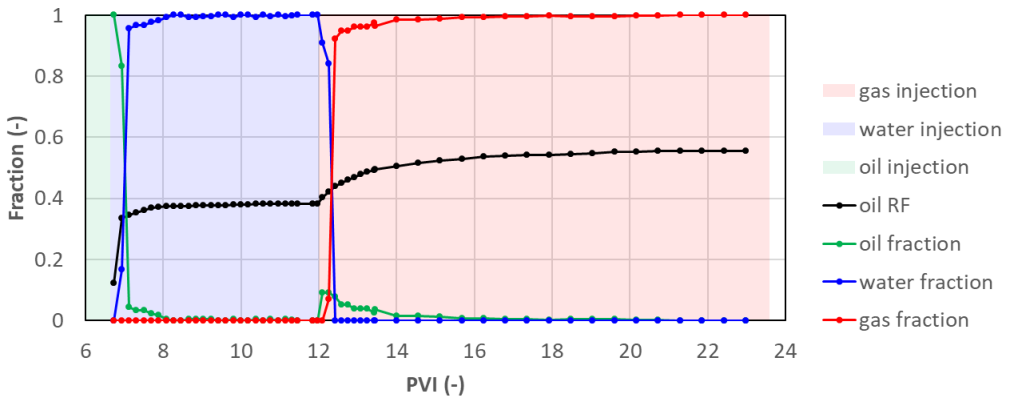

Figure 3.5. Oil recovery factor, and oil, water and gas cuts in experiment A4 during water flooding and gas flooding.

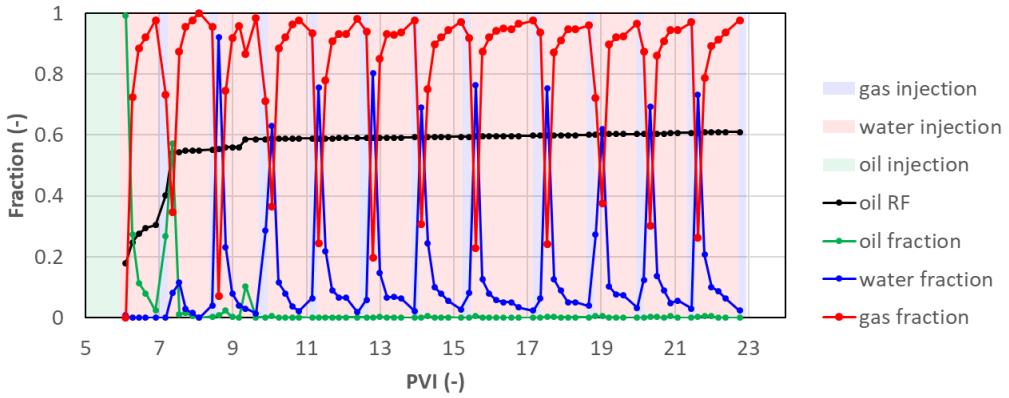

Figure 3.6. Oil recovery factor, and oil, water and gas cuts in experiment A5 during WAG.

3.1.6 Saturation

Calculations of averaged phase saturations were performed during the different injection stages in the experiments. Figure 3.7 and Figure 3.8 show ternary diagrams describing the saturation path followed during the test starting from primary drainage to the last flooding stage.

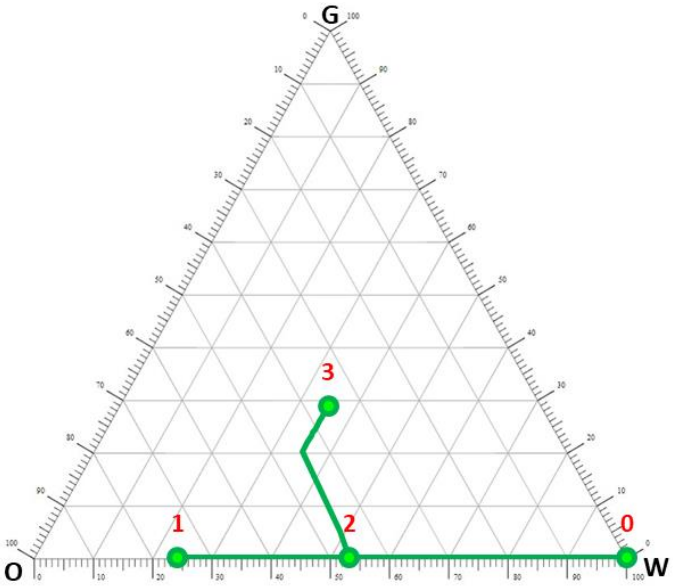

Figure 3.7. Saturation during experiment A4.
0 - 1: Primary drainage. 1 - 2: Forced imbibition. 2 - 3: Gas flooding.

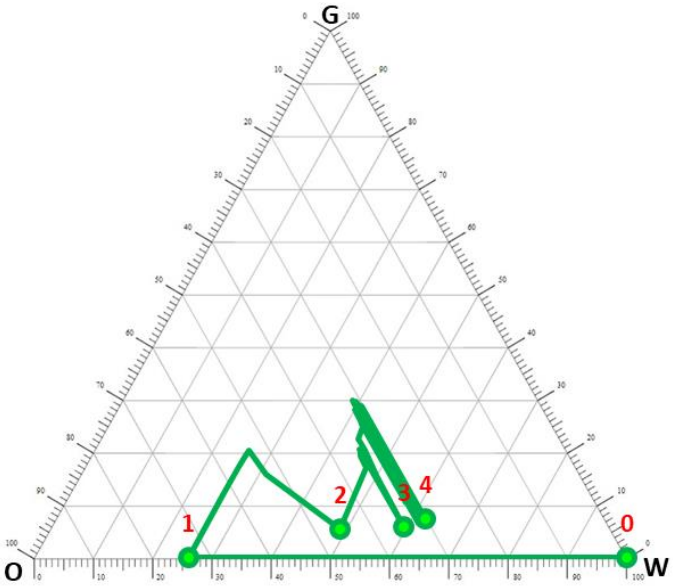

Figure 3.8. Saturation during experiment A5.
0 - 1: Primary drainage. 1 - 2: First WAG cycle. 2 - 3: Second WAG cycle. 3 - 4: Following WAG cycles with marginal oil recovery.

3.1.7 Summary

Table 3.7 shows required parameters for the calculation of the relative permeability curves obtained during experiments A4 and A5, as well as oil recovery factors. Here, k_{ro}^{0} and k_{rw}^{0} are the oil and water end-point relative permeabilities, S_{wc} the connate water saturation, S_{oi} the initial oil saturation, $S_{or}\,(WF)$ and $S_{or}\,(GF)$ the residual oil saturations after

waterflooding and gas flooding/WAG, and $RF\ (WF)$ and $RF\ (GF)$ the oil recovery factors after waterflooding and gas flooding/WAG as function of OIIP.

Table 3.7. Results of experiments A4 and A5.

Parameter	A4	A5
k_{ro}^0	0.65 ± 0.07	0.60 ± 0.05
k_{rw}^0	0.14 ± 0.01	-
S_{wc}	0.24 ± 0.02	0.26 ± 0.02
S_{oi}	0.76 ± 0.02	0.74 ± 0.02
$S_{or}\ (WF)$	0.46 ± 0.02	-
$S_{or}\ (GF)$	0.40 ± 0.02	0.30 ± 0.02
$RF\ (WF)$ (% of OIIP)	36 ± 4	-
$RF\ (GF)$ (% of OIIP)	53 ± 4	59 ± 4

3.2 Foam Assisted Chemical Flooding (FACF)

In this study, Janssen et al., (2019b) performed experiments on FACF flooding, a technique that combines lowering o/w IFT with foam as drive agent. The experiments consisted on CT-scanned core-floods which included alkaline-surfactant (AS) and FACF injection at different foam qualities (liquid and gas co-injection) as listed in Table 3.8. As with the previously described experiments, core samples were flushed with CO_2, saturated with brine, flooded with oil to resemble primary drainage and flooded with brine (WF) in a forced imbibition stage. In this way, all experiments started at residual oil after waterflooding and were performed at under-optimum salinity conditions. An additional experiment at near-optimum salinity conditions was carried out. All experiments were performed at a backpressure of 20 bar.

Table 3.8. Configuration of AS and FACF flooding experiments.

Experiment	Procedure	Salinity (NaCl wt%)	Gas Rate (co-injection) (cm^3/min)	Liquid Rate (co-injection) (cm^3/min)	Foam Quality (%)
B0	AS	0.4	-	-	-
B1	FACF	0.4	0.627	0.473	57
B2	FACF	0.4	0.847	0.253	77
B3	FACF	0.4	1.067	0.033	97
B4	AS	2.0	-	-	-

From this series of experiments allowed authors to conclude that (1) the methodology was successful in generating a foam drive which displaced a previously generated oil bank proving the mobilization of residual oil to WF, (2) total oil recovery is not affected by the quality of the foam, however, oil displacement was more stable with a low-quality foam, and (3) the amount of free oil (non-solubilized) is not affected by the quality of the foam. All the tests listed in Table 3.8 will be history-matched considering the good quality of CT scan images acquired during core flooding.

3.2.1 Fluid Properties

The chemical agents and fluids used in the experiments are described for each flooding stage, starting from primary drainage, as follows:

The oil used in the experiment corresponds to n-hexadecane ($CH_3(CH_2)_{14}CH_3$) with 0.006 wt% of $C_6H_{24}N_4O$, a red colorant for improving visualization. The oleic phase was doped with 1-iododecane ($CH_3(CH_2)_9I$). Table 3.9 shows the properties of the oleic phase per experiment.

Table 3.9. Oleic phase properties in experiments B0 to B4.

Experiment	**Dopant Concentration** (wt%)	**Density*** (g/cm^3)	**Viscosity*** (cP)
B0	20	0.841 ± 0.001	3.310 ± 0.03
B1	25	0.867 ± 0.001	3.377 ± 0.03
B2	20	0.841 ± 0.001	3.310 ± 0.03
B3	20	0.841 ± 0.001	3.310 ± 0.03
B4	20	0.841 ± 0.001	3.310 ± 0.03

* at 20 °C and atmospheric pressure

The brine used was solution of NaCl in demineralized water. Table 3.10 shows the properties of the brine used in the experiments.

Table 3.10. Brine properties in experiments B0 to B4.

Experiment	Type	Density* (g/cm³)	Viscosity* (cP)
B0	2.0 wt% NaCl	1.013 ± 0.001	1.03 ± 0.05
B1**	4.0 wt% NaCl 2.0 wt% NaCl	1.027 ± 0.001 1.013 ± 0.001	1.07 ± 0.05 1.03 ± 0.05
B2	2.0 wt% NaCl	1.013 ± 0.001	1.03 ± 0.05
B3	2.0 wt% NaCl	1.013 ± 0.001	1.03 ± 0.05
B4	3.6 wt% NaCl	1.024 ± 0.001	1.06 ± 0.05

* at 20 °C and atmospheric pressure
** two waterflooding stages

An internal olefin sulfonate (IOS2024 ENORDET O242) was used as surfactant agent. The surfactant aqueous solution has an active matter (AM) content of 19% and a CMC of 3E-3 wt% AM IOS2024 in the presence of 0.5 wt% sec-butanol ($C_4H_{10}O$), 0.4 wt% sodium chloride (NaCl) and 1.0 wt% sodium carbonate (Na_2CO_3).The Na_2CO_3, alkaline agent, was used to minimize surfactant adsorption. Since no naphthenic acids were added to the oleic phase, no saponification effect was generated. Table 3.11 shows the composition of the surfactant slug in experiments B0 to B4.

Table 3.11. Surfactant slug composition in experiments B0 to B4.

Experiment	NaCl (wt%)	Na_2CO_3 (wt%)	Sec-butanol (wt%)	IOS2024 (wt%)
B0	0.4	1.0	0.5	0.3
B1	0.4	1.0	0.5	0.3
B2	0.4	1.0	0.5	0.3
B3	0.4	1.0	0.5	0.3
B4	2.0	1.0	0.5	0.3

The drive stage consisted in the co-injection of a surfactant solution and Nitrogen (N_2). The surfactant solution formulation of experiments B1 to B4 is the same as in the slug phase, except that no sec-butanol was added. No co-injection was performed in experiment B0.

3.2.2 Phase Behavior

The alkaline-surfactant system used in the phase behavior analysis contained 0.3 wt% AM IOS2024, 1 wt% Na_2CO_3, 0.5 wt% sec-butanol and NaCl with concentrations between 0.0 and 6.0 wt%. The solution was mixed with n-hexadecane at an oil-to-water ratio of 1:2 and properly

equilibrated. The authors performed a salinity scan test to determine the optimum salinity. Figure 3.9 shows that the optimum salinity ranges between 2.5 and 3 wt% NaCl.

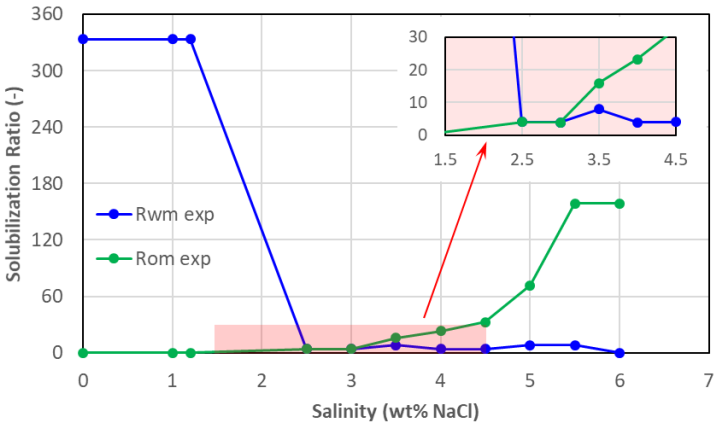

Figure 3.9. Solubilization ratios for the oil-water-surfactant system as a function of salinity.

3.2.3 Core Properties

Bentheimer sandstone core samples were used for experimental purposes. Table 3.12 shows the properties for each sample in each experiment as well as the calculated pore volume. Porosity reported in this table corresponds to averaged CT scan data and permeability was obtained during initial water injection using Darcy's law. The pore volumes reported as "recalculated" in Table 3.12 were obtained during this study. This will be discussed in section 4.1.

Table 3.12. Core properties for experiments on AS and FACF flooding.

Experiment	**Length** (cm)	**Diameter** (cm)	**Porosity** (%)	**Permeability** (D)	**Pore Volume (reported)** (cm^3)	**Pore Volume (recalculated)** (cm^3)
B0	96.8 ± 0.1	3.8 ± 0.1	24 ± 0.4	3.14 ± 0.11	263.5 ± 19	259.0
B1	96.2 ± 0.1	3.8 ± 0.1	24 ± 0.4	3.20 ± 0.11	261.8 ± 25	258.2
B2	96.9 ± 0.1	3.8 ± 0.1	24 ± 0.5	3.11 ± 0.15	263.7 ± 15	258.7
B3	97 ± 0.1	3.8 ± 0.1	23 ± 0.4	3.32 ± 0.1	253.0 ± 14	256.0
B4	97.1 ± 0.1	3.8 ± 0.1	24 ± 0.4	3.45 ± 0.1	264.3 ± 19	261.0

3.2.4 Core Flooding Procedure

Table 3.13 to Table 3.17 show the PVI and the injection rates at local conditions used for experiments B0 to B4. Figure 3.10 to Figure 3.14 show the local rates for each experiment. Note

that the variation in rates at the end of primary drainage and forced imbibition in each experiment was designed to calculate the relative permeabilities of oil and water, respectively. A large flow rate during a considerable time interval (bump flood) was applied to minimize the impact of the capillary-end effect.

Table 3.13. Injection in experiment B0.

Stage	PVI*	Oil Rate (cm^3/min)	Water Rate (cm^3/min)
Primary Drainage	3.06	0.2	-
Water Injection	6.56	-	0.25
Surfactant Flooding	3.43	-	0.15

* Based on recalculated PV from CT scan

Table 3.14. Injection in experiment B1.

Stage	PVI*	Oil Rate (cm^3/min)	Water Rate (cm^3/min)	Gas Rate (cm^3/min)
Primary Drainage	3.08	0.5	-	-
Water Injection (4 wt% NaCl)	6.94	-	0.25	-
Water Injection (2 wt% NaCl)	4.83	-	0.25	-
Surfactant Slug	0.47	-	0.15	-
Foam Drive	1.20	-	0.50	0.60

* Based on recalculated PV from CT scan

Table 3.15. Injection in experiment B2.

Stage	PVI*	Oil Rate (cm^3/min)	Water Rate (cm^3/min)	Gas Rate (cm^3/min)
Primary Drainage	3.87	0.5	-	-
Water Injection	5.75	-	0.25	-
Surfactant Slug	0.50	-	0.15	-
Foam Drive	6.00	-	0.25	0.85

* Based on recalculated PV from CT scan

Table 3.16. Injection in experiment B3.

Stage	PVI*	Oil Rate (cm^3/min)	Water Rate (cm^3/min)	Gas Rate (cm^3/min)
Primary Drainage	3.63	0.5	-	-
Water Injection	6.12	-	0.25	-
Surfactant Slug	0.47	-	0.15	-
Foam Drive	6.38	-	0.03	1.07

* Based on recalculated PV from CT scan

Table 3.17. Injection in experiment B4.

Stage	PVI*	Oil Rate (cm^3/min)	Water Rate (cm^3/min)	Gas Rate (cm^3/min)
Primary Drainage	3.16	0.2	-	-
Water Injection	10.16	-	0.25	-
Surfactant Slug	0.47	-	0.15	-

* Based on recalculated PV from CT scan

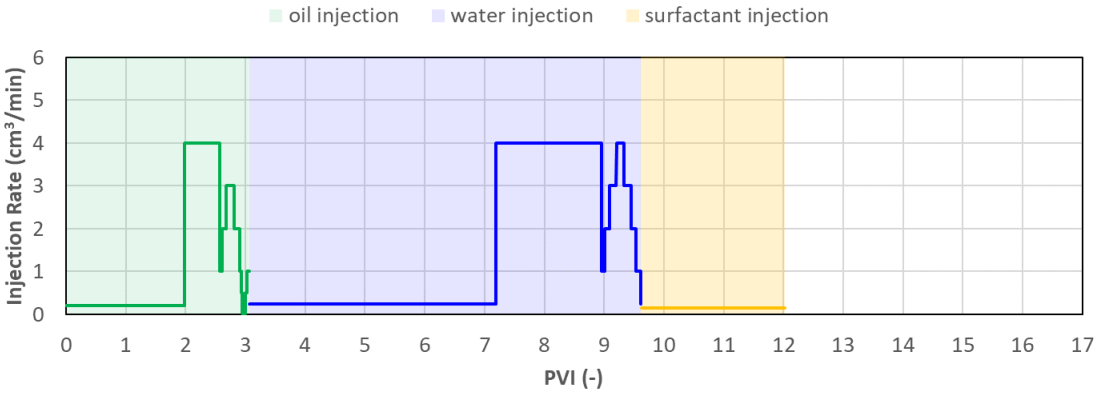

Figure 3.10. Injection rates in experiment B0.

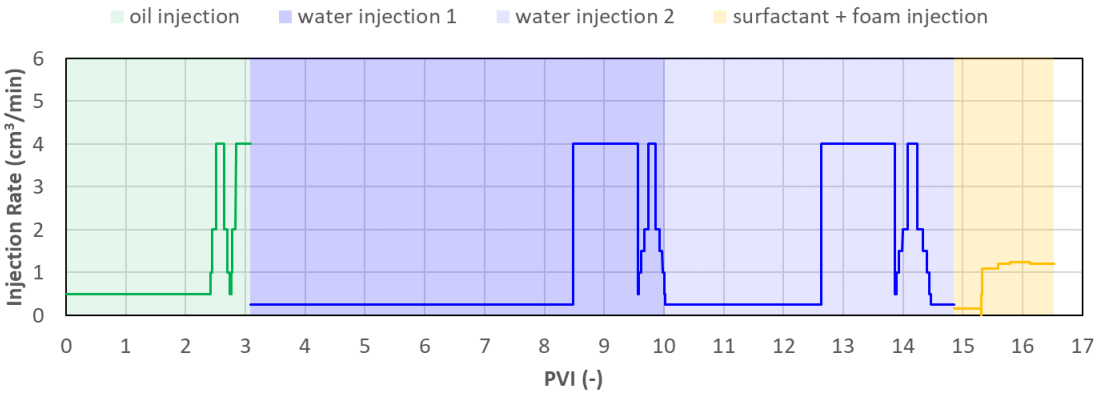

Figure 3.11. Injection rates in experiment B1.

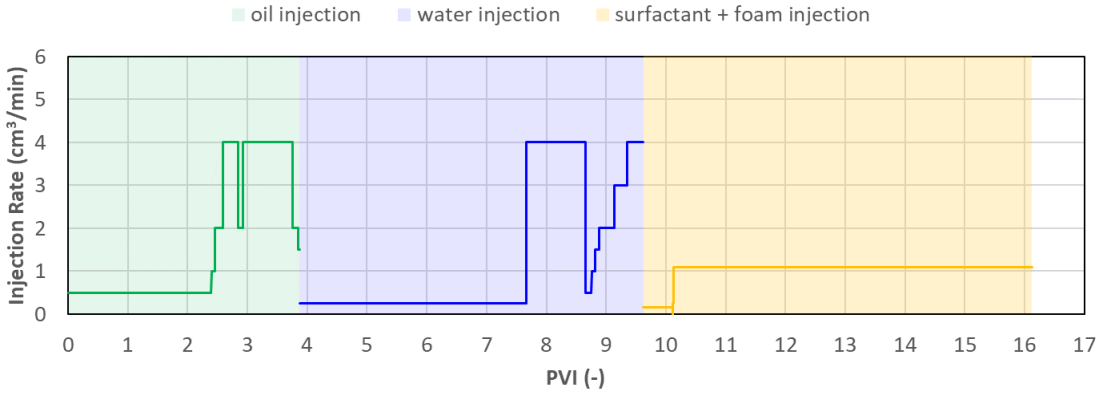

Figure 3.12. Injection rates in experiment B2.

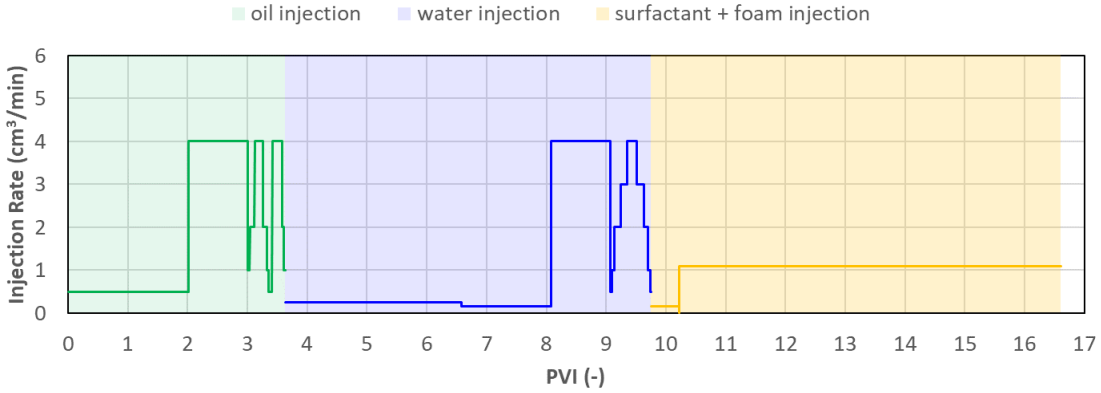

Figure 3.13. Injection rates in experiment B3.

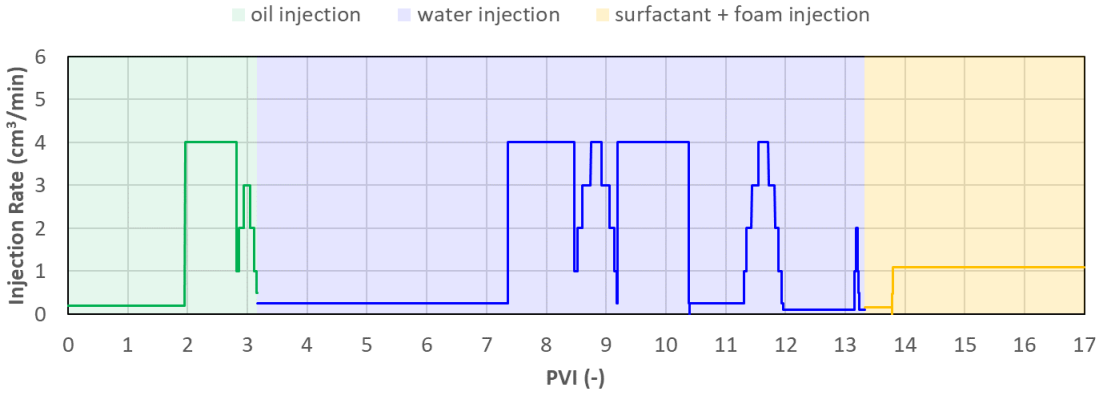

Figure 3.14. Injection rates in experiment B4.

3.2.5 Pressure Gradients

Figure 3.15 to Figure 3.19 present the total pressure drop versus PVI for experiments B0 to B4.

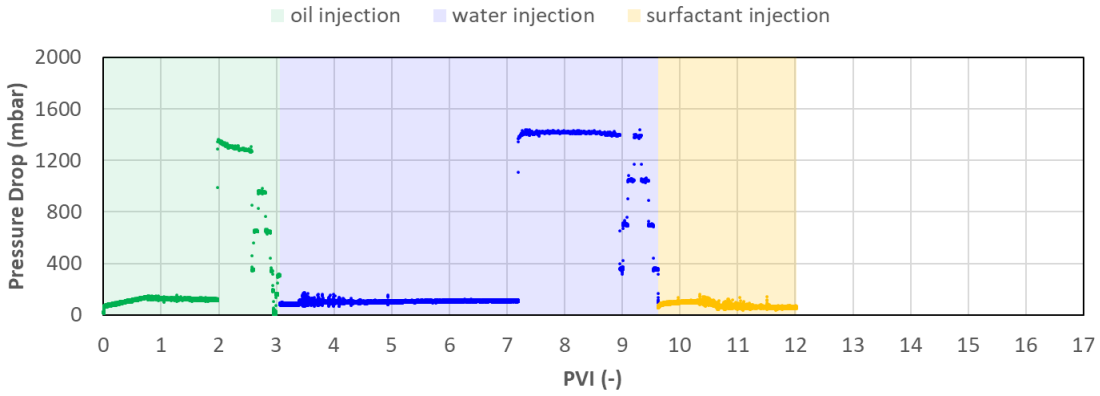

Figure 3.15. Pressure drop during experiment B0.

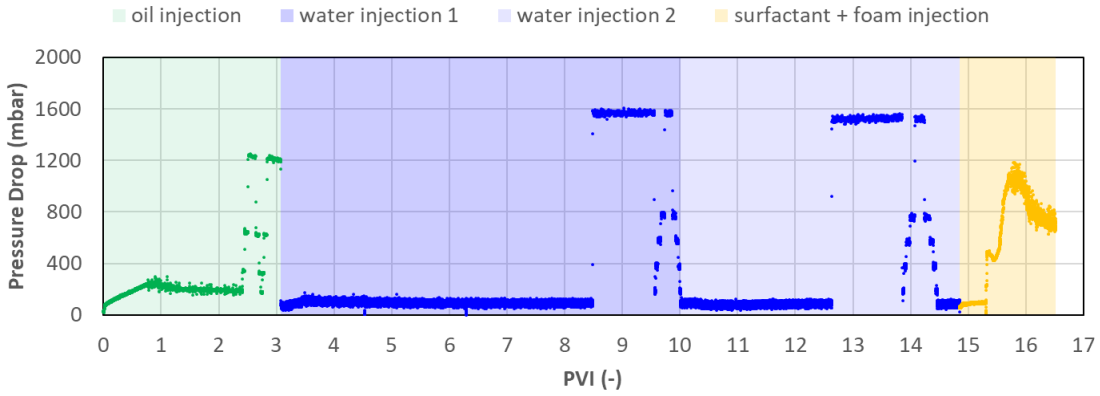

Figure 3.16. Pressure drop during experiment B1.

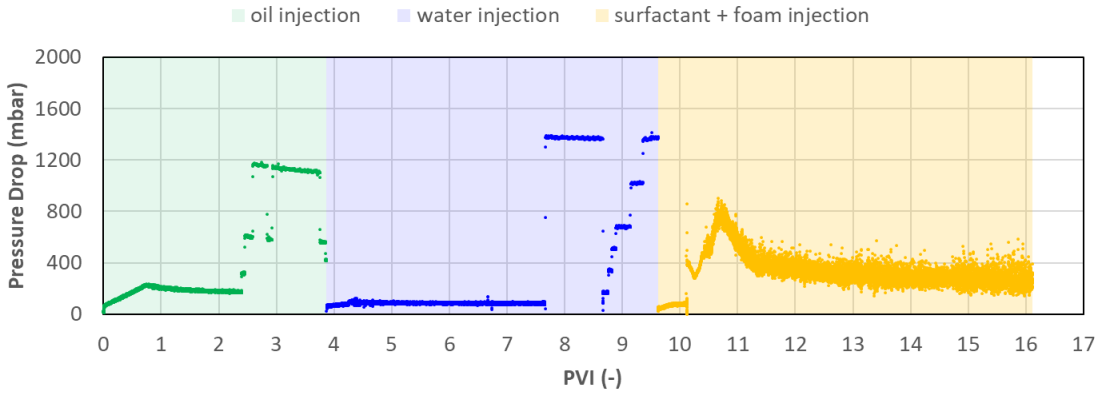

Figure 3.17. Pressure drop during experiment B2.

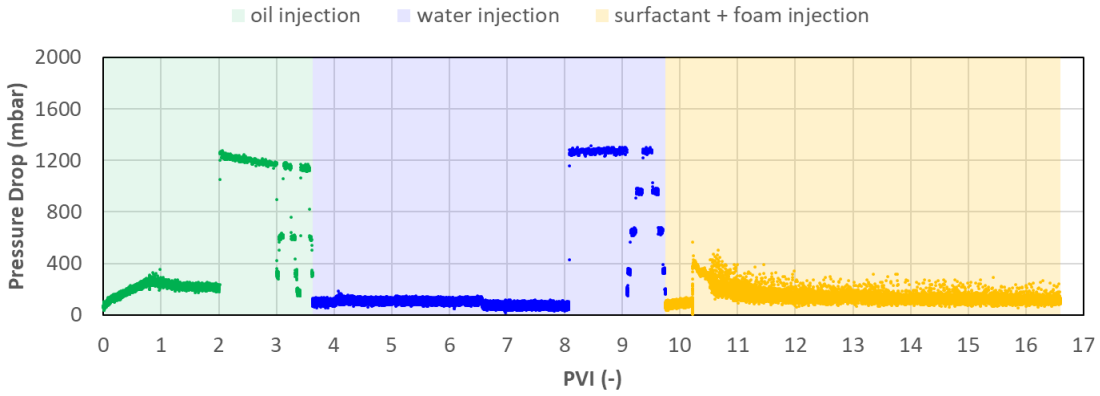

Figure 3.18. Pressure drop during experiment B3.

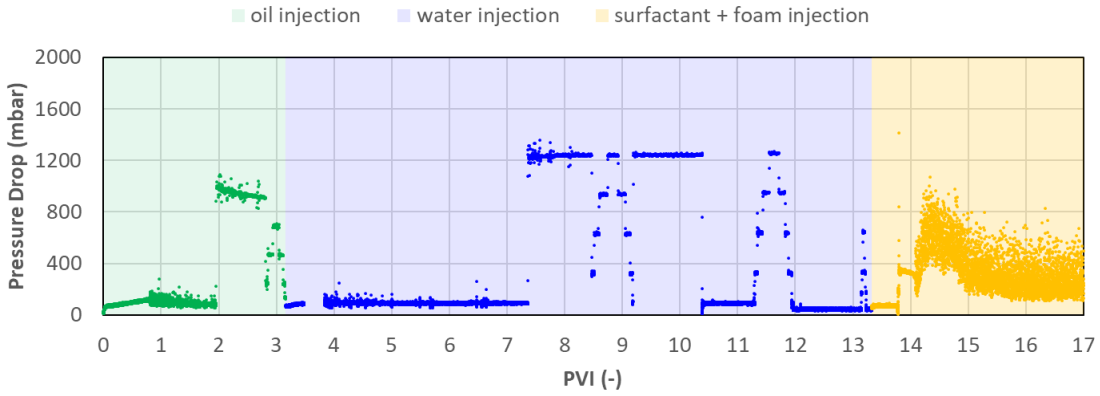

Figure 3.19. Pressure drop during experiment B4.

3.2.6 Production Data

Similar to the first data set, the experiments here include measurements of produced liquid rates. Coriolis measurements were available in some experiments for those stages in which no gas injection took place, it was used only for identifying the breakthrough times. The Coriolis mass flow and density measurements allow an accurate determination of breakthrough times given the enough contrast in densities between aqueous and oleic phases. In the case of primary drainage, a strong density fall indicates the oleic phase breakthrough, whilst for forced imbibition, a strong density increase indicates the aqueous phase breakthrough. Figure 3.20 to Figure 3.23 show the obtained oil recovery factor as well as the oil, water and gas cuts as a function of PVI for experiments B0 to B3. Although foam displacement was practiced in experiment B4, only the surfactant slug stage is relevant for this study; no oil production is derived from this stage in this experiment since the generated oil bank did not reach the end of the core.

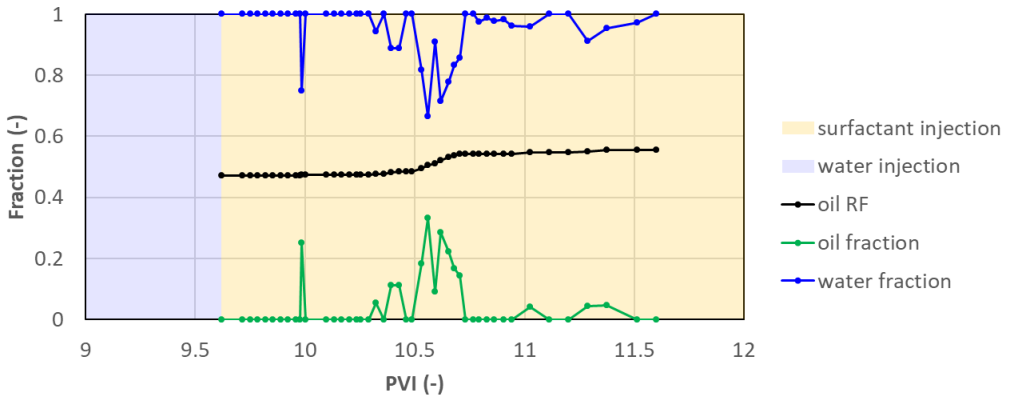

Figure 3.20. Oil recovery factor, oil cut, and water cut in experiment B0 during water flooding and surfactant flooding.

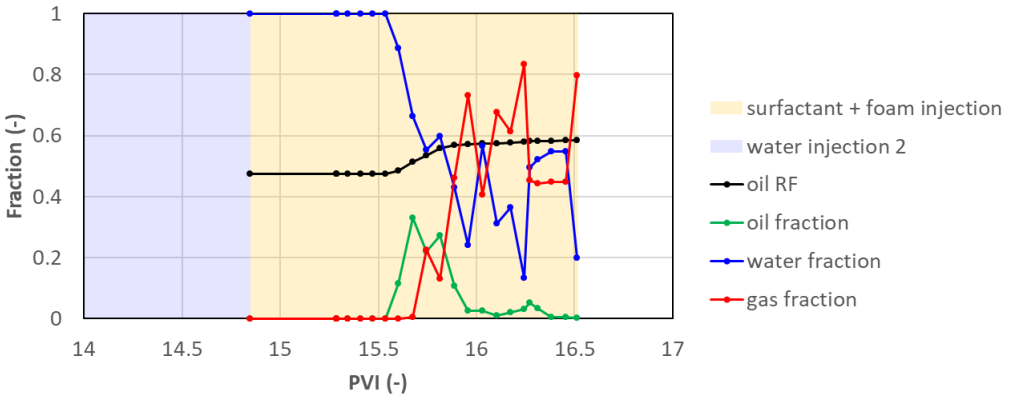

Figure 3.21. Oil recovery factor, and oil, water and gas cuts in experiment B1 during water flooding and surfactant/gas co-injection.

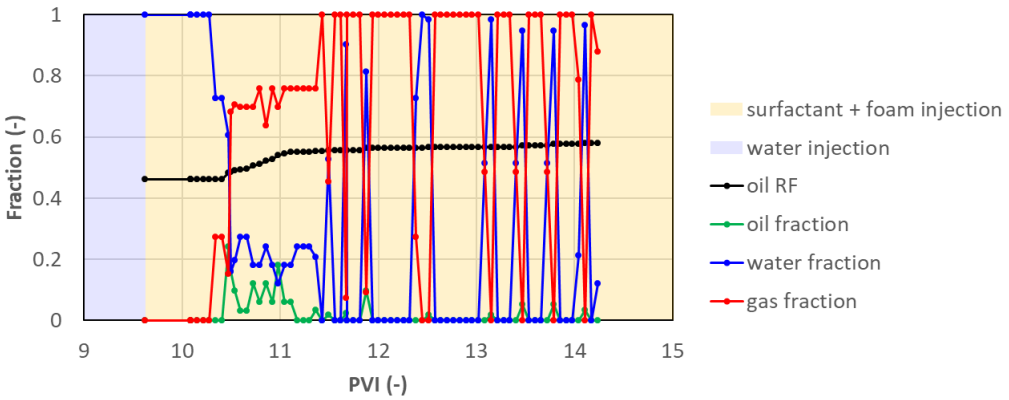

Figure 3.22. Oil recovery factor, and oil, water and gas cuts in experiment B2 during water flooding and surfactant/gas co-injection.

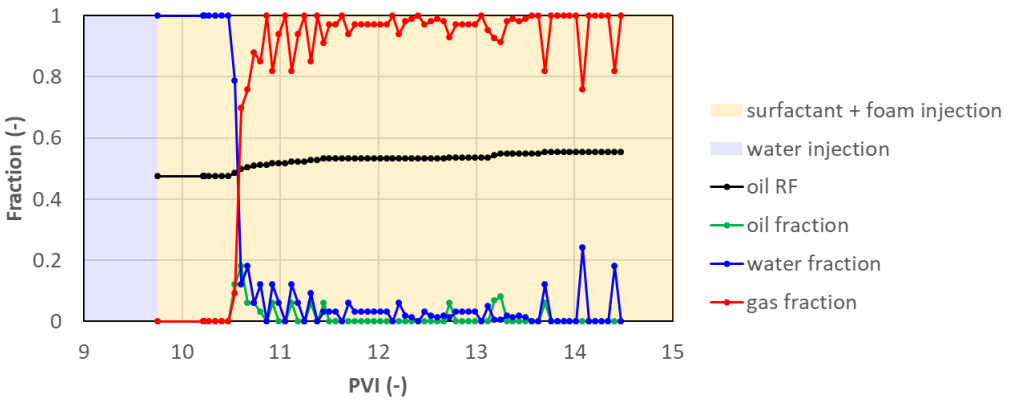

Figure 3.23. Oil recovery factor, and oil, water and gas cuts in experiment B3 during water flooding and surfactant/gas co-injection.

3.2.7 Saturation

Figure 3.24 to Figure 3.27 show ternary diagrams that illustrate the saturation path followed from tests B0 to B3 starting from primary drainage to the last flooding stage.

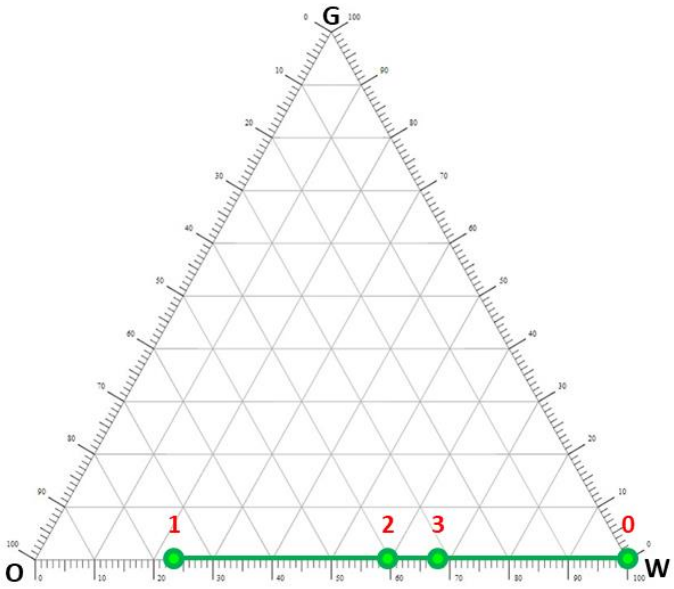

Figure 3.24. Saturation during experiment B0.
0 - 1: Primary drainage. 1 - 2: Forced imbibition. 2 - 3: Gas flooding.

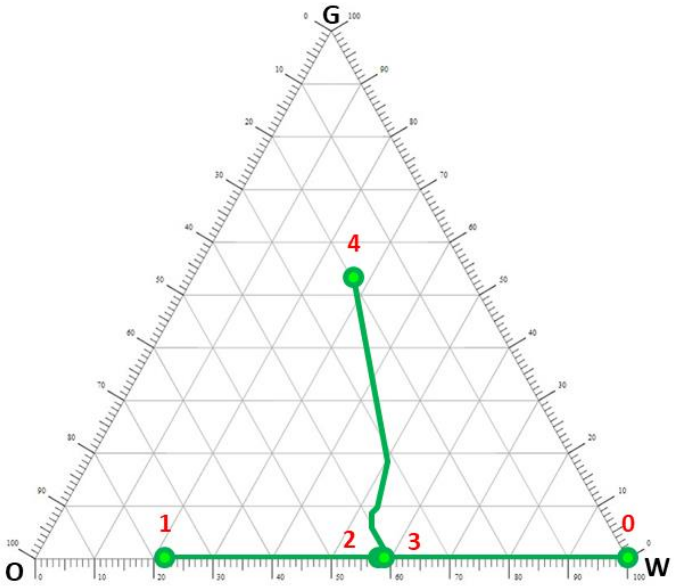

Figure 3.25. Saturation during experiment B1.
0 - 1: Primary drainage. 1 - 2: First forced imbibition. 2 - 3: Second forced imbibition. 3 – 4: Surfactant and foam flooding.

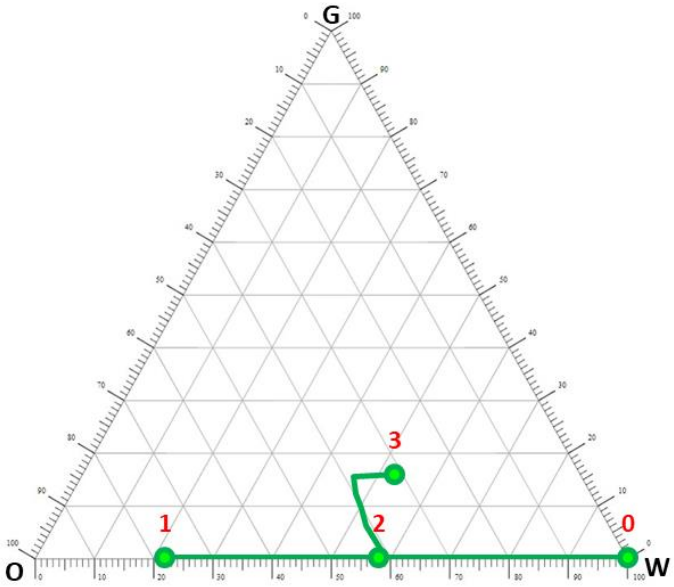

Figure 3.26. Saturation during experiment B2.
0 - 1: Primary drainage. 1 - 2: Forced imbibition. 2 - 3: Surfactant and foam flooding.

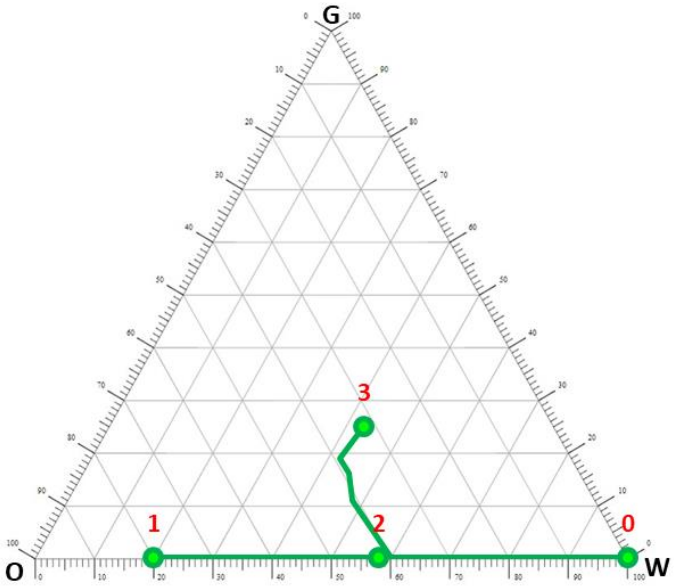

Figure 3.27. Saturation during experiment B3.
0 - 1: Primary drainage. 1 - 2: Forced imbibition. 2 - 3: Surfactant and foam flooding.

3.2.8 CT Scan Saturations

One of the great advantages of the data set presented in this section is the availability of saturation distributions along the core obtained from CT scan measurements. Figure 3.28 and Figure 3.29 show the oil saturation distribution at different PVI for primary drainage and water flooding in experiment B1. In the same way, Figure 3.30 show the oil saturation distribution at different PVI for surfactant flooding in experiment B0, and Figure 3.31 for foam flooding in experiment B2. Notice how in the case of primary drainage and forced imbibition the shock fronts are well defined. In the case of chemical and foam flooding, it is easy to observe the progression of an oil bank moving along the core. In all the cases, the injection is located at the left and production at the right. A complete summary of the available CT scan saturations is included in Appendix B.

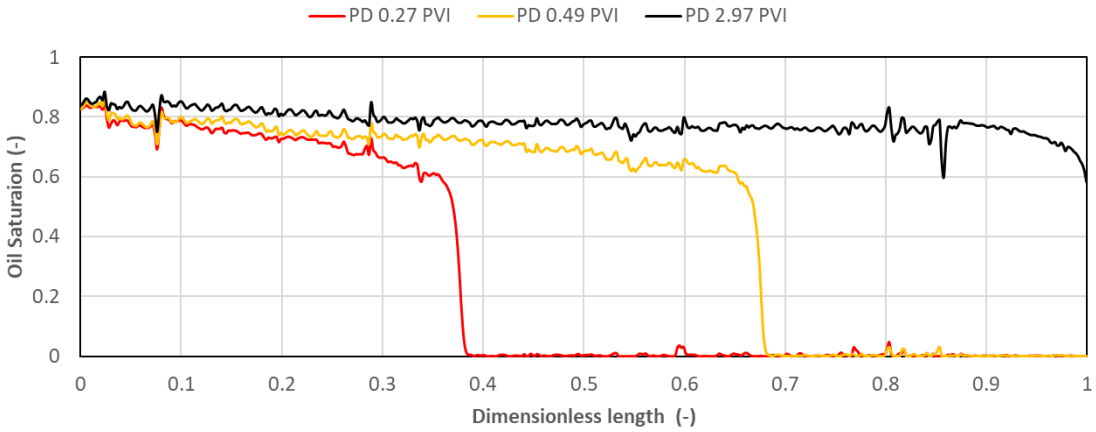

Figure 3.28. Oil saturation distribution in experiment B1 during primary drainage.

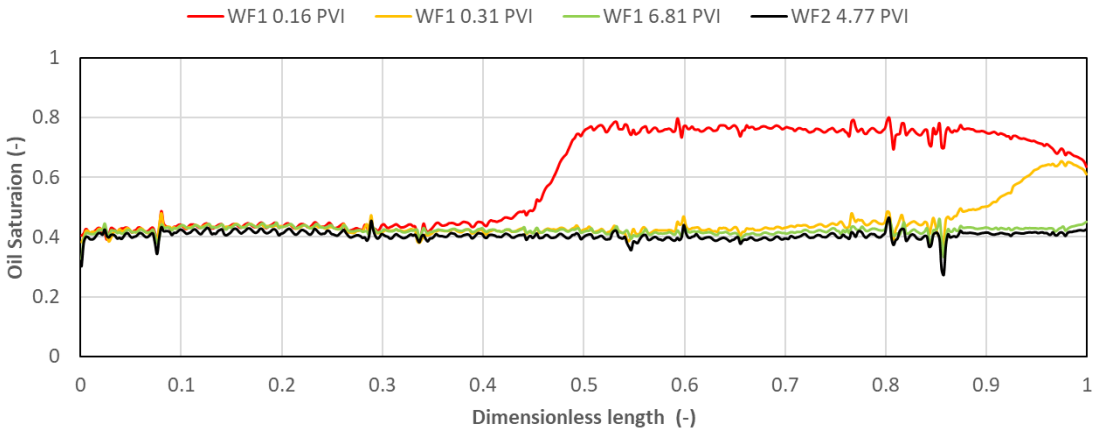

Figure 3.29. Oil saturation distribution in experiment B1 during water flooding.

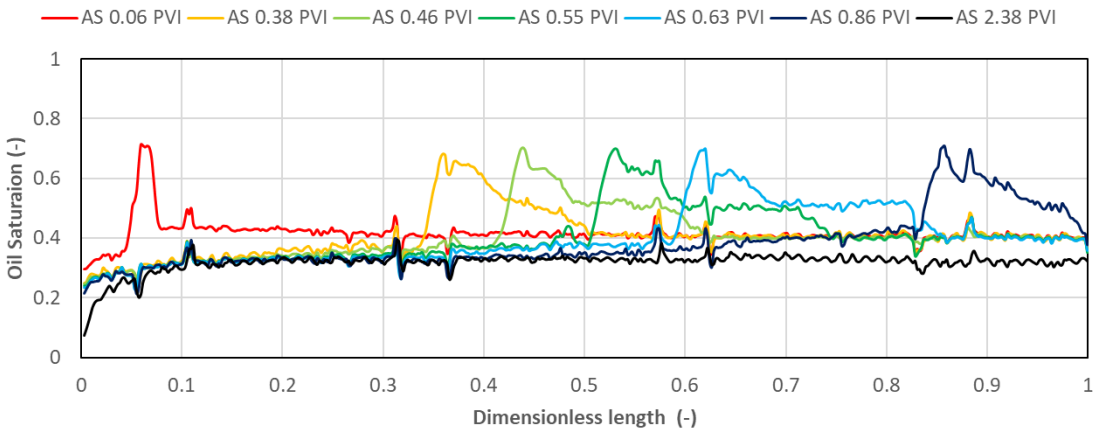

Figure 3.30. Oil saturation distribution in experiment B0 during surfactant flooding.

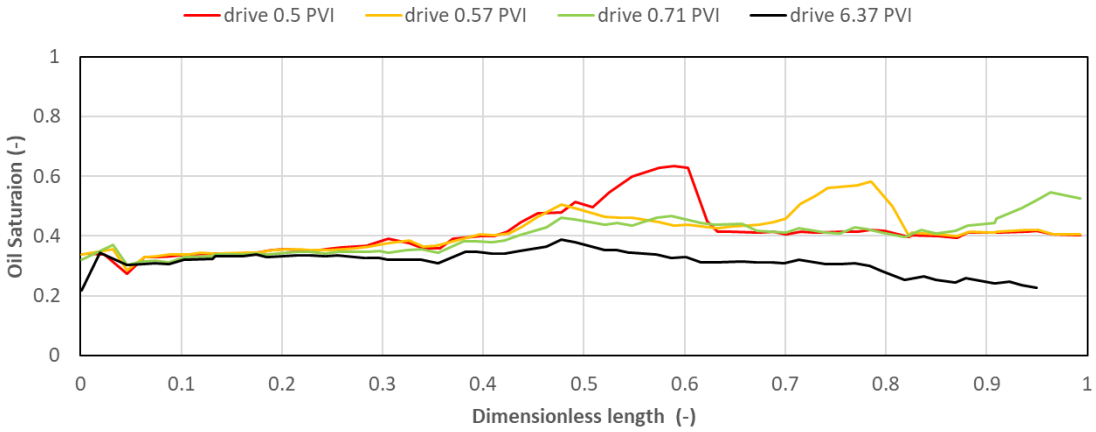

Figure 3.31. Oil saturation distribution in experiment B2 during foam flooding.

3.2.9 Summary

Table 3.18 shows a summary of the results of experiments B0 to B3. The same parameters as in Table 3.7 are listed, with the addition of S_{or} (CF) and RF (CF) that correspond to the residual oil saturation and the ultimate oil recovery factor after chemical flooding, respectively.

Table 3.18. Overview of the results of experiments B0 to B3

Parameter	B0		B1		B2		B3	
k_{ro}^0	0.53 ± 0.06		0.51 ± 0.02		0.57 ± 0.09		0.56 ± 0.11	
k_{rw}^0	0.14 ± 0.02		0.13 ± 0.01		0.14 ± 0.01		0.15 ± 0.02	
	MB	**CTS**	**MB**	**CTS**	**MB**	**CTS**	**MB**	**CTS**
S_{wc}	0.24 ± 0.03	0.23 ± 0.04	0.20 ± 0.04	0.22 ± 0.04	0.23 ± 0.04	0.22 ± 0.05	0.17 ± 0.04	0.20 ± 0.05
S_{oi}	0.76 ± 0.03	0.77 ± 0.04	0.80 ± 0.04	0.78 ± 0.04	0.77 ± 0.04	0.78 ± 0.05	0.83 ± 0.04	0.80 ± 0.05
S_{or} (WF)	0.39 ± 0.05	0.42 ± 0.01	0.43 ± 0.06	0.41 ± 0.02	0.39 ± 0.05	0.42 ± 0.01	0.42 ± 0.06	0.42 ± 0.02
S_{or} (CF)	0.32 ± 0.08	0.32 ± 0.03	0.34 ± 0.06	0.31 ± 0.03	0.30 ± 0.05	0.31 ± 0.04	0.33 ± 0.06	0.32 ± 0.04
RF (WF) (% of OIIP)	49 ± 5	45 ± 5	46 ± 10	47 ± 6	49 ± 9	46 ± 6	49 ± 10	48 ± 7
RF (CF) (% of OIIP)	57 ± 11	58 ± 6	58 ± 8	60 ± 5	61 ± 9	60 ± 7	60 ± 9	60 ± 7

4 METHODOLOGY

This chapter summarizes the methodology implemented in the present study. As stated in previous chapters, the numerical simulation tool used for the analysis was UTCHEM. All the matches were developed under a 1D configuration. For primary drainage and forced imbibition (water flooding), a two-phase scheme was preferred. Once the surfactant stage was implemented, an additional phase was involved. Finally, the four-phase model included in UTCHEM was used to analyze the surfactant/gas co-injection stage (i.e. foam flooding). A simple graphical user interface (GUI) was scripted in MATLAB® for pre and post-processing purposes given the absence of a tool with this functionality into UTCHEM.

4.1 Grid Setup

For experiments A4 and A5, a 1, 1, 100 (x, y, z) grid was implemented considering the vertical orientation of the core to promote gravity stable conditions. Porosity and permeability were assumed as constant given the almost homogeneous condition of the Bentheimer cores used in the experiments. Note that CT scan information was not available for porosity calculation in this experimental series. For this reason, the constant porosity used was derived from a volumetric balance calculation.

As stated in Chapter 3, the absolute permeability was obtained as the harmonic average of the permeabilities calculated for the different core sections (Figure 4.1) taking advantage of information on different flow rates, where Darcy's law was applied:

$$q_w = \frac{A\,k_i}{\mu_w}\nabla P_i, \qquad \nabla P_i = \frac{\Delta P_i}{\Delta l} \tag{4.1}$$

$$\bar{k} = \frac{\sum_{i=1}^{n}\Delta l_i}{\sum_{i=1}^{n}\frac{\Delta l_i}{k_i}} \tag{4.2}$$

where $\bar{k}$ is the average permeability, A is the transversal area of the core, q_w and μ_w the water injection rate and viscosity, and k_i, ∇P_i, ΔP_i and Δl_i the absolute permeability, pressure gradient (neglecting gravity effects), pressure differential and length for a given section i, respectively.

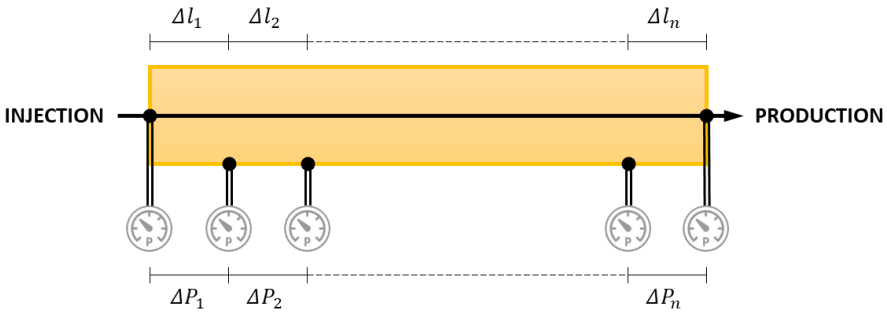

Figure 4.1. Schematic of core sections for permeability calculations. A section corresponds to the interval between pressure gauges.

For experiments B0 to B4, good quality CT scan information was available. The original information was obtained with a spacing of 2 mm, which means that for an average core length of 96 cm, about 480 data points were available (covering the entire space range). A sensitivity on cell size was performed to obtain a balanced grid configuration in terms of simulation run time and quality, considering the effect of numerical dispersion this simplification may cause. An initial grid with 480 cells was used (one cell per each data point available). Selection of cell size is a function of number of fine cells per coarse cell in the scaled grid, considering the exact length of each core. In this way, a ratio of four original fine cells per coarse cell was selected, which resulted in 120 to 121 coarse cells in total. More details on the results will be showed in the primary drainage description section. The remainder dimensions, both equal to Δh, were calculated for assuming a square transversal section with the same area as the transversal section of the core.

$$\Delta h = \sqrt{\pi\, r^2} \tag{4.3}$$

where r is the core radius.

Figure 4.2 defines a fine cell (original CT scan discretization), coarse cell (group of fine cells for scaling purposes) and core section (space between pressure gauges).

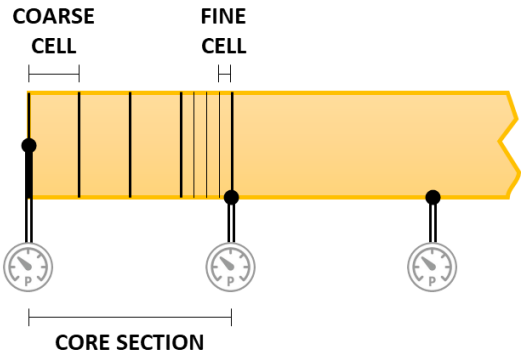

Figure 4.2. Core section, coarse cell and fine cell definition.

For each coarse cell, the porosity was calculated as the arithmetic average porosity of its corresponding fine cells. Permeability at each coarse cell was obtained as a function of its porosity using the Carman-Kozeny relation (Carman, 1937; Kozeny, 1927):

$$k = \frac{D_p^2}{\alpha} \frac{\phi^3}{(1-\phi^2)} \tag{4.4}$$

where D_p is the average grain diameter taken as 0.27 mm (Peksa, et al., 2015), and α the tortuosity factor. The tortuosity factor was obtained for each core section using the previous expression. In this step, the porosity was calculated as the average porosity of the fine cells contained in each core section.

Once a permeability value was obtained for each coarse cell, a harmonic average of the coarse cells contained in each core section was compared with the permeability obtained by Darcy's law for validating the procedure (Figure 4.3). Figure 4.4 (porosity) and Figure 4.5 (permeability) show a comparison between fine and coarse properties for experiment B0. The Appendix C summarizes the quality plots, as well as the porosity and permeability for fine and coarse grids for experiments B0 to B4.

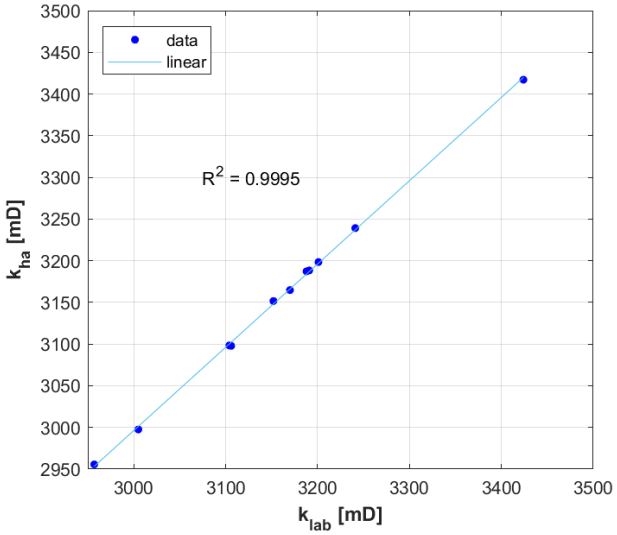

Figure 4.3. Absolute permeability quality control for experiment B0.

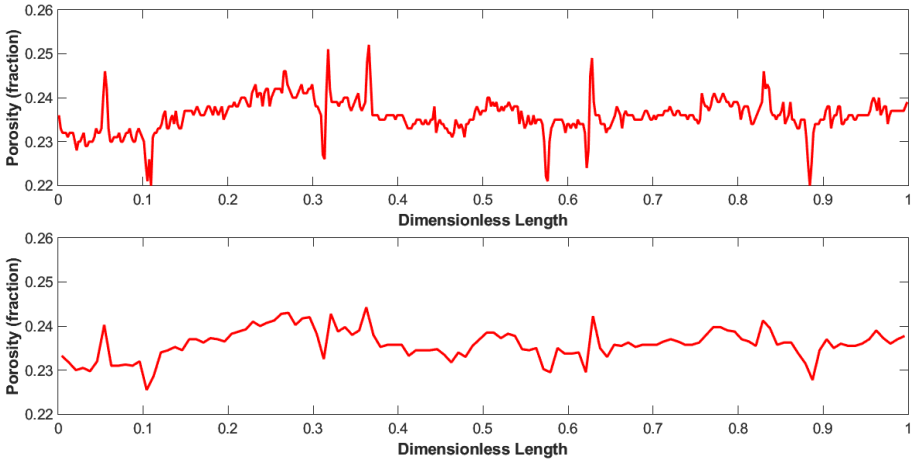

Figure 4.4. Comparison between fine (upper) and coarse (lower) porosity distribution for experiment B0.

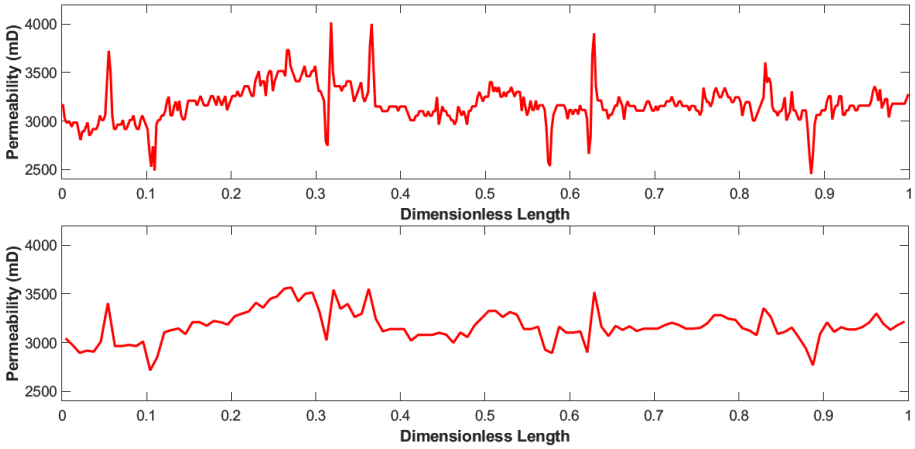

Figure 4.5. Comparison between fine (upper) and coarse (lower) permeability distribution for experiment B0.

Table 4.1 summarizes the grid configuration for each experiment. The total pore volume (PV) calculated considering the porosity estimation in the coarse grid slightly varies compared with the reported PV but is still an acceptable estimation considering the uncertainty, which is also reported (see Table 3.12). For the sake of consistency, the subsequent PVI are recalculated as well, however, the variation with the reported PVI is not significant.

Table 4.1. Grid properties for all experiments.

Experiment	Number of cells (x, y, z)	Δx (m)	Δy (m)	Δz (m)
A4	1, 1, 100	0.0346	0.0346	0.0017
A5	1, 1, 100	0.0346	0.0346	0.0017
B0	120, 1, 1	0.0081	0.0337	0.0337
B1	120, 1, 1	0.008	0.0337	0.0337
B2	121, 1, 1	1*0.0060 120*0.0080	0.0337	0.0337
B3	121, 1, 1	1*0.0060 120*0.0080	0.0337	0.0337
B4	121, 1, 1	0.008	0.0337	0.0337

Each stage needs an initial water saturation distribution. In the primary drainage stages, the water saturation is assumed as 100%. The initial water saturation for each subsequent stage corresponds to the final water saturation estimation calculated in the simulation of the previous stage. In this way, for a given stage other than primary drainage, quality in most of the initial water saturation distributions is controlled by the history matching process of the CT scan oil saturations of the previous stages. In the case of experiment A4, also initial gas saturation distributions are required since the WAG stage was divided into several cycles, each independently matched.

4.2 Relative Permeability

The relative permeability curves were modelled using the Brooks Corey equation (2.9). A different set of parameters was matched for primary drainage and forced imbibition in each experiment. Effective permeability values for oil (from primary drainage) and water (from forced imbibition) were calculated for each core section during the experimental studies.

For experiments A4 and A5, the average water saturation at the end of primary drainage, obtained from a mass balance calculation, was reported as connate water saturation, and the

average oil saturation at the end of forced imbibition was reported as residual oil saturation. For these experiments, the selected end-point relative permeabilities were calculated from the harmonic average of the effective permeability values at each section. In general, first and last sections were not considered since measured differential pressures were sometimes affected by the effect of the tubing adjacent to the core. Residual saturation values were selected considering the reported ranges. In some cases, since reported saturations were not actually residual saturations, slightly lower values than the low limit in the range were needed to properly match the experiments. The shape coefficients, also known as Corey exponents, were initially assumed as 2 and then fine-tuned representing the main history matching parameters. (see chapter 5 for the used parameters).

For experiments B0 to B5, as showed in section 3.2.8, saturation calculations from CT scan measurements at the end of primary drainage and forced imbibition stages were available. This information was used to calculate average saturation values for each section in the core. The smallest water saturation after primary drainage, and oil saturation after forced imbibition, were used as residual saturations. These values were consistently lower than the reported averaged residual saturations in the experimental study, which also confirms the validity of the lower residual saturations assumed in the history match of the previous data set (A4 and A5). The relative permeabilities obtained from the effective permeability measurements per section, along with the average water saturation calculation, also per section, were used to obtain the shape coefficients by linearizing the Brooks-Corey equation. Again, the first and last sections were discarded. An example of the process is showed in Figure 4.6, where the slope of the plot represents the shape coefficient.

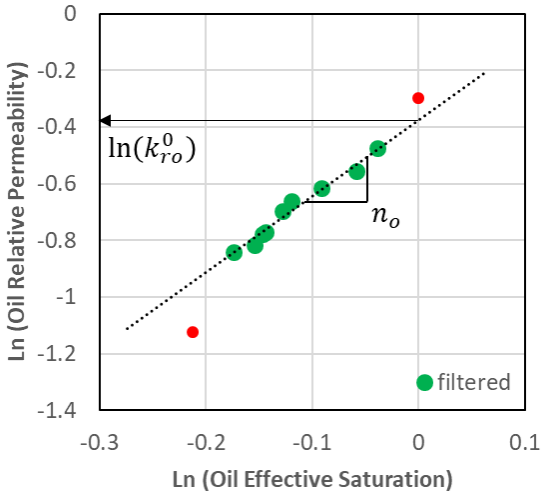

Figure 4.6. Shape coefficient estimation for oil relative permeability curves.

Once the shape coefficients were obtained, the end-point relative permeability is extrapolated using Brooks-Corey equation considering the selected residual saturation of the second phase. These values are taken as initial parameters but can be fine-tuned during the history matching process. Figure 4.7 shows an example of the final relative permeability curves (experiment B0).

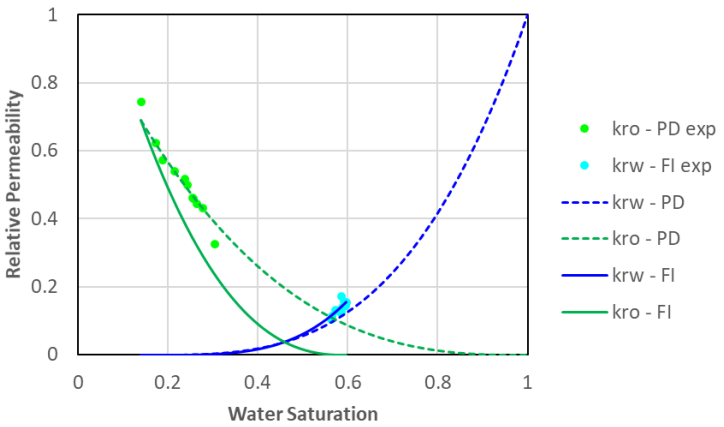

Figure 4.7. Primary drainage (PD) and forced imbibition (FI) relative permeability curves for experiment B0. Includes the experimental information (exp).

In the gas, surfactant and foam flooding stages, no experimental parameters were available. These parameters were obtained in the history matching process for each stage. However, the initial values were assumed as the previous stage ones and then fine-tuned.

4.3 Geochemical Modelling

EQBATCH, the geochemical program of UTCHEM, was used to obtain the equilibrium concentrations of various components, flow and solid species, based on the chemical reactions considered in UTCHEM simulations. The module assumes that all the flow species are dissolved in a single phase: water. These initial conditions serve as an input for the UTCHEM model.

The output of EQBATCH is used as the input data of UTCHEM for the geochemical variables. For surfactant flooding simulation, elements and chemical species in rock and formation water must be recognized as wells as ion exchange reactions with rock minerals, soap generation, dissolution/precipitation reactions and aqueous phase reactions.

The formation water of the study contains the following components: 2.0 wt% NaCl and small amounts of calcium and carbonate ions (Ca^{2+} and CO_3^{2-}) that came from the calcite mineral (carbonate minerals in Table 4.2).

Table 4.2. Mineralogical composition of Bentheimer sandstone core (Peksa, et al., 2015).

Quartz (wt%)	Feldspar (wt%)	Clay Minerals (wt%)	Carbonate Minerals (wt%)	Other (wt%)
91.70	4.86	2.68	0.41	0.35

Table 4.3 summarizes the aqueous reactions considered, as well as and the related equilibrium constants obtained from the MINTEQ thermodynamic database (Allison, et al., 1991; Nordstrom, et al., 1990; Plummer & Busenberg, 1982).

Table 4.3. Aqueous reactions and their equilibrium constants for EQBATCH.

Aqueous Reactions	Equilibrium Constant
$H_2O \leftrightarrow H^+ + OH^-$	K_{eq1} = 1.00E-14
$H^+ + {CO_3}^{2-} \leftrightarrow {HCO_3}^+$	K_{eq2} = 2.14E+10
$Ca^{2+} + H_2O \leftrightarrow Ca(OH)^+ + H^+$	K_{eq3} = 1.21E-13
$Ca^{2+} + H^+ + {CO_3}^{2-} \leftrightarrow Ca(HCO_3)^+$	K_{eq4} = 1.41E+11
$2H^+ + {CO_3}^{2-} \leftrightarrow H_2CO_3$	K_{eq5} = 3.98E+16
$Ca^{2+} + {CO_3}^{2-} \leftrightarrow CaCO_3$	K_{eq6} = 1.58E+03

Note that the rock used in the experiments is composed mainly of quartz grains (see Table 4.2); however, some clay minerals as kaolinite are present. The presence of kaolinite implies cation interchange reactions, i.e. between a cation in solution and another cation on the clay's surface.

Since some carbonate minerals are present in the rock, the dissolution reactions in Table 4.4 were considered. The solubility products are also listed.

Table 4.4. Dissolution reactions and their solubility products for EQBATCH.

Dissolution Reactions	Solubility Product
$CaCO_3 \leftrightarrow Ca^{2+} + {CO_3}^{2-}$	K_{sp1} = 4.95E-10
$Ca(OH)_2 \leftrightarrow Ca^{2+} + 2OH^-$	K_{sp2} = 4.73E+22

As Ca^{2+}, CO_3^{2-}, sodium ions (Na^+) and hydrogen ions (H^+) are all present in the formation water, the cation exchange reactions in Table 4.5 were considered. The exchange constants were taken from Sheng (2015).

Table 4.5. Exchange reactions and their exchange constants for EQBATCH.

Exchange Reactions	Exchange Constant
$2\overline{Na}^+ + Ca^{2+} \leftrightarrow 2Na^+ + \overline{Ca}^{2+}$	K_{ex1} = 2.62E+02
$\overline{H}^+ + Na^+ + OH^- \leftrightarrow \overline{Na}^+ + H_2O$	K_{ex2} = 1.46E+07

Formation brine in the presence of residual oil to waterflood was the initial condition for the geochemical model. On the other hand, initial concentrations for Ca^{2+} and CO_3^{2-} were assumed to be 0.00009 mole/L. The initial concentration of chloride ion (Cl^-) was equaled to 0.342 meq/mL (2.0 wt% NaCl); and the initial concentrations of Na^+ and H^+, 0.342 mole/L and 111.111 mole/L respectively, equivalent to the formation brine used in the core-flood experiment. A composition of 0.410 wt% of $CaCO_3$ in the rock with a porosity of 23.6% and water saturation of 58.2% corresponds to a concentration of 0.351 mole/L PV (liters of pore volume).

To determine the initial concentration H^+, all hydrogen was assumed to be in water. The exchange capacity of the rock was assumed to be 0.047±0.002 meq/mL (Hosseini-N & Zitha, 2015); it defines the number of cations that can be adsorbed into the rock. The average water

saturation was calculated from the end of the previous water flooding simulation, 58.2%. For the described model, the following assumptions were made:

- Quartz dissolution was assumed to be negligible since the experiment was performed at room temperature (Fournier & Rowe, 1977).

- Precipitation of divalent cations was ignored due the fact their initial concentrations were very low.

- The principal cause of alkali loss was assumed to be due to the cation exchange between Na^+ and H^+.

- In-situ generation of soap was ignored as the model oil used in our system does not contain naphthenic acids.

The EQBATCH geochemical model is most commonly used for processes in which the purpose of alkali is in-situ surfactant generation. Although in this study, the alkali is present only for reducing surfactant adsorption. Therefore, it was decided to investigate whether the implementation of EQBATCH, considering the characteristics of the chemical flooding processes in the performed experiments, is required.

4.4 Phase Behavior

For UTCHEM surfactant simulation it is necessary to define the accurate aqueous, organic and micro-emulsion phase behavior parameters. Oil and water solubilization ratios obtained from the lab should be fitted with equations (2.14) and (2.15). In order to evaluate the surfactant capability to decrease the oil-water interfacial tension at different salinities of the aqueous phase, the salinity scan conducted as part of the experimental study was used.

UTCHEM uses the height of binodal curve (HBNC) and the lower (CSEL) and upper (CSEU) effective salinity to solve the model as well as Hand's model (Hand, 1939) to represent the phase behavior. Such parameters can be found by matching the experimental phase behavior data. Several simulations of the three-phase system (oil, water, and surfactant) under batch mode

using model reservoir parameters were developed. Table 4.6 shows the parameters after fine-tuning the phase behavior model.

Table 4.6. Phase behavior model parameters for UTCHEM

Parameter	Value
Height of binodal curve at zero salinity (*HBNC70*)	0.061
Height of binodal curve at optimal salinity (*HBNC71*)	0.030
Height of binodal curve at twice optimal salinity (*HBNC72*)	0.061
Lower effective salinity (meq/mL) (*CSEL7*)	0.540
Upper effective salinity (meq/mL) (*CSEU7*)	1.070

Figure 4.8 shows that UTCHEM simulated results and laboratory data match very well. The computed optimum salinity occurs between 3.0 and 3.5 wt% NaCl (+ 1.0 wt% Na_2CO_3) which is in good agreement with experimental data.

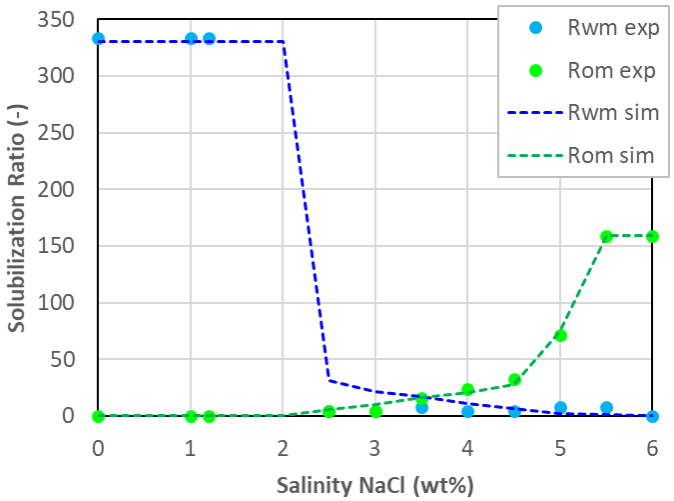

Figure 4.8. Comparison of experimental and simulated solubilization ratios.

Because the phase behavior analysis used a water-oil ratio of 2:1, phase behavior simulations were performed using 33/67 vol.% oil and water concentrations. Water and oil viscosities were set at 1.0 cP. Water, oil, surfactant and co-solvent were co-injected for several PV in order to reach steady state flow which represents the equilibrium conditions in the salinity scan conducted in the laboratory.

4.5 Interfacial Tension

In order to estimate microemulsion/oil and microemulsion/water interfacial tensions, a modified version of Huh's (1979) relationship was used:

$$\sigma_{l3} = \sigma_{ow} e^{-a\,R_{l3}} + \frac{c\,F_l}{R_{l3}}\left(1 - e^{-a\,R_{l3}{}^3}\right), \qquad for\ l = 1(water), 2(oil) \tag{4.5}$$

where σ_{l3} is the phase l/microemulsion interfacial tension in mN/m, σ_{ow} the oil/water interfacial tension in absence of surfactant in mN/m, R_{l3} the solubilization ratio of phase l in the microemulsion phase.

Equation (4.5) uses Hirasaki's correction factor F_l to ensure that the interfacial tension is zero at the plait-point (Hirasaki, 1981); it also contains two matching parameters, c (values around 0.10 and 0.35) and a (values from 5 to 20).

4.6 Trapping Number

In addition to the interfacial tension reduction, buoyancy forces can also modify the trapped oil mobilization. The relationship between viscous and capillary forces are represented by the capillary number described by equation (2.6). Buoyancy forces can be represented by the bond number, N_{Bl}, the relationship between gravity over capillary forces (Morrow & Songkran, 1982), defined as:

$$N_{Bl} = k\,g\frac{(\rho_l - \rho_{l'})}{\sigma_{ll'}}, \qquad for\ l = 1, \dots, n_p \tag{4.6}$$

where g, is the gravity constant, ρ_l and $\rho_{l'}$ the density of the phases, and $\sigma_{ll'}$ the interfacial tension. UTCHEM include a new dimensionless number called the trapping number, N_{Tl}, that combine gravity and viscous forces, bond and capillary numbers, respectively. The trapping number is defined for one-dimensional flow as:

$$N_{Tl} = |N_c + N_{Bl}| \tag{4.7}$$

Residual saturations change with the interfacial tension depending on this trapping number. They are calculated as follows:

$$S_{lr} = \min\left(S_l, S_{lr}^{high} + \frac{S_{lr}^{low} - S_{lr}^{high}}{1 + T_l\, N_{Tl}}\right), \qquad for\ l = 1, \dots, n_p \tag{4.8}$$

where exponents “high” and “low” indicate parameters at high and low trapping numbers. Exponents and endpoints of both the relative permeability curves and capillary pressure curves vary as the residual saturations change at high trapping numbers. In relative permeability functions, such parameters are calculated as a linear interpolation between the given input values at low and high trapping numbers (Delshad, et al., 1986), as follows:

$$k_{rl}^0 = k_{rl}^{0\ low} + \frac{S_{l'r}^{low} - S_{l'r}}{S_{l'r}^{low} - S_{l'r}^{high}}\left(k_{rl}^{0\ high} - k_{rl}^{0\ low}\right), \qquad for\ l = 1, \dots, n_p \tag{4.9}$$

$$n_l = n_l^{low} + \frac{S_{l'r}^{low} - S_{l'r}}{S_{l'r}^{low} - S_{l'r}^{high}}\left(n_l^{high} - n_l^{low}\right), \qquad for\ l = 1, \dots, n_p \tag{4.10}$$

4.7 Surfactant Adsorption

UTCHEM uses the Langmuir-type isotherm for modeling of surfactant adsorption. It is a function of surfactant concentration, salinity and rock permeability (Hirasaki & Pope, 1974), and is given by:

$$\hat{C}_3 = \min\left[\dot{C}_3, \frac{a_3\left(\dot{C}_3 - \hat{C}_3\right)}{1 + b_3\left(\dot{C}_3 - \hat{C}_3\right)}\right], \tag{4.11}$$

$$a_3 = (a_{31} + a_{32}\, C_{SE})\left(\frac{k_{ref}}{k}\right)^{0.5}$$

where $\hat{C}_3$ is the adsorbed concentration of surfactant, $\dot{C}_3$ the total surfactant concentration, a_3 and b_3 the adsorption parameters which can be found by matching laboratory data. The minimum is taken to guarantee that the adsorbed concentration does not exceed the total surfactant concentration. Surfactant adsorption increases linearly with effective salinity (C_{SE}) and decreased with increasing permeability (k). All input parameters (a_{31}, a_{32}, and b_3) must be specified at the reference permeability (k_{ref}).

The average surfactant adsorption in Bentheimer sandstones was measured by Battistutta et al., (2015) for the same type of surfactant slug and equaled 0.25 ± 0.12 mg/g rock. This value for surfactant retention lies within the ranges measured by Solairaj et al. (2012) who performed measurements for a considerable number of cores.

At first, model parameters matching the average surfactant adsorption of 0.25 mg/g rock were chosen. In a second stage, parameters were fine-tuned to obtain a better match regarding pressure drop and saturation profiles whilst ensuring that the surfactant adsorption remained within its boundaries (0.25±0.12 mg/g rock).

4.8 Microemulsion Viscosity

Since the micro-emulsion viscosity generated in the laboratory during the core flood experiments could not be measured (Janssen, et al., 2019b), default parameters that determine the micro-emulsion viscosity as a function of aqueous phase salinity were used at first stage.

The original UTCHEM microemulsion viscosity model uses the microemulsion phase composition. This variable is modeled with the following expression:

$$\mu_3 = C_{13}\,\mu_w e^{|\alpha_1(C_{23}+C_{33})|} + C_{23}\,\mu_o e^{|\alpha_2(C_{13}+C_{33})|} + C_{33}\,\alpha_3 e^{|\alpha_4 C_{13}+\alpha_5 C_{23}|} \quad (4.12)$$

Microemulsion viscosity parameters were adjusted between measured and simulated pressure drops where needed, and oil saturation profiles were obtained. Because more than 99% of the micro-emulsion consists of the aqueous phase, the calculated microemulsion viscosity is very similar to the surfactant slug viscosity (Table 3.10). Table 4.7 shows the obtained

parameters after the history matching process. The resulting microemulsion viscosity was 1.41 cP for experiments B0 to B3 and 1.67 cP for experiment B4.

Table 4.7. Microemulsion viscosity parameters for UTCHEM original model.

Parameter	Value
α_1	6
α_2	5
α_3	0
α_4	0
α_5	0

4.9 Foam Modelling

The foam model in UTCHEM is based on the work of Cheng et al., (2000). In this model, foam will be generated if:

- The surfactant concentration, C_s, exceeds a threshold value, C_s^*.
- Water saturation, S_w, exceeds a threshold value, S_w^*.
- Oil saturation, S_o, does not exceed a threshold value, S_o^*.

The first two threshold values will affect the gas relative permeability as follows:

$$k_{rg}^f = \begin{cases} k_{rg}, & S_w < S_w^* - \varepsilon \ \ or \ \ C_s < C_s^* \\ \dfrac{k_{rg}}{1 + \dfrac{(R-1)(S_w - S_w^* + \varepsilon)}{2\varepsilon}}, & S_w^* - \varepsilon \le S_w \le S_w^* + \varepsilon \ \ and \ \ C_s \ge C_s^* \\ \dfrac{k_{rg}}{R}, & S_w > S_w^* + \varepsilon \ \ and \ \ C_s \ge C_s^* \end{cases} \quad (4.13)$$

where k_{rg}^f is the gas relative permeability when foam is formed and ε determines the water saturation range determined as high-quality regime. The gas mobility reduction factor, R, is given by the following expression:

$$R = R_{ref}\left(\frac{u_g}{u_{g,ref}}\right)^{\sigma-1} \tag{4.14}$$

As it can be observed, R is modified depending on gas flow rate, u_g, resulting in shear thinning behavior of foam in low-quality regime. In the previous expression, R_{ref} is the reference gas mobility reduction factor at reference gas velocity, $u_{g,ref}$, and σ the power-law exponent ($\sigma = 1$ for Newtonian behavior or $\sigma < 1$ for shear thinning behavior). To affect the gas mobility reduction factor in presence of oil, the following expression is applied (Loftollahi, 2015):

$$R = \begin{cases} R_{max}, & S_o \leq S_{oL} \\ 1 + \left(\dfrac{S_o - S_{oM}}{S_{oL} - S_{oM}}\right)^{e_o}(R_{max} - 1), & S_{oL} < S_o < S_{oM} \\ 1, & S_o \geq S_{oM} \end{cases} \tag{4.15}$$

where S_{oL} is the maximum oil saturation below which foam is not altered by oil and the gas mobility reduction factor reaches its maximum value, i.e., $R = R_{max}$, S_{oM} is the minimum oil saturation above which foam is entirely destroyed, and e_o is the parameter by which oil saturation is scaled between S_{oL} and S_{oM}.

5 RESULTS AND DISCUSSION

This chapter presents the results of the modeling and history matching process for experiments A4 to B4. Figure 5.1 summarizes the simulated flooding sequence for each experiment. Each stage was simulated in an independent run. Note that the final water and gas saturations, as well as species concentrations in the aqueous phase (when necessary), obtained from the mechanistic modelling at each stage were loaded as initial conditions for the next one.

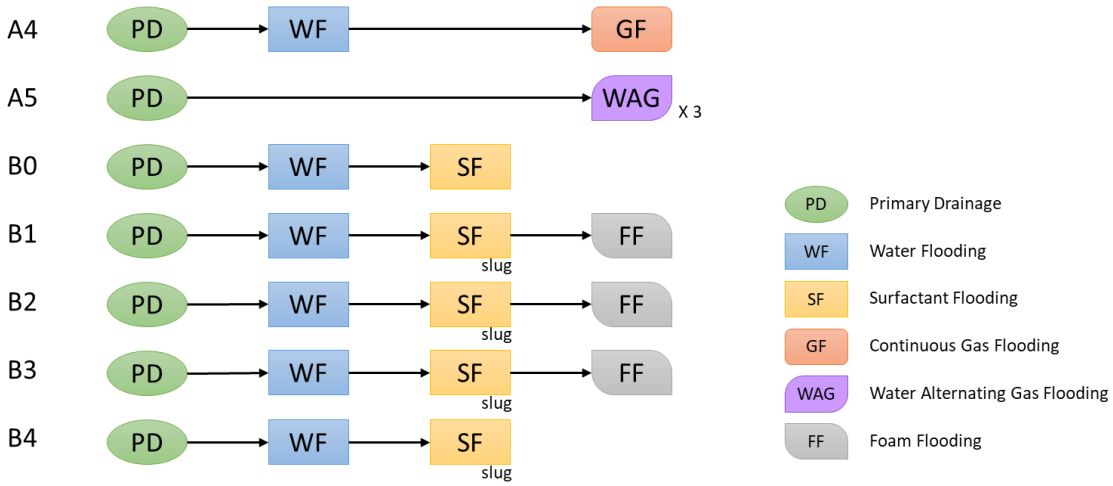

Figure 5.1. Summary of simulated stages per experiment.

During the mechanistic modelling of each injection stage, several assumptions were made:

- No rock compressibility
- Oil and water (and microemulsion) are incompressible. Only gas presents compressibility.
- Strongly water wet rock.
- No wettability alteration.

The history match process aimed to numerically reproduce the observed pressure drop along the core, the oil recovery evolution during each flood, the oil and water production fractions and, if available, the oil saturation distribution at different dimensionless injection times (PVI). Several experiments may share the same flooding stage, but only one representative

experiment for all other simulations will be discussed. Nonetheless, a complete graphical summary of the mechanistic modelling results for all the experiments is presented in Appendices E to K.

5.1 Primary Drainage and Forced Imbibition

For primary drainage and forced imbibition (water flooding), as for subsequent flooding stages, a correct identification of relative permeability curves is the most important aspect for a successful match. Figure 5.2 shows an example of a clear match between the relative permeability curves for water and oil during primary drainage and forced imbibition, and the available experimental data (see section 4.2) for experiment B1.

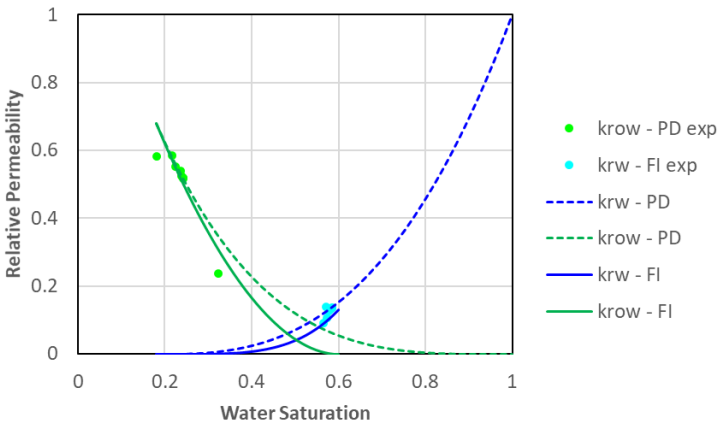

Figure 5.2. Primary drainage (PD) and forced imbibition (FI) relative permeability curves for experiment B1. Includes the experimental information (exp).

Table 5.1 and Table 5.2 summarize the relative permeability parameters for primary drainage and forced imbibition, respectively, for all the experiments. As it can be observed, most of the residual water saturation values are lower compared to the experimental information. Note that the reported experimental values correspond to the average final saturation condition of the corresponding stage. From the proposed regression process using the calculated water saturation and relative permeability values per section, it can be concluded that residual water saturations are indeed lower, which also validates the lower values used in experiments A4 and A5, even when no CT scan-based saturations were available.

Table 5.1. Primary drainage relative permeability parameters for experiments A4 to B4.

Parameter	A4	A5	B0	B1	B2	B3	B4
S_{wr}	0.200	0.210	0.140	0.180	0.098	0.070	0.120
S_{orw}	0.000	0.000	0.000	0.000	0.000	0.000	0.000
k_{rw}^0	1.000	1.000	1.000	1.000	1.000	1.000	1.000
k_{ro}^0	0.720	0.850	0.690	0.680	0.893	0.966	0.760
n_w	3.000	3.000	3.300	2.800	3.500	3.750	2.500
n_o	4.500	3.800	2.700	3.500	3.200	3.800	3.000

Table 5.2. Forced imbibition relative permeability parameters for experiments A4 to B4.

Parameter	A4	A5	B0	B1	B2	B3	B4
S_{wr}	0.200	-	0.140	0.180	0.098	0.701	0.120
S_{orw}	0.470	-	0.403	0.400	0.405	0.380	0.390
k_{rw}^0	0.145	-	0.154	0.130	0.148	0.170	0.170
k_{ro}^0	0.720	-	0.690	0.680	0.893	0.966	0.760
n_w	1.200	-	3.900	4.300	3.000	3.200	3.300
n_o	1.700	-	2.400	1.900	2.000	2.600	2.600

Figure 5.3 shows the obtained match between measured and simulated pressure drops for primary drainage in experiment B1, not only during the main flow, but also during the rate variation performed for end-point relative permeability calculations. Similar results were obtained during the forced imbibition stage with 4 wt% NaCl brine (Figure 5.4) and 2 wt% NaCl brine (Figure 5.5).

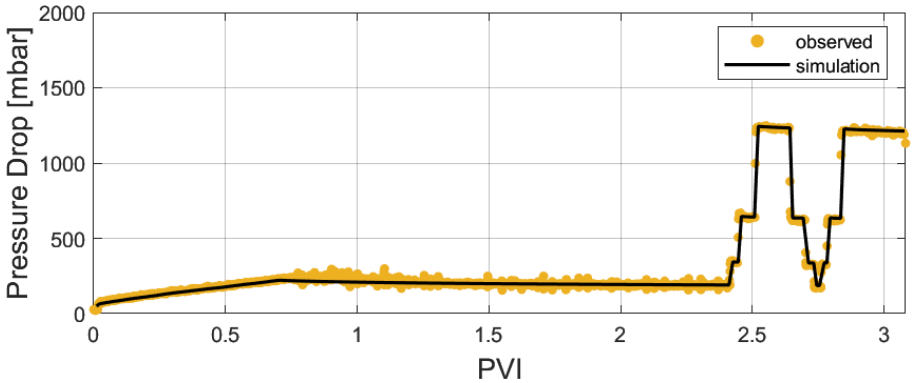

Figure 5.3. Pressure drop match for primary drainage, experiment B1.

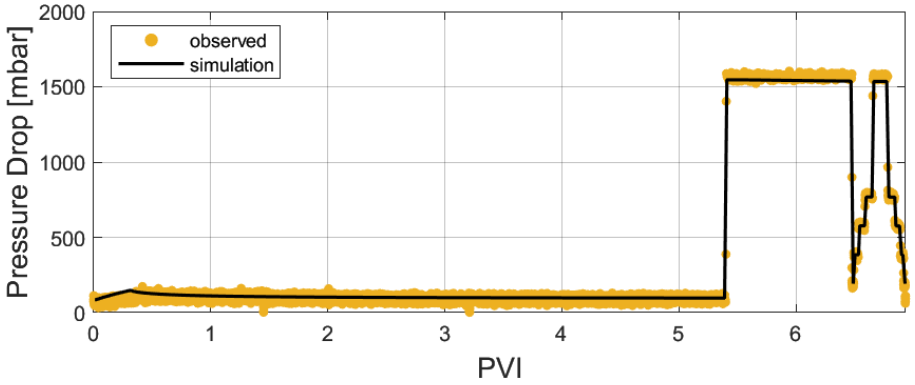

Figure 5.4. Pressure drop match for forced imbibition with 4 wt% NaCl brine, experiment B1.

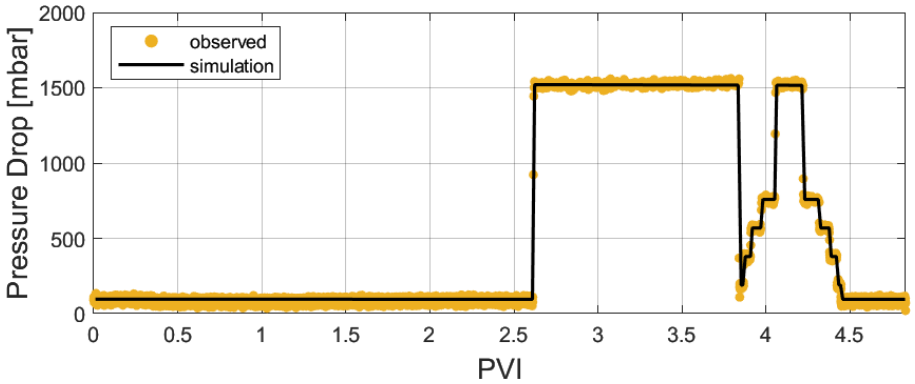

Figure 5.5. Pressure drop match for forced imbibition with 2 wt% NaCl brine, experiment B1.

Similarly, excellent match was obtained for the breakthrough times for oil (during primary drainage, Figure 5.6) and water (during forced imbibition, Figure 5.7). In some cases, simulation shows earlier breakthroughs compared with available information, with a difference of 0.04 ± 0.02 PVI.

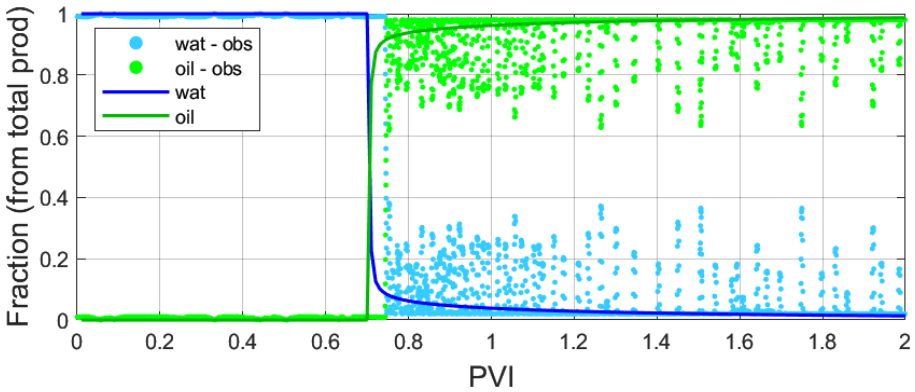

Figure 5.6. Oil breakthrough match for primary drainage (Coriolis data), experiment B1.

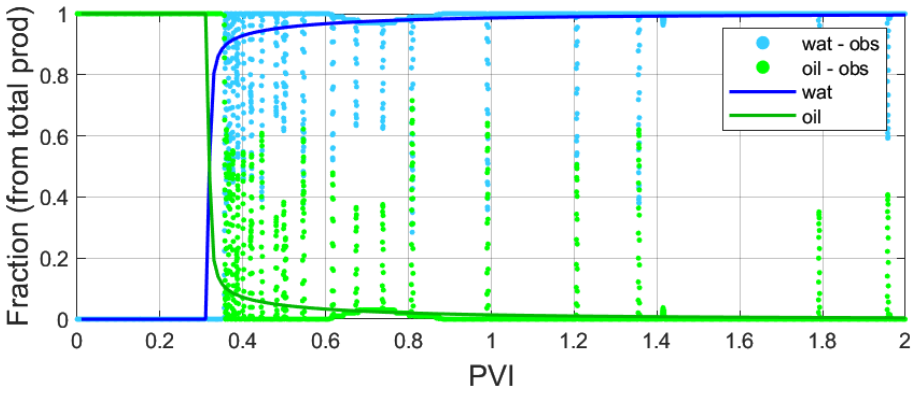

Figure 5.7. Water breakthrough match for forced imbibition (Coriolis data), experiment B1.

Another important parameter to match during mechanistic modelling is the saturation distribution along the core, when available. As stated in section 3.2.8, the available data sets for experiments B0 to B4 includes CT scan-based saturations. For experiment B1, a good match between simulation and observed data during primary drainage (Figure 5.8) and forced imbibition (Figure 5.9) was obtained at different PVI. A shock front and an upstream rarefaction wave, typical for a Buckley-Leverett displacement, can be observed (Buckley & Leverett, 1942). Note how capillary-end effect is evident in the final saturation profile of primary drainage, both in the experimental and simulated data, although magnified in the later one.

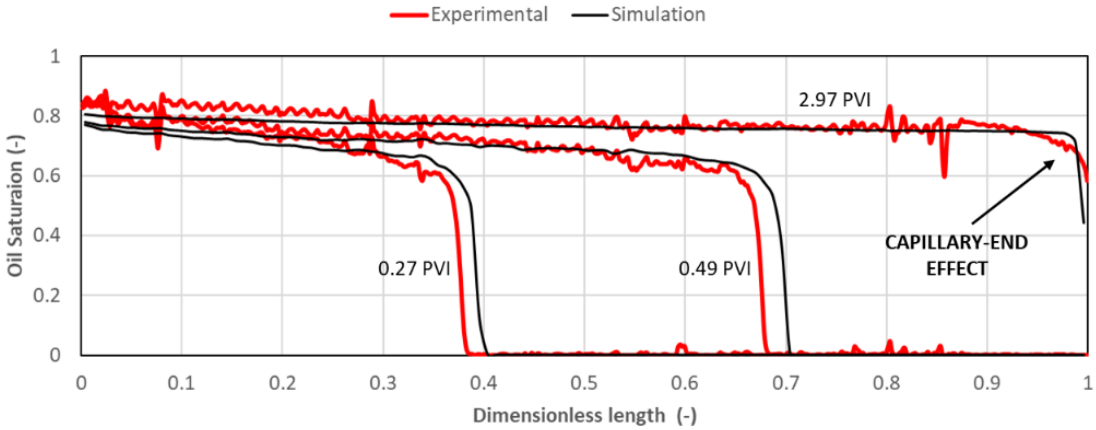

Figure 5.8. Oil saturation match at several PVI during primary drainage, experiment B1.

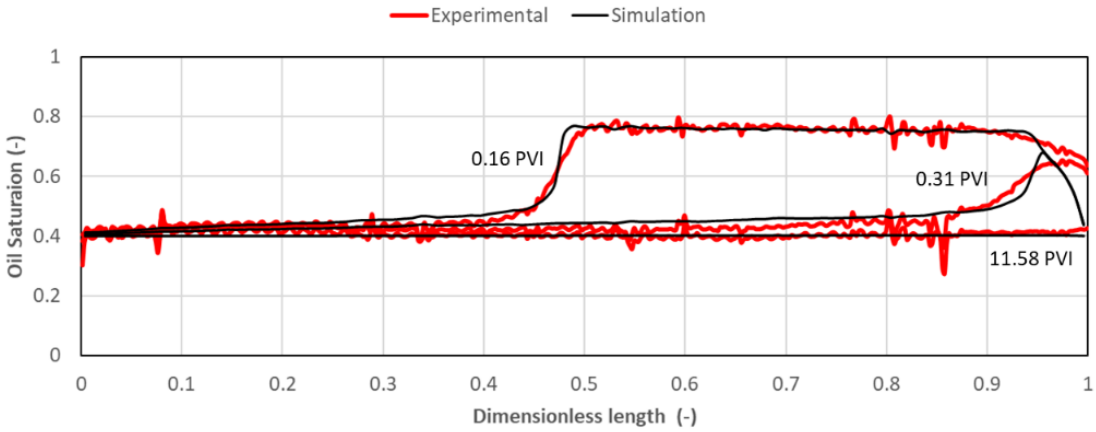

Figure 5.9. Oil saturation match at several PVI during forced imbibition, experiment B1.

In addition, observed average saturations during primary drainage (Figure 5.9) and forced imbibition (Figure 5.11) are in good agreement with the simulation data for experiment B1. Although some minor differences can be observed in terms of oil and water breakthroughs, a good reproduction of the final saturation condition was obtained. Note that this is crucial since final saturations obtained from simulations are used as initial conditions for following stages.

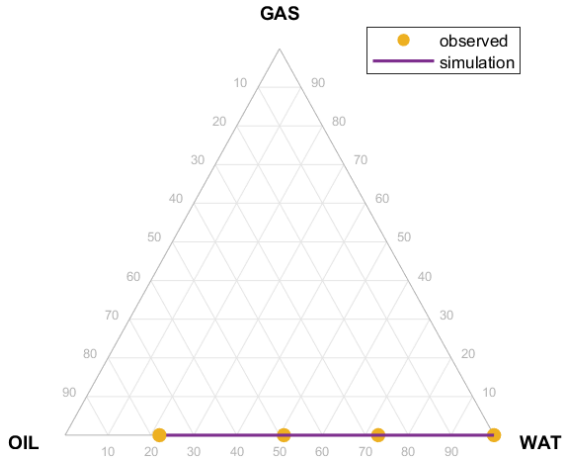

Figure 5.10. Average saturation match for primary drainage, experiment B1.

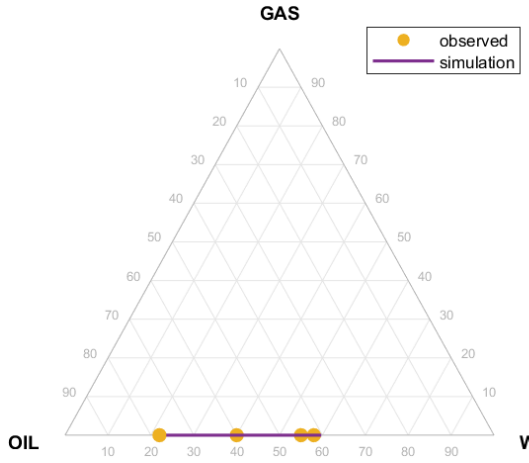

Figure 5.11. Average saturation match for primary drainage, experiment B1.

5.2 Gas Flooding

Gas injection was applied after waterflooding in experiment A4. Figure 5.12 to Figure 5.14 show the relative permeability curves that resulted from the history matching process and Table 5.3 summarizes the parameters involved.

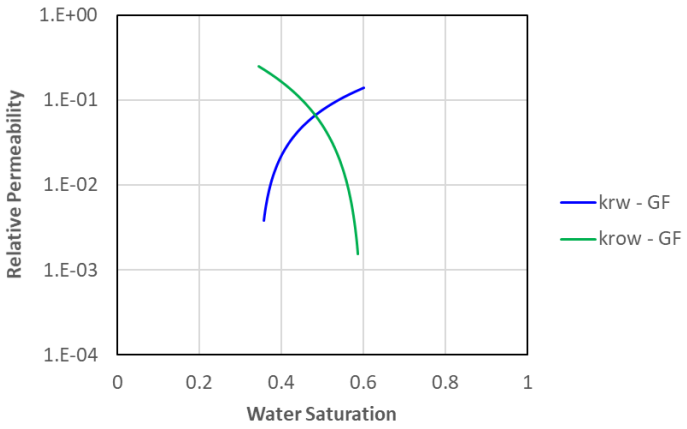

Figure 5.12. Oil (to water) and water relative permeability curves for gas flooding (GF), experiment A4.

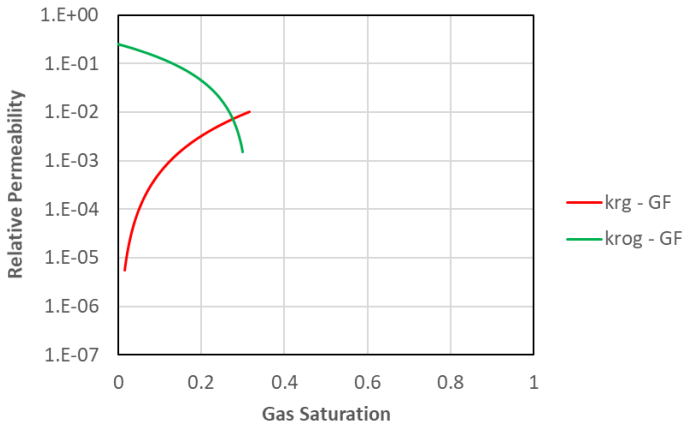

Figure 5.13. Oil (to gas) and gas relative permeability curves for gas flooding (GF), experiment A4.

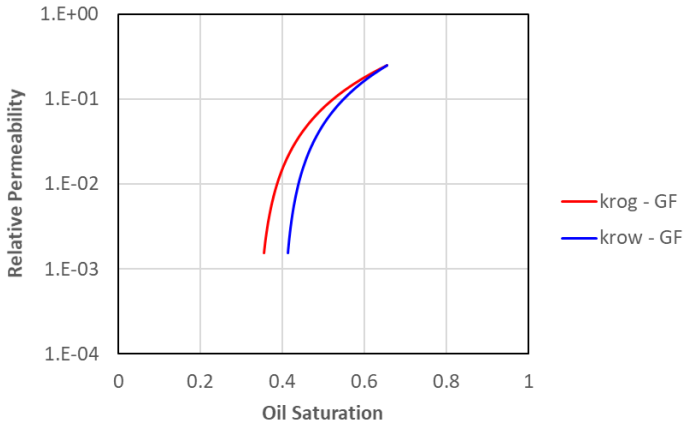

Figure 5.14. Oil relative permeability curves (to gas and water) for gas flooding experiment A4.

Table 5.3. Relative permeability parameters for gas flooding, experiment A4.

Parameter	A4
S_{wr}	0.345
S_{orw}	0.250
S_{gr}	0.000
S_{org}	0.340
k_{rw}^{0}	0.140
k_{ro}^{0}	0.250
n_w	0.010
n_o	1.200
n_w	1.700

Figure 5.15 shows a good pressure drop match between observed and simulation data for experiment A4 during gas flooding. In the same way, Figure 5.16 presents how the simulation model can reproduce the oil recovery factor increment during gas flooding. Finally, Figure 5.17

shows how observations on oil, water and gas ratios are in good agreement with the simulation results, however, the gas breakthrough arrives earlier, with a mismatch of 0.06 ± 0.02 PVI. Due to the time interval between measurements in the experimental information and given that gas fraction is not based on direct measurements, it is difficult to define if gas production increase should be gradual or abrupt. However, simulated average saturations are consistent with observations (Figure 5.18).

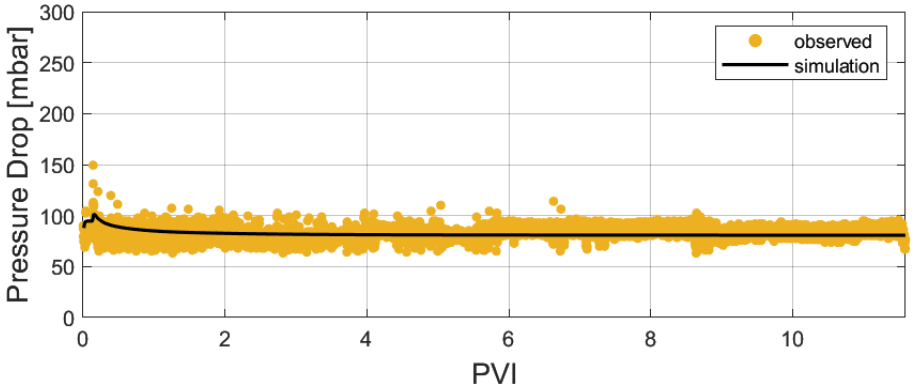

Figure 5.15. Pressure drop match for gas flooding, experiment A4.

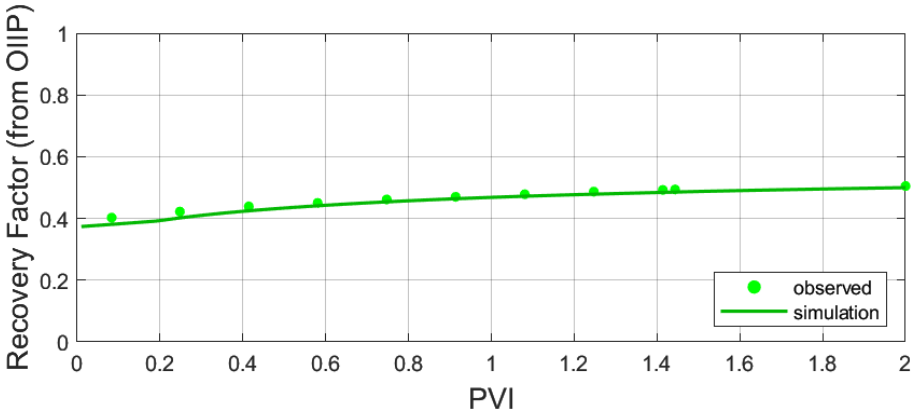

Figure 5.16. Oil recovery factor (from OIIP) match for gas flooding, experiment A4.

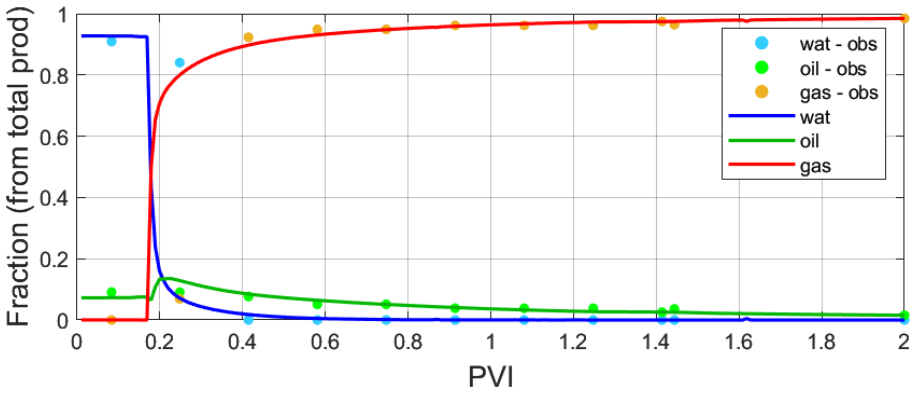

Figure 5.17. Production fractions match for gas flooding, experiment A4.

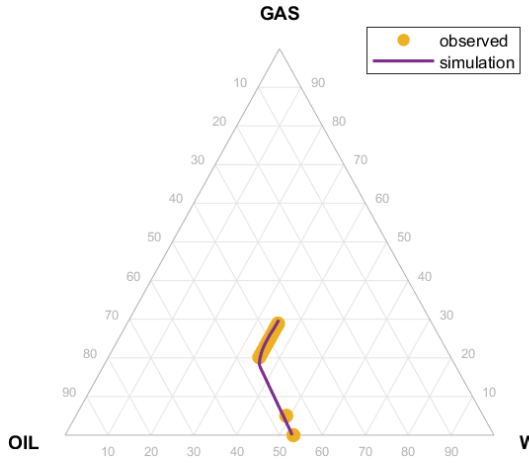

Figure 5.18. Average saturation match for gas flooding, experiment A4.

5.3 WAG

In experiment A5, several WAG cycles were performed. Although 12 cycles were applied in total, only the first three cycles generated incremental oil recovery. In a preliminary stage of the mechanistic modelling, only one set of relative permeability curves was used for all the cycles, but this strategy produced unsatisfactory results. The run was progressively segmented, and independent relative permeability curves were adjusted for each cycle. After the second segmentation (two runs of one cycle, C1 and C2, and one run with the additional cycles, Cn) no changes were needed in the relative permeability curves to successfully match the results.

Figure 5.19 shows the used gas/oil relative permeability curves. The typical progressive decrease in gas relative permeability as a result of a trapping effect can be observed. Table 5.4 resumes the relative permeability curve parameters.

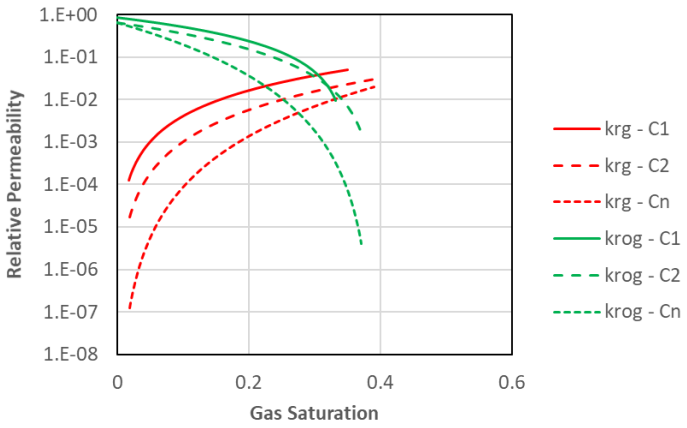

Figure 5.19. Gas/oil relative permeability curves for first (C1), second (C2) and subsequent (Cn) WAG cycles.

Table 5.4. Relative permeability parameters for WAG, experiment A5.

Parameter	C1	C2	Cn
S_{wr}	0.200	0.250	0.250
S_{orw}	0.500	0.240	0.240
S_{gr}	0.000	0.000	0.000
S_{org}	0.450	0.360	0.360
k_{rw}^0	0.050	0.040	0.040
k_{ro}^0	0.850	0.650	0.650
k_{rg}^0	0.050	0.030	0.020
n_w	4.000	1.500	2.000
n_o	1.500	2.000	4.000
n_g	2.000	2.500	4.000

Comparing gas and oil relative permeability curves for gas flooding (experiment A4) and WAG (experiment A5) (Figure 5.20 for C1 and Figure 5.21 for Cn), it can be observed how the set of relative permeabilities related to continuous gas injection is less favorable than the set corresponding to WAG. This can be explained if conditions prior to gas injection are considered. In the experiment A4, gas injection takes places after waterflooding, and water saturation is high, whilst in the experiment A5, water saturation corresponds to connate, i.e. a low, irreducible, value. In fact, there is more resemblance between gas flooding and WAG at later cycles since water saturation is progressively increasing with each new cycle and tends to reach the values observed prior to gas flooding in the experiment A4.

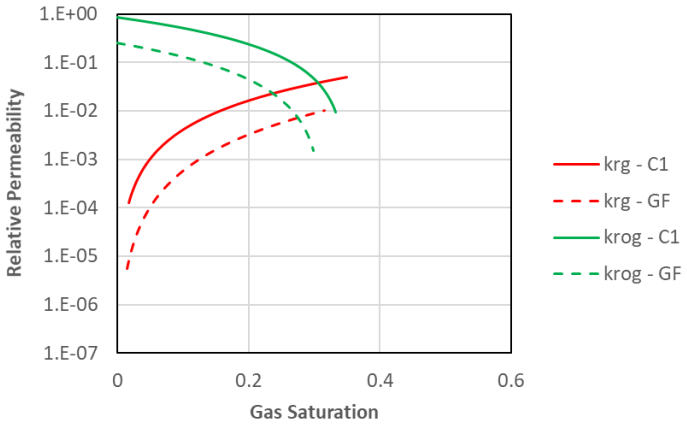

Figure 5.20. Gas/oil relative permeability curves for continuous gas injection (GF), experiment A4, and first (C1) WAG cycle, experiment A5.

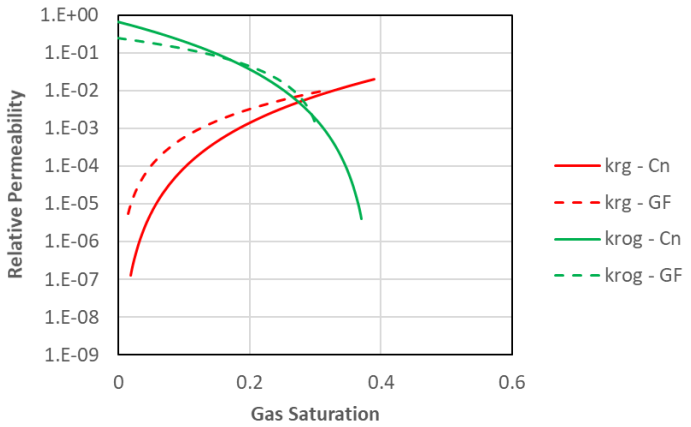

Figure 5.21. Gas/oil relative permeability curves for continuous gas injection (GF), experiment A4, and subsequent (Cn) WAG cycles, experiment A5.

Lower gas relative permeabilities during tertiary recovery compared to those during secondary have been documented by others. After conducting a series of gas displacement experiments under different wettability conditions, Skauge & Larsen (1994), found that k_{rg} is strongly reduced when gas injection is applied after waterflooding, compared to k_{rg} in primary gas injection processes. They also found that due to hysteresis, gas relative permeability during secondary and tertiary injection has been reduced after water saturation increased above connate saturation.

Figure 5.22 shows the measure and modelled pressures for the WAG (experiment A5). A good match for all the cycles (except a couple spikes) was achieved. Figure 5.23 shows simulated and measured oil recovery and Figure 5.24 shows the produced fractions per phase for the same experiment. Although the match for the first cycle is good, some mismatches in oil production can be observed for the following cycles. For the second cycle (Figure 5.24 b), an oil production delay of 0.05 ± 0.02 PVI can be observed. For the subsequent cycles, although it is true that oil recovery incremental is evidenced only in the third cycle, an initial high peak is observed, which is not evidenced in the observed data, where oil production shows a progressive small increment and then stops. Nonetheless, in terms of oil recovery, there is still a very good match. A good agreement in average saturations is observed between experimental data and simulation results (Figure 5.25).

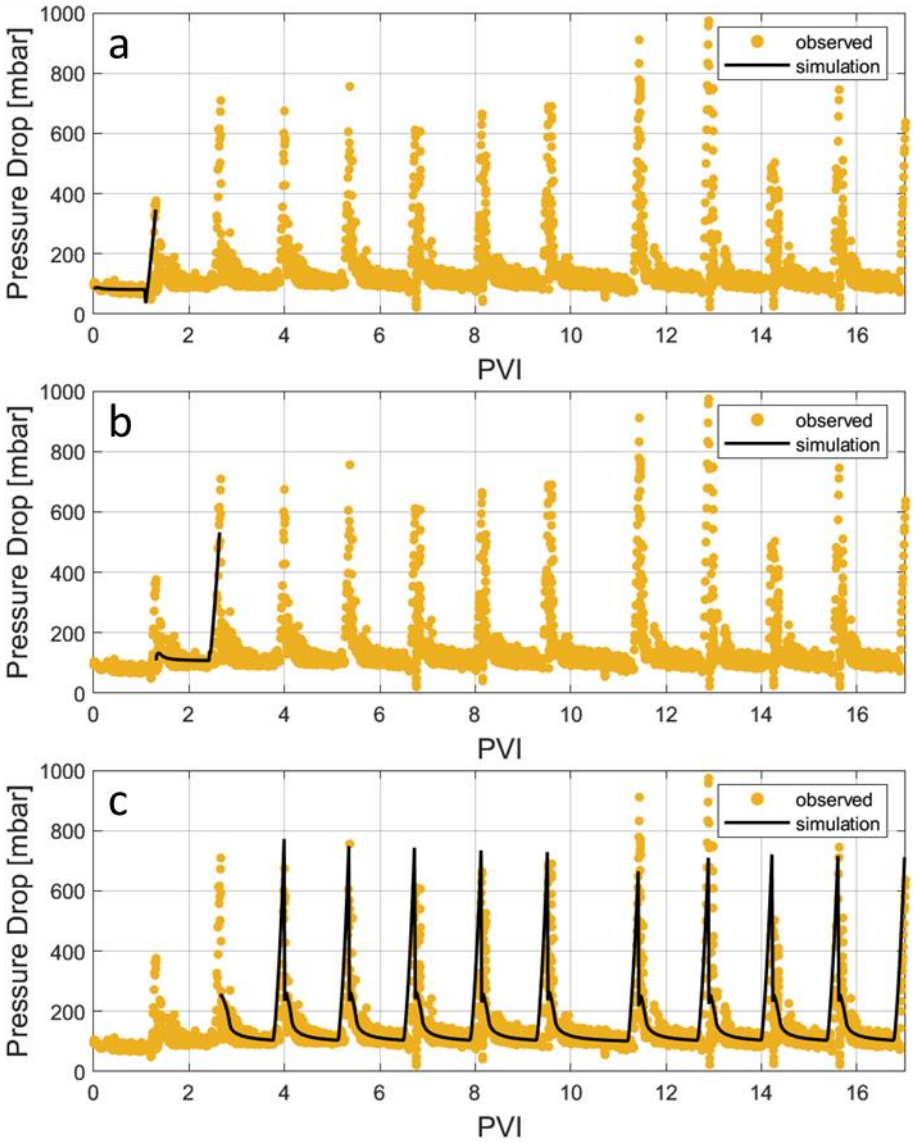

Figure 5.22. Pressure drop match for WAG, first (a), second (b) and subsequent (c) cycles, experiment A5.

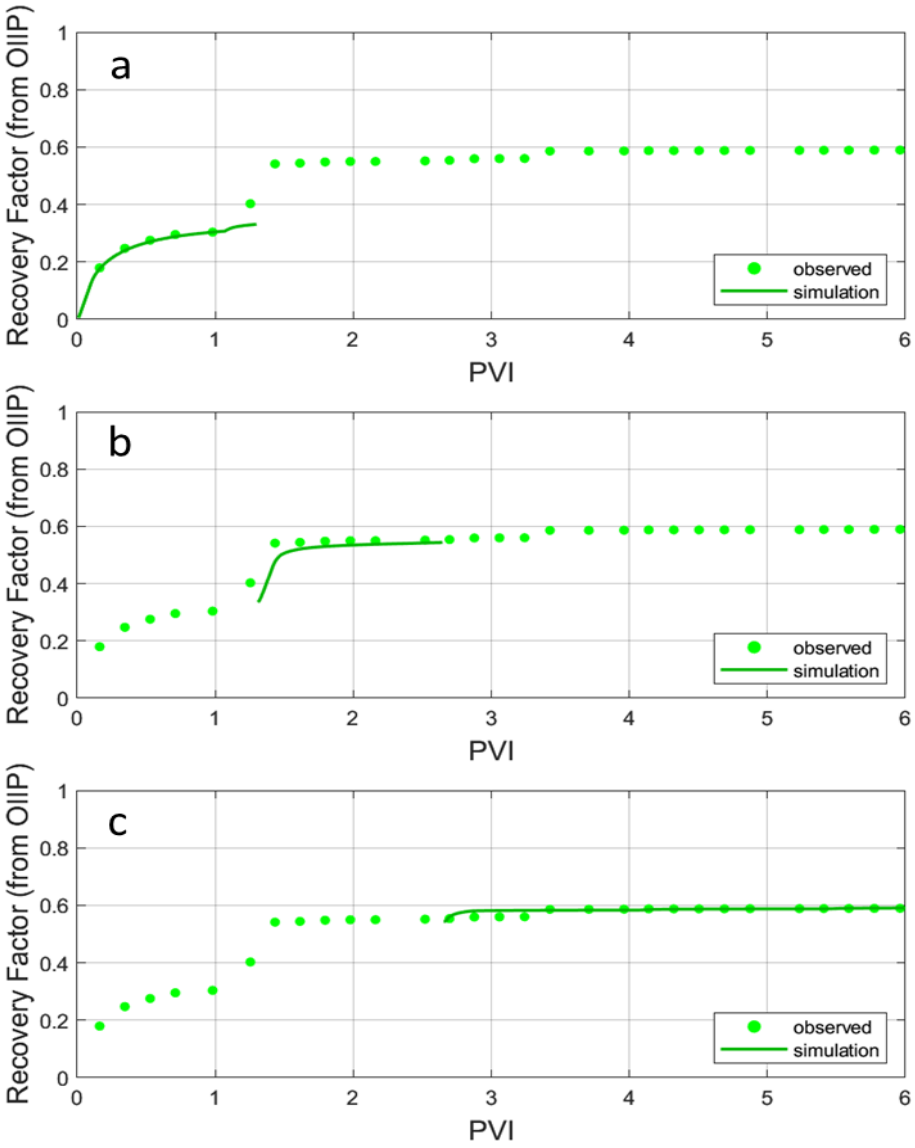

Figure 5.23. Oil recovery factor match for WAG, first (a), second (b) and subsequent (c) cycles, experiment A5.

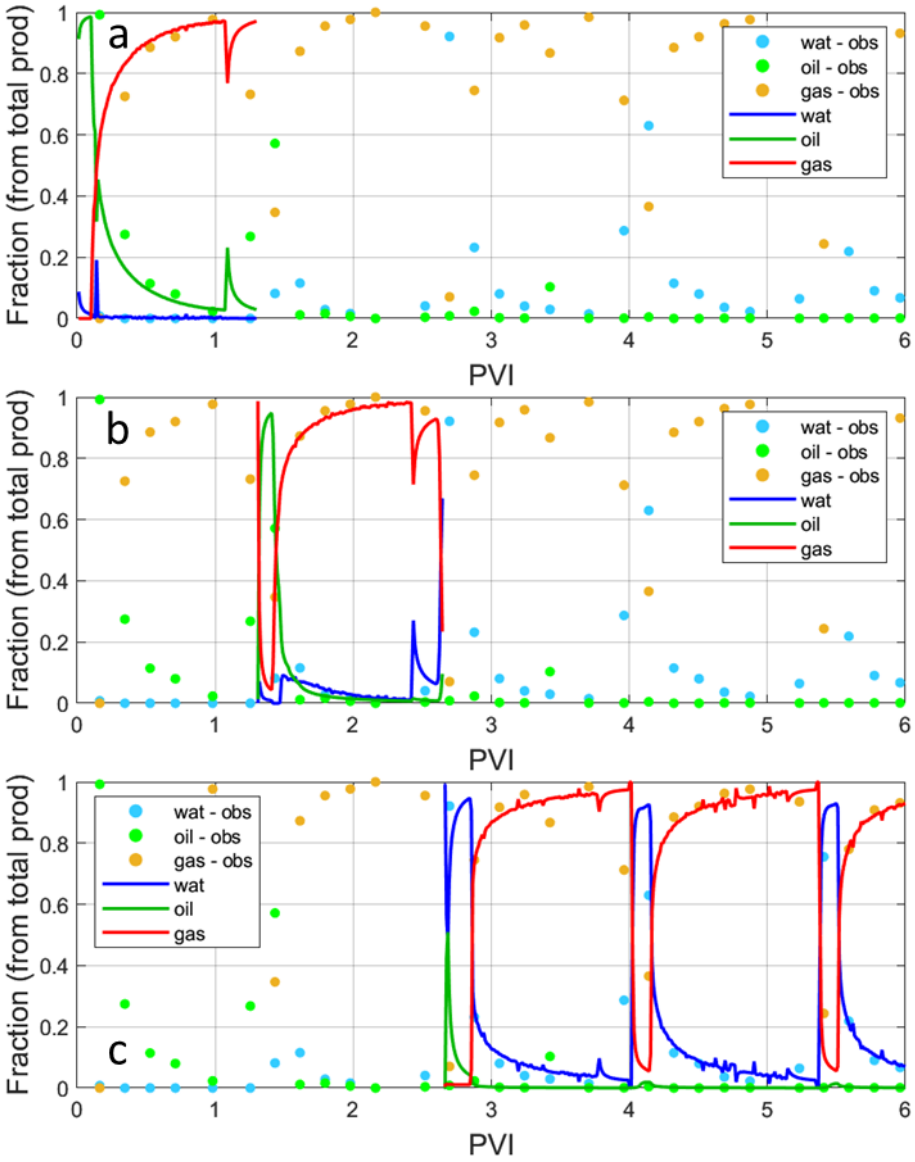

Figure 5.24. Production fractions match for WAG, first (a), second (b) and subsequent (c) cycles, experiment A5.

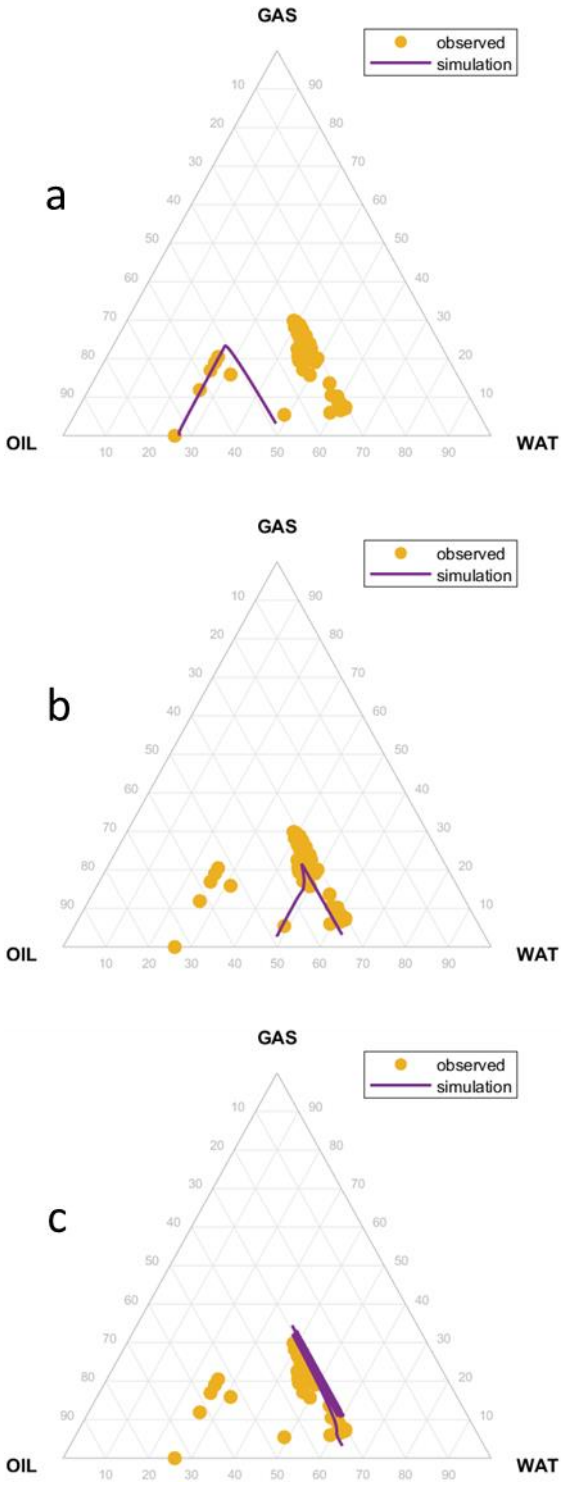

Figure 5.25. Average saturation match for WAG, first (a), second (b) and subsequent (c) cycles, experiment A5.

5.4 Surfactant Flooding

Surfactant injection was performed in the last four experiments (Figure 5.1), as continuous flooding in experiment B0 and as a slug before drive foam generation in experiments B1 to B4. In this section, results on B0 will be presented as they are representative for all the experiments on surfactant injection. In addition, B4 will be briefly analyzed given that surfactant was injected using a solution with a higher salinity at (near-) optimum conditions, this to validate the phase behavior model.

It is good to note that experiments are performed under type II(-) conditions. This results in a microemulsion composed of water and surfactant, plus minor quantities of oil. In UTCHEM, once water enters in contact with surfactant under type II(-) conditions, it is considered microemulsion (see results in production fractions later in this section, Figure 5.31). This means that coexistence of aqueous and microemulsion phases in the same cell of the grid is not possible.

One of the main aspects to consider during history match of surfactant flooding is the variation of residual saturation for all the phases as a function of its trapping number, or CDC. As mentioned in previous chapters, this relation is known as CDC and can be tuned in UTCHEM using T_l in equation (4.8). Figure 5.26 shows the CDC used in the simulation of surfactant flooding for experiment B0. In this plot, the continuous lines represent a wide trapping number range calculated from the abovementioned equation and the dots correspond to the condition at the end of the flooding. End-point relative permeabilities and shape coefficients are also presented in Figure 5.26.

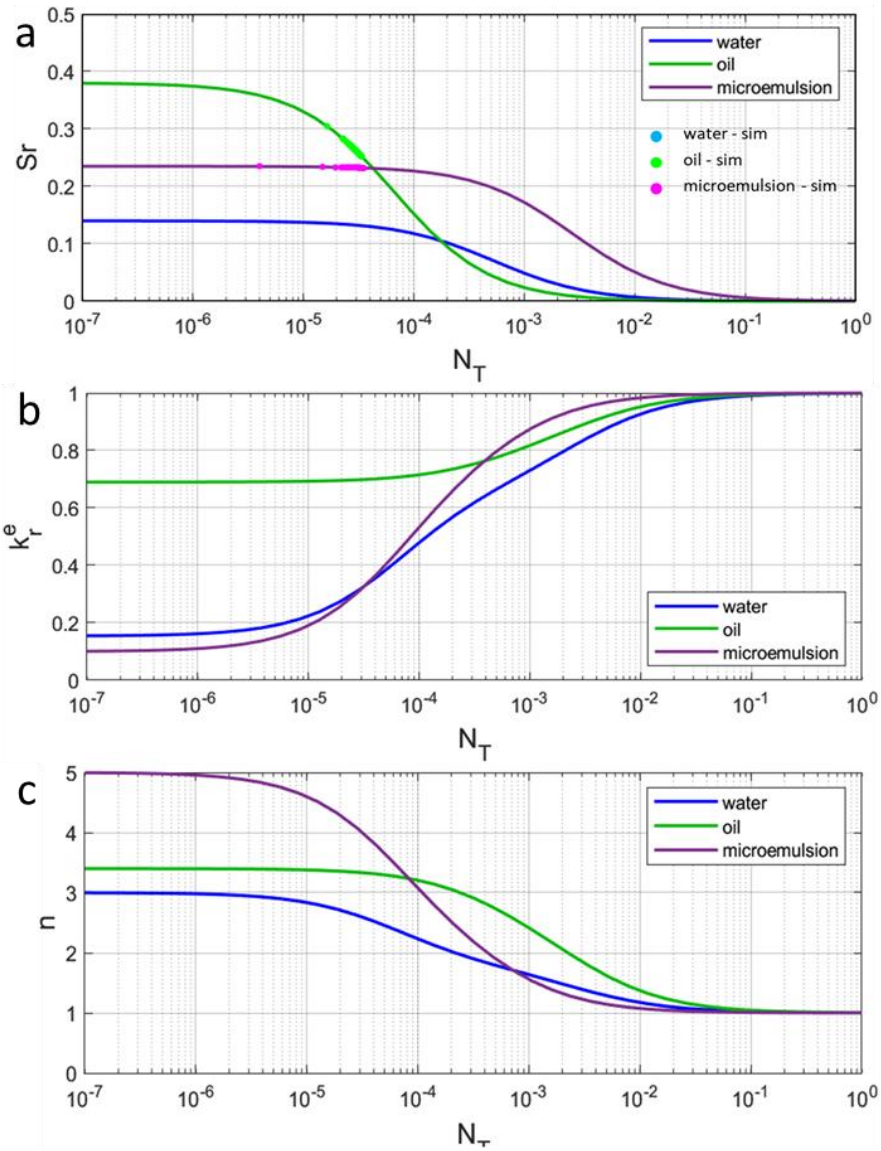

Figure 5.26. Residual saturation (a), end-point relative permeability (b), and shape coefficient (c) evolution for surfactant flooding, experiment B0.

Table 5.5 summarizes the trapping parameters for the CDC calculations (UTCHEM input), Table 5.6 the input relative permeability curve parameters for low and high trapping numbers (UTCHEM input), and Table 5.7 the trapping numbers at the end of the surfactant flooding for oil and water (microemulsion) in each experiment, as well as the corresponding relative permeability curve parameters at such conditions (UTCHEM output).

Table 5.5. Trapping parameters for CDC calculations.

Parameter	B0	B1	B2	B3	B4
T_w	1865	1865	1865	1865	1865
T_o	15000	50000	25000	15000	50000
T_{me}	364.2	364.2	364.2	364.2	364.2

Table 5.6. Relative permeability curve parameters for CDC calculations at low and high trapping numbers.

Parameter	Low N_{Tl}					High N_{Tl}
	B0	B1	B2	B3	B4	All
S_{wr}	0.140	0.180	0.098	0.070	0.120	0.000
S_{orw}	0.380	0.350	0.400	0.380	0.300	0.000
S_{mer}	0.235	0.235	0.235	0.235	0.235	0.000
k_{rw}^0	0.154	0.130	0.148	0.170	0.170	1.000
k_{ro}^0	0.690	0.690	0.893	0.966	0.760	1.000
k_{rme}^0	0.100	0.100	0.100	0.100	0.100	1.000
n_w	3.000	3.500	3.500	3.500	3.500	1.000
n_o	3.400	3.400	3.400	3.400	3.400	1.000
n_{me}	5.000	5.000	5.000	5.000	5.000	1.000

Table 5.7. Trapping numbers and relative permeability parameters at final surfactant flooding conditions.

Parameter	B0	B1	B2	B3	B4
N_{To}	3.36E-05	5.91E-05	4.80E-05	6.00E-05	9.66E-05
N_{Tme}	3.47E-05	5.81E-05	4.43E-05	3.53E-05	6.71E-05
S_{orw}	0.253	0.089	0.182	0.200	0.051
S_{mer}	0.232	0.230	0.231	0.232	0.229
k_{ro}^0	0.700	0.710	0.900	0.970	0.780
k_{rme}^0	0.350	0.580	0.850	0.400	0.620
n_o	3.300	3.300	3.300	2.700	3.200
n_{me}	3.900	2.900	1.700	2.000	2.700

Figure 5.27 illustrates the previously described data for experiment B4. Notice how once the trapping numbers increase, relative permeability curves tend to a miscible-like behavior. This is the effect of the o/w IFT deduction and demonstrates the mechanistic modelling has been successfully implemented.

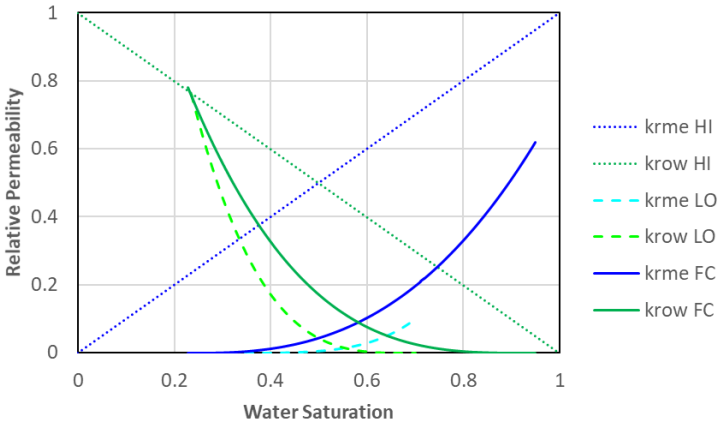

Figure 5.27. Oil and water relative permeability curves for surfactant flooding at high (HI) and low (LO) trapping numbers, and final conditions (FC), experiment B4.
High trapping number conditions equals fully miscible system and low trapping number equals forced imbibition conditions.

Another important parameter to consider during mechanistic modelling of surfactant flooding is surfactant adsorption. Table 5.8 summarizes the parameters for the Langmuir-type isotherm in UTCHEM for experiments B0 to B4. Figure 5.28 shows the resultant adsorption for experiment B0 (0.4 wt% NaCl) and B4 (2 wt% NaCl). Note that although surfactant slug took 0.47 PVI in the experiment B4, its simulation was extended up to 2.5 PVI to verify the maximum surfactant adsorption at such salinity conditions. It is important to notice that the match in experiment B4 needed a higher surfactant adsorption; this is consistent with the literature (Sheng, 2010). As it can be observed in Figure 5.28, stable adsorption values are consistent with reference values in the literature (see section 4.7).

Table 5.8. Parameters for surfactant adsorption modelled with a Langmuir-type isotherm.

Parameter	B0	B1	B2	B3	B4
$a31$	2.6	2.9	2.6	2.6	5.5
$a32$	0.5	0.5	0.5	0.5	0.5
$b3d$	1000	1000	1000	1000	1000

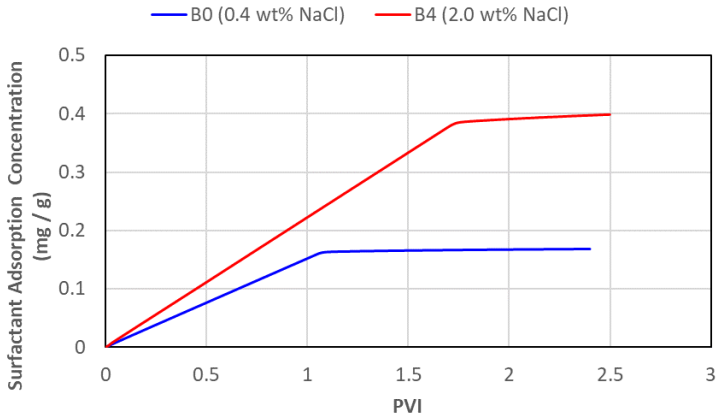

Figure 5.28. Simulation results on surfactant adsorption concentration for experiments B0 and B4.

Figure 5.29 shows a good match in pressure drops between observations and simulation results in experiment B0. The same can be observed in the case of oil recovery (Figure 5.30) and production fraction (Figure 5.31). In these figures, it can be seen a good representation of oil incremental arrival with a small delay in the simulation of 0.04 ± 0.01 PVI. Note that the simulation results for oil include the oil volume in the microemulsion, despite the volume is almost neglectable.

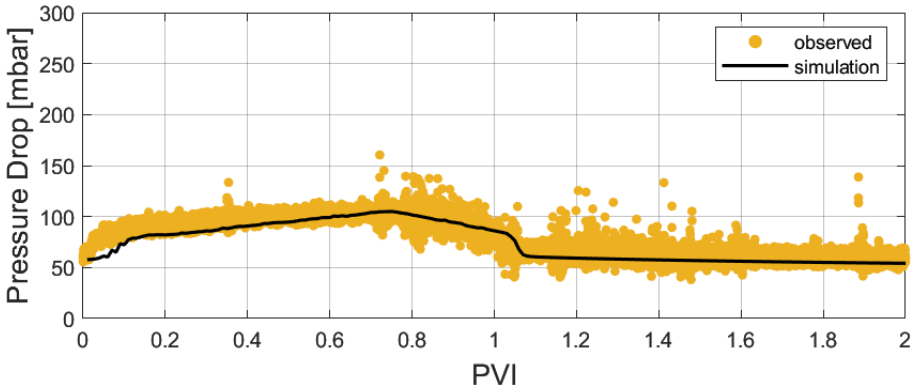

Figure 5.29. Pressure drop match for surfactant slug, experiment B0.

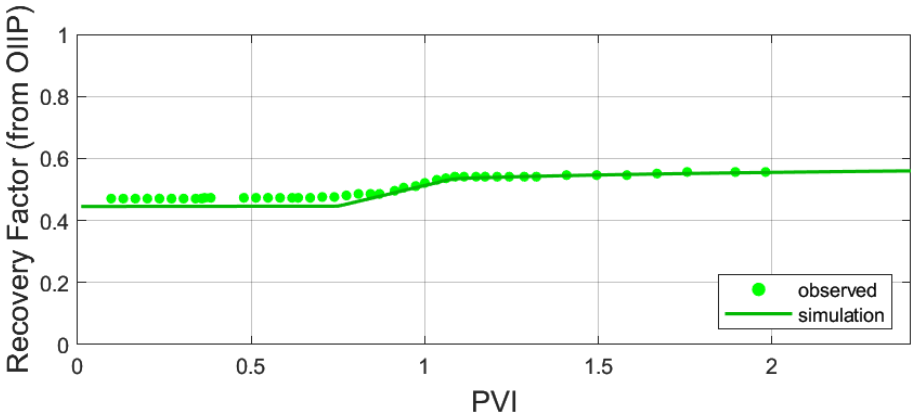

Figure 5.30. Oil recovery factor (as function of OIIP) match for surfactant flooding, experiment B0.

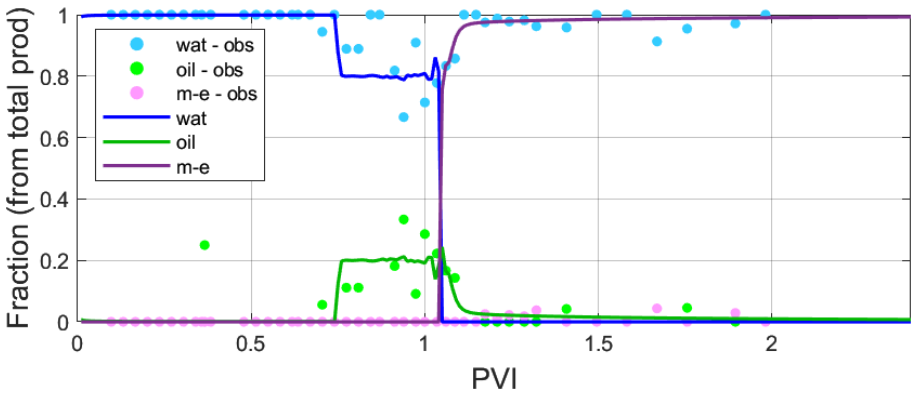

Figure 5.31. Production fractions match for surfactant flooding, experiment B0. Aqueous phase (wat), oleic phase (oil) and microemulsion phase (m-e).

Figure 5.32 shows fluid (oil, water and microemulsion) fractions in the effluents, i.e. versus PVI. The shape and the size in the oil bank as well as its displacement along the core are reasonably well represented by the simulation. In the later stage prior to the oil bank production, a delay in saturation can be observed, although the velocity of the oil bank seems to be well represented in the earlier part of the process. This could indicate the presence of heterogeneities towards the end of the core that could result in higher tortuosity and less flow capacity which was not properly captured during the grid population. Another possible explanation, although less probable, could be a slight mismatch in the reported PVI for that specific CT scan.

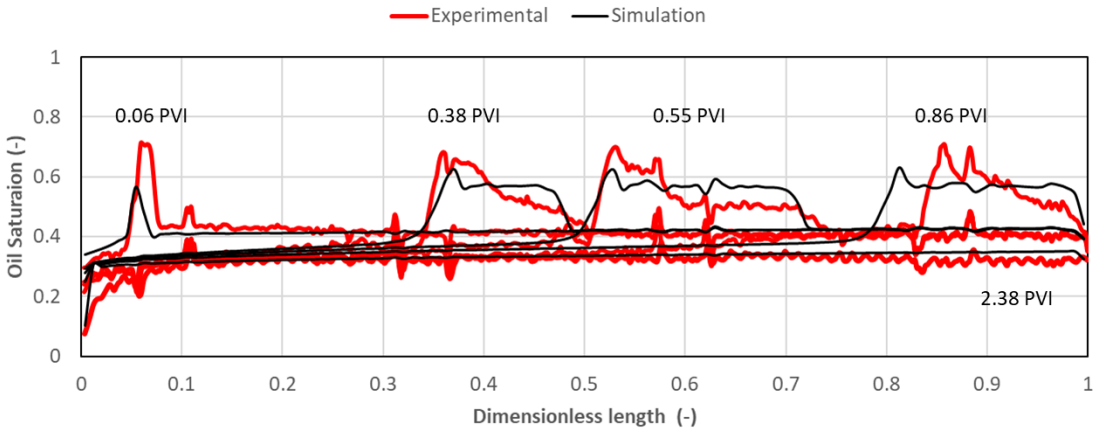

Figure 5.32. Oil saturation match at several PVI during surfactant flooding, experiment B0.

To understand the relevance of the geochemical model in the matching process of the presented surfactant flooding experiments, a case without its implementation was simulated. Figure 5.33 shows the simulation results on oil saturation at the same pore volumes as in Figure 5.32. As observed, practically no changes are identified, confirming that in absence of naphthenic acids in the oleic phase, or complex ion concentrations, the geochemical modelling stage can be neglected.

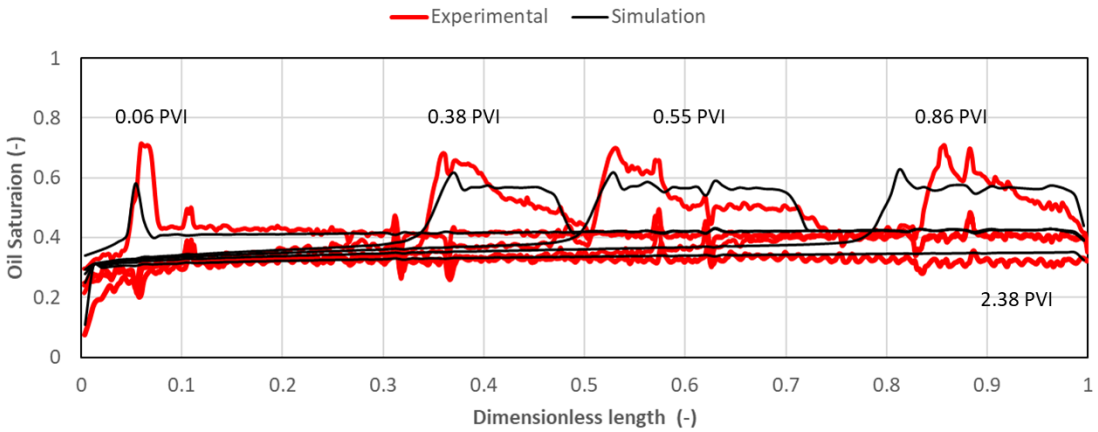

Figure 5.33. Oil saturation match at several PVI during surfactant flooding (no geochemical model), experiment B0.

To confirm the robustness of the adjusted parameters in the phase behavior model, it is ideal to match experiments at different salinity conditions, either at the same or at a different microemulsion type environments. In this case, it was decided to include in the simulation study the surfactant slug stage in experiment B4, which was conducted using the same fluid properties and concentrations, except for the surfactant solution salinity, 2 wt% NaCl, in contrast with 0.4 wt% NaCl in all the other surfactant experiments. Figure 5.34 shows a good match between the

simulated and observed pressure drops for this experiment. In the same way, Figure 5.35 presents a good match in terms of oil saturation distribution at several PVI. Note that since the surfactant flooding was intended as a slug followed by a foam flooding stage in this experiment, no information on oil recovery or produced fractions was available. It is important to realize that, although no modification in the phase behavior parameters was needed, which confirms its robustness, an increment in surfactant adsorption was needed to match the oil bank propagation velocity (Table 5.8 and Figure 5.28). However, the latter was expected.

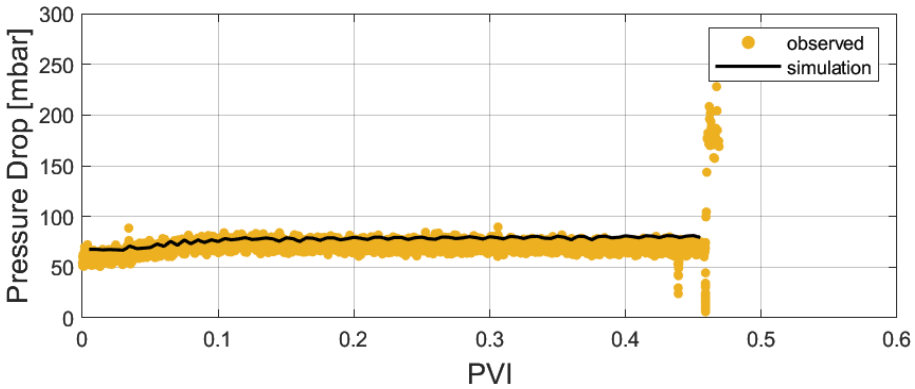

Figure 5.34. Pressure drop match for surfactant slug, experiment B4.

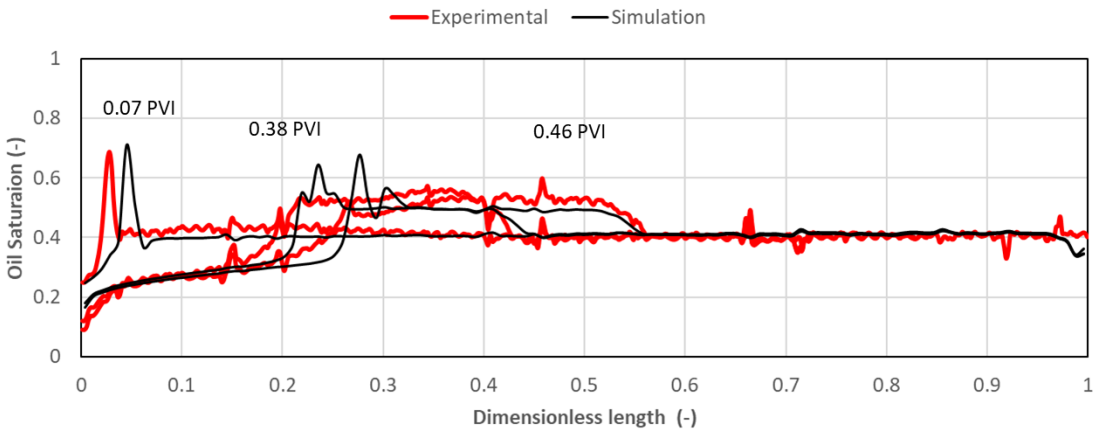

Figure 5.35. Oil saturation match at several PVI during surfactant flooding, experiment B4.

5.5 Foam-Assisted Chemical Flooding (FACF)

The most challenging part during this study was the mechanistic modelling of foam injection experiments. This section presents the principal results after implementing the local equilibrium model for foam representation included in UTCHEM (see section 4.9). In three experiments drive foam injection was simulated (experiments B1, B2 and B3), each with a different foam quality of 57%, 77% and 97%, respectively.

As a first step, it is necessary to understand the complexity behind the results obtained during the experimental study. From their experiments, Janssen et al. (2019b) found that during tests B1 and B2, there was weak foam generation in presence of residual oil. In addition, the foam strength seemed to increase once it contacted the oil bank generated by a previous surfactant slug, i.e. a high oil saturation zone, which resulted in effective oil bank displacement. The authors also suggested that foam strength is controlled by the oil saturation and the possible presence of microemulsion. At first sight, this is in contrast with the commonly accepted concept that presence of oil is detrimental to foam generation. However, as stated in section 4.9, the foam model in UTCHEM uses the oil saturation as a threshold above that foam will not be generated. Foam strengthens at 50 ± 1 cm from the inlet, which is the approximated location of the oil bank generated during the surfactant slug. This means that during the first half of the core, it is possible that the oil itself slows down strong and stable foam generation.

Janssen et al. (2019b) proposed that if the oil (with presence of potential microemulsion) forms a zone where the effective porosity is significantly reduced over a large core cross-sectional area (i.e. the zone of the oil bank) it might promote foam generation, as a result of an increase in interstitial gas velocity and, consequently, in local pressure drop. Note that once local pressure exceeds a certain threshold, lamellae division occurs and generation of smaller bubbles takes place, increasing foam strength (Rossen & Gauglitz, 1990).

To support this argument, Janssen et al. (2019b) performed an additional experiment on a core that was already flooded with a surfactant slug up to a point at which the entire oil bank, and related microemulsion, were completely produced by the slug. The additional test consisted of the injection of a 57% quality drive foam, the same as in the experiment were foam generation and oil bank displacement was evidenced. However, during this new test, no foam evidence was found, and no incremental oil recoveries were generated. This seems to support the aforementioned suggestion, i.e. presence of the oil bank might control foam generation, since the only variation here is the absence of the oil bank.

For the purpose of mechanistic modelling of oil displacement by foam, the experimental evidence can be summarized as follows:

- Experimental evidence suggest that foam strength increases in presence of oil. The UTCHEM foam model includes a functionality for affecting foam strength as a function of oil saturation, however, it is designed to decrease foam strength when oil saturation increases.

- The CT scans suggest the presence of a high gas saturation zone upstream of the oil bank in the upper part of the core. It seems that gas segregated before even entering the core due to the presence of liquid between the end cap and the inlet core face. However, foam seems to become stronger as it reaches and overtakes the oil bank. This means there are two well defined zones in the core with contrasting foam capacity (Figure 5.36). The weak-foam zone corresponds to the high-surfactant, low-oil saturation, low-interstitial velocity zone, but these criteria, excluding the low-interstitial velocity condition, does not match the philosophy of the foam model in UTCHEM.

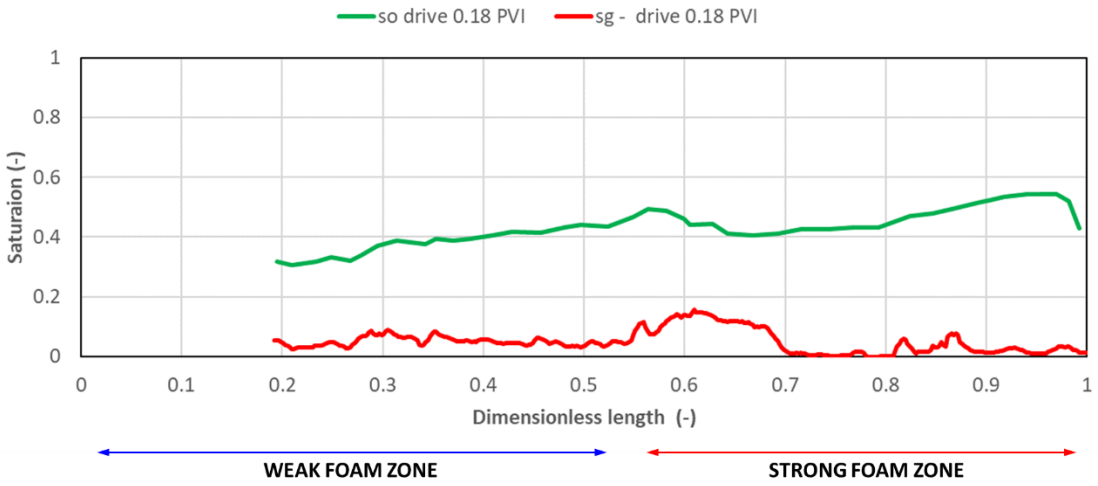

Figure 5.36. Schematic of core downstream (weak foam generation) and upstream (strong foam generation) zones in experiment B1.

- CT scan gas saturation data show that a high gas saturation remains in the downstream zone, suggesting that once the foam has been created, it will preserve its strength if constant rates are maintained, independently from oil saturation (although oil saturation is eventually decreased as a consequence of a successful foam drive that pushes the oil bank).

The foam model in UTCHEM does not capture the physics of foam development observed in the experiments. To address this deficiency, it was decided to use the variable $SWSTAR$ (S_w^* in equation (4.13)), i.e. the water saturation at which foam will collapse, as a predefined local condition per grid cell. In this way, it was possible to selectively control how the mobility

reduction factor behaves during the simulation. Note that this variable is, in fact, the only parameter in the foam model that can be set independently for different grid-cells.

When analyzing the simulation results in the case of a constant S_w^*, gas saturation remains almost constant at the end of the foam drive for extreme high and low values of S_w^*. However, in the case of an intermediate S_w^* value, a steady decrease in gas saturation occurs starting at the inlet. Figure 5.37, Figure 5.38 and Figure 5.39 show the gas saturation at different PVI in experiment B1 for $S_w^* = 0.9$, $S_w^* = 0.45$ and $S_w^* = 0.1$, respectively. In the first case (high S_w^*), it seems a very weak foam is generated. In the second case (medium S_w^*) a stronger foam is observed. Finally, in the third case (low S_w^*), a very strong foam is generated along the whole core. The experimental data suggests that gas saturation remains high at the second half of the core, even when the oil bank has been completely produced.

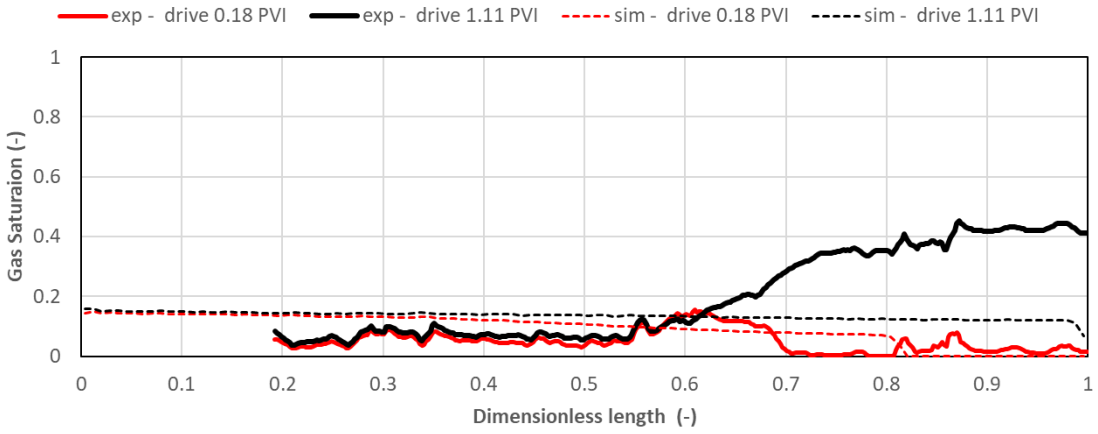

Figure 5.37. Observed and simulated gas saturation at different PVI, $S_w^* = 0.9$, experiment B1.

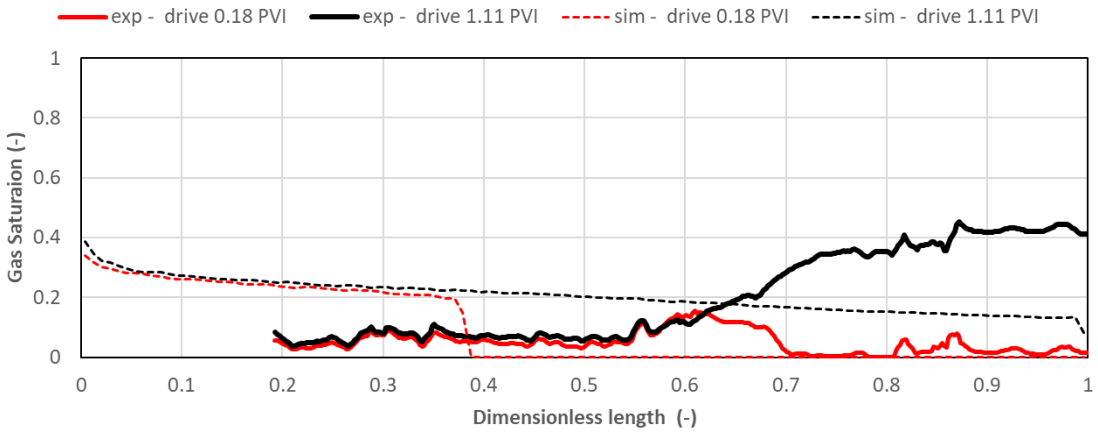

Figure 5.38. Observed and simulated gas saturation at different PVI, $S_w^* = 0.45$, experiment B1.

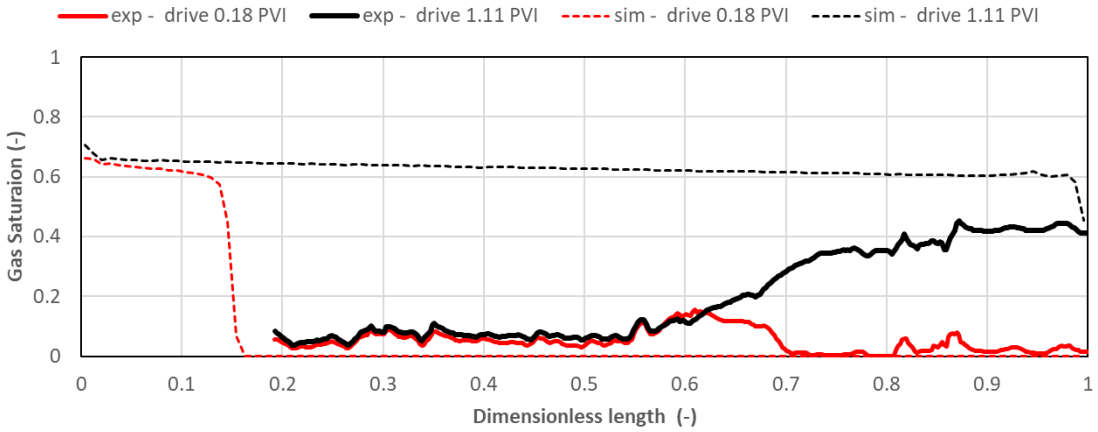

Figure 5.39. Observed and simulated gas saturation at different PVI, $S_w^* = 0.1$, experiment B1.

The abovementioned behavior indicates that to reproduce the behavior of the gas saturation, S_w^* must not be assumed as constant. The following equation was used to generate an increasing S_w^* along the core:

$$S_{w\,i}^* = S_l + \frac{(S_h - S_l)}{1 + a(10^{(x_{Di}-1)b})} \tag{5.1}$$

where a and b are fitting parameters, S_l and S_h correspond to the lower and higher limit values for $S_{w\,i}^*$, and x_{Di} is the dimensionless distance in x-direction (core length) of the cell i.

As first step, the parameters a and b are adjusted in a way that S_w^* resembles the liquid saturation (1 - S_g) at the end of the foam drive. S_h and S_l will be assumed as the higher and lower gas saturation values. The parameters a and b control the position at which the curve starts decreasing and the maximum slope of the curve, respectively. Second step is adjusting the position where S_w^* starts a rapid decrease by tuning a; the oil bank position before the start of the foam drive was selected as initial mark. After this, S_h and S_l will be tuned until an acceptable match is obtained. Figure 5.40 shows the S_w^* distribution for experiments B1 to B3. Table 5.9 summarizes the parameters used in the matching process for experiments B1 to B3. Note that in the literature most of the reported values for S_w^* are in the range between 0.2 to 0.4 (Loftollahi, 2015), while the obtained values in the previous description cover a much wider range.

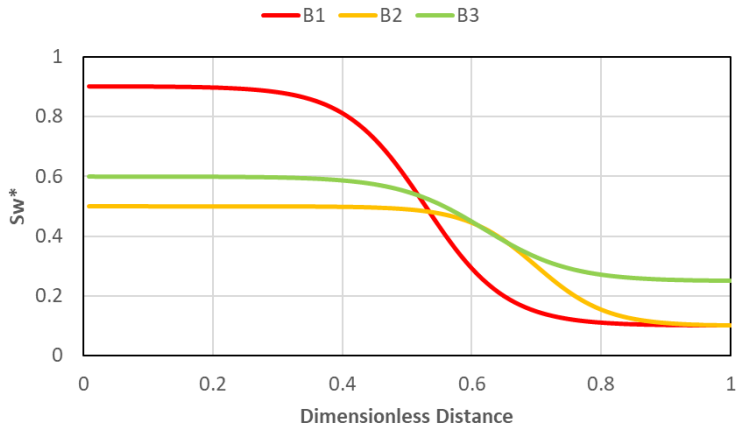

Figure 5.40. SWSTAR distribution for experiment B2.

Table 5.9. Parameters for obtaining SWSTAR.

Parameter	B1	B2	B3
S_h	0.9	0.5	0.6
S_l	0.1	0.1	0.25
a	2000	250	300
b	7	8	6.5

Table 5.10 shows the remaining parameters of the local equilibrium model for experiments B1 to B3. Some parameters as $SOSTAR$ (S_o^*) and $CSTAR$ (C_s^* in equation (4.13)) were assumed as extreme values to make sure that the only parameter controlling R was S_w^*.

Table 5.10. Parameters for gas mobility reduction in UTCHEM.

Parameter	B1	B2	B3
RFMAX	1000	200	20
SOSTAR	0.8	0.8	0.8
CSTAR	1E-5	1E-5	1E-5
EPXLO	1E-2	1E-2	1E-2
SHRTN	1.4	1.4	1.4
VELGR	5E-2	5E-2	5E-2

Figure 5.41 shows the resulting gas mobility reduction factors after the matching process. As observed, foam is successfully generated in the parts of the core that exhibit major gas saturations in the experimental information.

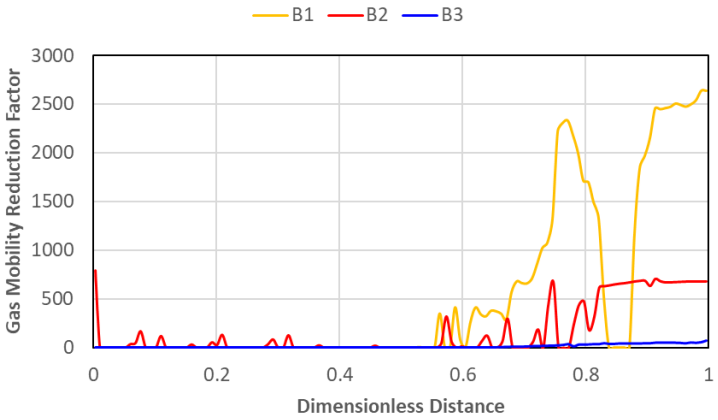

Figure 5.41. Gas mobility reduction factor for experiments B1, B2 and B3.

Figure 5.42, Figure 5.43 and Figure 5.44 show the comparison between observed and simulated pressure drops during FACF for experiments B1 to B3. As it can be observed, a good representation of pressure drop was obtained for B1, and B3, however there is a considerable mismatch of 0.2 ± 0.05 PVI at the peak value.

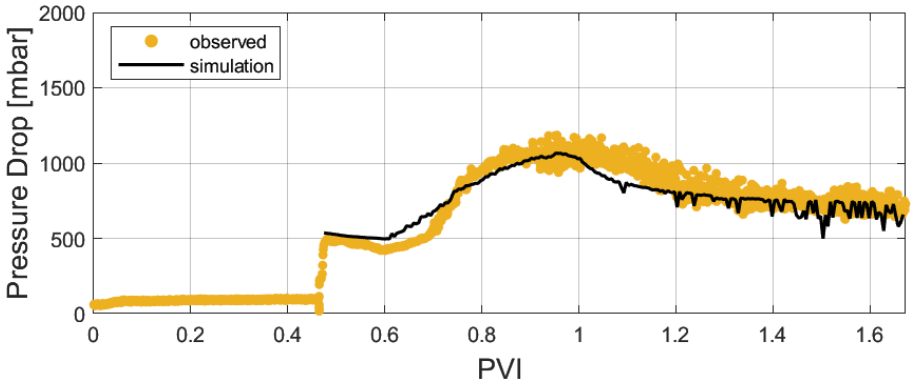

Figure 5.42. Pressure drop match for FACF, experiment B1.

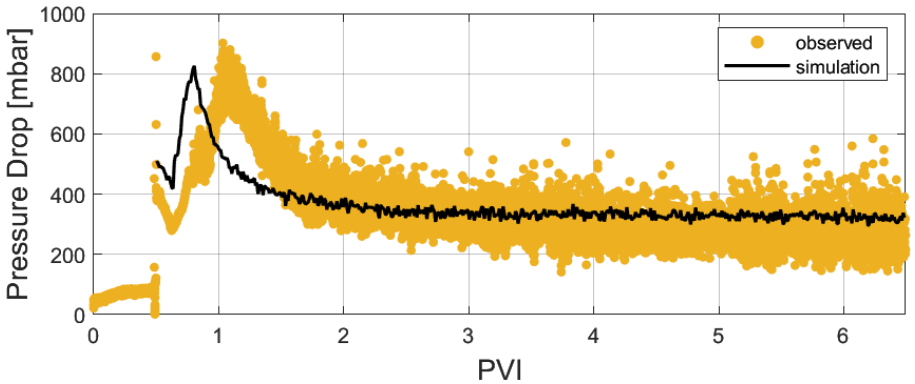

Figure 5.43. Pressure drop match for FACF, experiment B2.

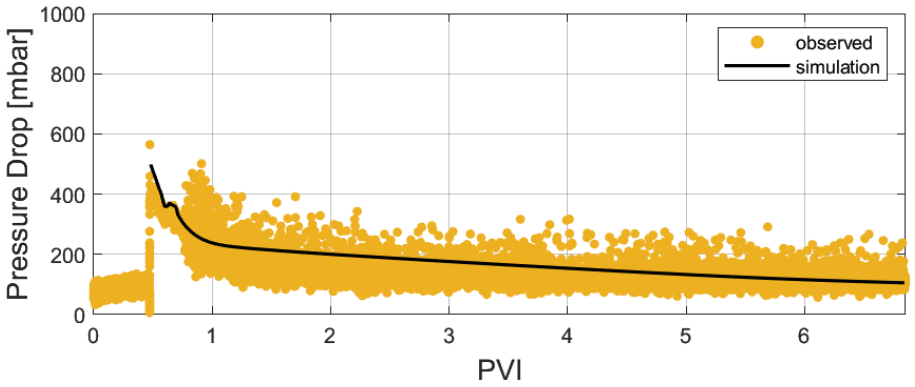

Figure 5.44. Pressure drop match for FACF, experiment B3.

Figure 5.45 to Figure 5.47 compare the simulated and the observed oil recoveries. In experiment B1, a good match is observed, however, for experiments B2 and B3, a mismatch in oil incremental arrivals of 0.08 ± 0.02 can be observed.

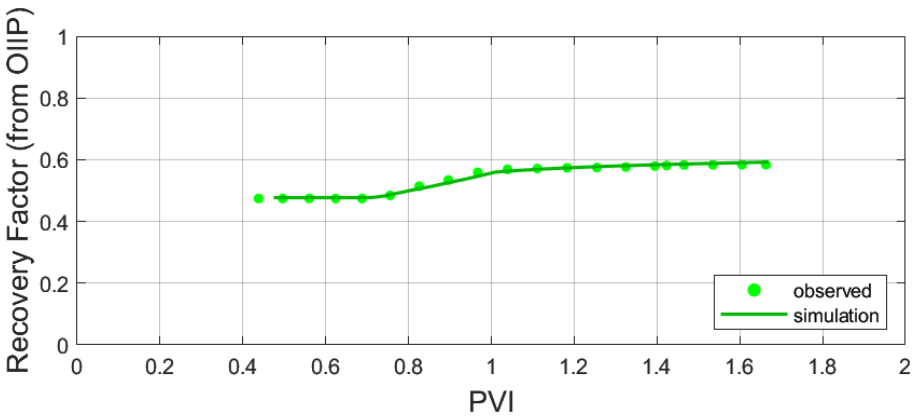

Figure 5.45. Oil recovery factor (from OIIP) match for FACF, experiment B1.

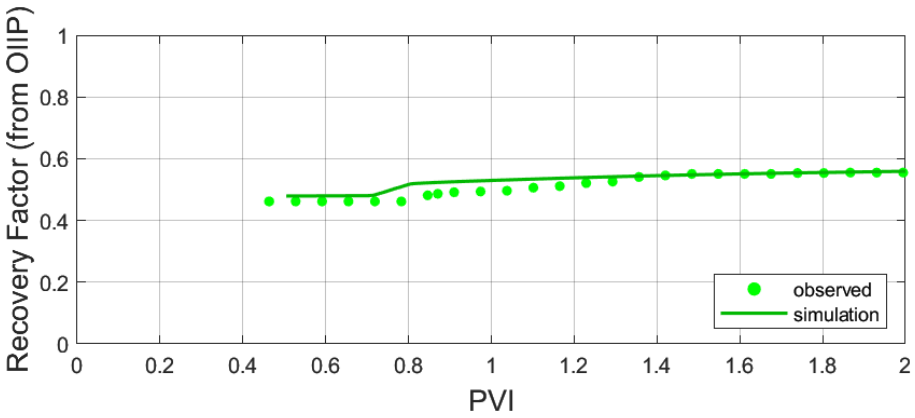

Figure 5.46. Oil recovery factor (from OIIP) match for FACF, experiment B2.

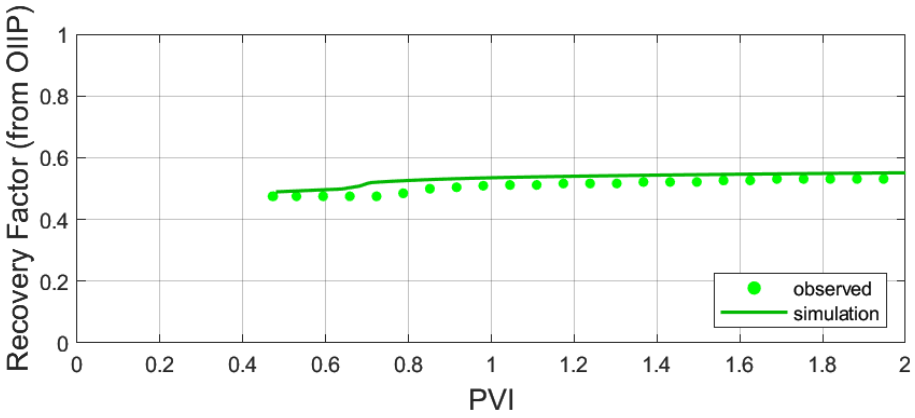

Figure 5.47. Oil recovery factor (from OIIP) match for FACF, experiment B3.

In terms of production fractions, a good match was observed for experiment B1 (Figure 5.48) but again, there is an early breakthrough very similar to the suggested by the recovery factors in experiments B2 (Figure 5.49) and B3 (Figure 5.50).

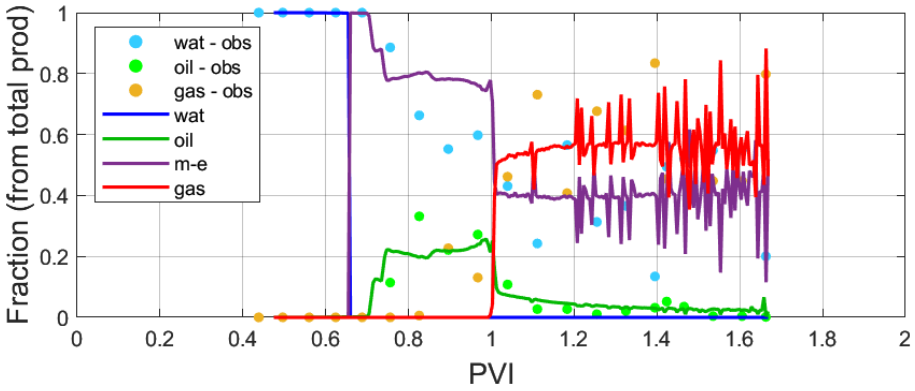

Figure 5.48. Production fractions match for FACF, experiment B1.

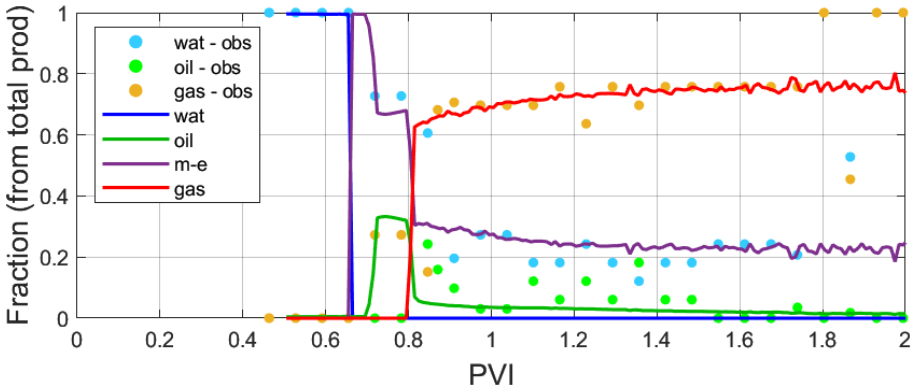

Figure 5.49. Production fractions match for FACF, experiment B2.

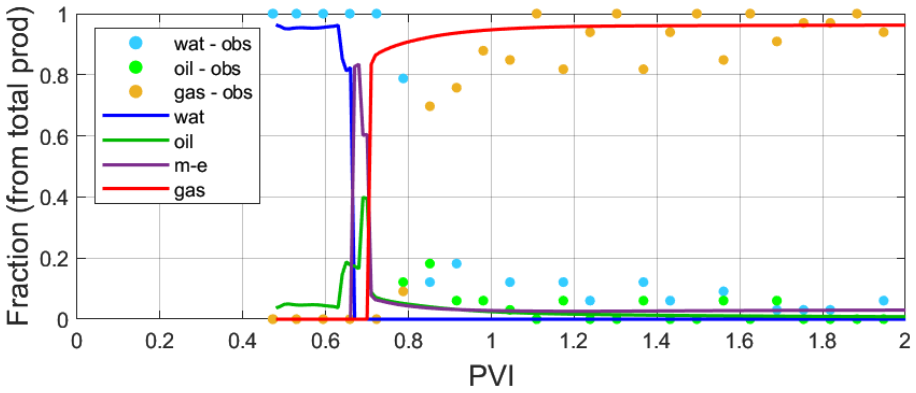

Figure 5.50. Production fractions match for FACF, experiment B3.

Finally, saturations for oil and gas (if available) are compared in Figure 5.51 to Figure 5.56. The best match corresponds to experiment B1, whilst experiments B2 and B3, show a significant delay of the oil bank of about 0.07 ± 0.05 PVI in the simulation. In terms of gas saturation, there is an evident mismatch towards the final half of the core in which the overall magnitude increases with a factor of 1.5 ± 0.2 for experiment B1 and B2, and 1.3 ± 0.1 for experiment B3.

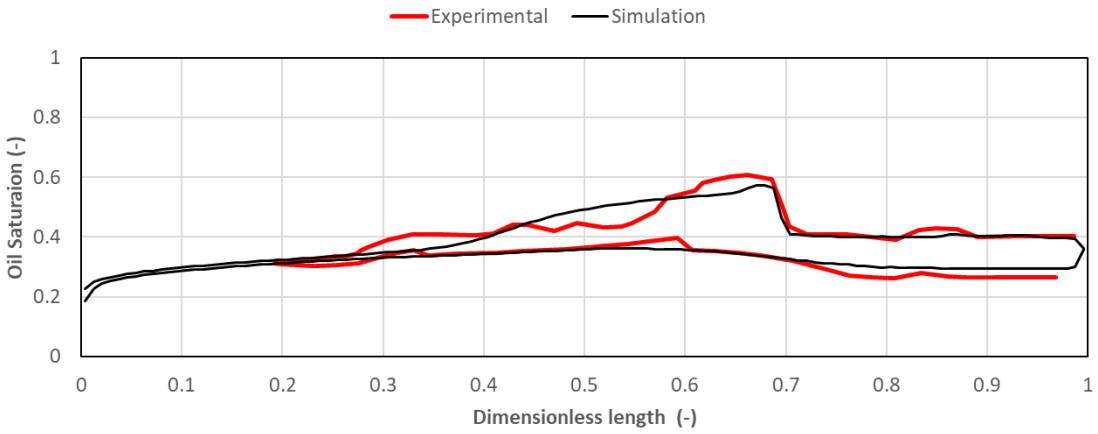

Figure 5.51. Oil saturation match at several PVI during FACF, experiment B1.

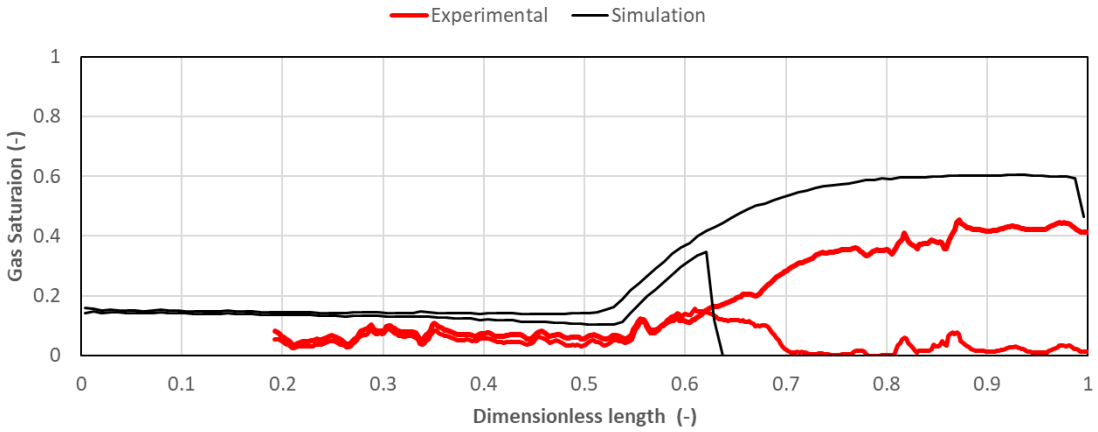

Figure 5.52. Gas saturation match at several PVI during FACF, experiment B1.

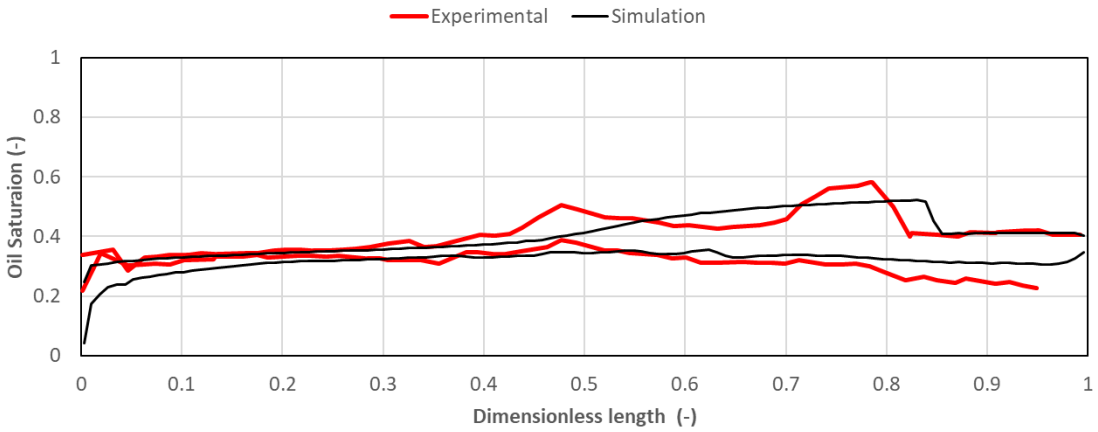

Figure 5.53. Oil saturation match at several PVI during FACF, experiment B2.

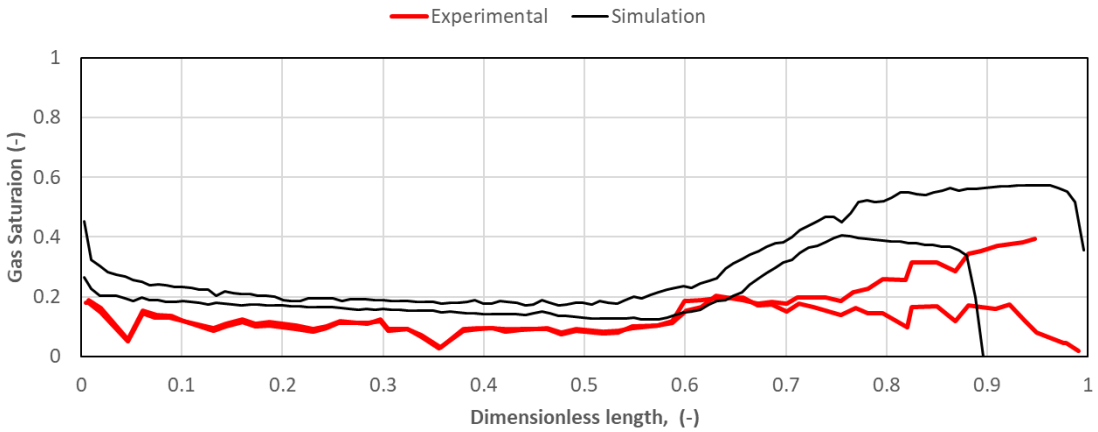

Figure 5.54. Gas saturation match at several PVI during FACF, experiment B2.

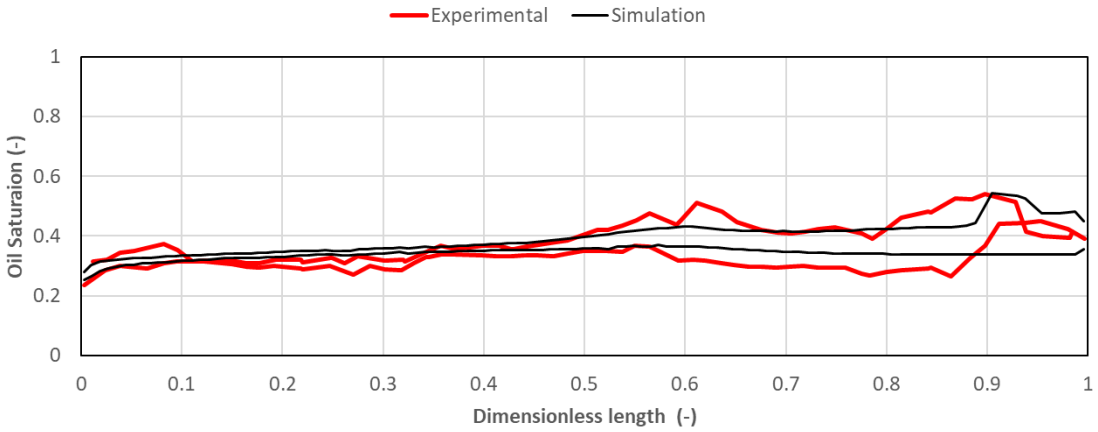

Figure 5.55. Oil saturation match at several PVI during FACF, experiment B3.

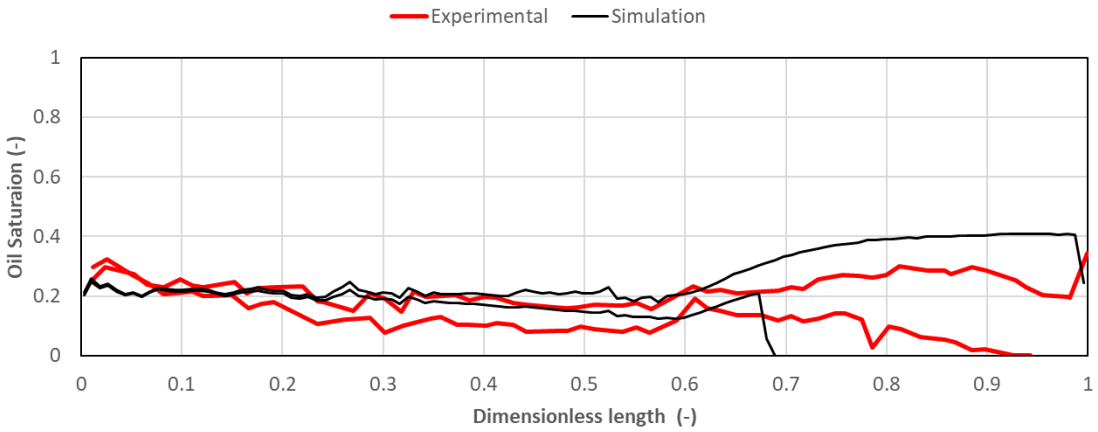

Figure 5.56. Gas saturation match at several PVI during FACF, experiment B3.

6 CONCLUSIONS AND RECOMMENDATIONS

A mechanistic modelling study on seven different experiments based on the work by Janssen et al., (2018) and Janssen et al., (2019b), involving continuous gas injection, WAG, surfactant injection and FACF was successfully performed. CT scan data represented a valuable piece of information for identifying the principal mechanisms behind complex recovery processes as those investigated during this study.

In terms of grid setup, the selected cell sizes work efficiently in terms of running times and data quality. However, this study only included 1D simulation. It is also advised to include a 2D stage, especially for the cases that involve gas injection since gravity segregation can significantly impact the phase distributions along the porous media.

The availability of CT scan-based saturation distributions and effective permeability measurements based on pressure drops per section in the core, allowed a proper estimation of relative permeability curve parameters for primary drainage and forced imbibition, crucial variables for successfully matching the observed pressure drops, oil recovery, production fractions per phase and the evolution of the saturation distribution.

A simple fitting curve schema based on linearization of the Brooks-Corey equation, allows a reduction in the number of variables to fine-tune a proper match with the observations. This simple methodology led to the conclusion that residual water saturation values are lower than the reported average values for the experiments B0 to B4 as connate water saturation. This also explains the need of lower values to replicate experiments A4 and A5, even when no CT scan-based saturations were available.

A successful reproduction of primary drainage and forced imbibition stages, although in principle straightforward, represents an essential starting point for identifying the initial conditions over which surfactant and gas injection may take place. In general, the matches obtained for these stages of the experimental sequence were satisfactory. However, there is still a small mismatch related to the capillary-end effect during primary drainage that could be investigated in future works.

The history matching process of the WAG stage in experiment A5 allowed to visualize the progressive gas mobility reduction as a result of the gas trapping effect. The gas relative permeability to match observations during continuous gas injection in experiment A4 was lower compared to all the gas relative permeability values that resulted from the matching of the WAG experiment. This can be explained by the fact that initial water saturation in experiment A4 was much higher due to extensive water flooding that took place before the gas flooding stage.

Surfactant flooding history match robustness is greatly based on the quality of the preliminary phase behavior match process. This study succeeded in the determination of the parameters involved in the estimation of water and oil solubilization ratios in a microemulsion phase based on salinity and surfactant concentration of the experiments in analysis, given the good matches obtained in experiments B0 to B4 in which different salinity conditions were present. In addition, it was possible to identify the correct trapping number parameters to dynamically modify the water, oil and gas relative permeability curves when o/w IFT reduction occurs. Moreover, the obtained surfactant adsorption estimations are in the range of results of experimental studies under similar conditions (Battistutta, et al., 2015; Solairaj, et al., 2012). In the same way, it was concluded that to properly match the surfactant flooding experiments studied, no geochemical modelling is needed, given that no naphthenic acids are present in the oleic phase.

The foam flooding history match proved to be the most challenging stage in this study, yet there is large room for improvement here. UTCHEM proved to be a very versatile simulation tool able to represent the complex phenomena involved in four-phase systems for a wide range of EOR processes. However, it was observed that the local equilibrium foam model available might still not entirely cover the whole range of possible mechanisms for foam generation, as the one proposed by Janssen et al., (2019b) suggested after experimental evidence that indicates foam strength could be controlled by the presence of oil and microemulsion which induce an effective porosity decrease at the location of a pre-existent oil bank, increasing the interstitial gas velocity, the local pressure drop to generate lamellae division, hence stable foam.

This study did not cover the population balance method for foam modelling, also included in UTCHEM. Further simulation studies in the experimental information here analyzed should include this technique since it can more closely honor the physics involved in the generation and destruction of foam.

REFERENCES

Allison, J. D., Brown, D. S. & Novo-Gradac, K. J., 1991. *MINTEQA2/PRODEFA2, A Geochemical Assessment Model for Environmental Systems, Version 3.0, User's Manual,* s.l.: s.n.

Alvarez, J., Rivas, H. & Rossen, W., 2001. Unified model for steady-state foam behavior at high and low foam qualities. *Society of Petroleum Engineers Journal. 6,* pp. 325-333.

Anderson, G. A., 2006. *Simulation of Chemical Flood Enhanced Oil Recovery Processes Including the Effects of Reservoir Wettability (MSc Thesis),* s.l.: The University of Texas at Austin.

Battistutta, E., van Kuijk, S. R., Groen, K. V. & Zitha, P. L. J., 2015. *Alkaline-Surfactant-Polymer (ASP) Flooding of Crude Oil at Under-Optimum Salinity Conditions.* s.l., Society of Petroleum Engineers.

Belhaj, A. F. et al., 2019. The efect of surfactant concentration, salinity, temperature, and pH on surfactant adsorption for chemical enhanced oil recovery: a review. *Journal of Petroleum Exploration and Production Technology.*

Berger, P. D. & Lee, C. H., 2006. Improved ASP Process Using Organic Alkali. *Society of Petroleum Engineers.*

Bhoendie, K. S., Moe Soe Let, K. P. & Li, T., 2014. Laboratory Evaluation of Gas-Injection EOR for the Heavy-Oil Reservoirs in Suriname. *SPE Heavy and Extra Heavy Oil Conference: Latin America.*

Bikerman, J. J., 1973. *Foams.* s.l.:Springer-Verlag Berlin Heidelberg.

Brooks, R. & Corey, A., 1964. Hydraulic Properties of Porous Media. *Hydrology Papers, No. 3.*

Buckley, S. & Leverett, M., 1942. Mechanism of fluid displacements in sands. *Transactions of the AIME (146),* p. 107–116.

Carman, P. C., 1937. Fluid flow through granular beds. *Transactions, Institution of Chemical Engineers,* Volume 15, pp. 150-166.

Center for Petroleum and Geosystems Engineering, 2018. *UTCHEM Technical Documentation,* Austin: s.n.

Cheng, L. et al., 2000. Simulating Foam Processes at High and Low Foam Qualities. *Society of Petroleum Engineers.*

Claridge, E. L., 1972. Prediction of Recovery in Unstable Miscible Flooding. *SPE Journal,* 12(2), pp. 143-155.

Cottin, C. et al., 2012. (Alkali) Surfactant Gas Injection: Attractive Laboratory Results Under the Harsh Salinity and Temperature Conditions of Middle East Carbonates. *Society of Petroleum Engineers.*

Craig, F. F. J., 1971. *The Reservoir Engineering Aspects of Waterflooding.* s.l.:Society of Petroleum Engineers.

Delshad, M., Bhuyan, D., Pope, G. A. & Lake, L. W., 1986. Effect of Capillary Number on the Residual Saturation of a Three-Phase Micellar Solution. *Fifth Symposium on Enhanced Oil Recovery.*

Delshad, M., Pope, G. A. & Sepehrnoori, K., 1996. A Compositional Simulator for Modeling Surfactant Enhanced Aquifer Remediation, 1 Formulation. *Journal of Contaminant Hydrology,* 23(4), pp. 303-327.

Dyes, A. B., Caudle, B. H. & Erickson, R. A., 1954. Oil Production After Breakthrough as Influenced by Mobility Ratio. *Journal of Petroleum Technology,* Volume 6, pp. 27-32.

Falls, A. H., Musters, J. J. & Ratulowsky, J., 1989. The Apparent Viscosity of Foams in Homogeneous Bead Packs. *Society of Petroleum Engineers,* pp. 155-164.

Farajzadeh, R. et al., 2012. Foam-oil interaction in porous media: Implications for foam assisted enhanced oil recovery. *Advances in Colloid and Interface Science,* Volume 183-184, pp. 1-13.

Fournier, R. & Rowe, J., 1977. The solubility of amorphous silica in water at high temperatures and high pressures. *American Mineralogist 62,* pp. 1052-1056.

Guo, H., Faber, R., Buijse, M. & Zitha, P. L. J., 2011. A Novel Alkaline-Surfactant-Foam EOR Process. *Society of Petroleum Engineers.*

Hand, D. B., 1939. Dineric Distribution: I. The Distribution of a Consolute Liquid Between Two Immiscible Liquids. *Journal of Physics and Chemistry,* Volume 34, pp. 1961-2000.

Hematpour, H., Mahmood, S. M., Akbari, S. & Shabib Asl, A., 2016. Foam Modeling Appoaches in Enhanced Oil Recovery: A review.. *Indian Journal of Science and Technology, Vol 9.*

Hirasaki, G. J., 1981. Application of the theory of multicomponent, multiphase displacement to three-component, two-phase surfactant flooding. *SPEJ Petroleum Engineering Journal,* Volume 21, pp. 191-204.

Hirasaki, G. J., 1989. The steam-foam process-- review of steam-foam process mechanisms. *Society of Petroleum Engineers.*

Hirasaki, G. J. & Lawson, J. B., 1985. Mechanisms of Foam Flow in Porous Media: Apparent Viscosity in Smooth Capillaries. *Society of Petroleum Engineers.*

Hirasaki, G. J. & Pope, G. A., 1974. Analysis of factors Influencing mobility and adsorption in the Flow of polymer solution through porous media. *SPE Journal,* Volume 14, pp. 337-346.

Hosseini-N, S. M. & Zitha, P. L. J., 2015. Systematic Phase Behaviour Study and Foam Stability Analysis for Optimal Alkaline/Surfactant/Foam Enhanced Oil Recovery. *European Association of Geoscientists & Engineers.*

Huh, C., 1979. Interfacial Tension and Solubilizing Ability of a Microemulsion Phase that Coexists with Oil and Brine. *Journal of Colloid and Interface Science,* Volume 71, pp. 408-426.

Jadid, M. & Mustapha, M. F., 2007. A Performance Review of 14 Horizontal Wells in Baronia Field After 12 Years of Production. *Society of Petroleum Engineers.*

Janssen, M. T. G., Azimi, F. & Zitha, P. L. J., 2018. Immiscible Nitrogen Flooding in Bentheimer Sandstones: Comparing Gas Injection Schemes for Enhanced Oil Recovery. *Society of Petroleum Engineers.*

Janssen, M. T. G., Azimi, F. & Zitha, P. L. J., 2019. Immiscible Nitrogen Flooding in Bentheimer Sandstones: Comparing Gas Injection Schemes for Enhanced Oil Recovery. *Society of Petroleum Engineers.*

Janssen, M. T. G., Mutawa, A. S., Pilus, R. M. & Zitha, P. L. J., 2019a. Foam-Assisted Chemical Flooding for Enhanced Oil Recovery: Effects of Slug Salinity and Drive Foam Strength. *Energy and Fuels,* Volume 33, p. 4951−4963.

Janssen, M. T. G., Pilus, R. M. & Zitha, P. L. J., 2019c. A Comparative Study of Gas Flooding and Foam-Assisted Chemical Flooding in Bentheimer Sandstones. *Transport in Porous Media.*

Janssen, M. T. G., Zitha, P. L. J. & Pilus, R. M., 2019b. Oil Recovery by Alkaline/Surfactant/Foam Flooding: Effect of Drive Foam Quality on Oil Bank Propagation. *Society of Petroleum Engineers Journal.*

Janssen, M. T. G., Zitha, P. L. J. & Pilus, R. M., 2019. Oil Recovery by Alkaline/Surfactant/Foam Flooding: Effect of Drive Foam Quality on Oil Bank Propagation. *Society of Petroleum Engineers Journal.*

Jong, S. et al., 2016. Low Tension Gas Flooding as a Novel EOR Method: An Experimental and Theoretical Investigation. *Society of Petroleum Engineers.*

Kamal, M. & Marsden, S. S., 1973. Displacement of a Micellar Slug Foam in Unconsolidated Porous Media. *Society of Petroleum Engineers.*

Khatib, Z. I., Hirasaki, G. J. & Falls, A. H., 1988. Effects of Capillary Pressureon Coalescence and Phase Mobilities in Foams Flowing Though Porous Media. *SPE Reservoir Engineering,* Volume 3, pp. 919-926.

Knol, M. I., 2015. *Developing and evaluating a model for Surfactant-Foam Flooding (MSc Thesis),* s.l.: Delft University of Technology.

Kovscek, A. & Radke, C., 1993. *Fundamentals of foam transport in porous media,* United States: s.n.

Kozeny, M., 1927. Uber kapillare Leitung des Wassers im Boden. *Sitzber. Akad. Wiss. Wein, Math-naturw,* Volume 136, pp. Abt. II a, P. 277.

Lake, L. W., 1989. *Enhanced Oil Recovery.* Englewood Cliffs, N.J.: Prentice Hall.

Lake, L. W., Johns, R. T., Rossen, W. R. & Pope, G. A., 2014. *Fundamentals of Enhanced Oil Recovery.* s.l.:Society of Petroleum Engineers.

Lashgari, H. R., Sepehrnoori, K. & Delshad, M., 2015. Modeling of Low-Tension Surfactant-Gas Flooding Process in a Four-Phase Flow Simulator. *Society of Petroleum Engineers.*

Lawson, J. B. & Reisberg, J., 1980. Alternate Slugs of Gas and Dilute Surfactant for Mobility Control During Chemical Flooding. *Society of Petroleum Engineers.*

Li, R. F. et al., 2008. Foam Mobility Control for Surfactant EOR. *Society of Petroleum Engineers.*

Loftollahi, M., 2015. *Development of a Four-Phase Flow Simulator to Model Hybrid Gas/Chemical EOR Processes (PhD Dissertation),* s.l.: The University of Texas at Austin.

Melrose, J. C. & Brandner, C. F., 1974. Role of Capillary Forces in Determining Microscopic Displacement Efficiency for Oil Recovery by Waterflooding. *The Journal of Canadian Petroleum,* pp. 54-62.

Mohammadi, H., 2008. *Mechanistic Modeling, Design, and Optimization of Alkaline/Surfactant/Polymer Flooding (Dissertation),* s.l.: The University of Texas at Austin.

Morrow, N. R. & Songkran, B., 1982. Surface Phenomena in Enhanced Oil Recovery. pp. 387-411.

Muskat, M., 1949. *Physical Principles of Oil Production.* New York: McGraw-Hill.

Nguyen, Q. P., Currie, P. K. & Zitha, P. L. J., 2005. Effect Crossflow on Foam-Induced Diversion in Layered Formations. *Society of Petroleum Engineers.*

Nordstrom, D. K. et al., 1990. Revised chemical equilibrium data for major water-mineral reactions and their limitations. *American Chemical Society Symposium,* Volume 416, pp. 398-413.

Peksa, A. E., Wolf, K. H. A. & Zitha, P. L., 2015. Bentheimer Sandstone Revisited for Experimental Purposes. *Marine and Petroleum Geology,* Volume 67, pp. 701-719.

Plummer, L. N. & Busenberg, E., 1982. The solubilities of calcite, aragonite and vaterite in CO2 solutions between 0 and 90°C, and an evaluation of the aqueous model for the system CaCO3-CO2-H2O. *Geochimica et Cosmochimica Acta,* Volume 46, pp. 1011-1040.

Pratap, M., Ibrahim, Z. B. & Karim, M. G., 2000. Reservoir Simulation Study of Baronia Field, Offshore Sarawak, Malaysia Indicates Higher Reserves and OIIP. *Society of Petroleum Engineers.*

Reed, R. L. & Healy, R. N., 1977. Some Physico-Chemical Aspects of Microemulsion Flooding: A Review.

Rijks, E. J. H., 1981. Baram Delta Geology and Hydrocarbon Occurrence. *Geological Society and Hydrocarbon Occurrence,* Volume 14, pp. 1-18.

Rossen, W. R. & Gauglitz, P. A., 1990. Percolation Theory of Creation and Mobilization of Foams in Porous Media. *AIChE,* Volume 36, pp. 1176-1188.

Sheng, J. J., 2010. *Modern Chemical Enhanced Oil Recovery..* s.l.:Elsevier.

Sheng, J. J., 2015. Investigation of Alkaline-Crude Oil Reaction. *Petroleum,* 1(1), pp. 31-39.

Skauge, A. & Larsen, J. A., 1994. *Three-phase relative permeabilities and trapped gas measurements related to WAG processes..* s.l., s.n.

Sofian, M. A. et al., 2014. Optimized Platform Placement to Cover All Geological Targets in Baronia Field. *Offshore Technology Conference.*

Solairaj, S. et al., 2012. Measurement and Analysis of Surfactant Retention. *Society of Petroleum Engineers.*

Srivastava, M., 2010. *Foam Assisted Low Interfacial Tension Enhanced Oil Recovery (Dissertation),* s.l.: The University of Texas at Austin.

Srivastava, M., Zhang, J., Nguyen, Q. P. & Pope, G. A., 2009. A Systematic Study of Alkaline-Surfactant-Gas Injection as an EOR Technique. *Society of Petroleum Engineers.*

Stadnes, D. C. & Austad, T., 2002. Wettability alteration in carbonates Interaction between cationic surfactant and carboxylates as a key factor in wettability alteration from oil-wet to water-wet conditions. *Colloids and Surfaces A: Physicochem. Eng. Aspects,* Volume 216, pp. 243-259.

Sudirman, S. B., Samsudin, Y. B. & Darman, N. H., 2007. Planning for Regional EOR Pilot for Baram Delta, Offshore Sarawak, Malaysia: Case Study, Lesson Learnt and Way Forward. *Society of Petroleum Engineers.*

Szlendak, S. M., Nguyen, N. M. & Nguyen, Q. P., 2013. Laboratory Investigation of Low-Tension-Gas Flooding for Improved Oil Recovery in Tight Formations. *Society of Petroleum Engineers.*

Szlendak, S. M., Nguyen, N. M. & Nguyen, Q. P., 2016. Investigation of Localized Displacement Phenomenon for Low-Tension-Gas (LTG) Injection in Tight Formations. *Journal of Petroleum Science and Engineering,* pp. 36-45.

Tanzil, D., Hirasaki, G. J. & Miller, C. A., 2002. Mobility of Foam in Heterogeneous Media: Flow Parallel and Perpendicular to Stratfication. *SPE Journal,* Volume 7, pp. 203-212.

van Lingen, P., 1998. *Quantification and Reduction of Capillary Entrapment in Cross-Laminated Oil Reservoirs (PhD Thesis),* s.l.: Delft University of Technology.

Wang, D. et al., 2001. Successful Field Test of the First Ultra-Low Interfacial Tension Foam Flood. *Society of Petroleum Engineers.*

Wang, L., 2006. *Alkali-Surfactant-Polymer Foams (ASPF): Laboratory Investigation of Displacement Mechanisms (Thesis),* s.l.: University of Calgary.

Zain, N. et al., 2005. Gas Injection Feasibility Study of the Baram Delta Fields, Malaysia. *Society of Petroleum Engineers.*

APPENDIX A Comparing Simulation Tools

A brief comparison between UTCHEM and most commonly used simulators is presented in Table A.1 (surfactant modelling) and Table A.2 (foam modelling). From this information, UTCHEM was chosen as simulation tool in this study. Blank spaces indicate the specific feature is not included or no information was found.

Table A.1. Comparison between UTCHEM and commercial simulators (surfactant modelling features).

Surfactant Modelling Features	UTCHEM	STARS	ECLIPSE	REVEAL	GEM
Microemulsion Viscosity	Included: *It can be modeled as a function of water, oil and surfactant concentrations in the microemulsion phase*			Included	Included
Interfacial Tension (IFT)	Included: *Healy & Reed (1974), and Chun Huh (1979) correlations available, and a correction to ensure the IFT approaches oil/water in the absence of surfactant*	Included: *A table of IFT as a function of surfactant concentration is provided*	Included: *A table of IFT as a function of surfactant concentration is provided*	Included	Included
Phase Behavior	Included: *Based on Hand's rule (Hand, 1939). Uses the ternary diagram for representing different microemulsion phases and tie lines which are distributive curves*	Not included: *No microemulsion phase, but provides two options to specify surfactant partitioning between phases*		Included: *Similar to UTCHEM and can define different phase behavior (Type I, Type II, and Type III) based on salinities*	Included
Surfactant Adsorption	Included: *Uses the Langmuir-type isotherm equation to describe surfactant adsorption*	Included	Included	Included: *Retardation and permeability reduction effects*	
Ion Exchange Effect	Included	Included	Included		
Effective Salinity Window	Included			Included	Included

REFERENCES

Goudarzi, A., Delshad, M., & Sepehrnoori, K. (2012). A Critical Assessment of Several Reservoir Simulators for Modeling Chemical Enhanced Oil Recovery Processes. *SPE 163578*.
Petroleum Experts. (2012). *PETROLEUM ENGINEERING AND STRUCTURAL GEOLOGY SOFTWARE*.
Sarkyt, K. (2015). Alkaline/Sufactant/Polymer (ASP) Flooding.
Sheng, J. (2011). *Modern Chemical Enhanced Oil Recovery*.
Computer Modeling Group. (2012) GEM Compositional & Unconventional Simulator

Table A.2. Comparison between UTCHEM and commercial simulators (foam modelling features).

Foam Modelling Characteristics	UTCHEM	STARS	ECLIPSE	REVEAL	GEM
Component reactions		Included			**Included**
Interfacial Tension (IFT)	Included	Included: *Simulates IFT reduction and relative permeability changes from varying foam concentration*			
Foam adsorption			Included: *Analytical models or tabulated isotherms*		
Modeling of changes to foam properties		Included	Included: *Foam decay effects as a function of oil and water saturations*	Included: *Foam model for increasing gas phase viscosity especially in heavy oil reservoirs*	Included
Used for heavy oil and light oil	Included				Included
Empirical Foam model	Included	Included	Included		Included
Mechanistically model complex foam-flooding physics		Included			
Show fully dry-out phenomenon at water saturation below the limiting water saturation	Included: *It is able to make the mobility reduction factor to 1 when the water saturation reaches limiting water saturation*				
General comments	*Use discontinues function to simulate the limiting water saturation phenomenon on foam flow on the porous media.*	*Utilizes continuos function*	*Utilizes continuos function*		*Only simulator that models Miscible Injection + Foam + ASP + Low salinity in a single model.*

REFERENCES

Computer Modeling Group. (2012). *Simulating Foam Injection using the STARS Mechanistic Model.*
Schlumberger. (2013). *ECLIPSE Industry Reference Reservoir Simulator*
Hematour, H et al., (2018). *Foam flow in porous media: Concepts, models and challenges*

APPENDIX B CT Scan Saturation

A complete summary of available CT scan saturation information per experiment/stage is presented in the following figures. Although most common information is oil saturation, some scans in the foam flooding stages also have gas saturation information.

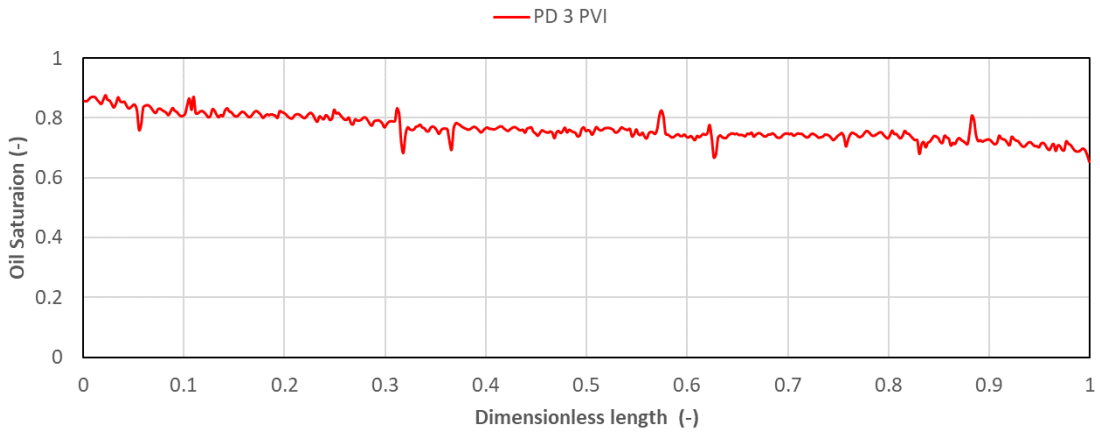

Figure B.1. Oil saturation distribution in experiment B0 during primary drainage.

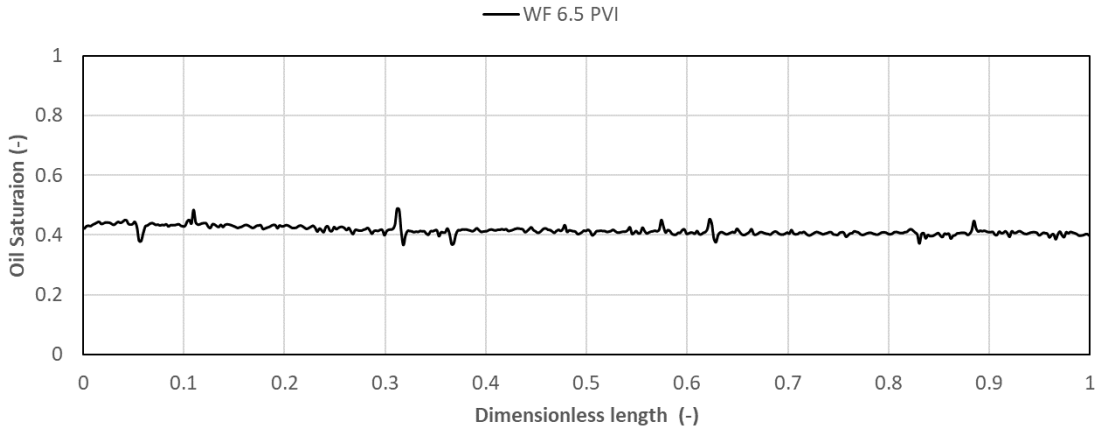

Figure B.2. Oil saturation distribution in experiment B0 during water flooding.

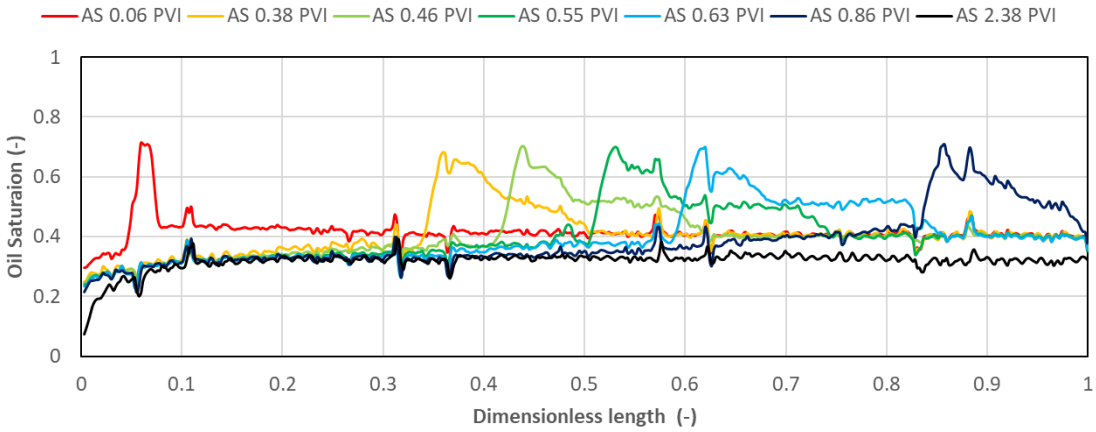

Figure B.3. Oil saturation distribution in experiment B0 during surfactant flooding.

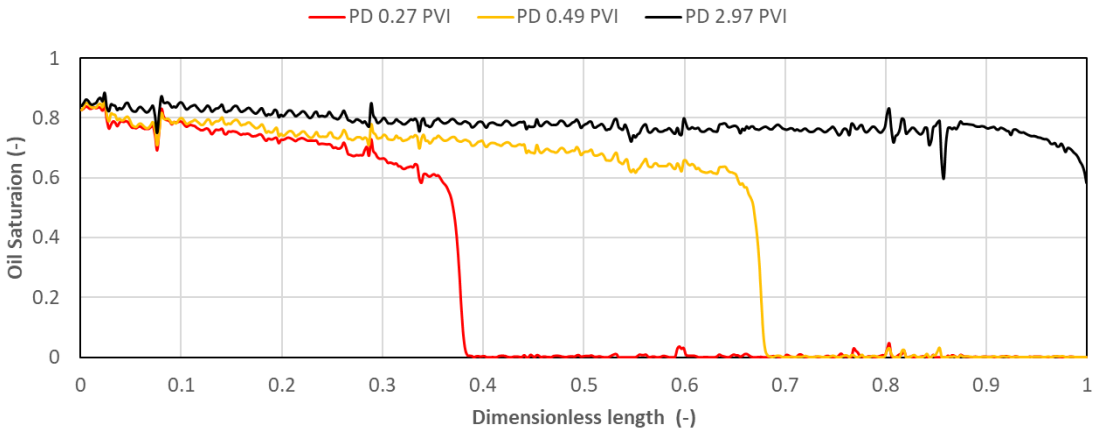

Figure B.4. Oil saturation distribution in experiment B1 during primary drainage.

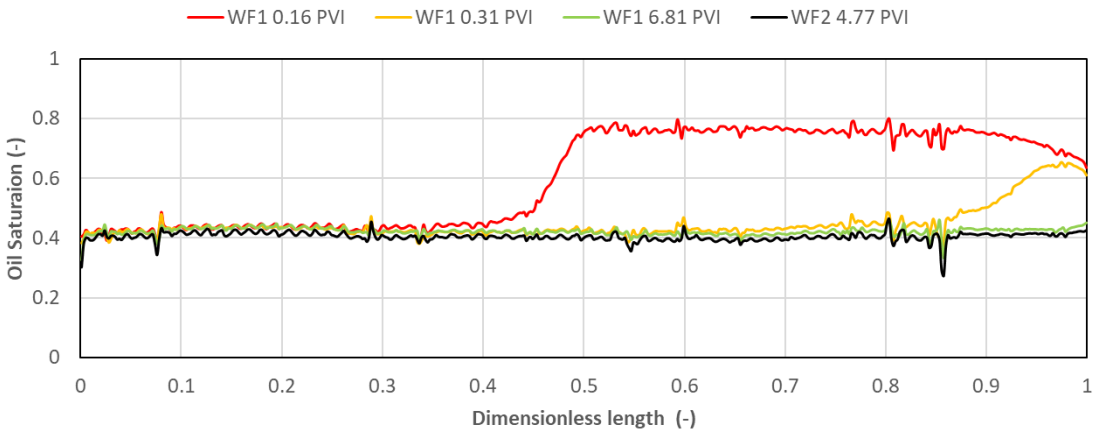

Figure B.5. Oil saturation distribution in experiment B1 during water flooding.

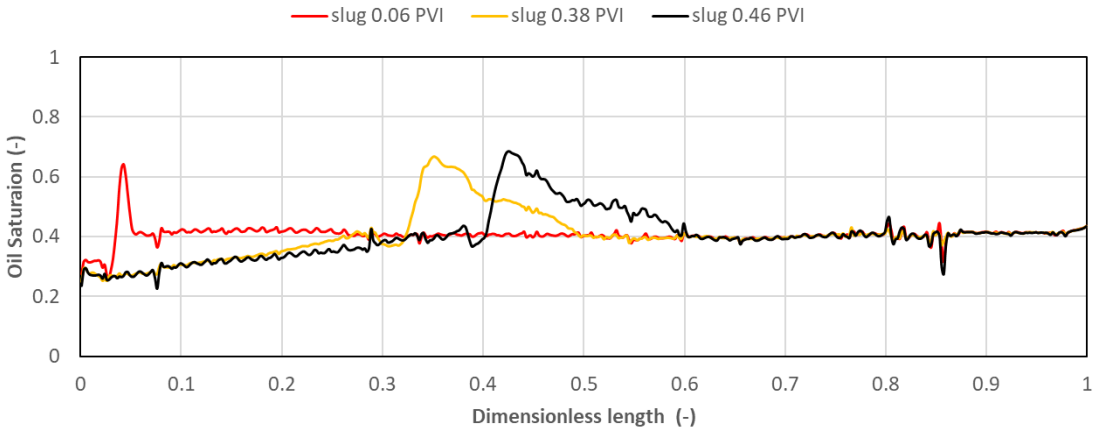

Figure B.6. Oil saturation distribution in experiment B1 during surfactant slug.

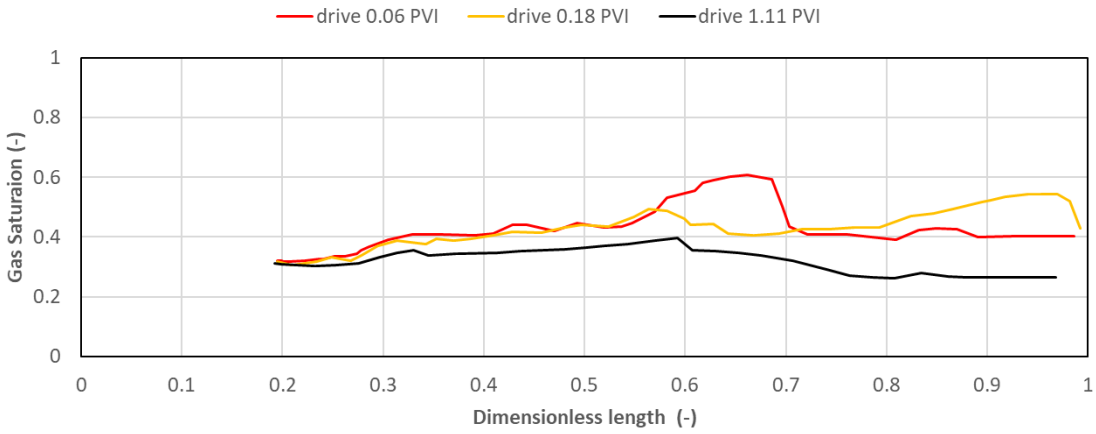

Figure B.7. Oil saturation distribution in experiment B1 during foam flooding.

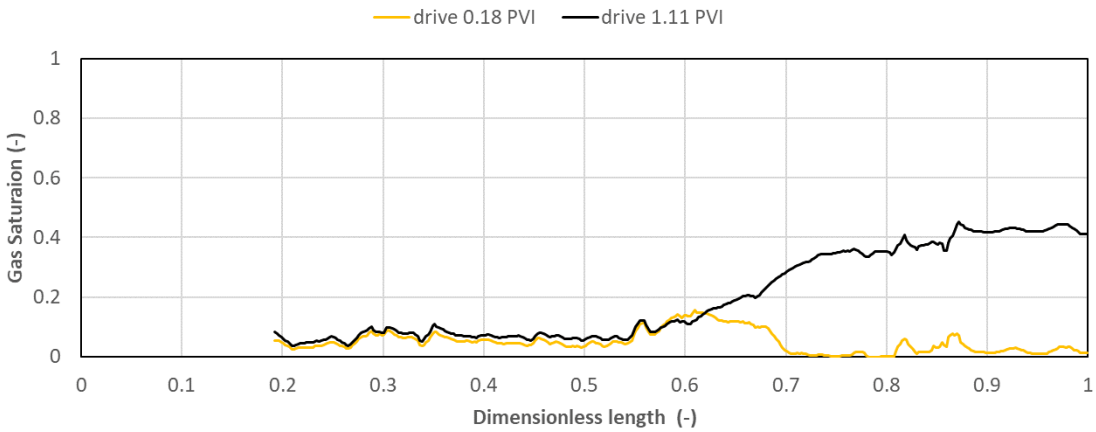

Figure B.8. Gas saturation distribution in experiment B1 during foam flooding.

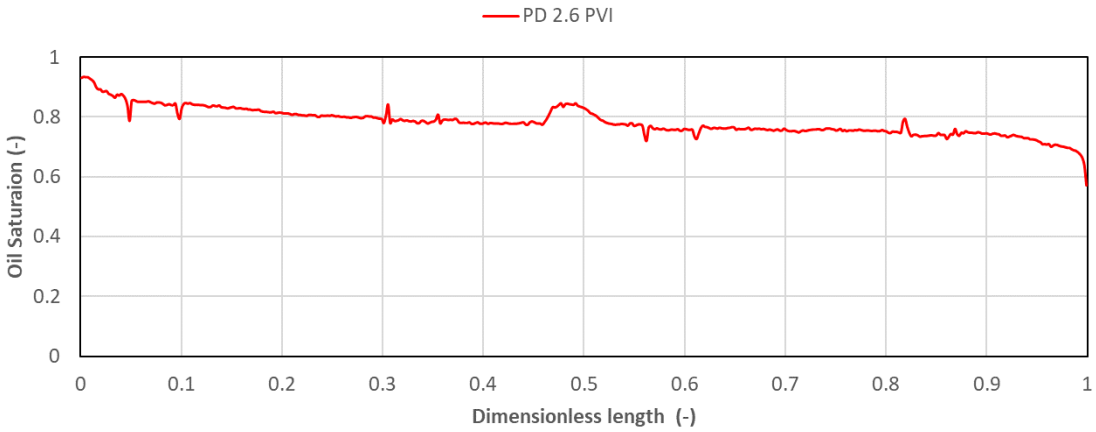

Figure B.9. Oil saturation distribution in experiment B2 during primary drainage.

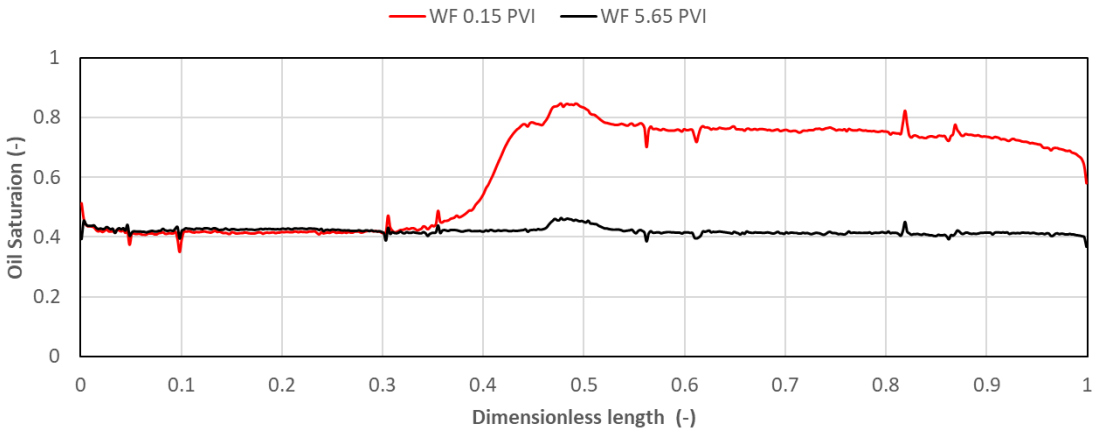

Figure B.10. Oil saturation distribution in experiment B2 during water flooding.

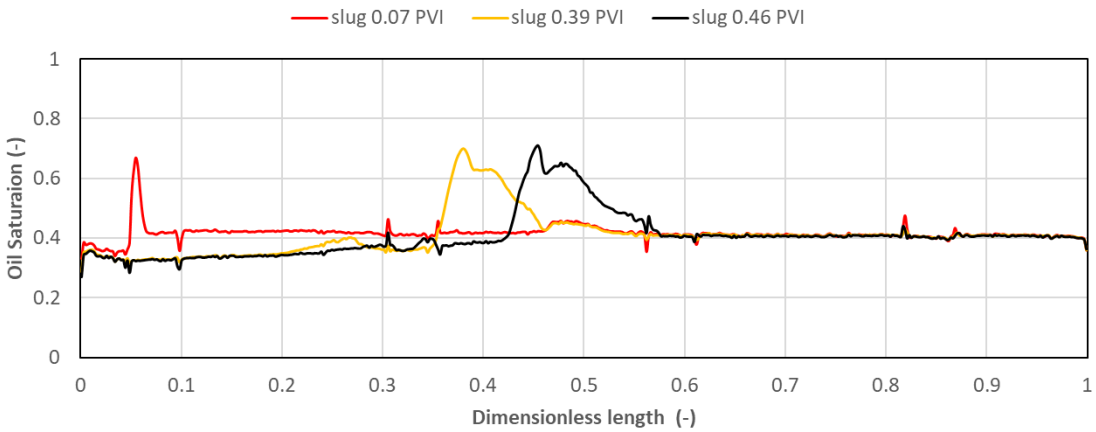

Figure B.11. Oil saturation distribution in experiment B2 during surfactant slug.

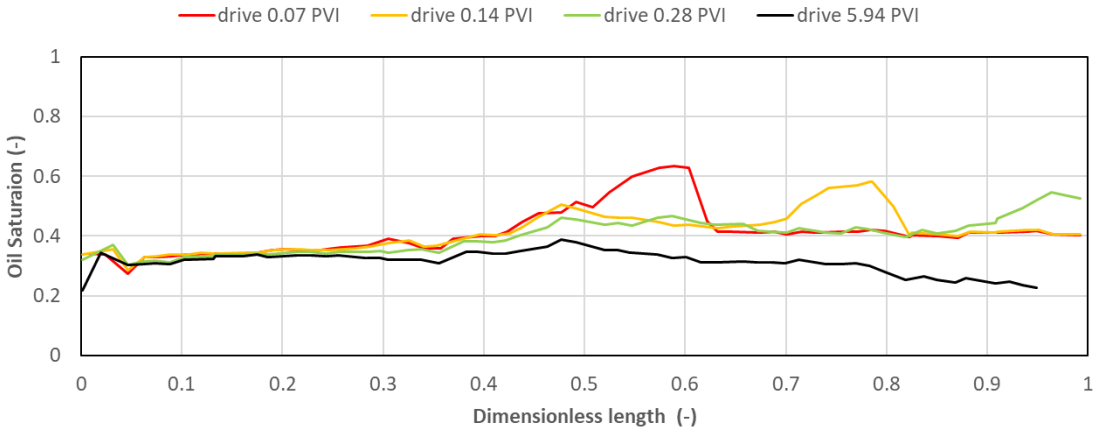

Figure B.12. Oil saturation distribution in experiment B2 during foam flooding.

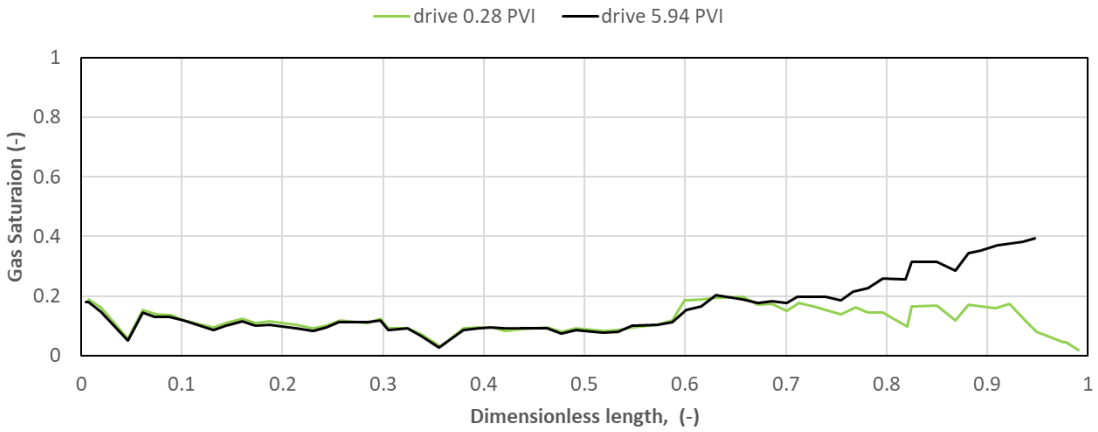

Figure B.13. Gas saturation distribution in experiment B2 during foam flooding.

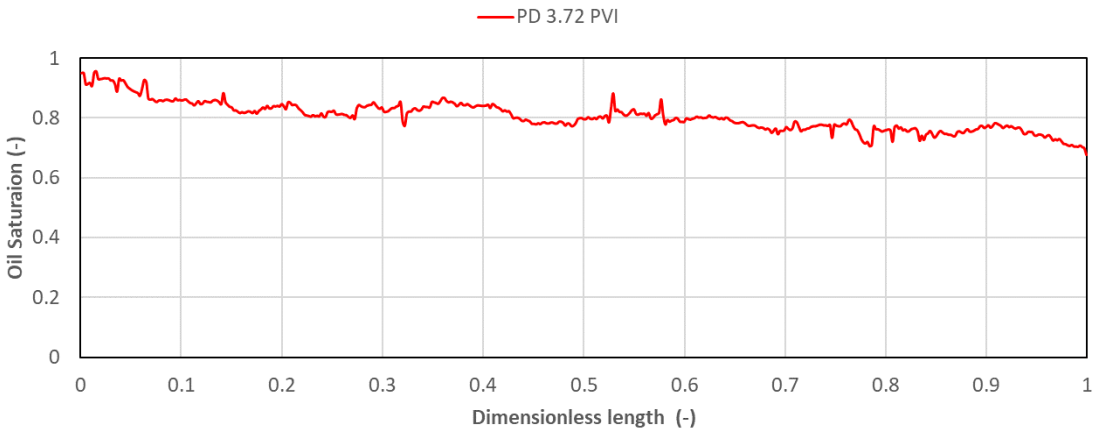

Figure B.14. Oil saturation distribution in experiment B3 during primary drainage.

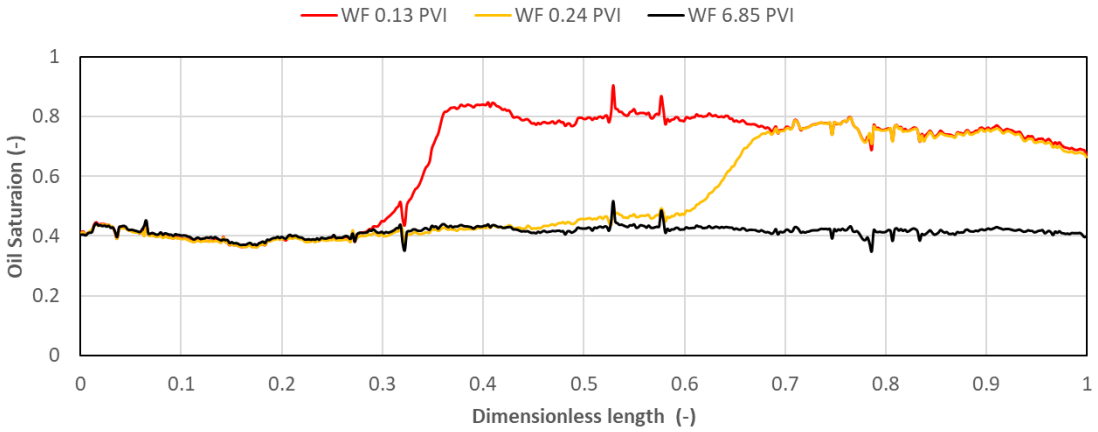

Figure B.15. Oil saturation distribution in experiment B3 during water flooding.

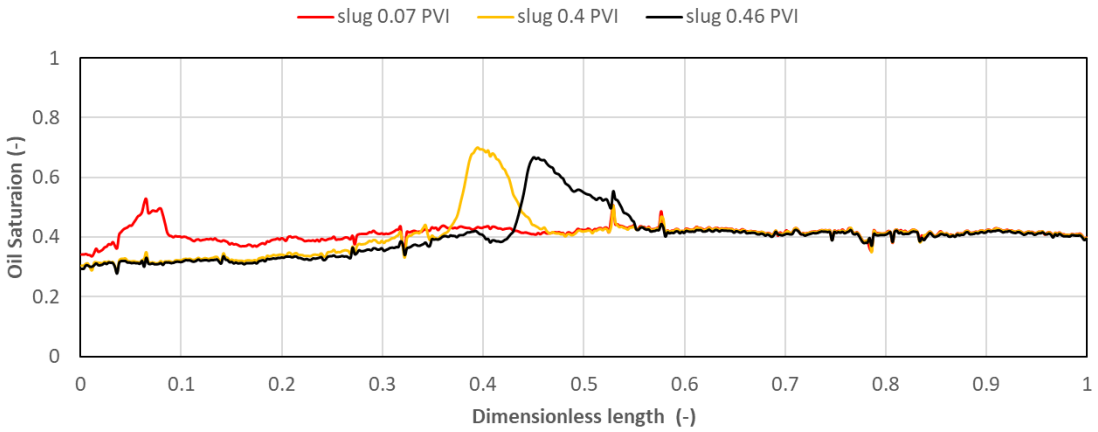

Figure B.16. Oil saturation distribution in experiment B3 during surfactant slug.

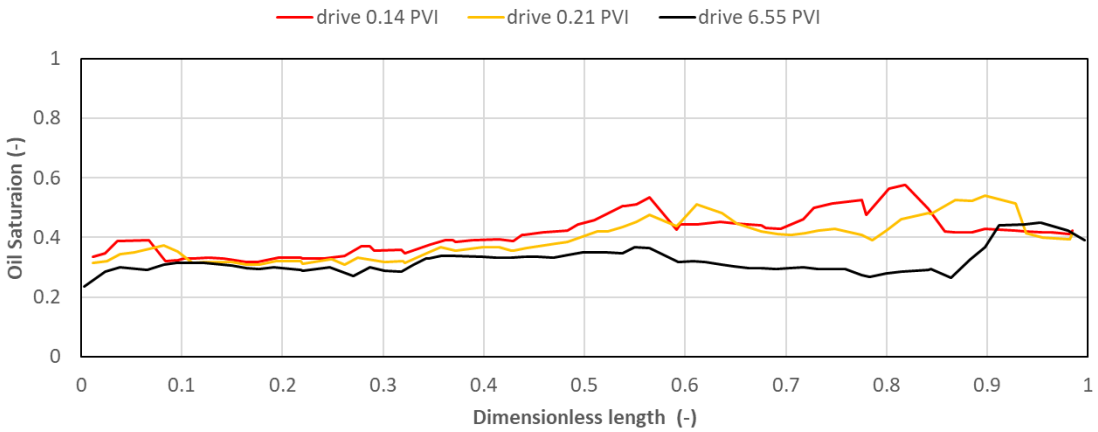

Figure B.17. Oil saturation distribution in experiment B3 during foam flooding.

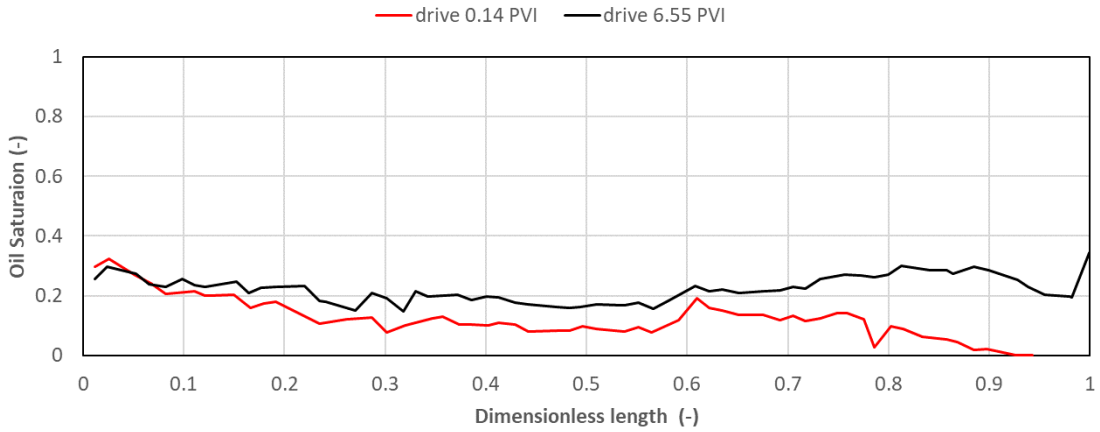

Figure B.18. Gas saturation distribution in experiment B3 during foam flooding.

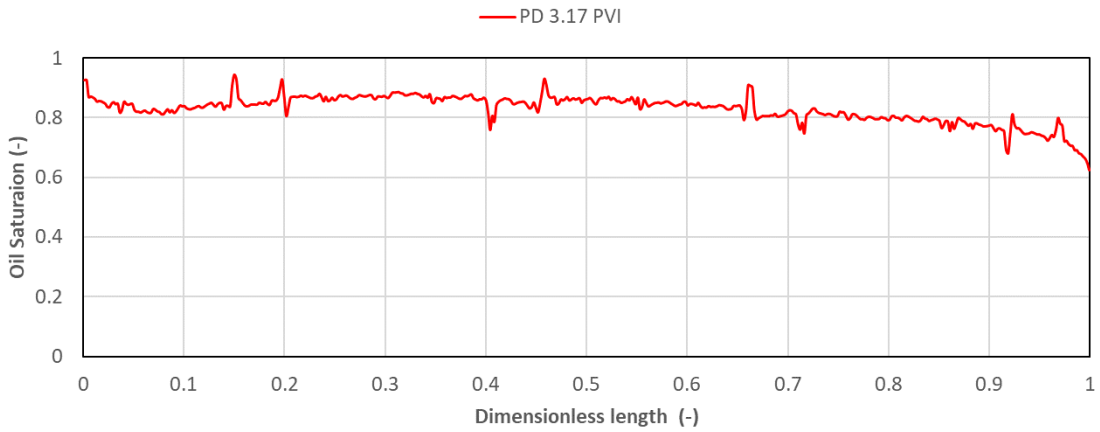

Figure B.19. Oil saturation distribution in experiment B4 during primary drainage.

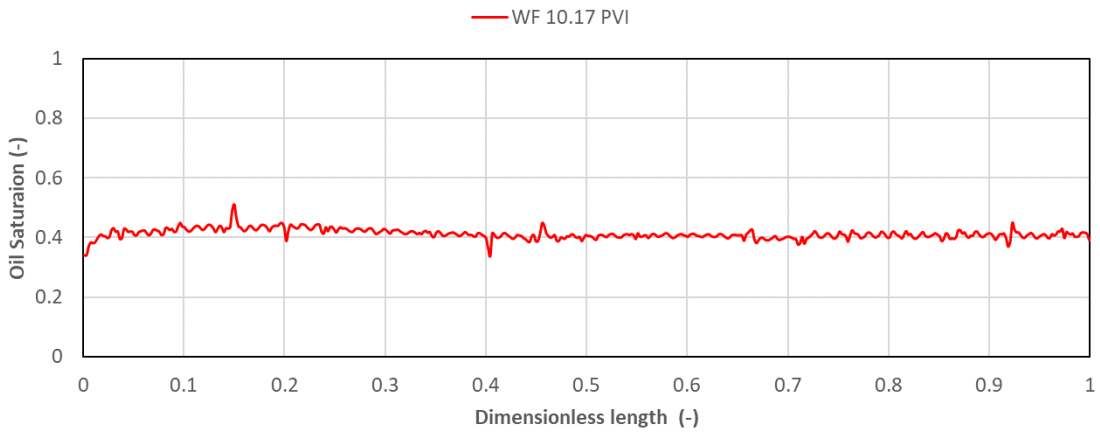

Figure B.20. Oil saturation distribution in experiment B4 during water flooding.

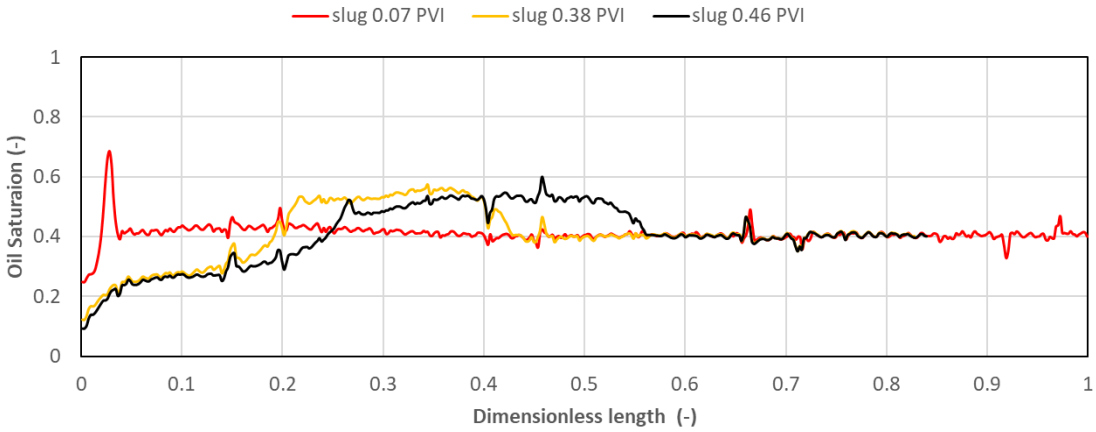

Figure B.21. Oil saturation distribution in experiment B4 during surfactant slug.

APPENDIX C Cell Size Selection

Once initial parameters for modelling relative permeability curves were obtained, the next step was cell size selection. Since 1D modelling was performed during this study, the number of grid cells was only dependent on the x-direction cell size, or in other words, the number of cells in the x-direction.

A simple sensitivity analysis on the number of cells in x-direction was performed using the available information for experiment B1 during primary drainage; this section summarizes the results.

The finest grid used as starting point was assumed to be composed by the number of discrete elements during the CT scan, 480. It was observed that this resolution allowed a good representation of the shock, compared to the experimental observations at 0.27 PVI (Figure C.1).

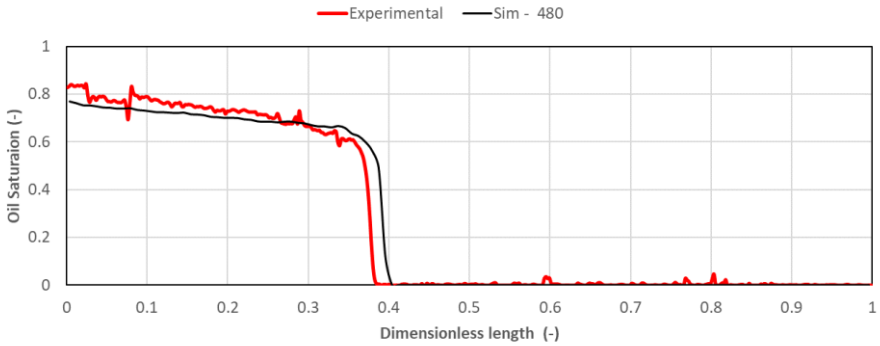

Figure C.1. Observed and simulated oil saturation for 480 cells in x-direction, primary drainage (0.27 PVI), experiment B1.

This value (480) was selected as a base case and every other case was compared with it. Figure C.2 shows the shock detail for all the cases. From this information, a cell number in x-direction of 120 was selected since it still resembles the shape of the shock front and simulations can be performed at less than a quarter of the time it takes the base case to run the same PVI.

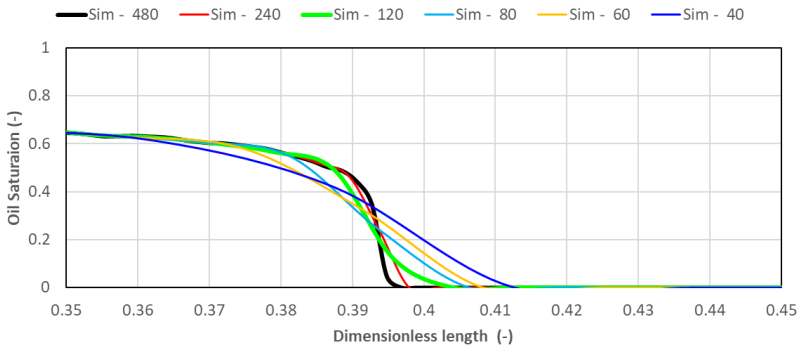

Figure C.2. Detail of shock front at 0.27 PVI during primary drainage for different number of cells in x, exercise B1.

APPENDIX D Porosity and Permeability

A summary of porosity and permeability distributions for fine and coarse grids, as well as permeability quality plots is presented in this section.

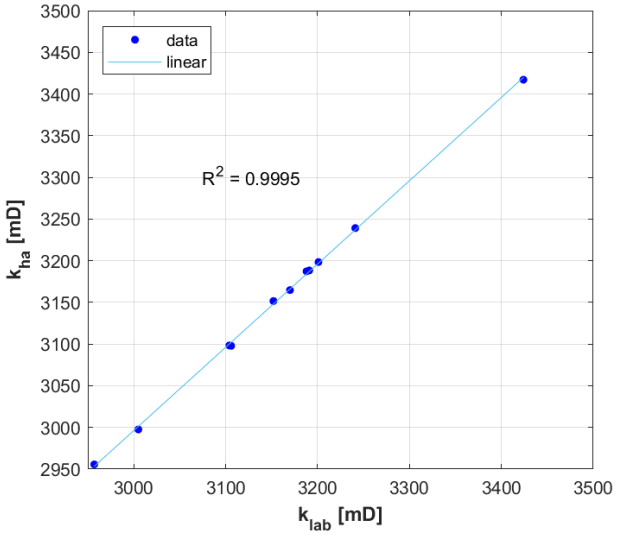

Figure D.1. Absolute permeability quality control for experiment B0.

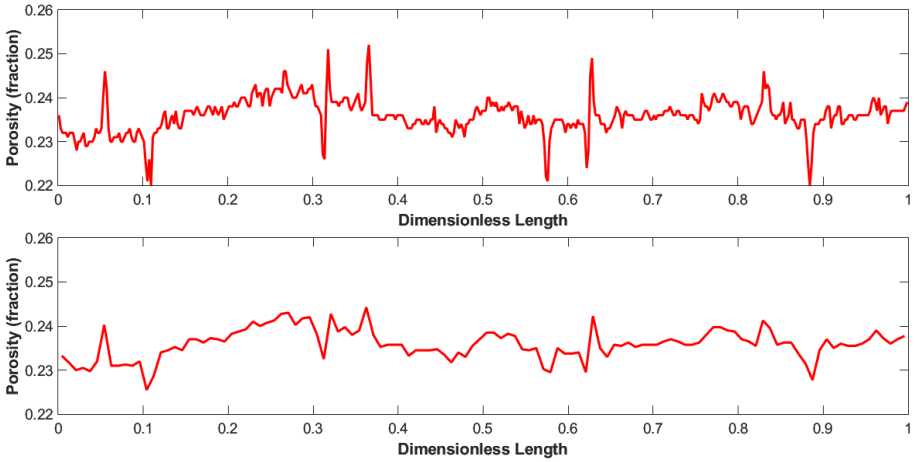

Figure D.2. Comparison between fine (upper) and coarse (lower) porosity distribution for experiment B0.

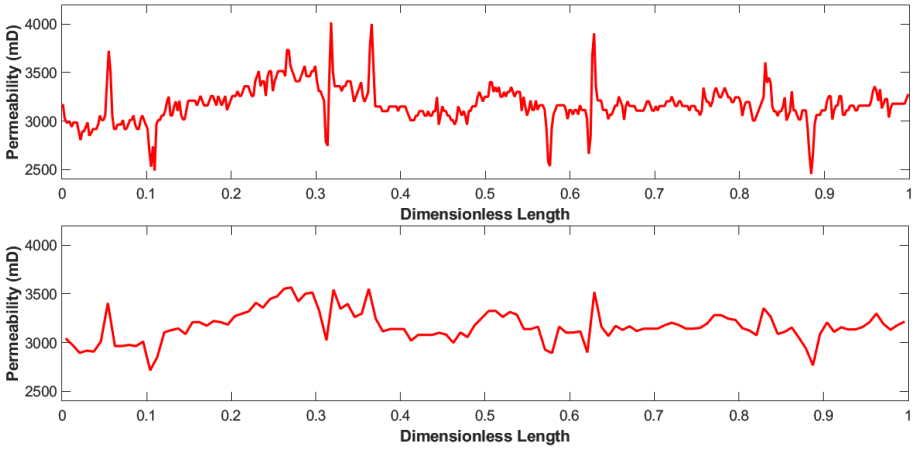

Figure D.3. Comparison between fine (upper) and coarse (lower) permeability distribution for experiment B0.

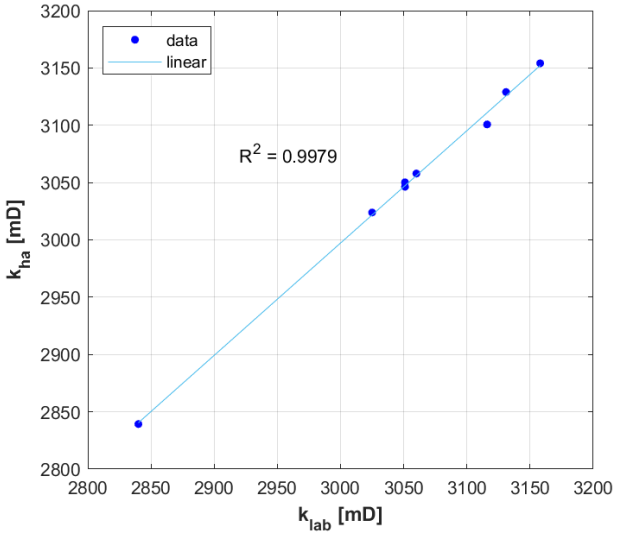

Figure D.4. Absolute permeability quality control for experiment B1.

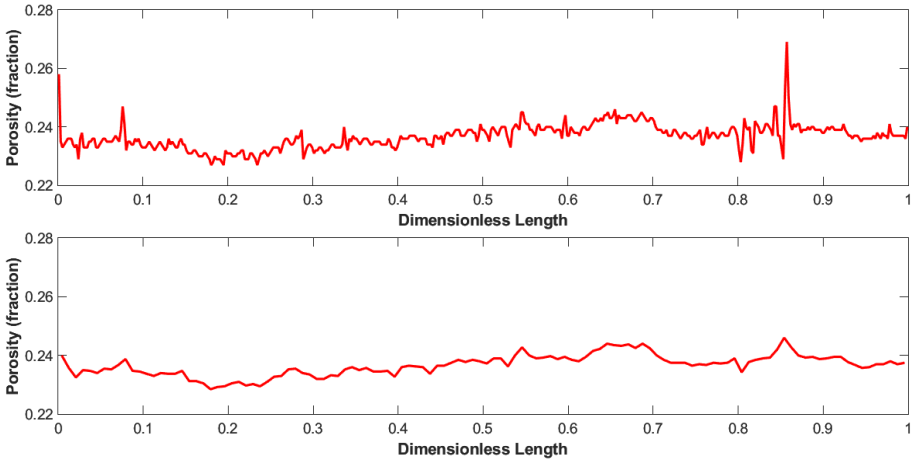

Figure D.5. Comparison between fine (upper) and coarse (lower) porosity distribution for experiment B1.

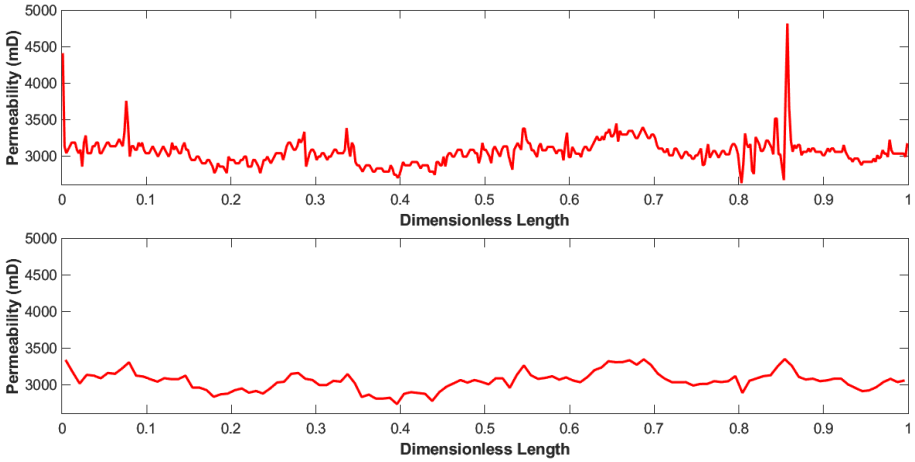

Figure D.6. Comparison between fine (upper) and coarse (lower) permeability distribution for experiment B1.

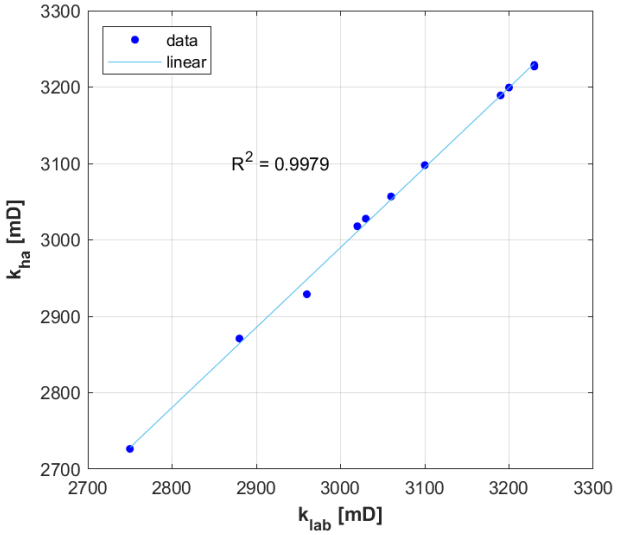

Figure D.7. Absolute permeability quality control for experiment B2.

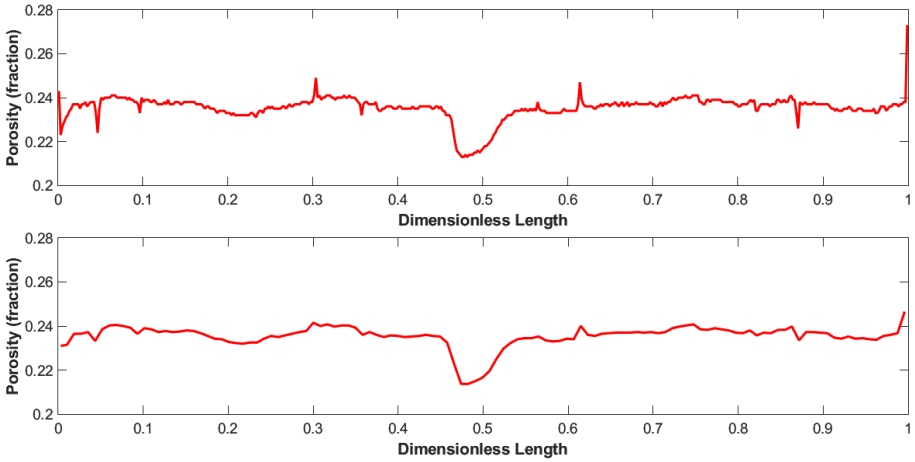

Figure D.8. Comparison between fine (upper) and coarse (lower) porosity distribution for experiment B2.

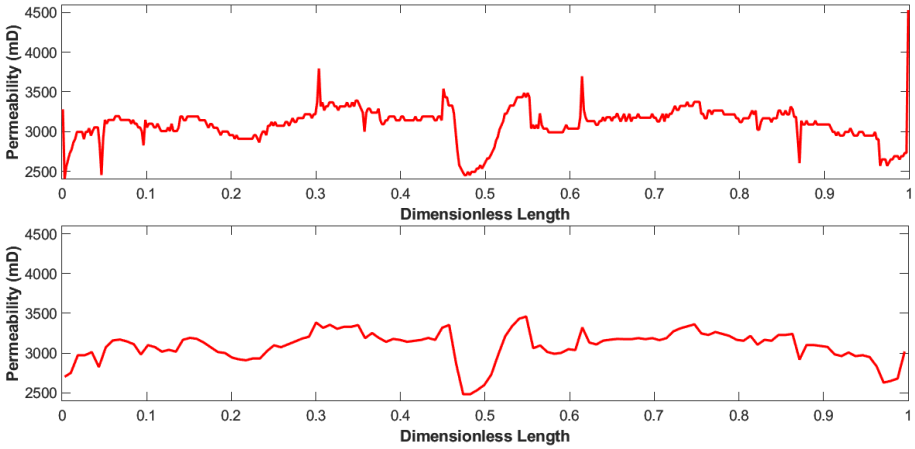

Figure D.9. Comparison between fine (upper) and coarse (lower) permeability distribution for experiment B2.

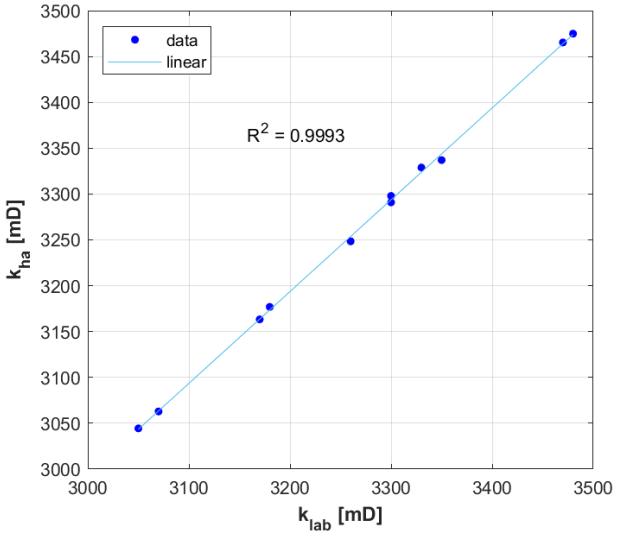

Figure D.10. Absolute permeability quality control for experiment B3.

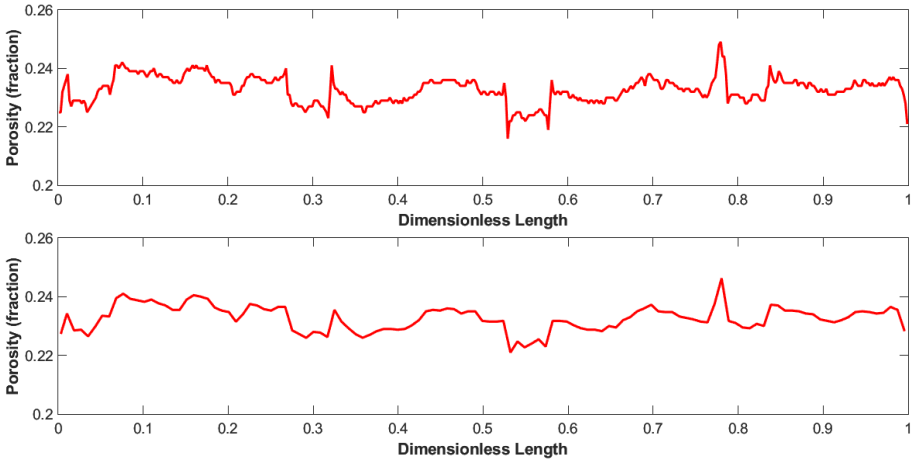

Figure D.11. Comparison between fine (upper) and coarse (lower) porosity distribution for experiment B3.

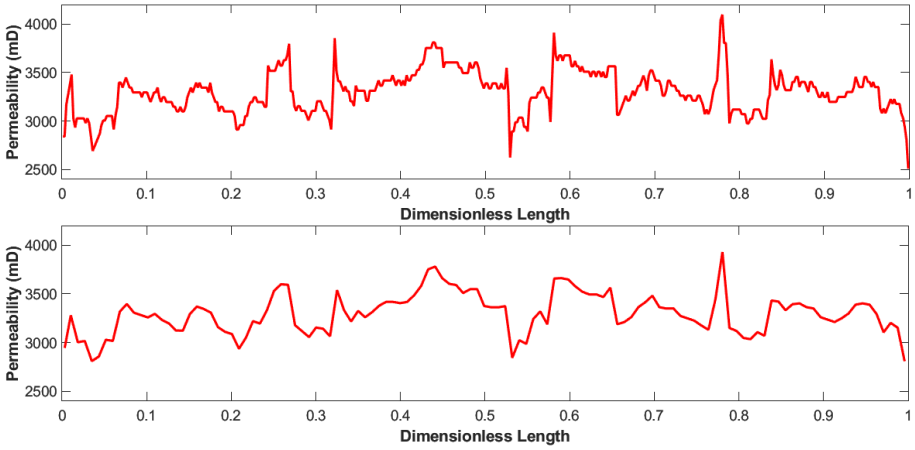

Figure D.12. Comparison between fine (upper) and coarse (lower) permeability distribution for experiment B3.

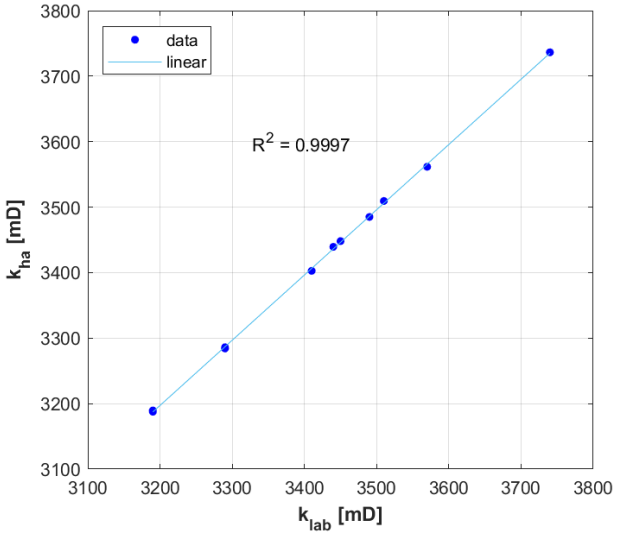

Figure D.13. Absolute permeability quality control for experiment B4.

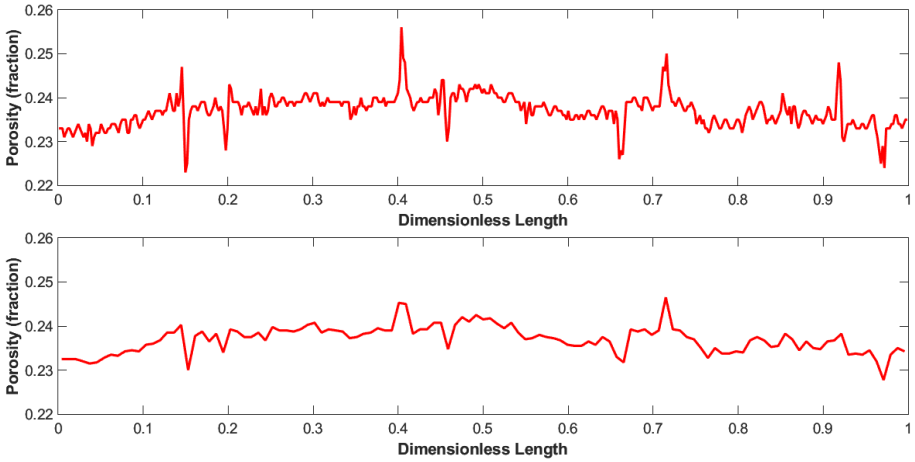

Figure D.14. Comparison between fine (upper) and coarse (lower) porosity distribution for experiment B4.

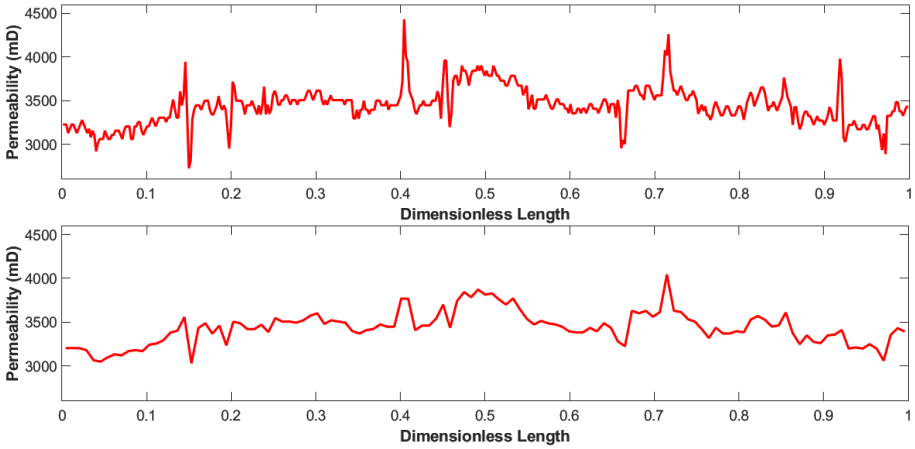

Figure D.15. Comparison between fine (upper) and coarse (lower) permeability distribution for experiment B4.

APPENDIX E Experiment A4 History Match Results

E.1 Primary Drainage and Forced Imbibition

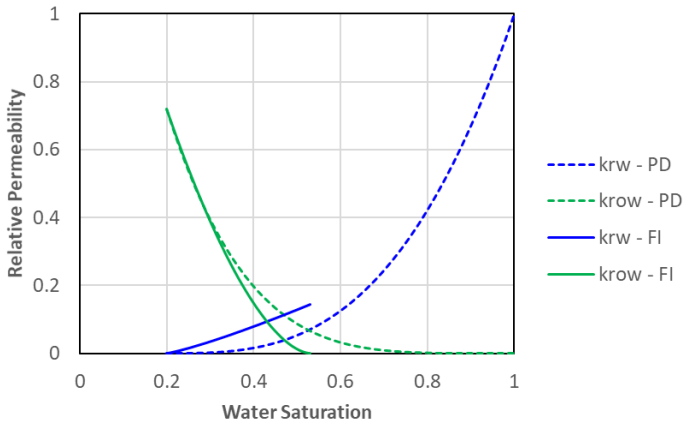

Figure E.1. Oil and water relative permeability curves for primary drainage (PD) and forced imbibition (FI), experiment A4.

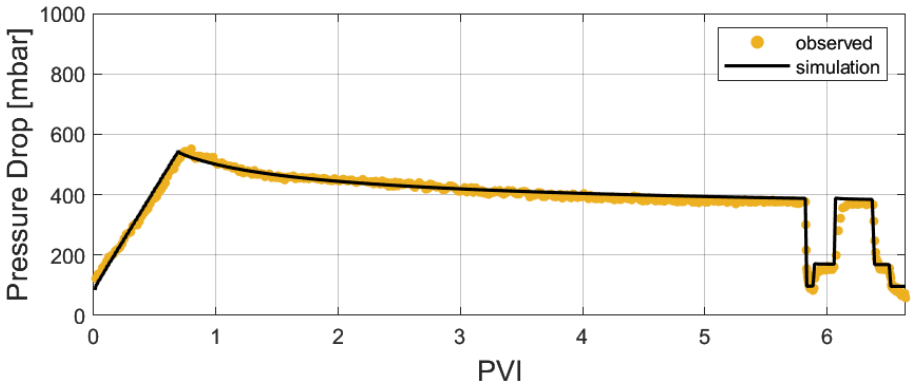

Figure E.2. Pressure drop match for primary drainage, experiment A4.

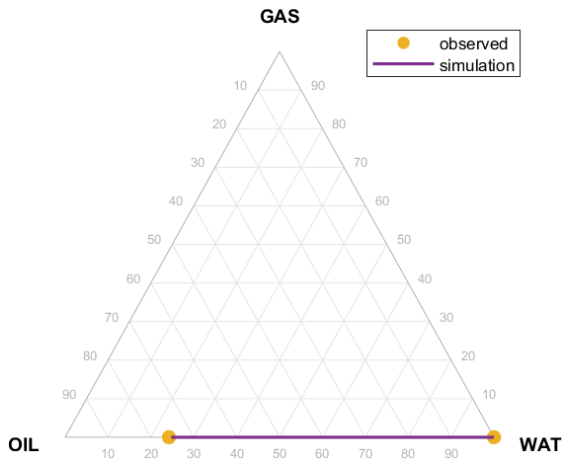

Figure E.3. Average saturation match for primary drainage, experiment A4.

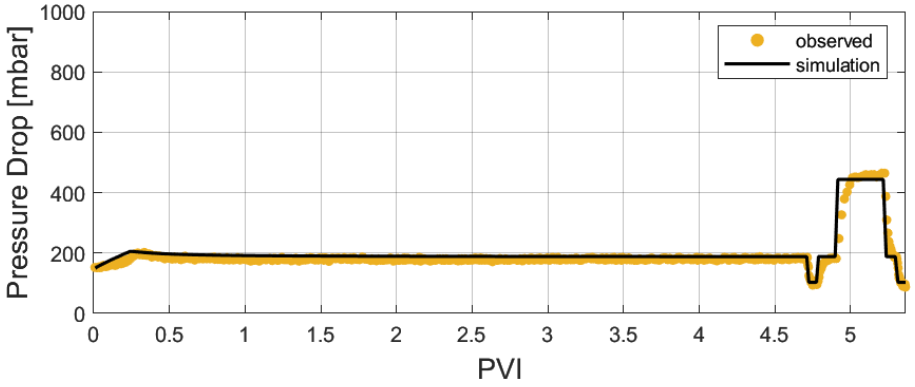

Figure E.4. Pressure drop match for forced imbibition, experiment A4.

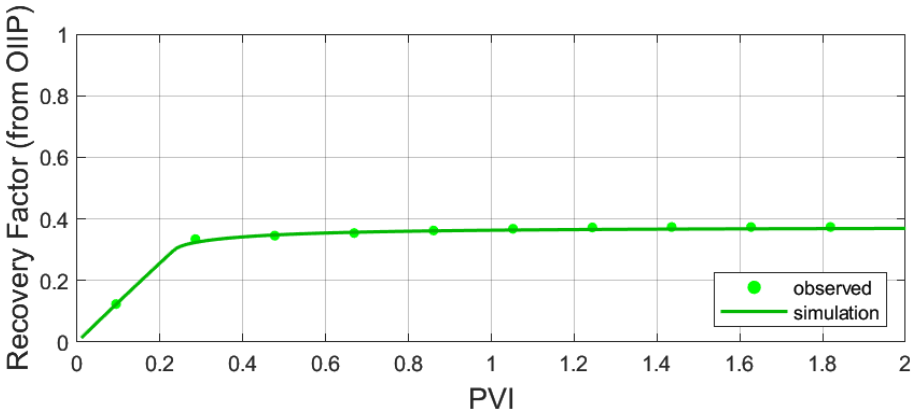

Figure E.5. Oil recovery factor (from OIIP) match for forced imbibition, experiment A4.

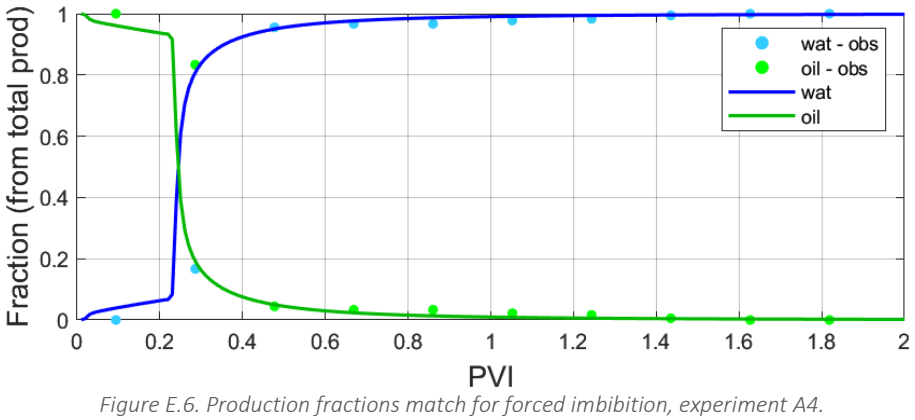

Figure E.6. Production fractions match for forced imbibition, experiment A4.

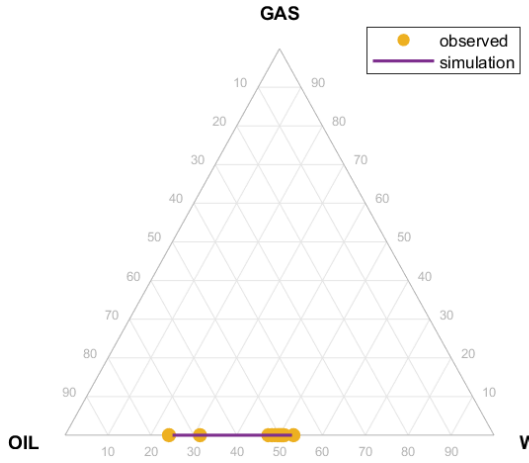

Figure E.7. Average saturation match for primary drainage, experiment A4.

E.2 Gas Flooding

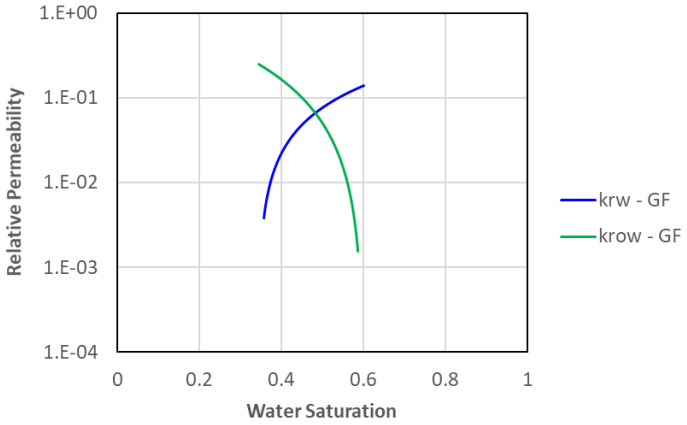

Figure E.8. Oil (to water) and water relative permeability curves for gas flooding (GF), experiment A4.

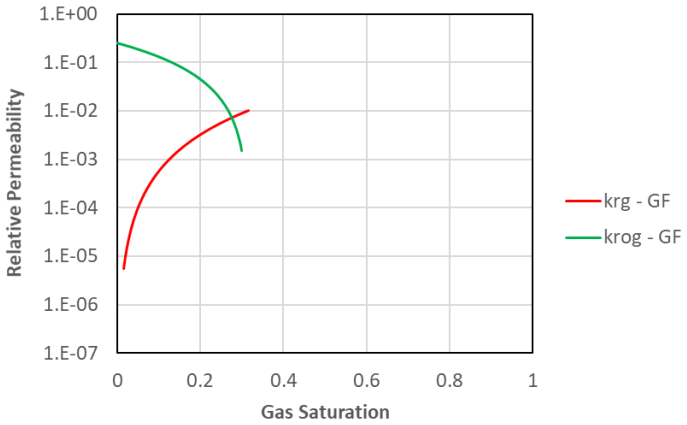

Figure E.9. Oil (to gas) and gas relative permeability curves for gas flooding (GF), experiment A4.

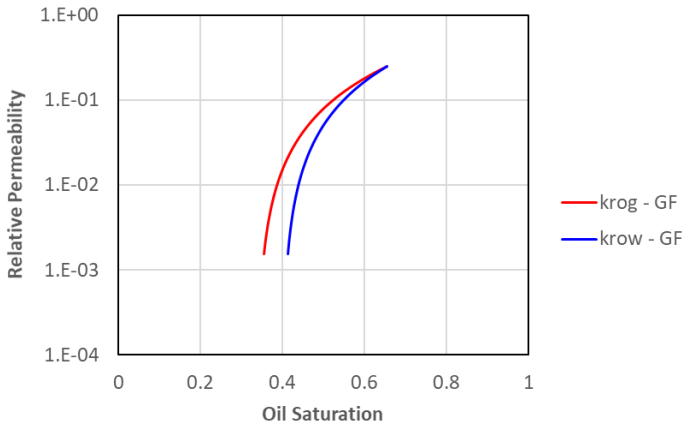

Figure E.10. Oil relative permeability curves (to gas and water) for gas flooding experiment A4.

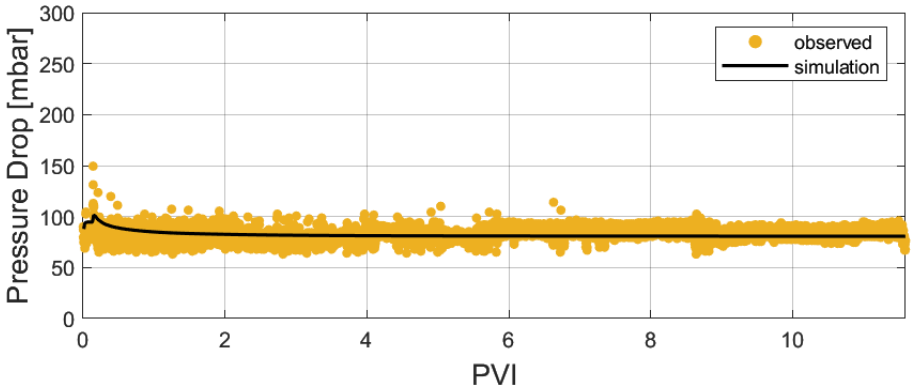

Figure E.11. Pressure drop match for gas flooding, experiment A4.

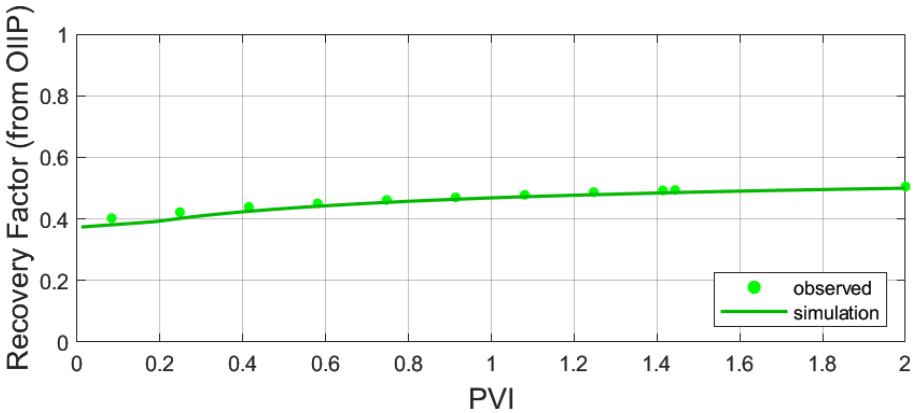

Figure E.12. Oil recovery factor (from OIIP) match for gas flooding, experiment A4.

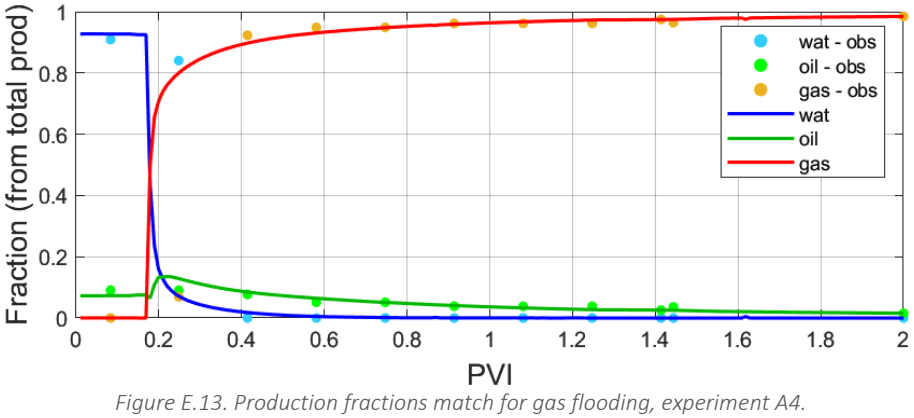

Figure E.13. Production fractions match for gas flooding, experiment A4.

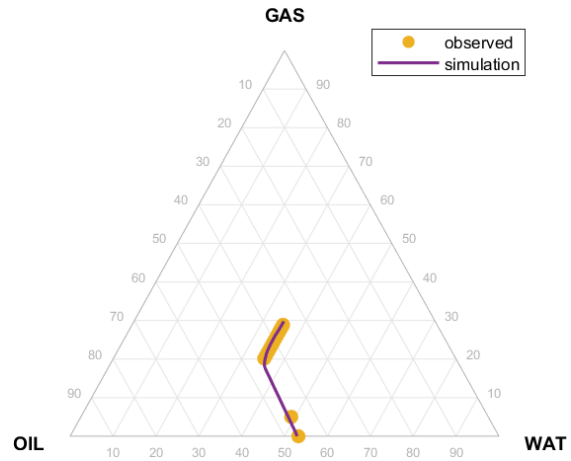

Figure E.14. Average saturation match for gas flooding, experiment A4.

APPENDIX F Experiment A5 History Match Results

F.1 Primary Drainage

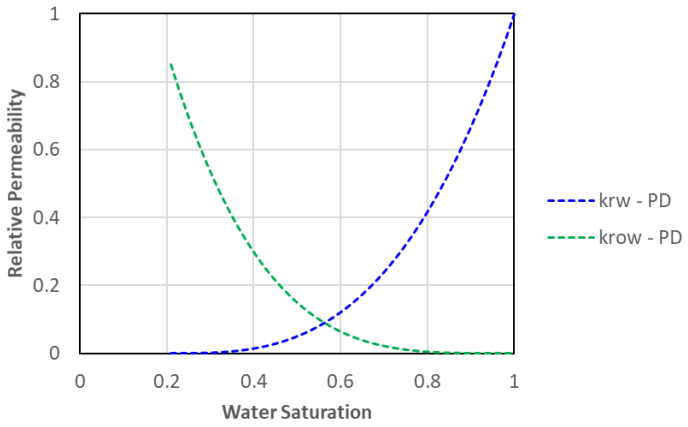

Figure F.1. Oil and water relative permeability curves for primary drainage (PD), experiment A5.

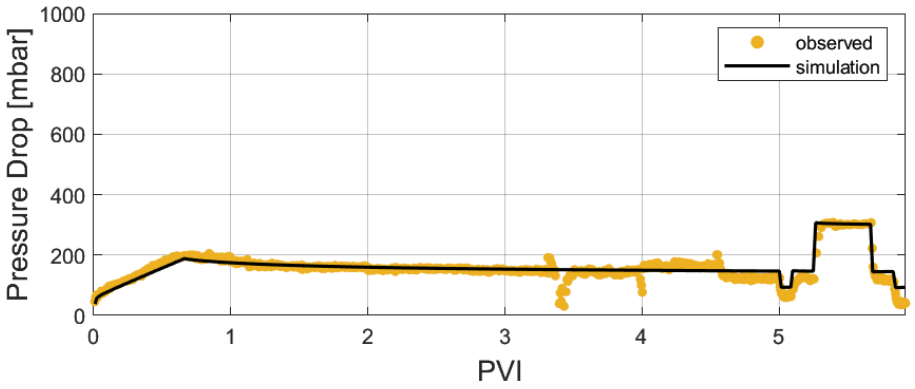

Figure F.2. Pressure drop match for primary drainage, experiment A5.

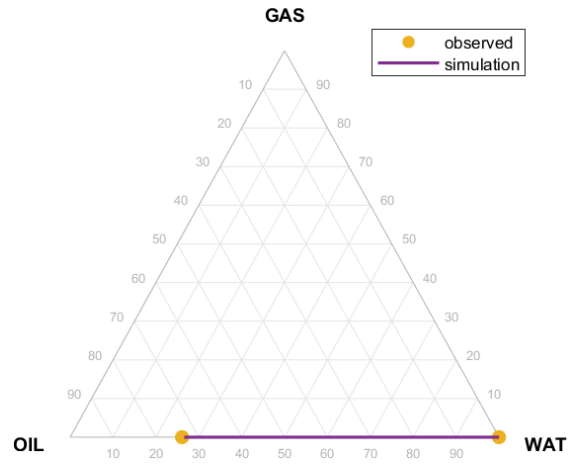

Figure F.3. Average saturation match for primary drainage, experiment A5.

F.2 First WAG Cycle

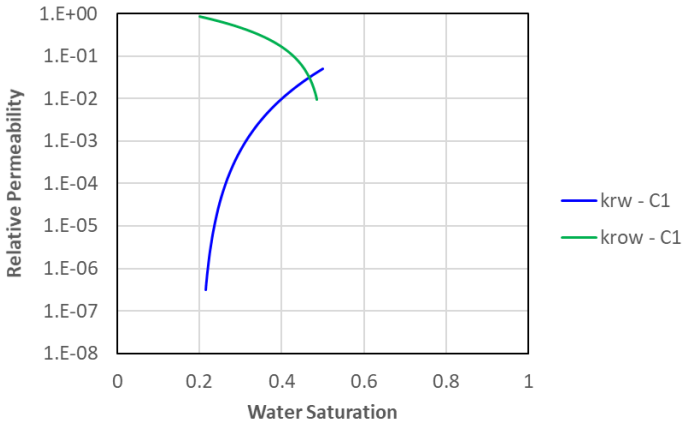

Figure F.4. Oil (to water) and water relative permeability curves for first WAG cycle (C1), experiment A5.

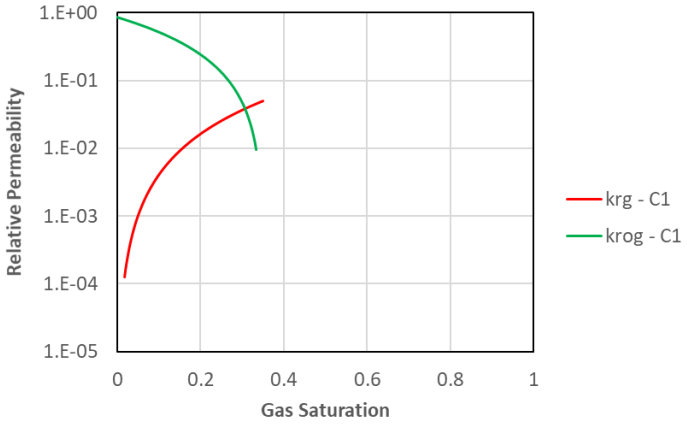

Figure F.5. Oil (to gas) and gas relative permeability curves for first WAG cycle (C1), experiment A5.

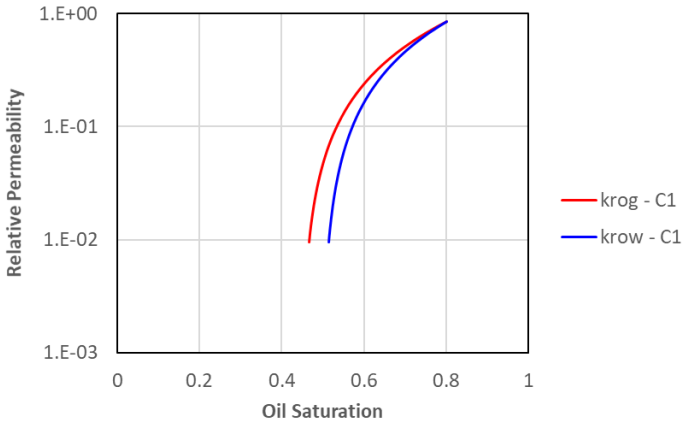

Figure F.6. Oil relative permeability curves (to gas and water) for first WAG cycle experiment A5.

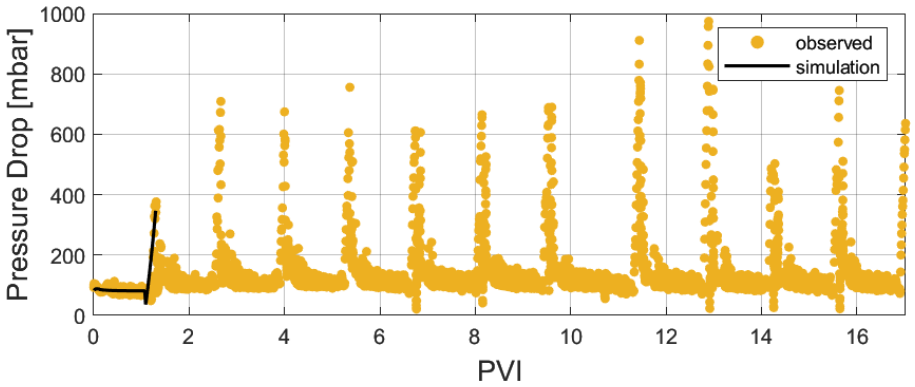

Figure F.7. Pressure drop match for first WAG cycle, experiment A5.

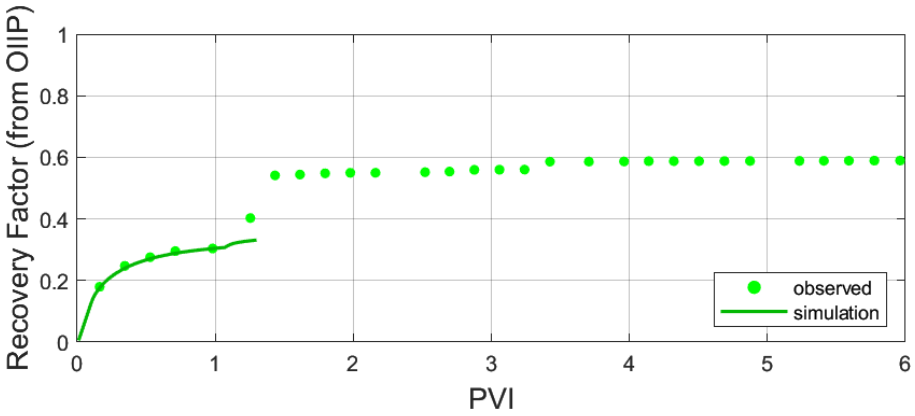

Figure F.8. Oil recovery factor (from OIIP) match for first WAG cycle, experiment A5.

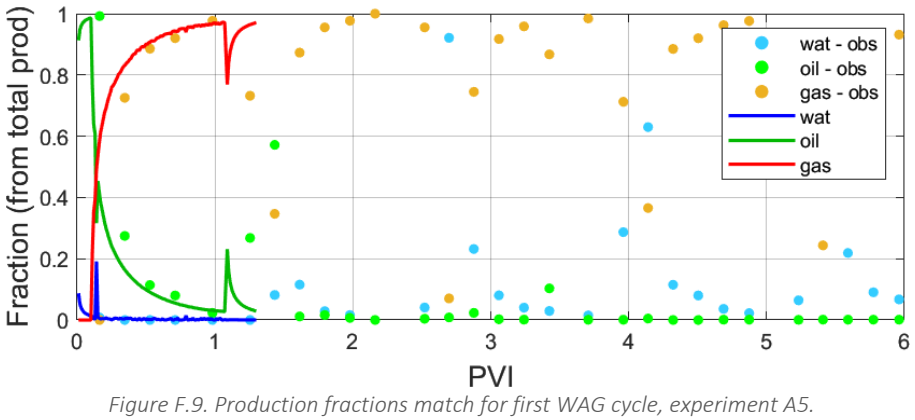

Figure F.9. Production fractions match for first WAG cycle, experiment A5.

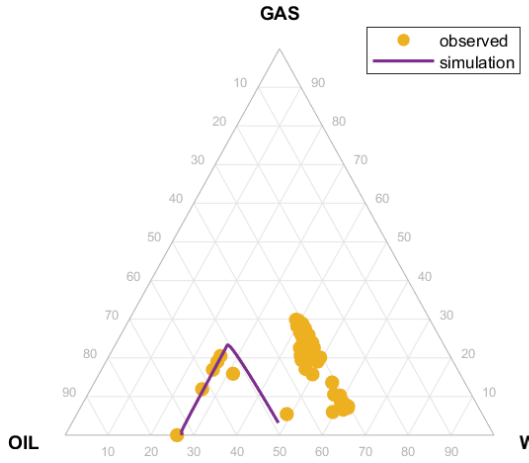

Figure F.10. Average saturation match for first WAG cycle, experiment A5.

F.3 Second WAG Cycle

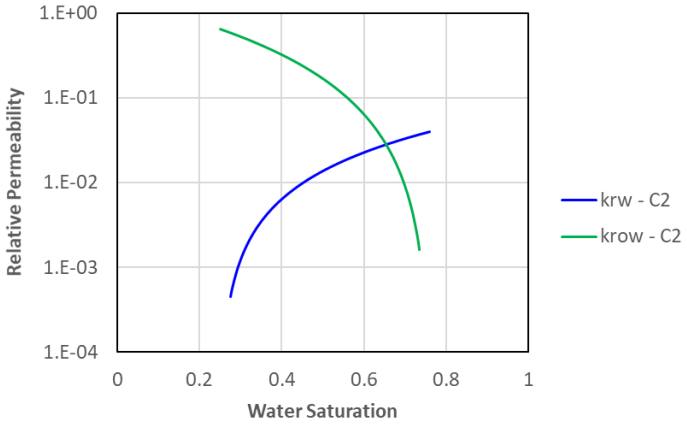

Figure F.11. Oil (to water) and water relative permeability curves for second WAG cycle (C2), experiment A5.

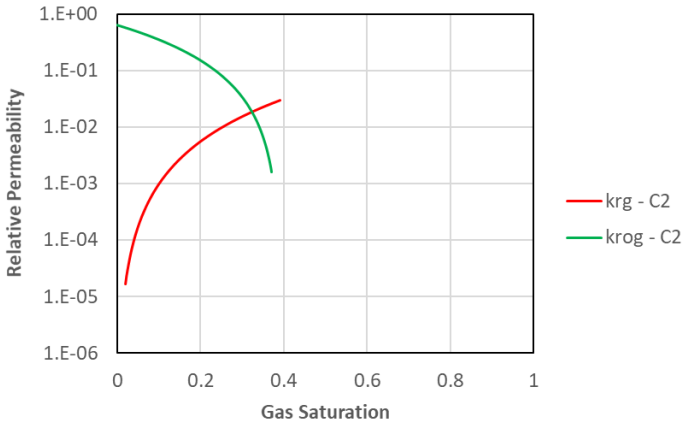

Figure F.12. Oil (to gas) and gas relative permeability curves for second WAG cycle (C2), experiment A5.

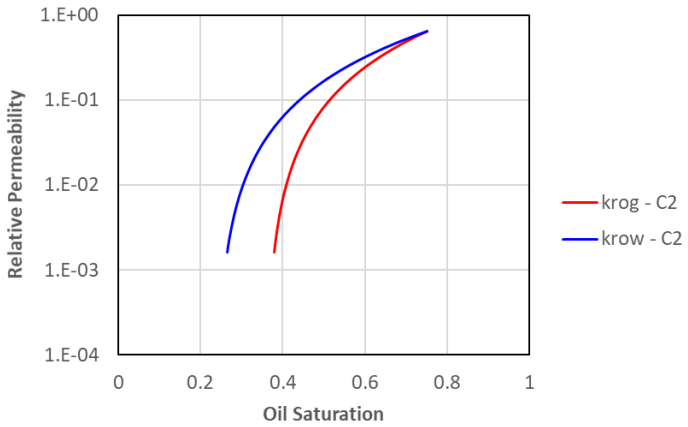

Figure F.13. Oil relative permeability curves (to gas and water) for second WAG cycle experiment A5.

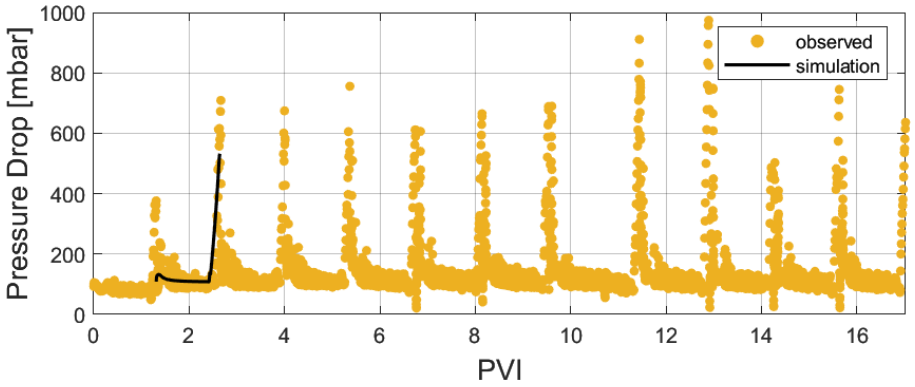

Figure F.14. Pressure drop match for second WAG cycle, experiment A5.

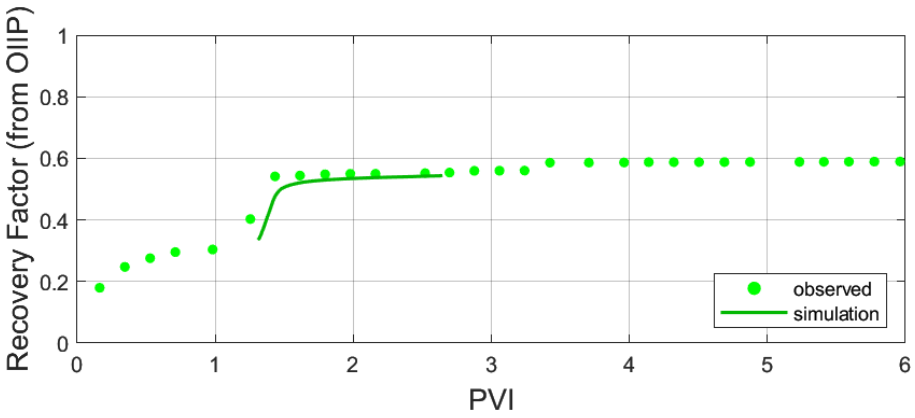

Figure F.15. Oil recovery factor (from OIIP) match for second WAG cycle, experiment A5.

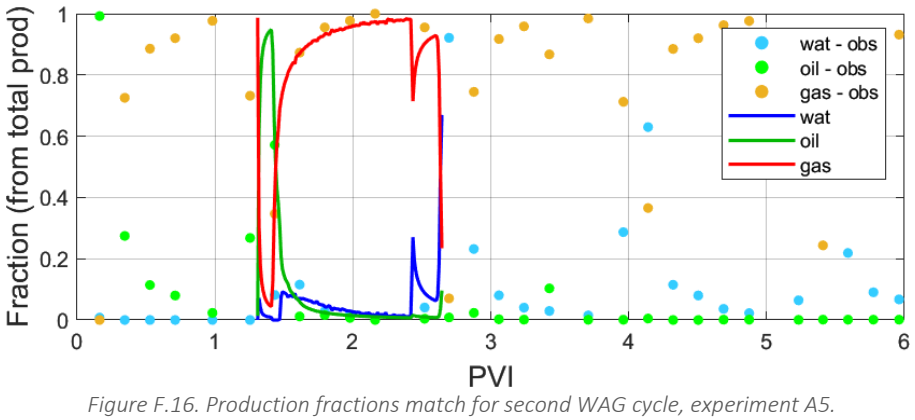

Figure F.16. Production fractions match for second WAG cycle, experiment A5.

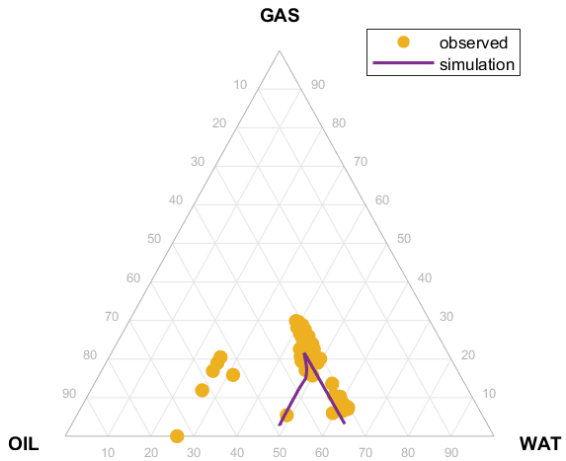

Figure F.17. Average saturation match for second WAG cycle, experiment A5.

F.4 Subsequent WAG Cycles

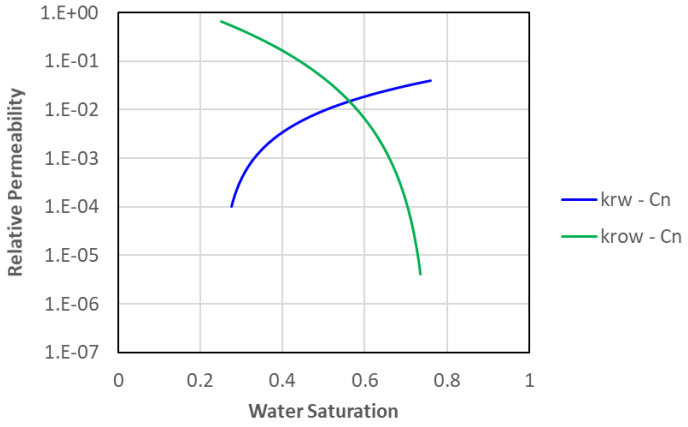

Figure F.18. Oil (to water) and water relative permeability curves for subsequent WAG cycles (Cn), experiment A5.

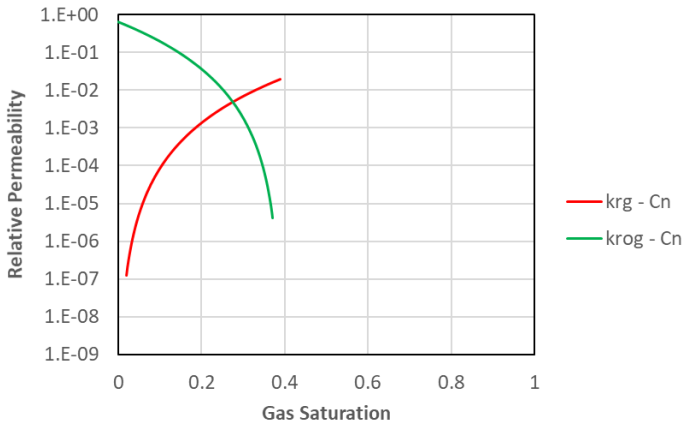

Figure F.19. Oil (to gas) and gas relative permeability curves for subsequent WAG cycles (Cn), experiment A5.

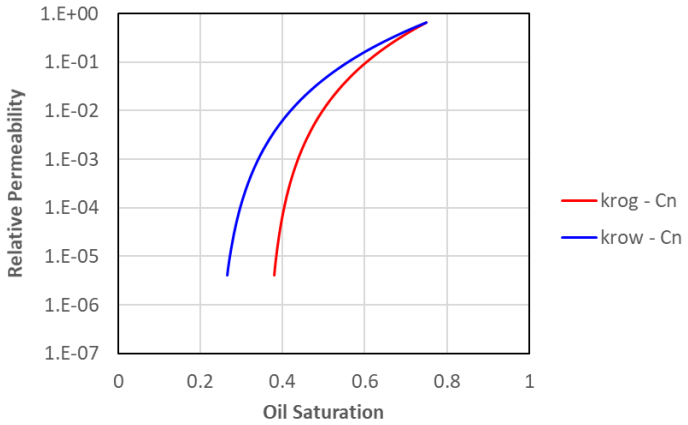

Figure F.20. Oil relative permeability curves (to gas and water) for subsequent WAG cycles experiment A5.

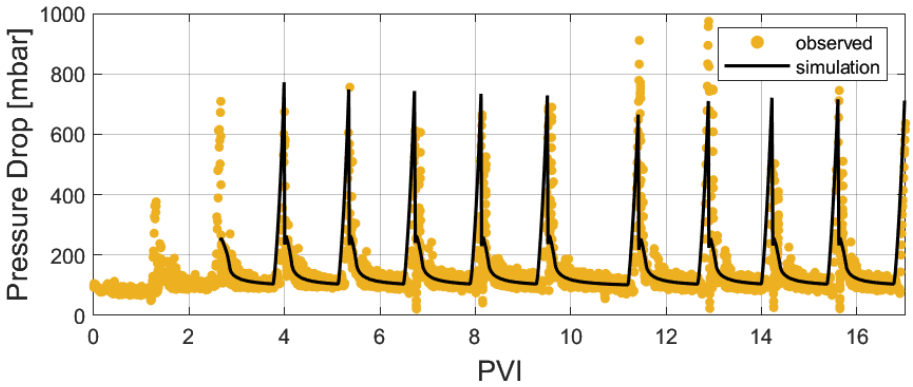

Figure F.21. Pressure drop match for subsequent WAG cycles, experiment A5.

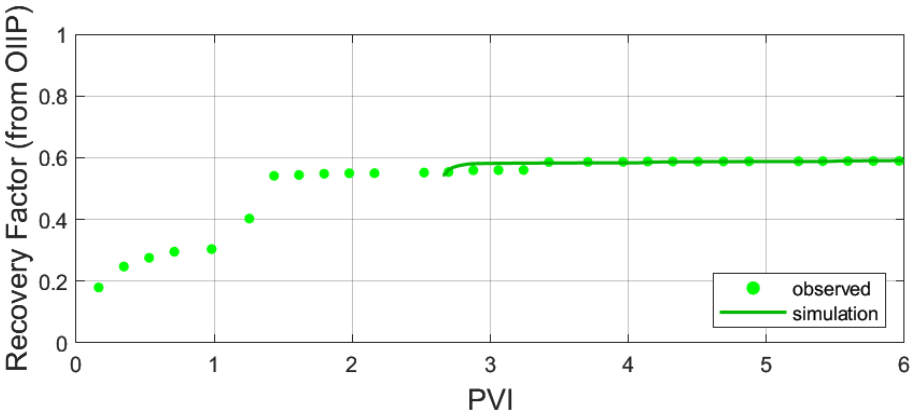

Figure F.22. Oil recovery factor (from OIIP) match for subsequent WAG cycle, experiment A5.

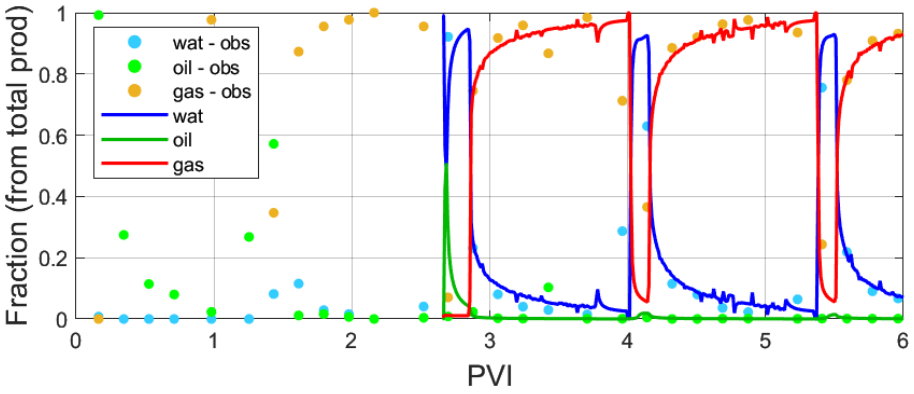

Figure F.23. Production fractions match for subsequent WAG cycles, experiment A5.

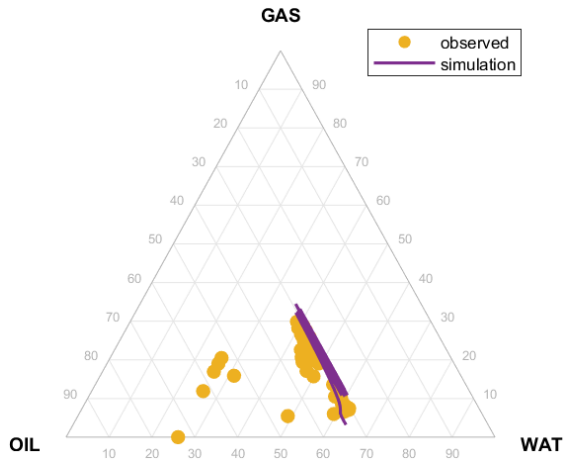

Figure F.24. Average saturation match for subsequent WAG cycles, experiment A5.

APPENDIX G Experiment B0 History Match Results

G.1 Primary Drainage and Forced Imbibition

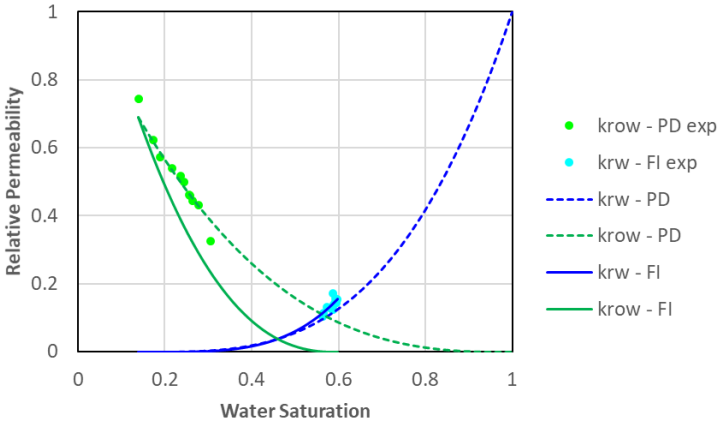

Figure G.1. Oil and water relative permeability curves for primary drainage (PD) and forced imbibition (FI), experiment B0.

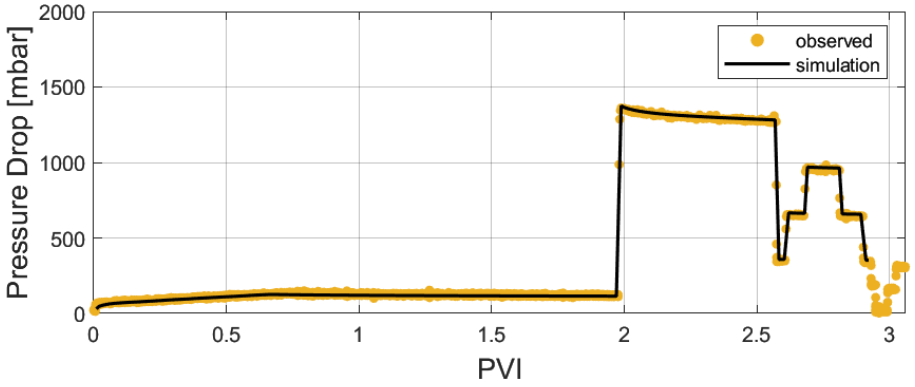

Figure G.2. Pressure drop match for primary drainage, experiment B0.

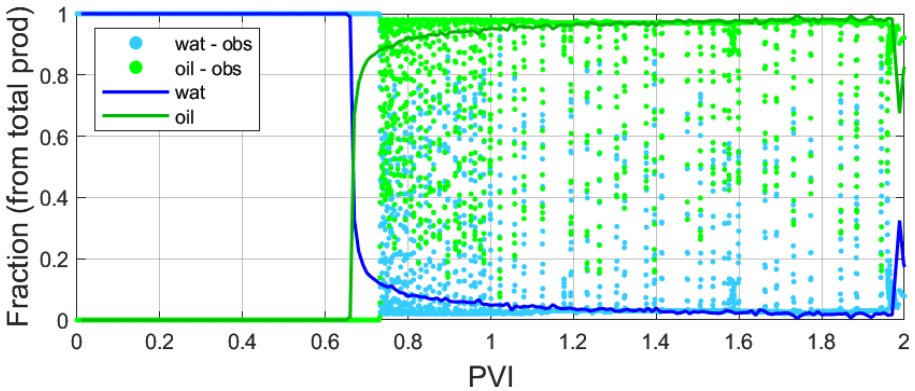

Figure G.3. Oil breakthrough match for primary drainage (Coriolis data), experiment B0.

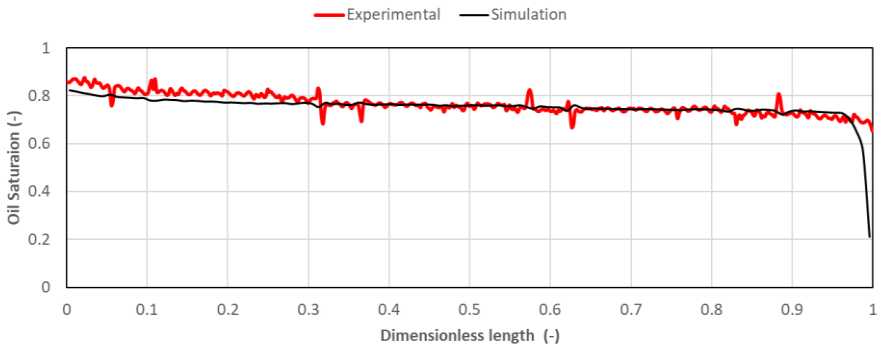

Figure G.4. Oil saturation match at the end of primary drainage, experiment B0.

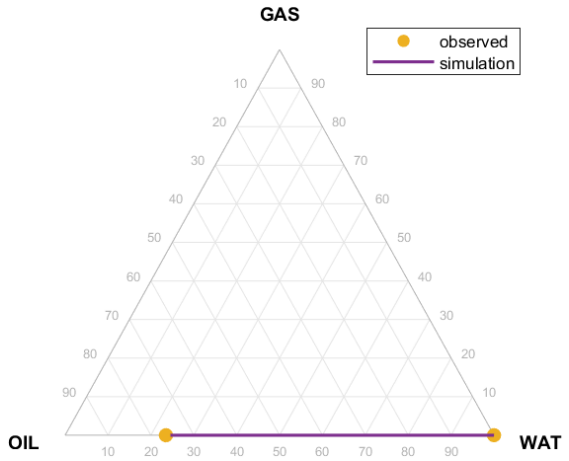

Figure G.5. Average saturation match for primary drainage, experiment B0.

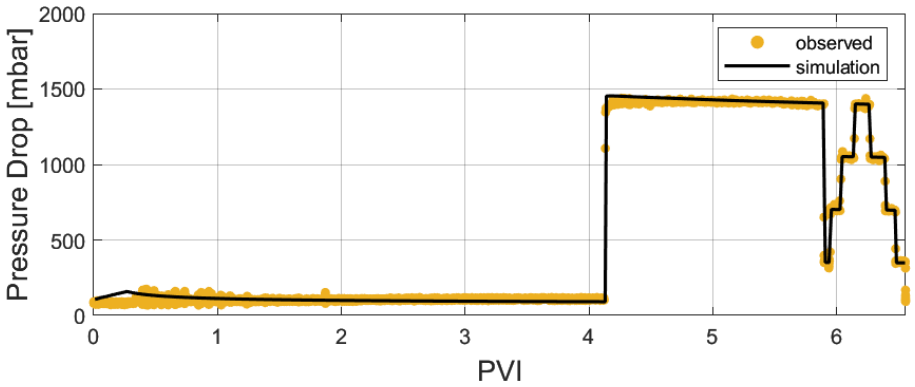

Figure G.6. Pressure drop match for forced imbibition, experiment B0.

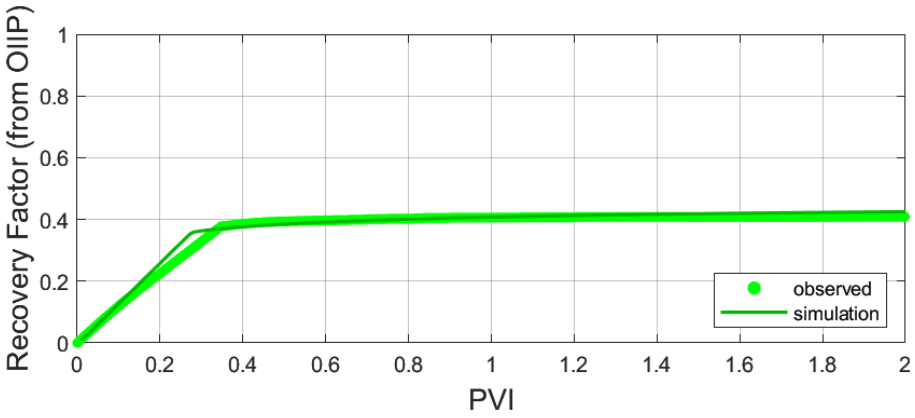

Figure G.7. Oil recovery factor (from OIIP) match for forced imbibition, experiment B0.

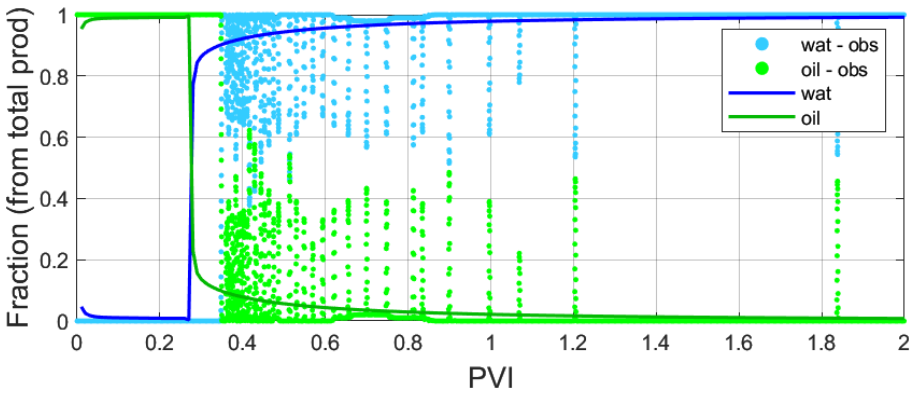

Figure G.8. Water breakthrough match for forced imbibition (Coriolis data), experiment B0.

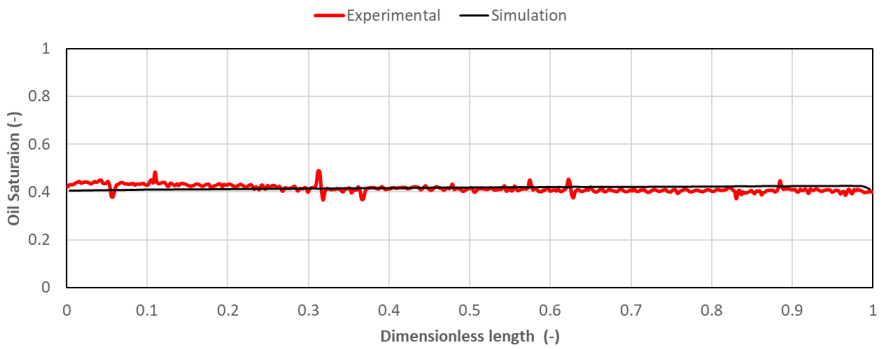

Figure G.9. Oil saturation match at the end of forced imbibition, experiment B0.

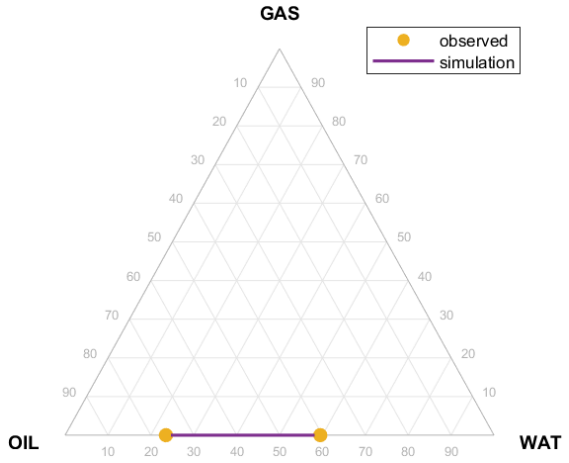

Figure G.10. Average saturation match for primary drainage, experiment B1.

G.2 Surfactant Flooding

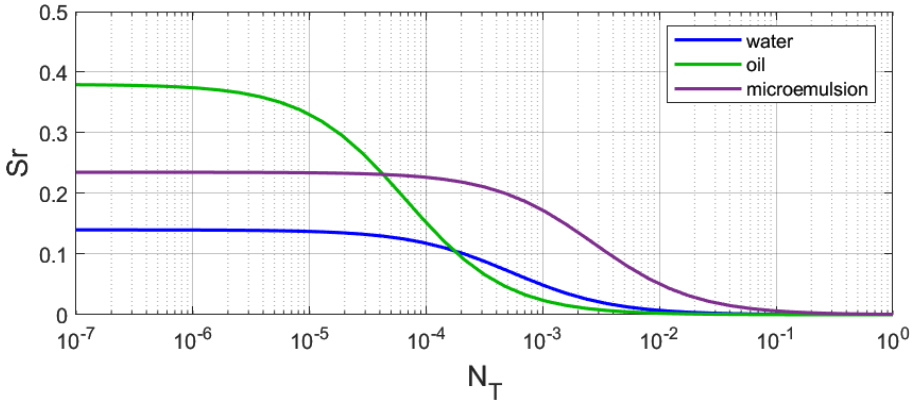

Figure G.11. Capillary Desaturation Curve (CDC) for surfactant flooding, experiment B0.

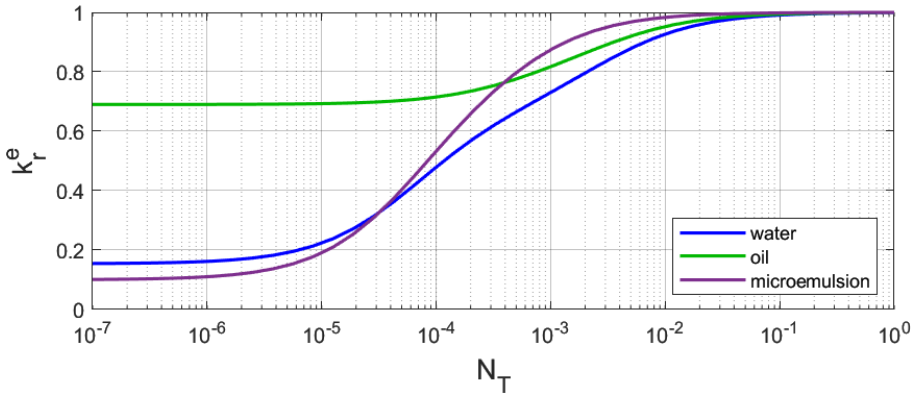

Figure G.12. End-point relative permeability as a function of trapping number for surfactant flooding, experiment B0.

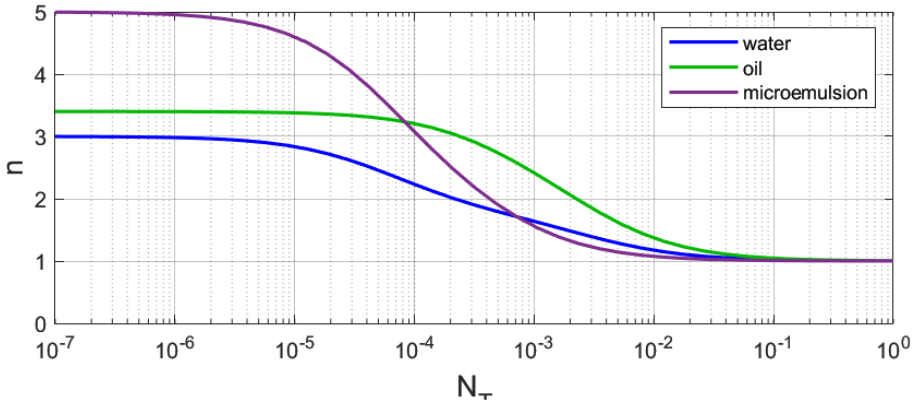

Figure G.13. Shape coefficients as a function of trapping number for surfactant flooding, experiment B0.

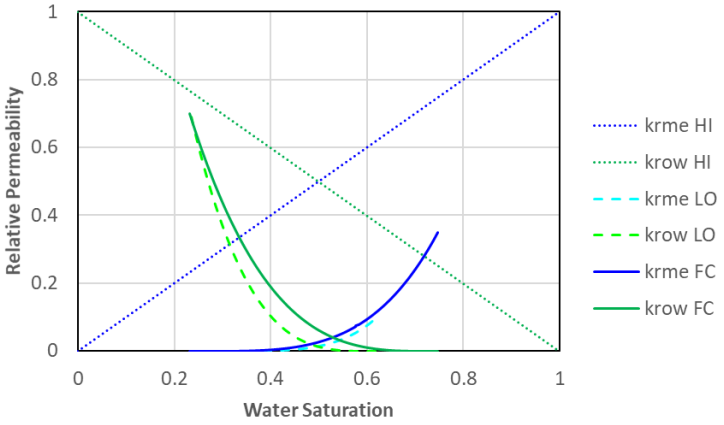

Figure G.14. Oil and water relative permeability curves for surfactant flooding at high (HI) and low (LO) trapping numbers, and final conditions (FC), experiment B0.

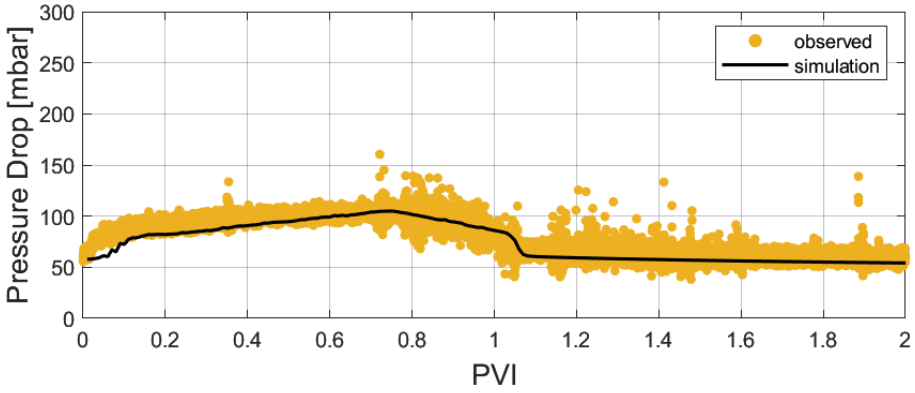

Figure G.15. Pressure drop match for surfactant slug, experiment B0.

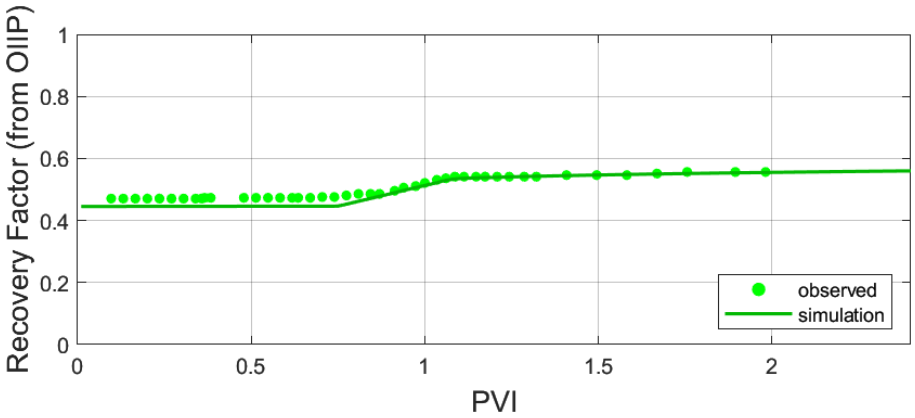

Figure G.16. Oil recovery factor (from OIIP) match for surfactant flooding, experiment B0.

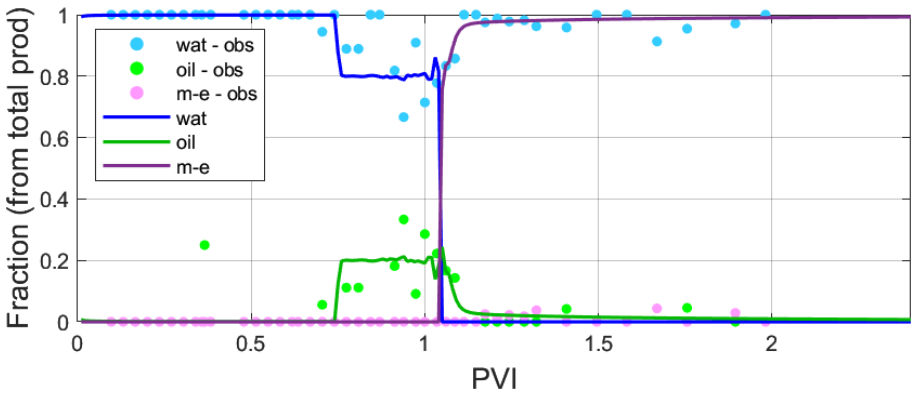

Figure G.17. Production fractions match for surfactant flooding, experiment B0.

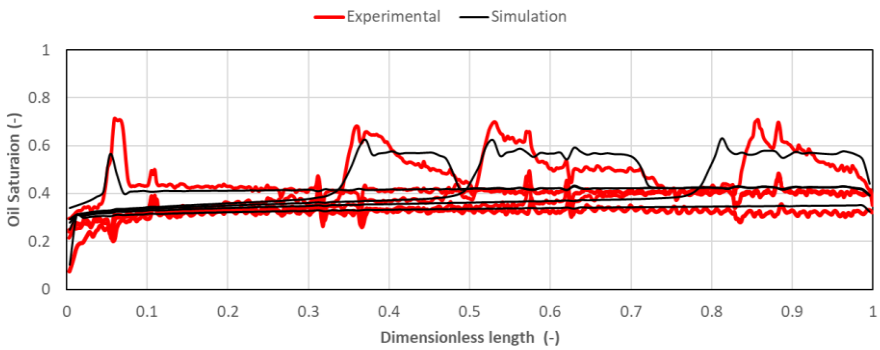

Figure G.18. Oil saturation match at several PVI during surfactant flooding, experiment B0.

APPENDIX H Experiment B1 History Match Results

H.1 Primary Drainage and Forced Imbibition

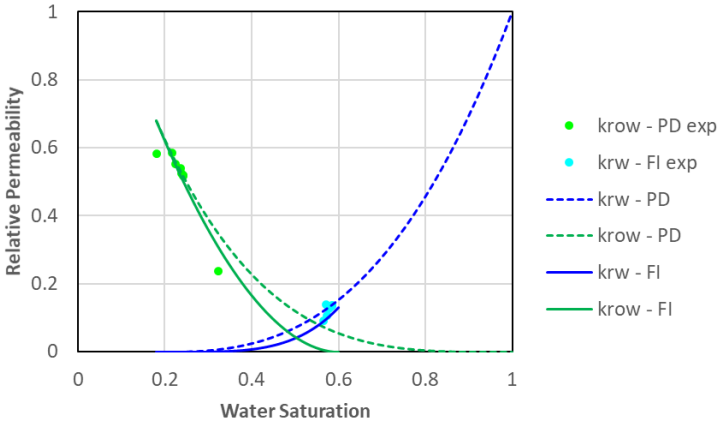

Figure H.1. Oil and water relative permeability curves for primary drainage (PD) and forced imbibition (FI), experiment B1.

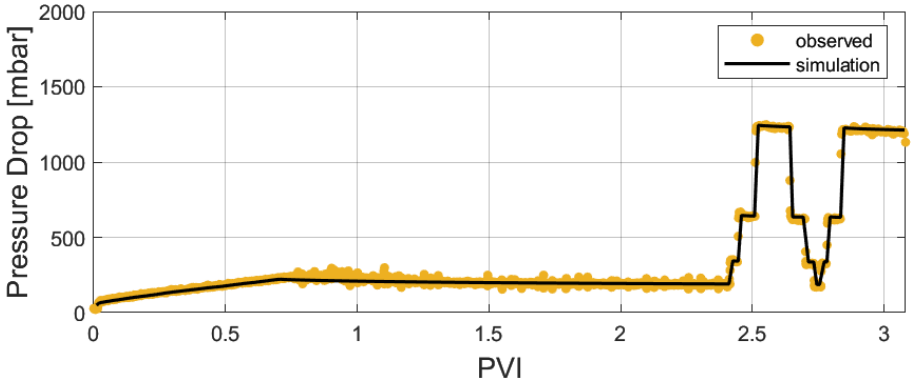

Figure H.2. Pressure drop match for primary drainage, experiment B1.

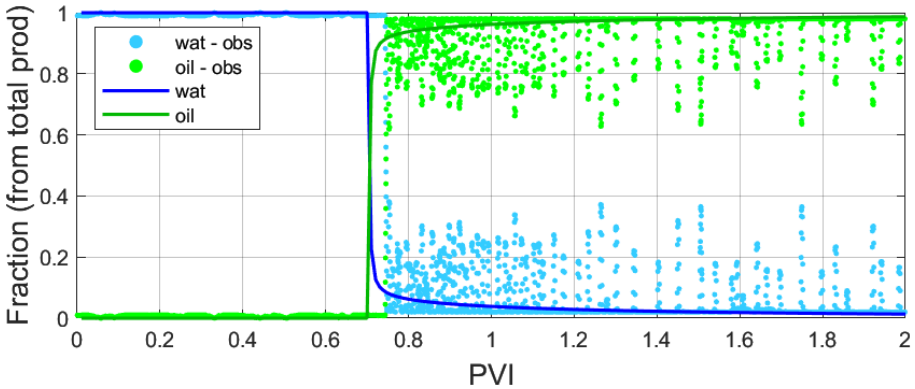

Figure H.3. Oil breakthrough match for primary drainage (Coriolis data), experiment B1.

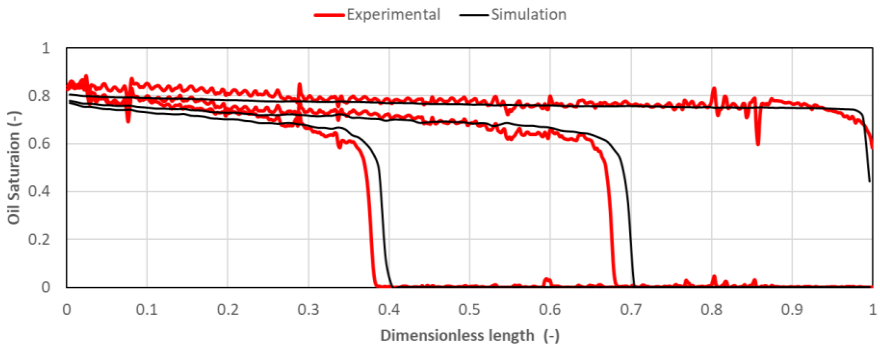

Figure H.4. Oil saturation match at several PVI during primary drainage, experiment B1.

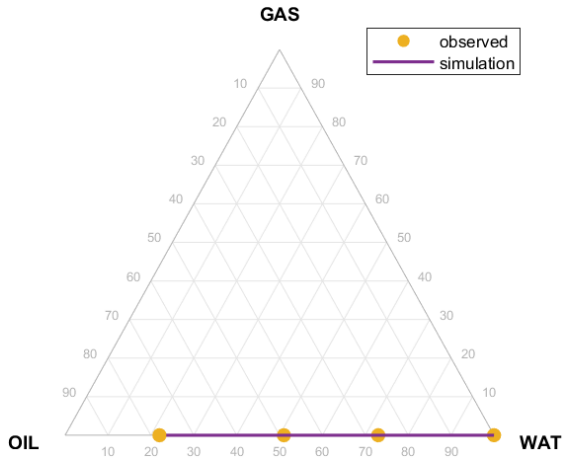

Figure H.5. Average saturation match for primary drainage, experiment B1.

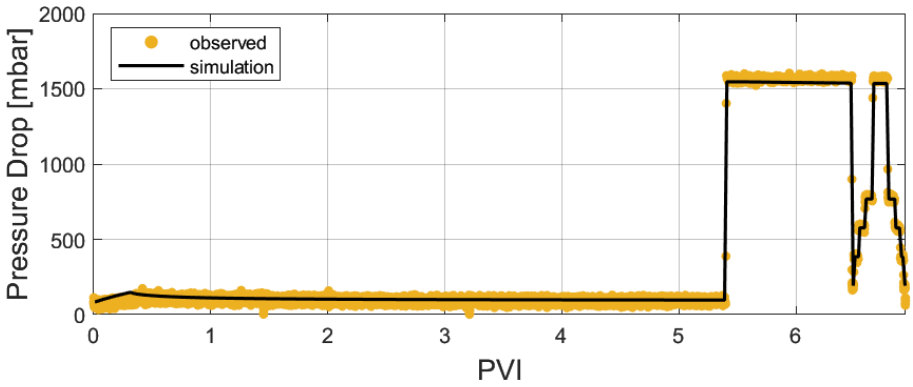

Figure H.6. Pressure drop match for forced imbibition with 4 wt% NaCl brine, experiment B1.

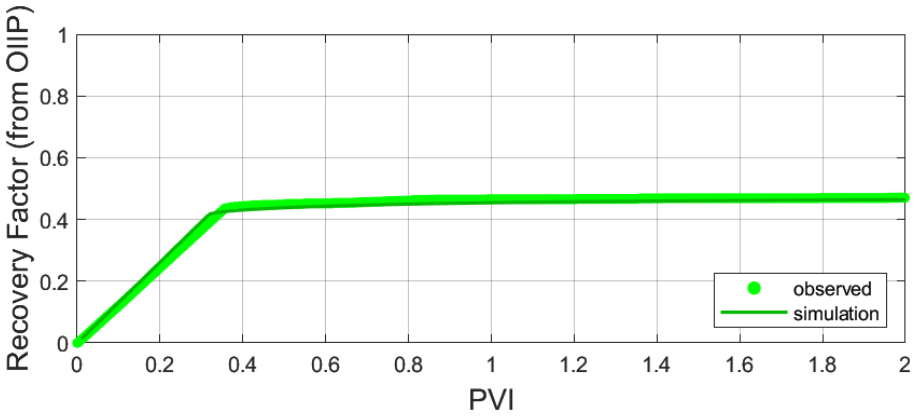

Figure H.7. Oil recovery factor (from OIIP) match for forced imbibition, experiment B1.

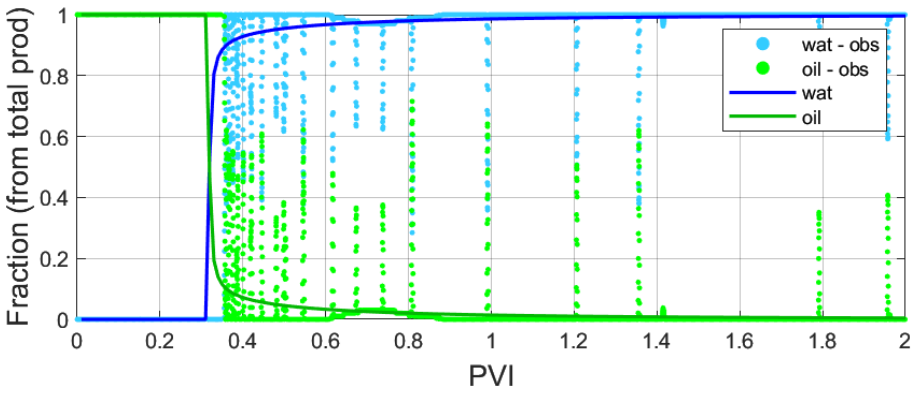

Figure H.8. Water breakthrough match for forced imbibition (Coriolis data), experiment B1.

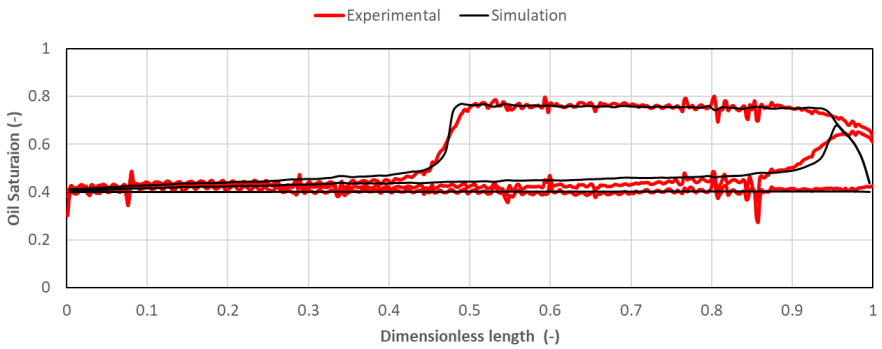

Figure H.9. Oil saturation match at several PVI during forced imbibition, experiment B1.

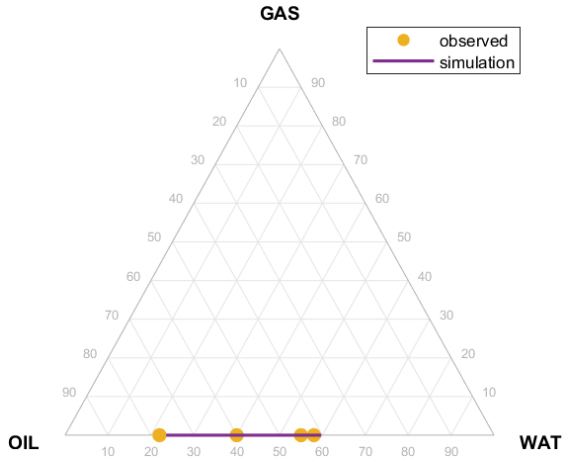

Figure H.10. Average saturation match for primary drainage, experiment B1.

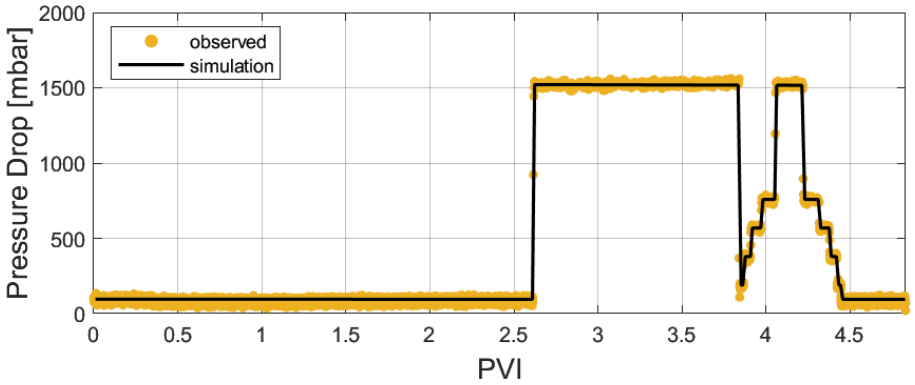

Figure H.11. Pressure drop match for forced imbibition with 2 wt% NaCl brine, experiment B1.

H.2 Surfactant Slug

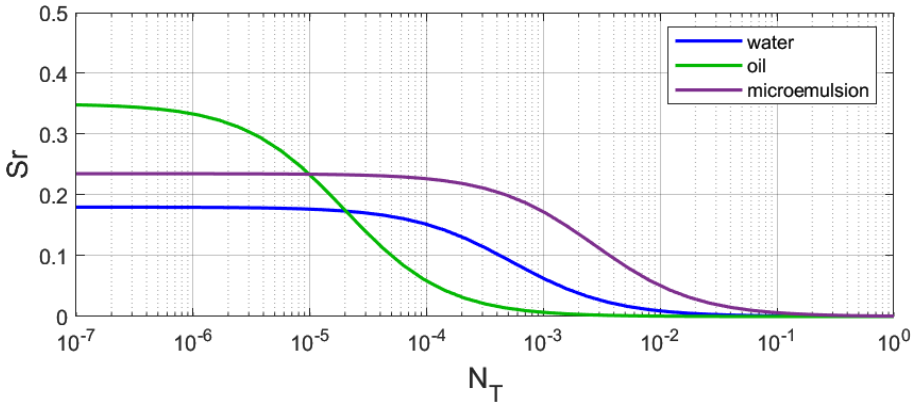

Figure H.12. Capillary Desaturation Curve (CDC) for surfactant slug, experiment B1.

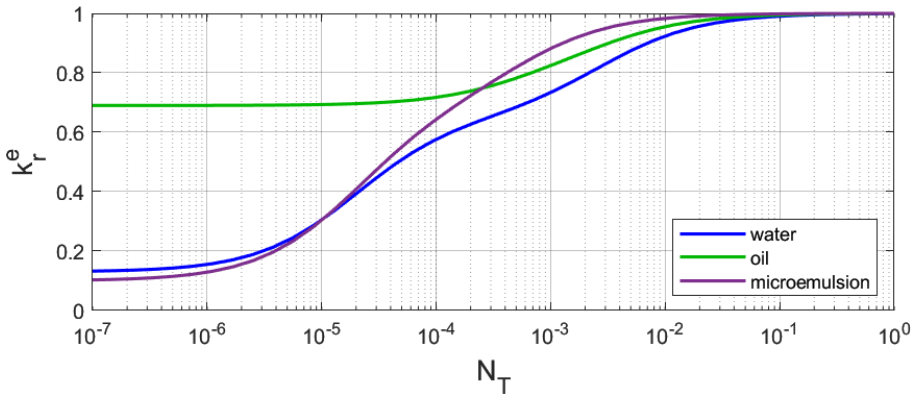

Figure H.13. End-point relative permeability as a function of trapping number for surfactant slug, experiment B1.

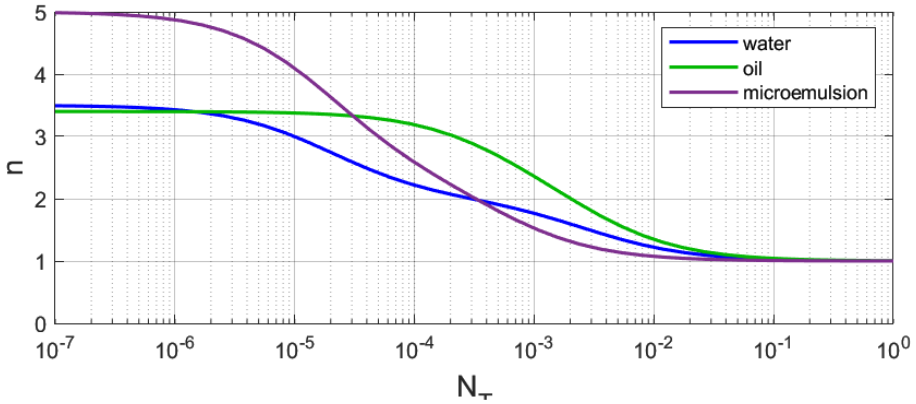

Figure H.14. Shape coefficients as a function of trapping number for surfactant slug, experiment B1.

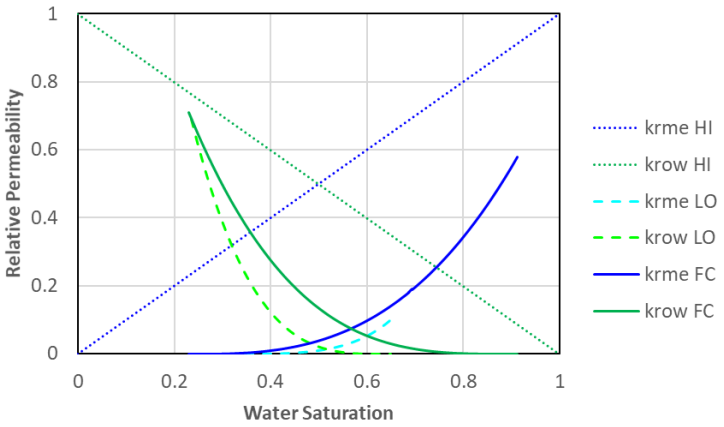

Figure H.15. Oil and water relative permeability curves for surfactant flooding at high (HI) and low (LO) trapping numbers, and final conditions (FC), experiment B1.

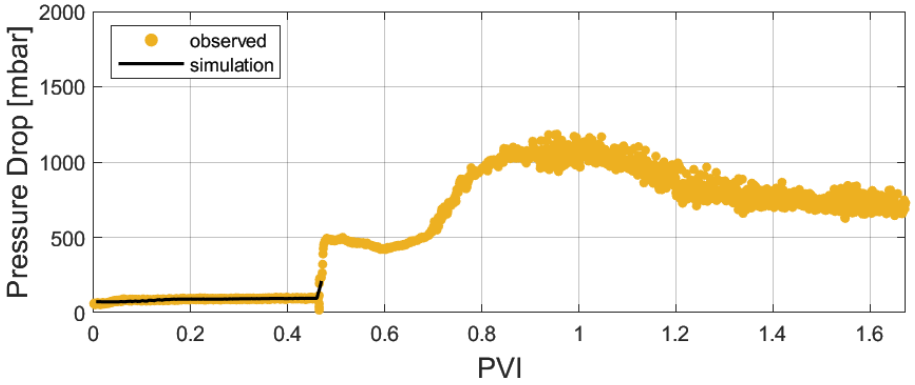

Figure H.16. Pressure drop match for surfactant slug, experiment B1.

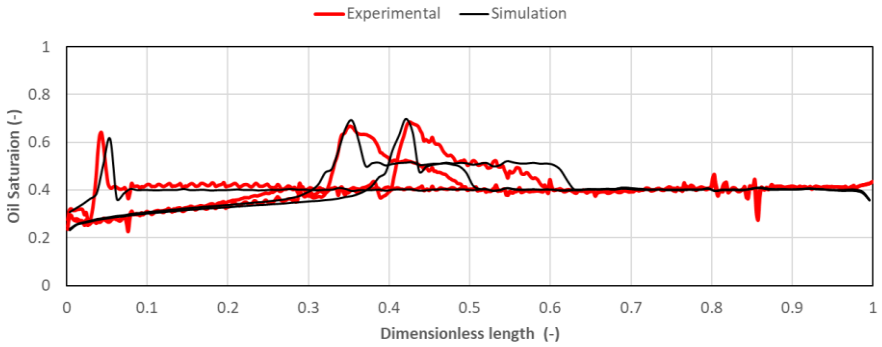

Figure H.17. Oil saturation match at several PVI during surfactant slug, experiment B1.

H.3 Foam Drive

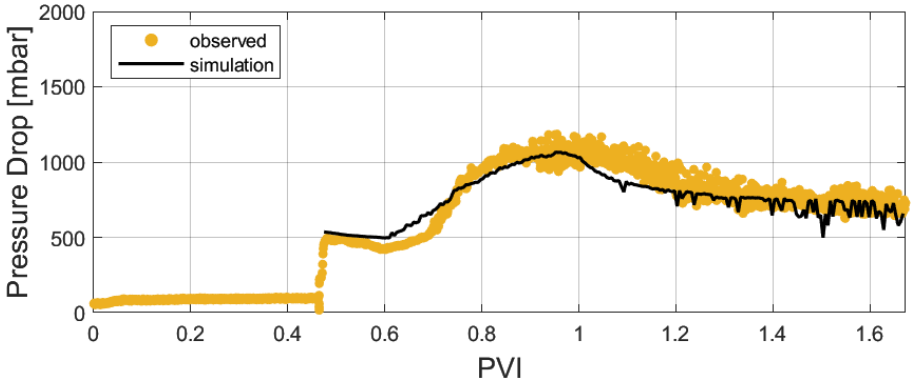

Figure H.18. Pressure drop match for FACF, experiment B1.

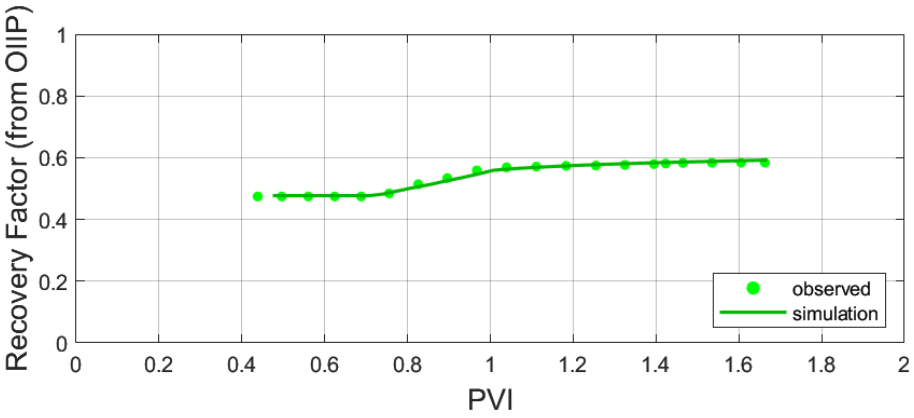

Figure H.19. Oil recovery factor (from OIIP) match for FACF, experiment B1.

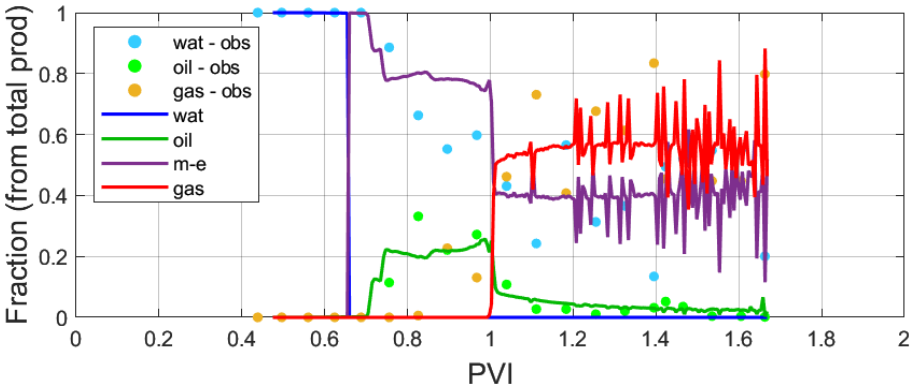

Figure H.20. Production fractions match for FACF, experiment B1.

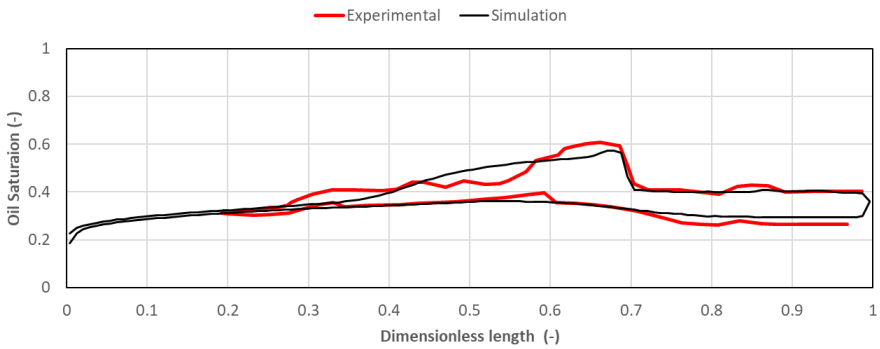

Figure H.21. Oil saturation match at several PVI during FACF, experiment B1.

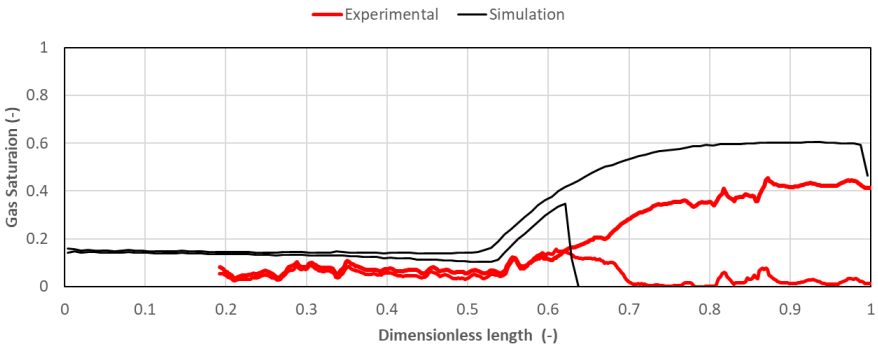

Figure H.22. Gas saturation match at several PVI during FACF, experiment B1.

APPENDIX I Experiment B2 History Match Results

I.1 Primary Drainage and Forced Imbibition

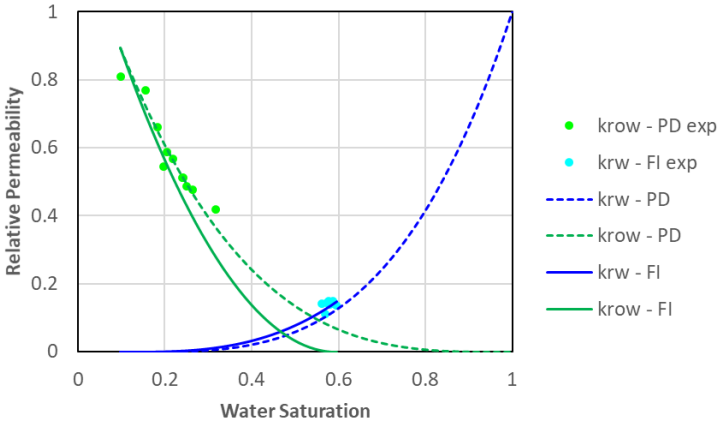

Figure I.1. Oil and water relative permeability curves for primary drainage (PD) and forced imbibition (FI), experiment B2.

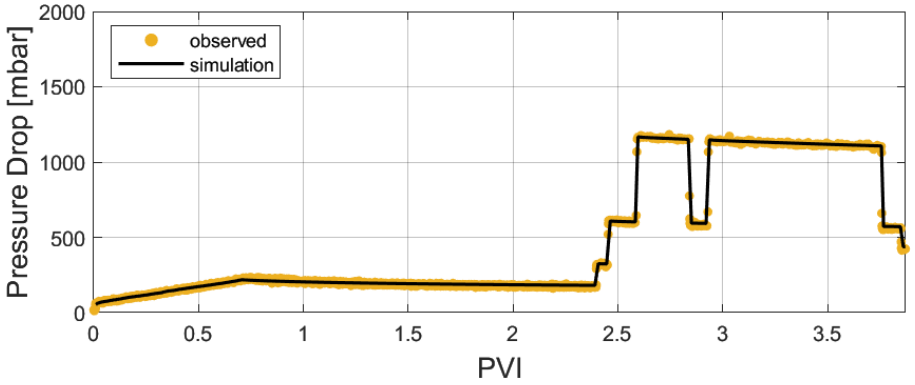

Figure I.2. Pressure drop match for primary drainage, experiment B2.

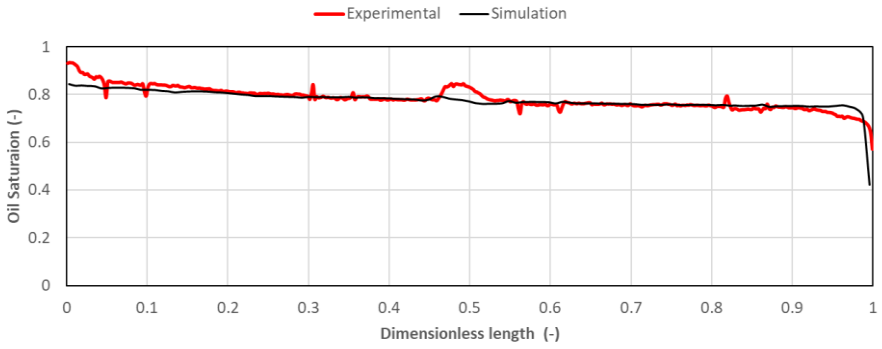

Figure I.3. Oil saturation match at the end of primary drainage, experiment B2.

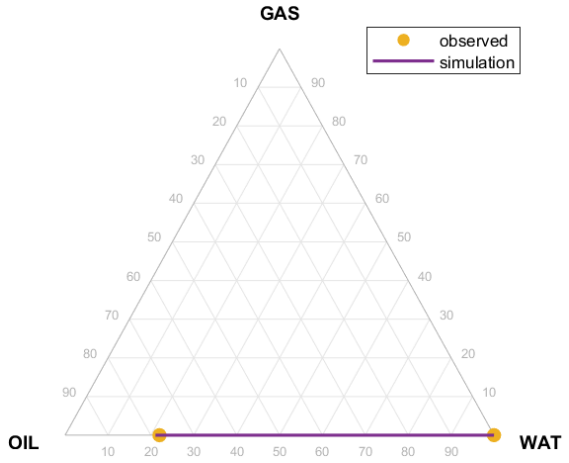

Figure I.4. Average saturation match for primary drainage, experiment B2.

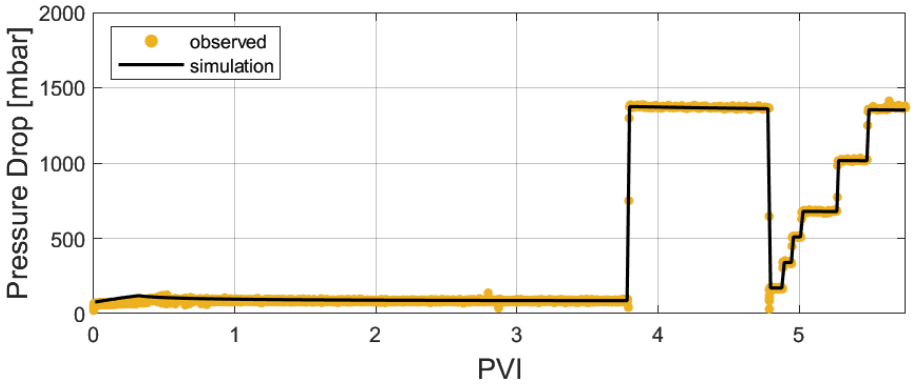

Figure I.5. Pressure drop match for forced imbibition, experiment B2.

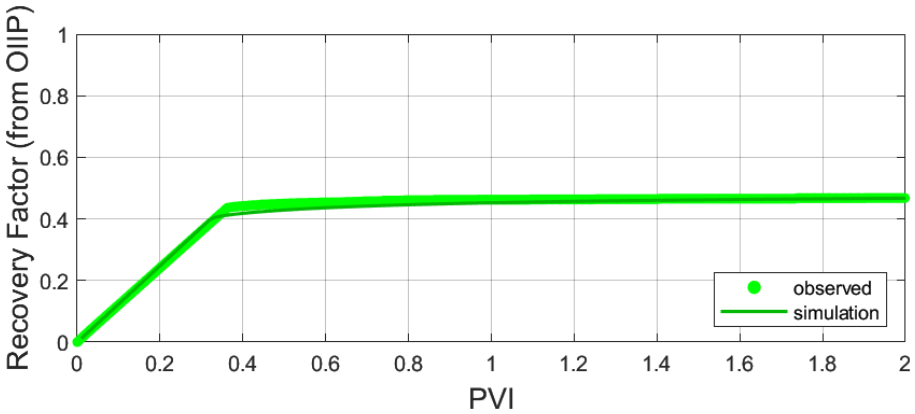

Figure I.6. Oil recovery factor (from OIIP) match for forced imbibition, experiment B2.

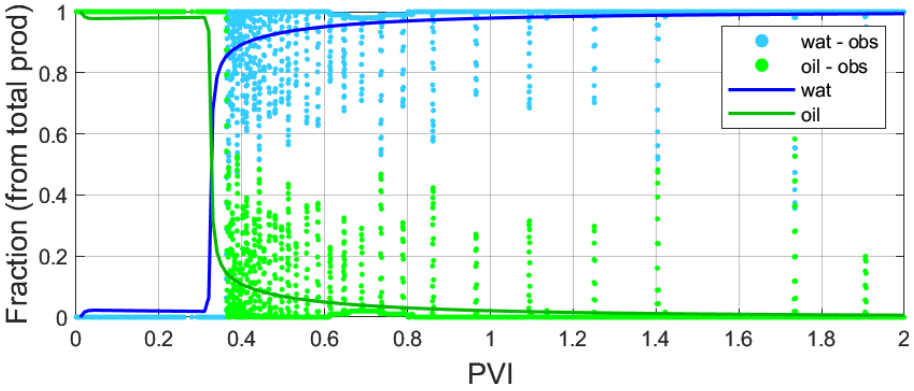

Figure I.7. Water breakthrough match for forced imbibition (Coriolis data), experiment B2.

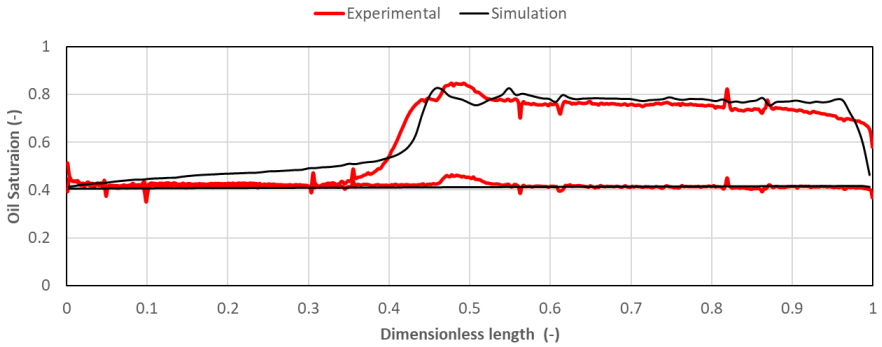

Figure I.8. Oil saturation match at several PVI during forced imbibition, experiment B2.

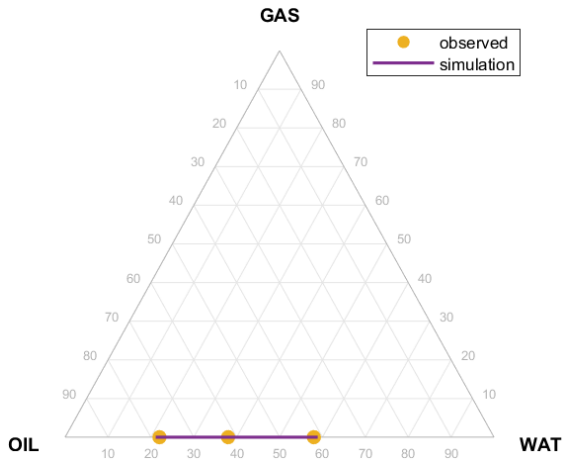

Figure I.9. Average saturation match for primary drainage, experiment B2.

I.2 Surfactant Slug

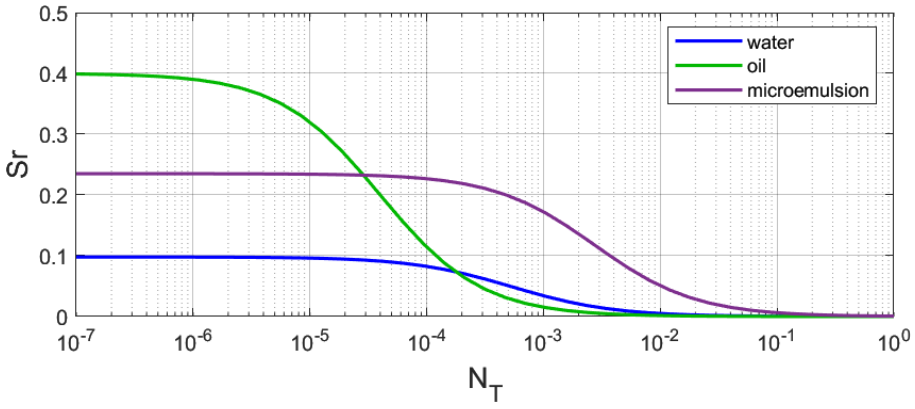

Figure I.10. Capillary Desaturation Curve (CDC) for surfactant slug, experiment B2.

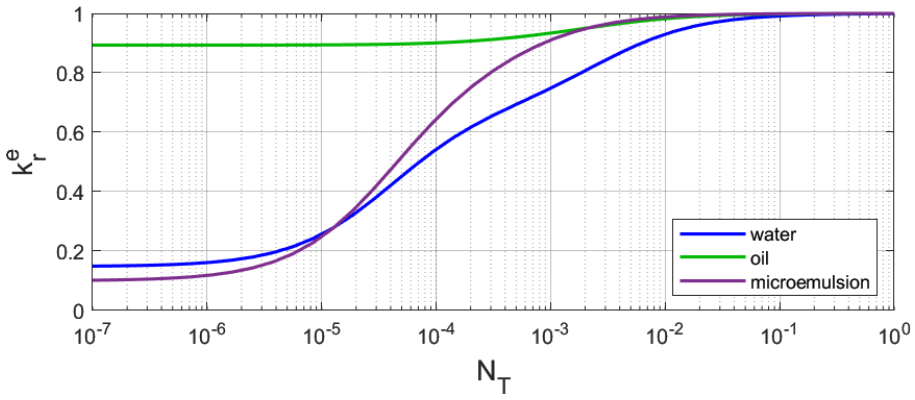

Figure I.11. End-point relative permeability as a function of trapping number for surfactant slug, experiment B2.

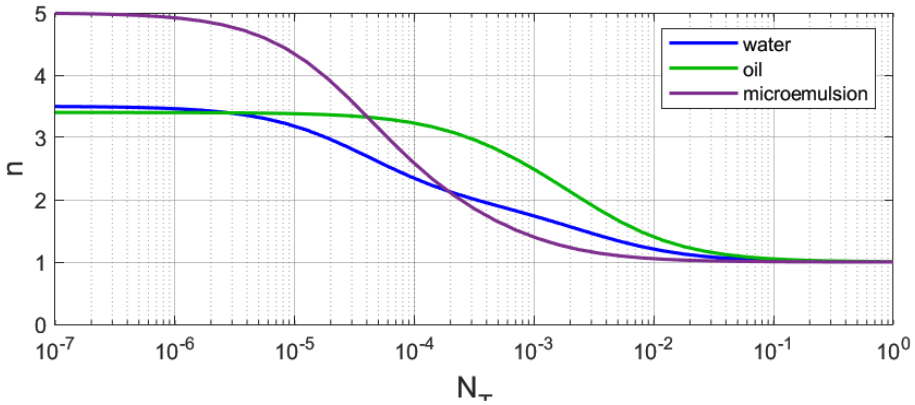

Figure I.12. Shape coefficients as a function of trapping number for surfactant slug, experiment B2.

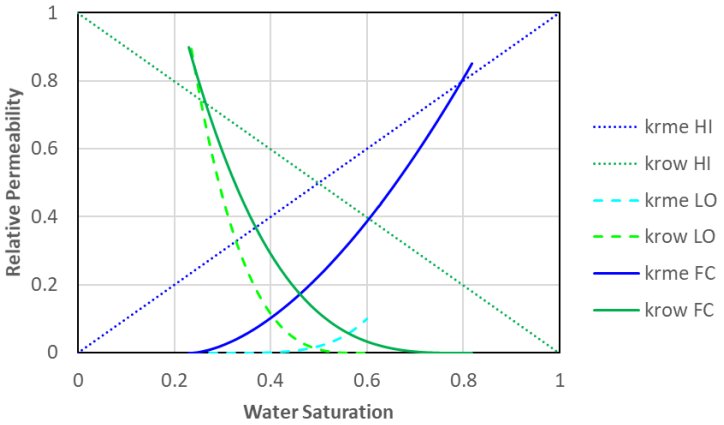

Figure I.13. Oil and water relative permeability curves for surfactant flooding at high (HI) and low (LO) trapping numbers, and final conditions (FC), experiment B2.

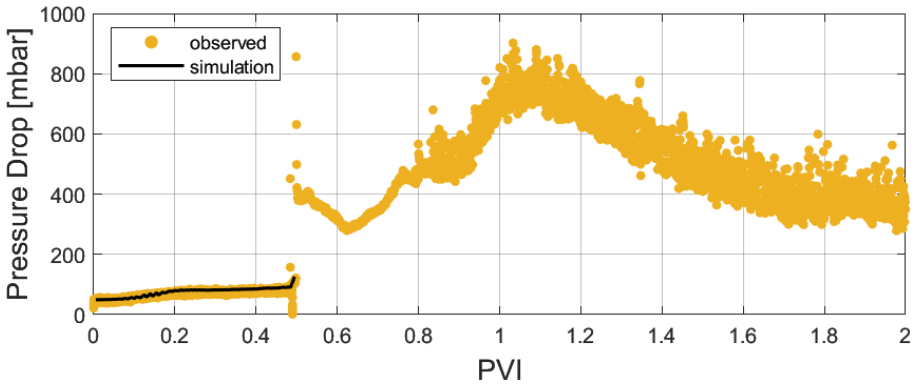

Figure I.14. Pressure drop match for surfactant slug, experiment B2.

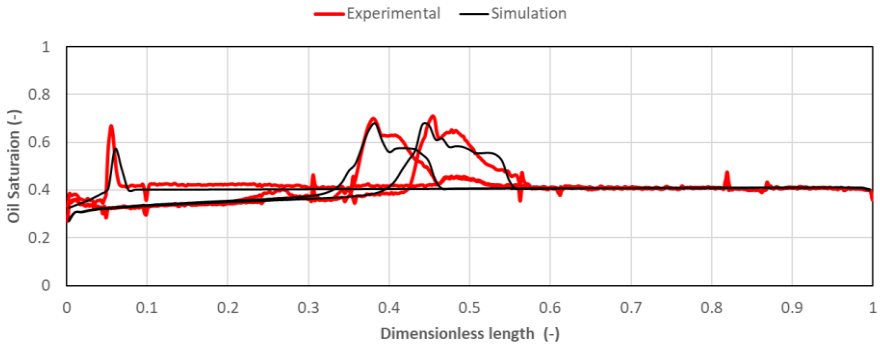

Figure I.15. Oil saturation match at several PVI during surfactant slug, experiment B2.

I.3 Foam Drive

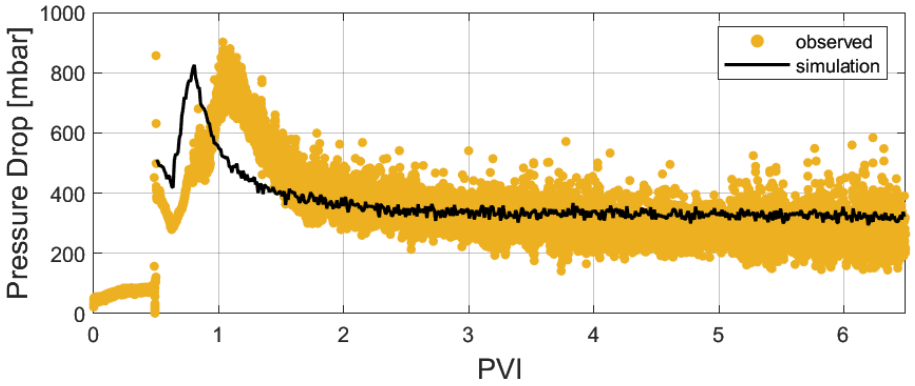

Figure I.16. Pressure drop match for FACF, experiment B2.

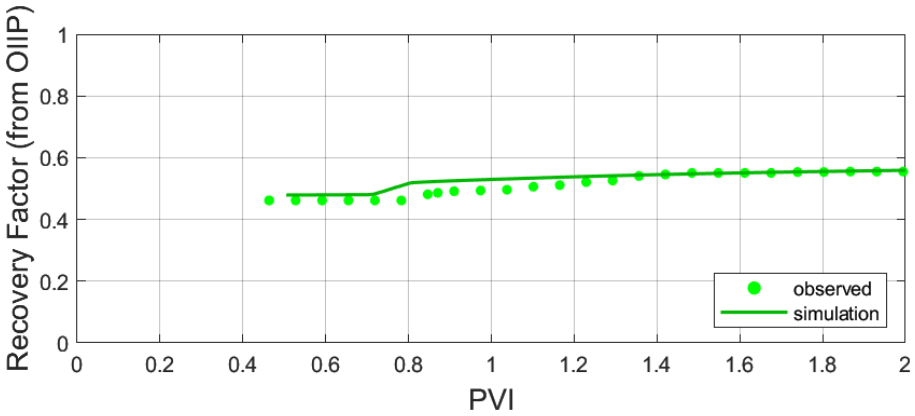

Figure I.17. Oil recovery factor (from OIIP) match for FACF, experiment B2.

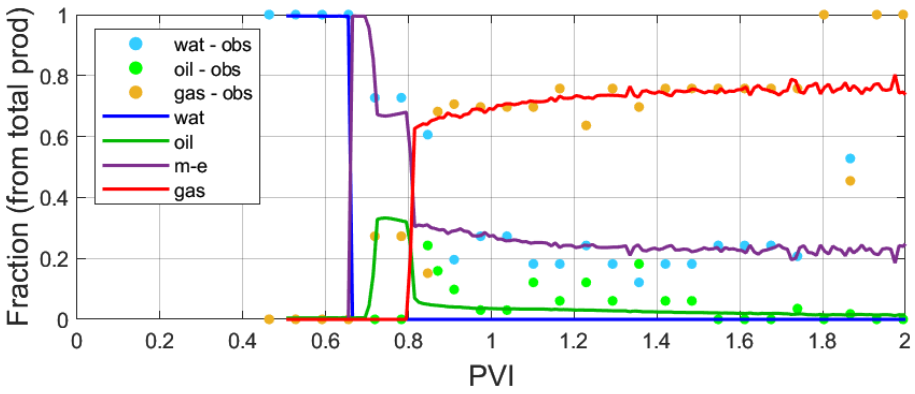

Figure I.18. Production fractions match for FACF, experiment B2.

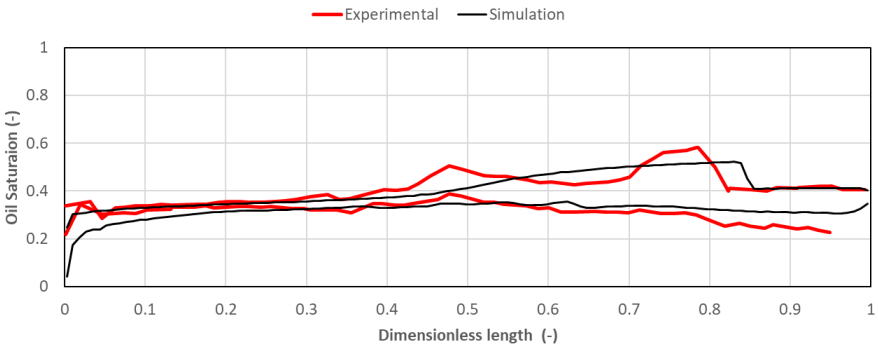

Figure I.19. Oil saturation match at several PVI during FACF, experiment B2.

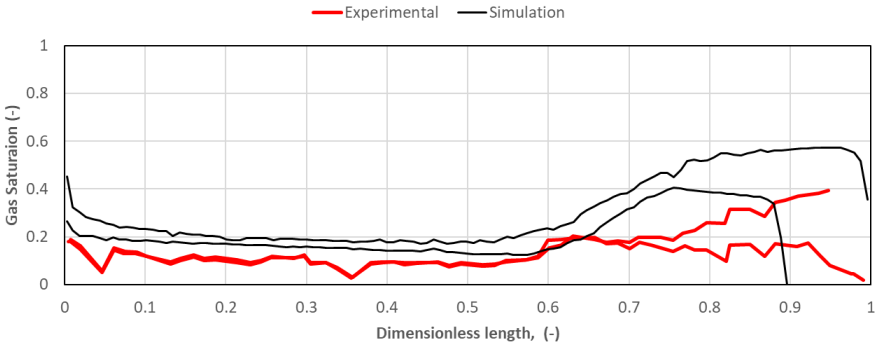

Figure I.20. Gas saturation match at several PVI during FACF, experiment B2.

APPENDIX J Experiment B3 History Match Results

J.1 Primary Drainage and Forced Imbibition

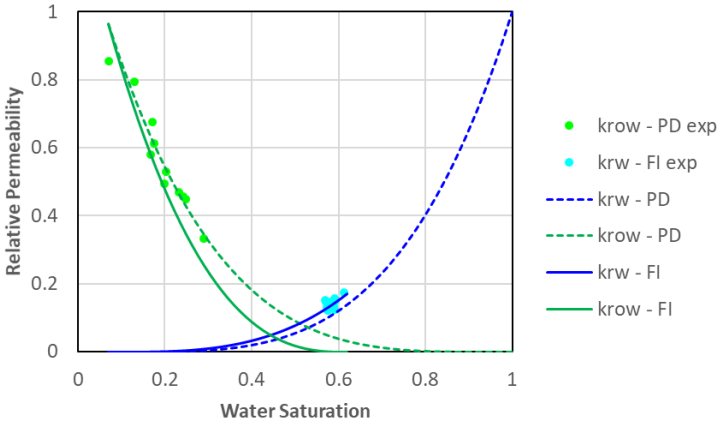

Figure J.1. Oil and water relative permeability curves for primary drainage (PD) and forced imbibition (FI), experiment B3.

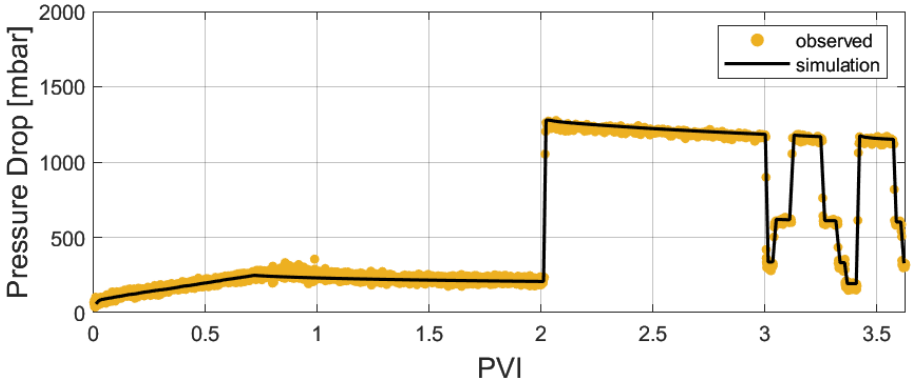

Figure J.2. Pressure drop match for primary drainage, experiment B3.

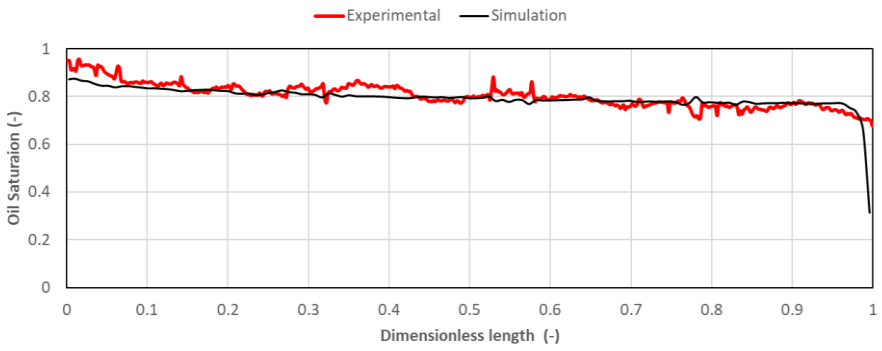

Figure J.3. Oil saturation match at the end of primary drainage, experiment B3.

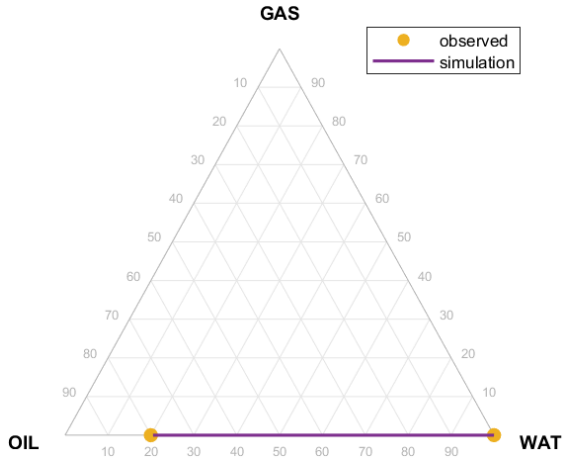

Figure J.4. Average saturation match for primary drainage, experiment B3.

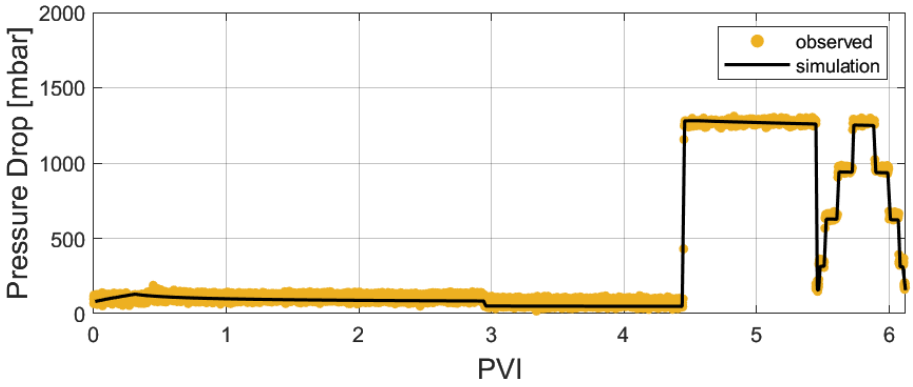

Figure J.5. Pressure drop match for forced imbibition, experiment B3.

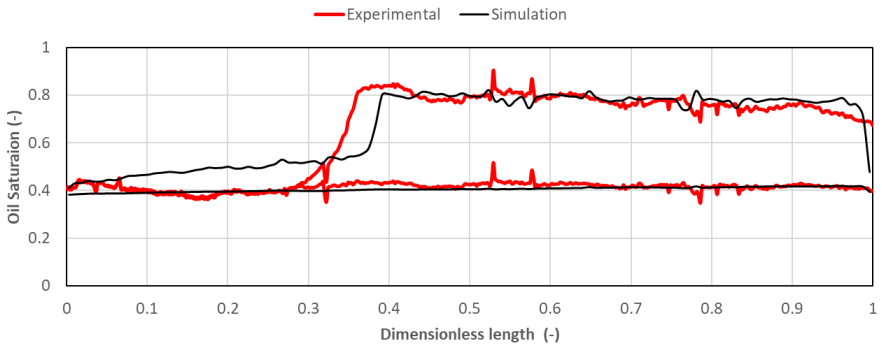

Figure J.6. Oil saturation match at several PVI during forced imbibition, experiment B3.

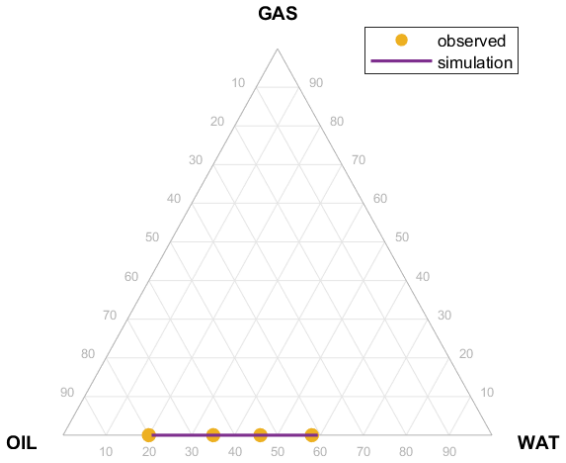

Figure J.7. Average saturation match for primary drainage, experiment B3.

J.2 Surfactant Slug

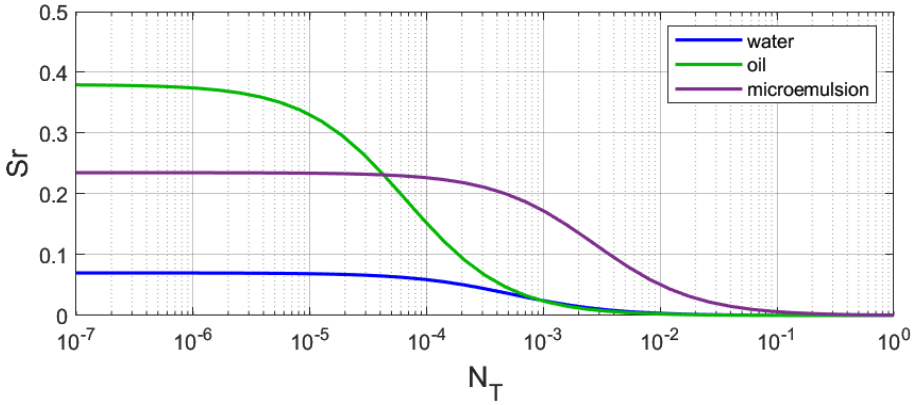

Figure J.8. Capillary Desaturation Curve (CDC) for surfactant slug, experiment B3.

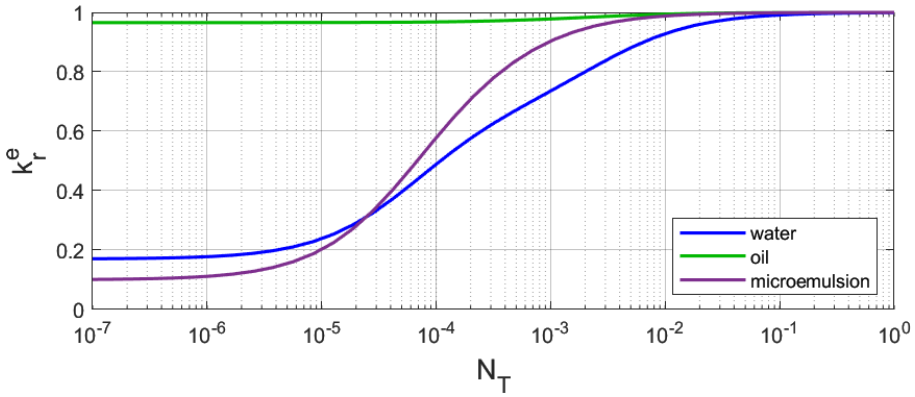

Figure J.9. End-point relative permeability as a function of trapping number for surfactant slug, experiment B3.

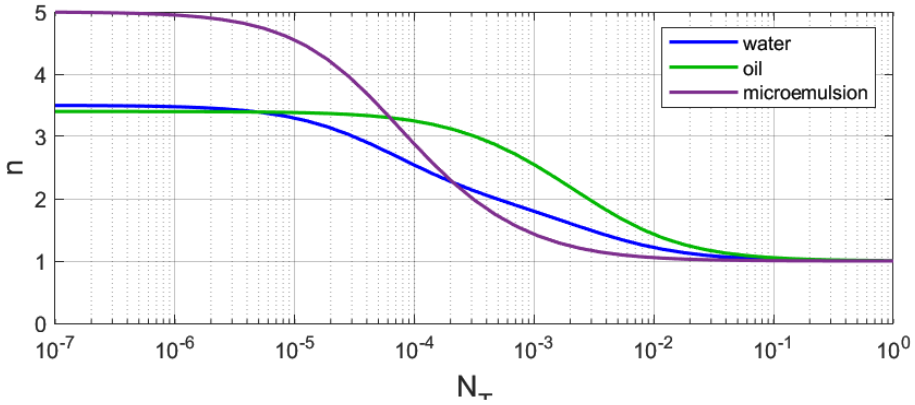

Figure J.10. Shape coefficients as a function of trapping number for surfactant slug, experiment B3.

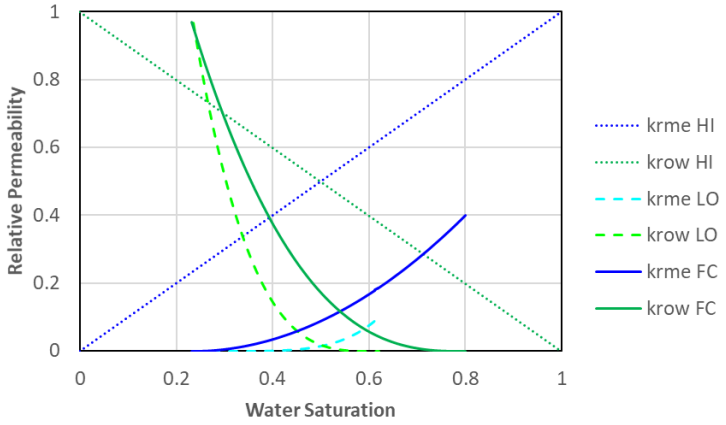

Figure J.11. Oil and water relative permeability curves for surfactant flooding at high (HI) and low (LO) trapping numbers, and final conditions (FC), experiment B3.

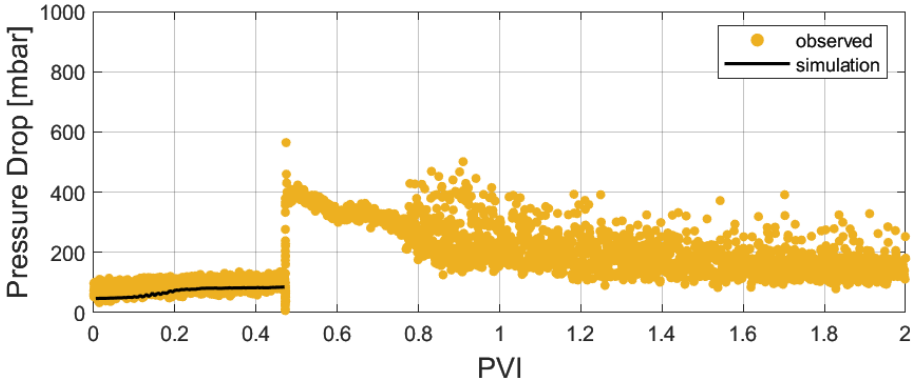

Figure J.12. Pressure drop match for surfactant slug, experiment B3.

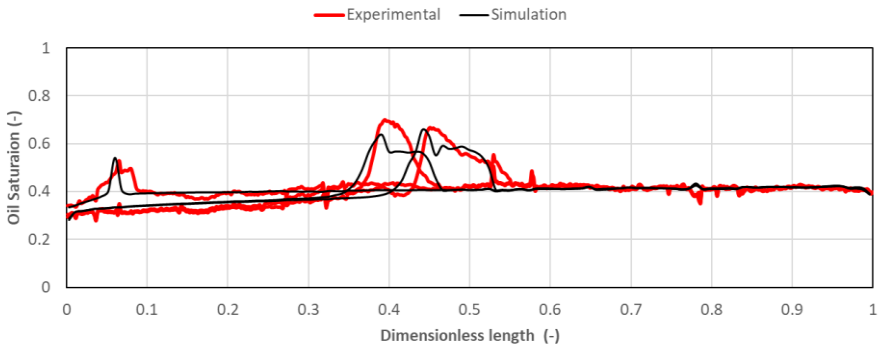

Figure J.13. Oil saturation match at several PVI during surfactant slug, experiment B3.

J.3 Foam Drive

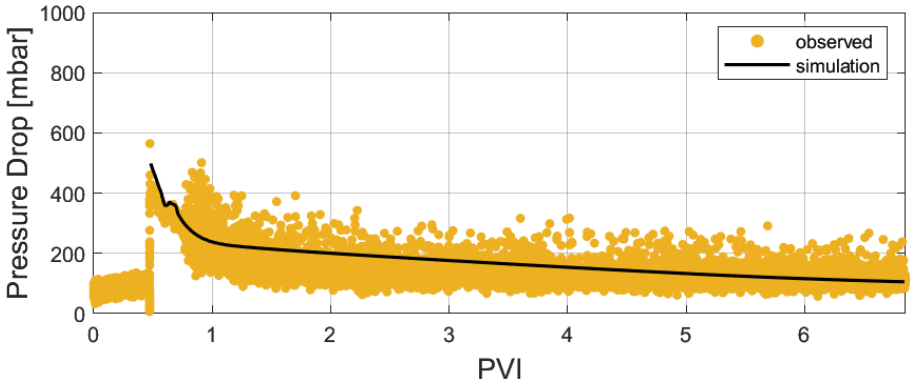

Figure J.14. Pressure drop match for FACF, experiment B3.

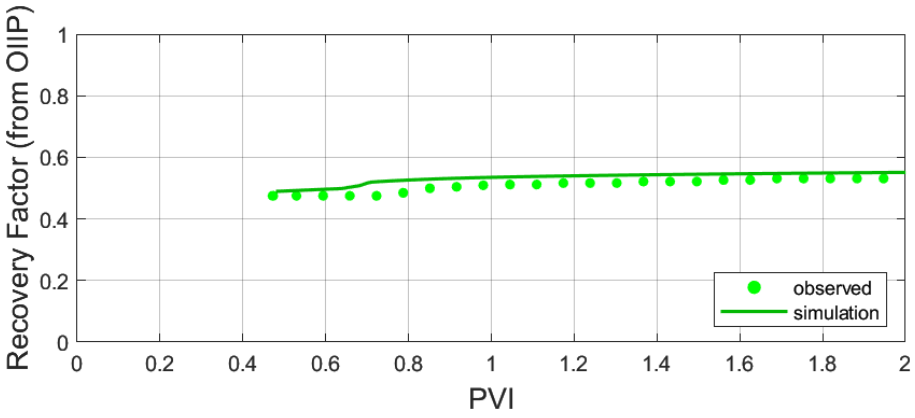

Figure J.15. Oil recovery factor (from OIIP) match for FACF, experiment B3.

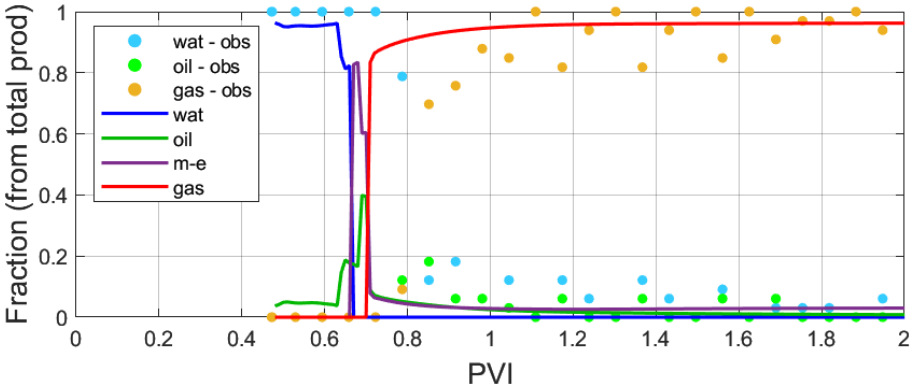

Figure J.16. Production fractions match for FACF, experiment B3.

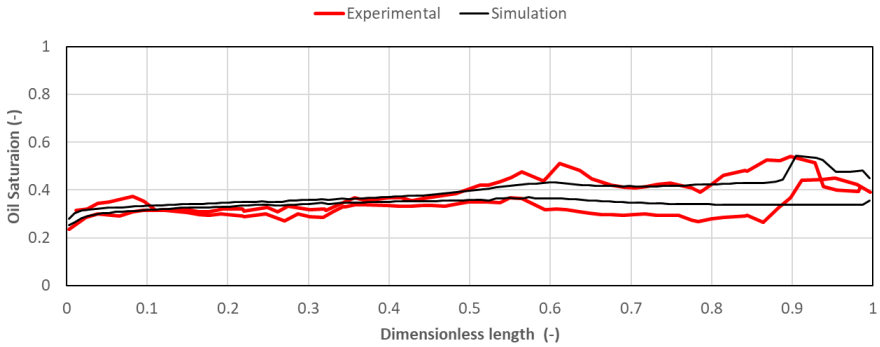

Figure J.17. Oil saturation match at several PVI during FACF, experiment B3.

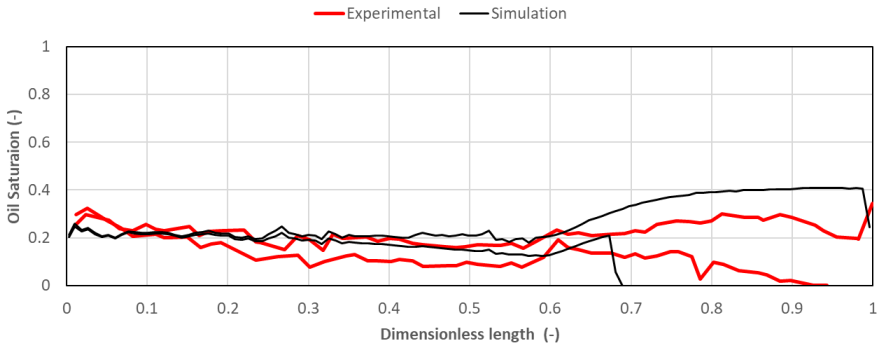

Figure J.18. Gas saturation match at several PVI during FACF, experiment B3.

APPENDIX K Experiment B4 History Match Results

K.1 Primary Drainage and Forced Imbibition

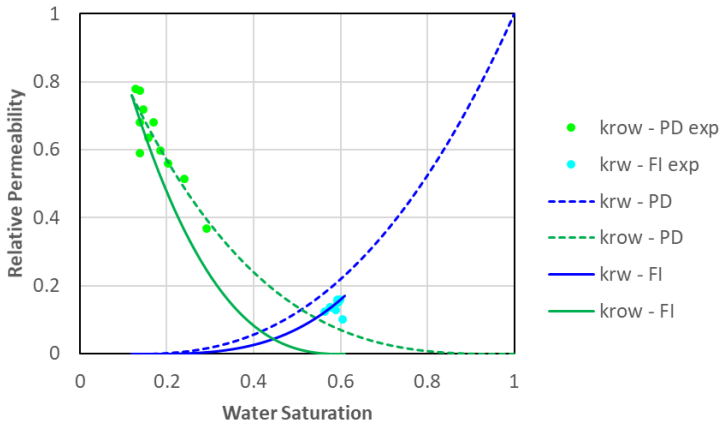

Figure K.1. Oil and water relative permeability curves for primary drainage (PD) and forced imbibition (FI), experiment B4.

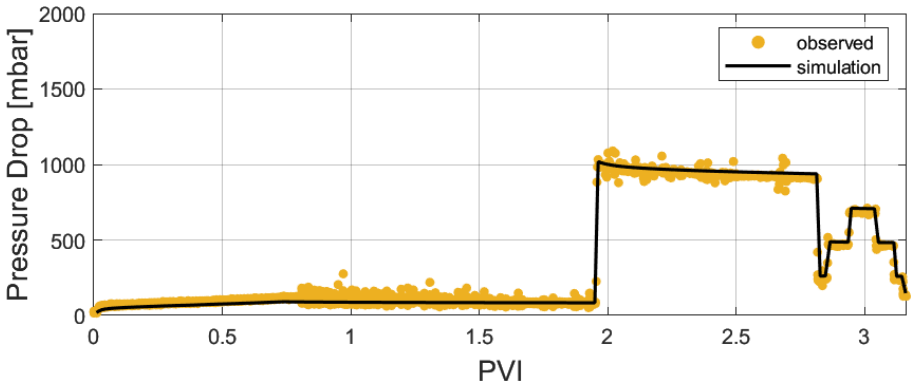

Figure K.2. Pressure drop match for primary drainage, experiment B4.

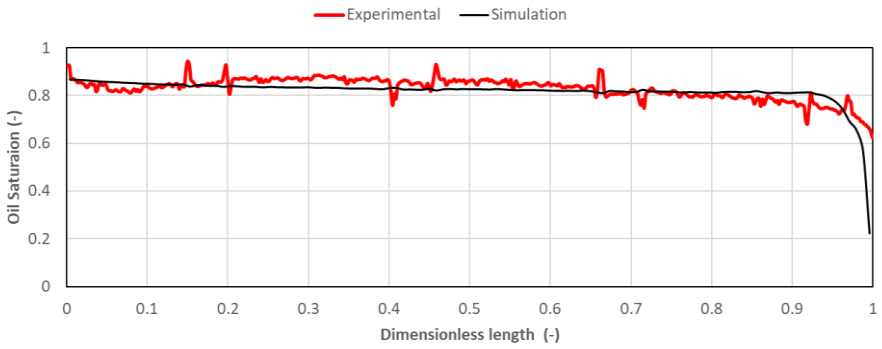

Figure K.3. Oil saturation match at the end of primary drainage, experiment B4.

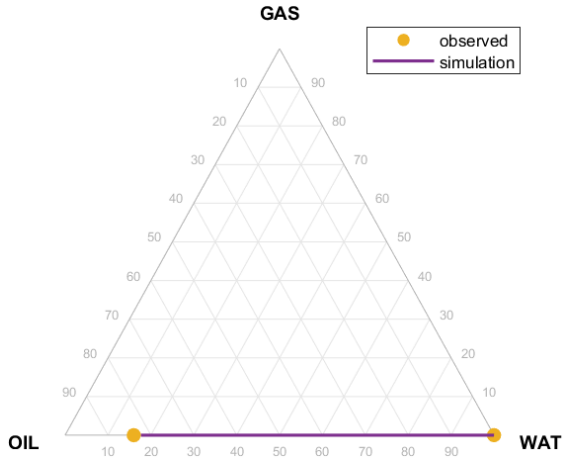

Figure K.4. Average saturation match for primary drainage, experiment B4.

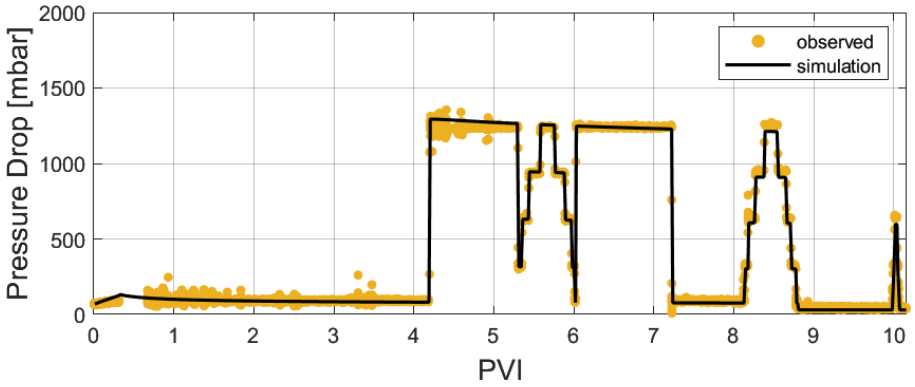

Figure K.5. Pressure drop match for forced imbibition, experiment B4.

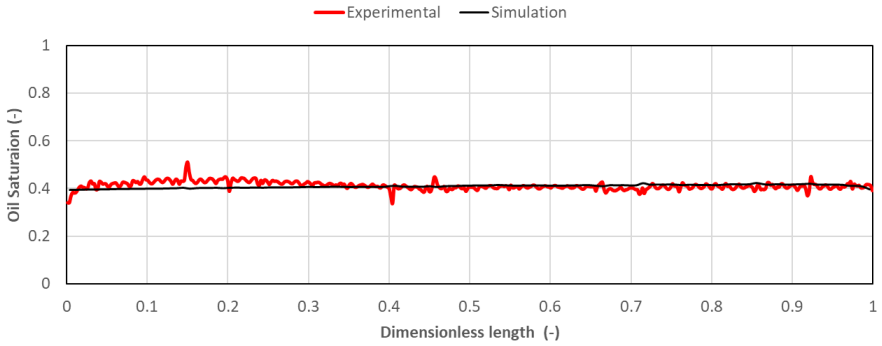

Figure K.6. Oil saturation match at the end of forced imbibition, experiment B4.

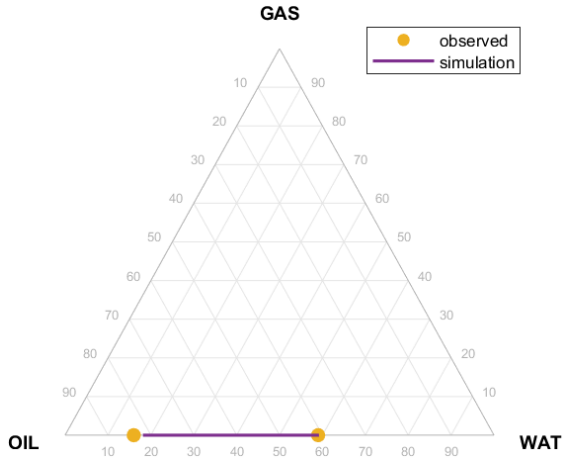

Figure K.7. Average saturation match for primary drainage, experiment B4.

K.2 Surfactant Slug

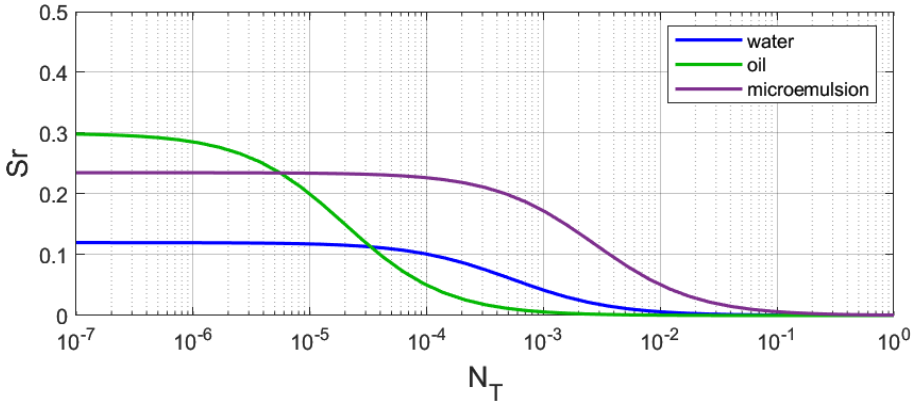

Figure K.8. Capillary Desaturation Curve (CDC) for surfactant slug, experiment B4.

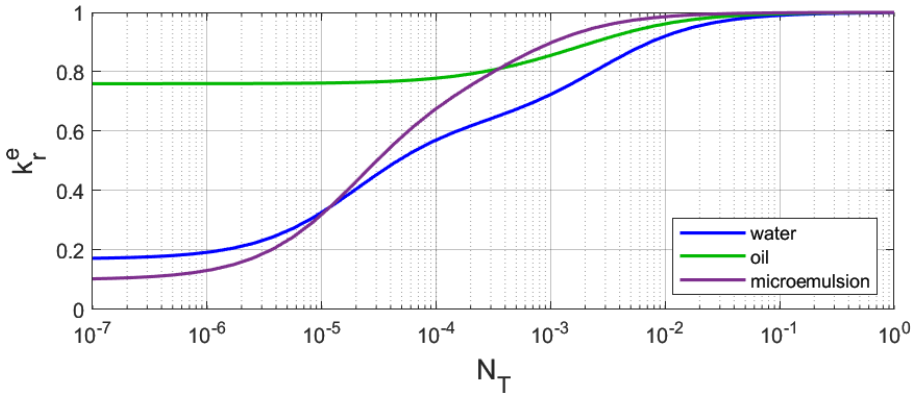

Figure K.9. End-point relative permeability as a function of trapping number for surfactant slug, experiment B4.

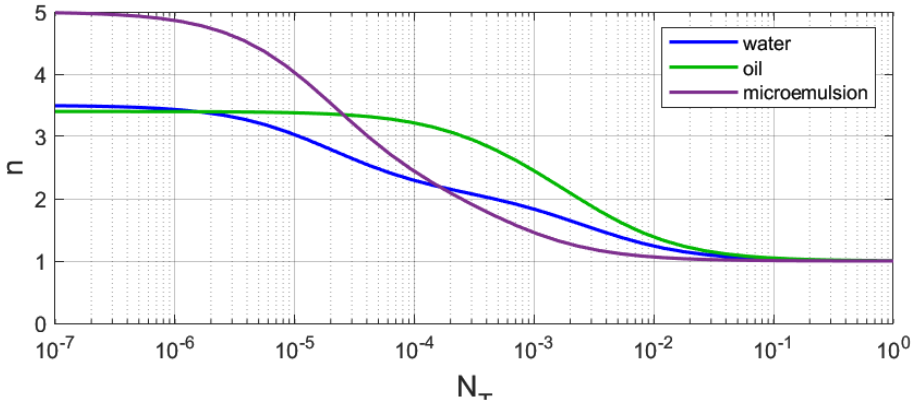

Figure K.10. Shape coefficients as a function of trapping number for surfactant slug, experiment B4.

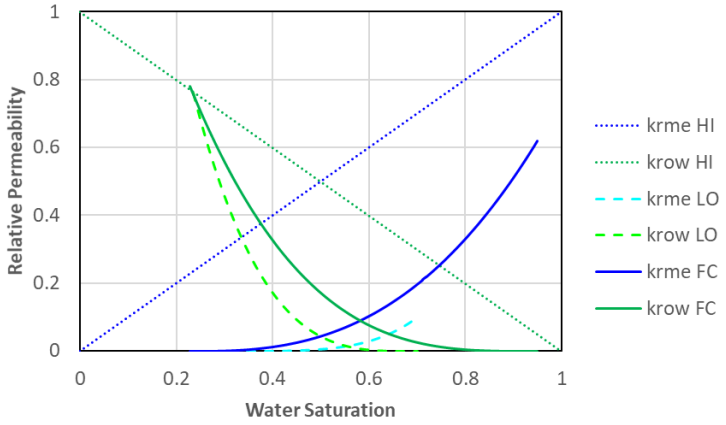

Figure K.11. Oil and water relative permeability curves for surfactant flooding at high (HI) and low (LO) trapping numbers, and final conditions (FC), experiment B4.

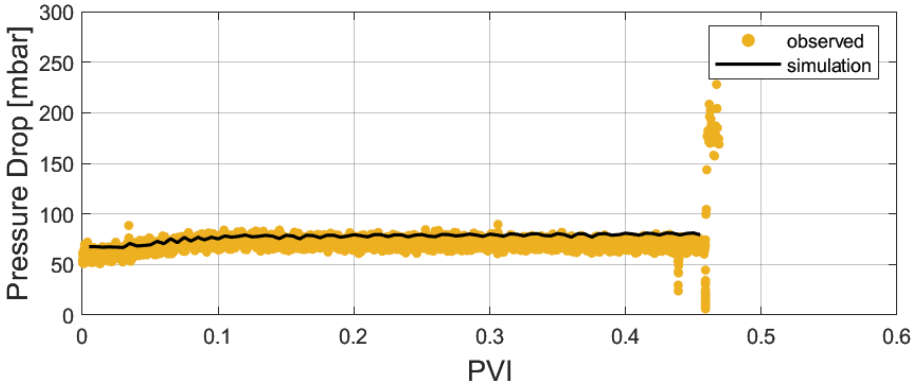

Figure K.12. Pressure drop match for surfactant slug, experiment B4.

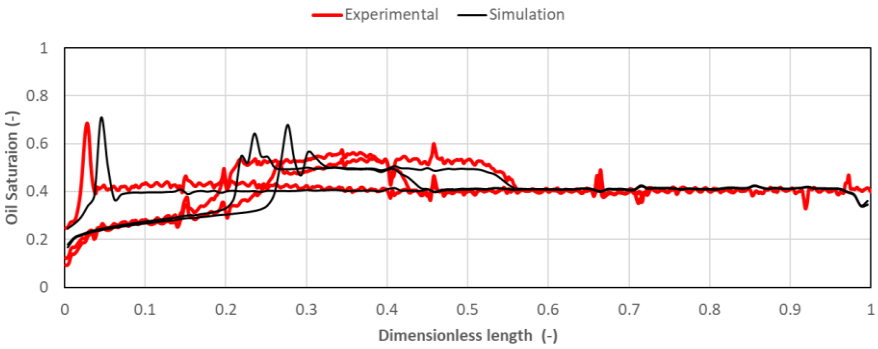

Figure K.13. Oil saturation match at several PVI during surfactant slug, experiment B4.